UNIVERSITÀ degli STUDI di CATANIA

Dipartimento di Scienze
Biologiche, Geologiche e Ambientali

PhD Course in "Earth and Environmental Sciences"

Dottorato di Ricerca in "Scienze della Terra e dell'Ambiente"

XXXIII Cycle

ASCENT RATES VS. DEGASSING AT BASIC VOLCANOES: QUANTIFICATION OF THE PARAMETER TEMPO AS PRIMARY FACTOR CONTROLLING THE EXPLOSIVITY OF ERUPTIONS

Francesco Zuccarello

Advisor:
Prof. Marco Viccaro

Coordinator:
Prof. Agata Di Stefano

January 2021

ACKNOWLEDDGEMENTS

I wish to thank my tutor prof. *Marco Viccaro* with sincere heart for guiding me through the PhD project and for his precious teachings which allowed me to grow up during these years. I owe him a lot.

Many thanks to all the people (researchers, technicians, PhD students, post-doc…) of LMV (Clermont-Ferrand, France), which helped me a lot in data collection during the abroad period of the PhD project. In particular, special thanks to my dear friend *Federica Schiavi*, who supervised me during collection of Raman and FTIR data, as well she was fundamental for the achievement of the aim of the work thanks to the many constructive discussions about data interpretation. I'm grateful also to *Jean-Luc Devidal* for his support in the collection of EMPA and LA- ICPMS data, and to the director of LMV, *Didier Laporte*.

Many thanks to prof. Alessandro Aiuppa and prof. Sumit Chakraborty for their availability in reviewing the thesis and for their comments which helped to improve the draft of this work.

Finally, thanks to all my colleagues and friends who shared this important experience with me during these three years.

INDEX

ABSTRACT

The rate of magma ascent is a crucial parameter in determining the explosivity of an eruption. Its role must be evaluated especially for violent eruptive episodes involving basic magma at open conduit volcanic systems, where low viscosity magmas generally feed weak explosive and/or effusive activity. A recent approach of investigation based on diffusion chronometry of volatile species along olivine-hosted embayments has been used to fix ascent rates for some eruptions occurred in arc volcanoes. This approach measures compositional gradients of volatile elements (i.e. H_2O, CO_2, S) that are produced by diffusion from the inner part of the embayment toward the outer melt as a response of degassing-driven decompression. Numerical modeling can retrieve timescales of diffusion, allowing an estimation of ascent rates. Quantification of volatile species dissolved in olivine-hosted melt inclusions is necessary for recognizing the original volatile contents in the magma, in order to track the degassing path and get the exsolution depth for each volatile component. Initial volatile contents and initial pressure before decompression need to be therefore constrained through melt inclusion-based studies.

Mt. Etna volcano has been chosen as case study, which is one of the most active open conduit volcanoes worldwide. Specifically, three eruptive episodes characterized by different explosive intensity have been selected from the post-2011 recent activity, in order to figure out a range of ascent rates related to the different explosive intensities. The recent eruptive episodes include: 1) the paroxysmal episode of the February 19, 2013 at the New South East Crater (NSEC); 2) the violent eruption of the December 3, 2015 occurred at the Voragine Crater; 3) the flank eruption that affected the southeastern sector of the volcanic edifice on December 24-27, 2018.

Modeling of volatile diffusion along melt embayment furnishes important indications on differences in the decompression-driven timescales of degassing for magmas emitted with

markedly distinct eruptive dynamics at Mt. Etna volcano, starting from very similar physical and chemical conditions. Indeed, the intense paroxysmal activity at NSEC and Voragine are characterized by fast rates of magma ascent (0.11-0.57 MPa/s), really one order of magnitude greater than values obtained for the flank eruption occurred on Christmas 2018 (0.017-0.045 MPa/s). Results point out a crucial contribution of syn-eruptive degassing kinetics in controlling the intensity of explosive activity at Mt. Etna, which generally have been ascribed to the overpressurization of the shallowest reservoir due to gas injection coming from the deepest levels of the plumbing system.

Keywords: Mt. Etna, explosive eruptions, magma ascent rates, volatiles, melt inclusions, embayments, diffusion modeling

RIASSUNTO

Il tasso di risalita del magma rappresenta un parametro fondamentale nella determinazione dell'esplosività di una eruzione. Il suo ruolo deve essere valutato in particolar modo in casi di episodi eruttivi violenti in cui sono coinvolti magmi basici in vulcani a condotto aperto, dove le basse viscosità dei magmi generalmente alimentano attività debolmente esplosive e/o effusive. Un recente approccio di studio basato sulla diffusione degli elementi volatili lungo gli *embayments* presenti in cristalli di olivina è stato impiegato per la stima dei tassi di risalita del magma per alcune eruzioni in vulcani di arco. Questo approccio misura i gradienti composizionali degli elementi volatili (ovvero H_2O, CO_2, S) che sono generati dalla loro diffusione dalla parte interna degli *emabyments* verso il fuso esterno in risposta al degassamento indotto dalla decompressione. Modelli numerici permettono di calcolare il tempo in cui avviene il processo di diffusione, riuscendo così a determinare una stima del tasso di risalita. La quantificazione delle concentrazioni delle specie volatili disciolte nelle inclusioni presenti in cristalli di olivina è necessaria per risalire ai contenuti originari dei volatili nel magma, in modo da definire il percorso di degassamento e vincolare le profondità di essoluzione per ciascuna componente volatile. Le concentrazioni iniziali dei volatili e le pressioni iniziali alle quali ha inizio la decompressione devono essere quindi vincolate tramite lo studio delle inclusioni vetrose.

Il vulcano Mt. Etna è stato scelto come caso studio, il quale rappresenta uno dei più attivi vulcani a condotto aperto nel mondo. Specificamente, 3 episodi eruttivi caratterizzati da differente esplosività sono stati selezionati dalla recente attività post-2011, in modo da definire un intervallo di tassi di risalita associate alle differenti intensità esplosive. I recenti episodi eruttivi includono: 1) L'episodio parossistico del 19 febbraio 2013 al Nuovo Cratere di Sud Est (NSEC); 2) la violenta eruzione del 3 dicembre 2015, verificatasi al Cratere Voragine (VOR);

3) l'eruzione di fianco che ha interessato il settore sudorientale dell'edificio vulcano nei giorni 24-27 dicembre 2018.

La modellizzazione della diffusione degli elementi volatili lungo gli *embayments* ha permesso di ricavare importanti informazioni sui tempi di degassamento indotti dalla decompressione per magmi emessi con dinamiche eruttive marcatamente distinte al vulcano Mt. Etna, partendo da condizioni fisico-chimiche molto simili. Infatti, le intense attività parossistiche al NSEC e alla Voragine sono caratterizzate da alti tassi di risalita (0.11-0.57 MPa/s), un ordine di grandezza più grande dei valori ottenuti per l'eruzione di fianco avvenuta a Natale 2018 (0.017-0-045 MPa/s). I risultati indicano un contributo cruciale delle cinetiche di degassamento sin-eruttivo nel controllo dell'intensità delle eruzioni esplosive al Mt. Etna, che generalmente sono state attribuite alla sovrappressione della camera più superficiale dovuto dall'apporto di gas proveniente dalle zone più profonde del sistema di alimentazione.

Parole chiave: Mt. Etna, eruzioni esplosive, tassi di risalita del magma, volatili, inclusioni vetrose, embayments, modelli di diffusione

1. INTRODUCTION

The intensity of an explosive eruption is chiefly dependent on the magnitude of overpressure produced by gas bubbles, which originate through volatile exsolution from the melt, and on the consequent style of magma fragmentation (Gonnermann and Manga, 2007, Gonneramann, 2015). The exsolution process starts when volatiles reach the saturation pressure, which is in turn function of the initial concentrations of volatile elements, lithostatic pressure and solubility of each dissolved volatile element. Saturation conditions can be reached mainly for two reasons: 1) crystallization and fractionation of anhydrous mineral phases, which lead to an increase of volatile concentrations in the melt; 2) decompression of the magmatic system during the ascent toward the surface, which induces solubility decrease of volatile elements, with major effects on H_2O, CO_2 and S. Many studies highlighted how the decompression rate, induced by the ascent, plays a key role on the determination of the explosivity of an eruption, since it strongly affects the kinetics of nucleation, growing and coalescence of bubbles, and consequent gas overpressure (Mangan and Cashmann, 1996; Rutherford, 2008; Gonnermann, 2015). Generally, low rates of magma ascent promote efficient separation of the volatile phase from the magma, leading to a more effusive character of an eruption (Parfitt, 2004; Gonnermann and Manga, 2007). On the contrary, high rates of magma ascent preclude the effective loss of volatile elements from the magma, because volatile diffusion into the bubble is not counterbalanced by the progressive decrease of solubility due to decompression. The viscosity-limited bubble growth leads to a consequent growing of volatile pressure contained in the bubbles (Houghton and Gonnermann, 2008). Kinetics of syn-eruptive degassing has also significant effect on the rheological magma properties, mainly depending on the crystallinity (which may increase due to ascent-driven crystallization of the groundmass), on the presence of bubbles not escaped from the melt and from the temperature

variation and for the increasing of melt polymerization due to volatile exsolution. Such parameters strongly control the magma viscosity, producing potentially increases of several orders of magnitude during the syn-eruptive ascent and leading therefore to explosive eruptions (e.g. Arzilli et al., 2019).

Importance of the magma ascent rate in controlling the explosive intensity of an eruption with respect to other factors (e.g. viscosity, volatile budget, conduit geometry, interaction with external water) must be evaluated even in basaltic and open-conduit system volcanoes. The relative low viscosity of basic magmas promotes generally effusive or weak explosive activity (e.g. Strombolian activity), differently from more acid magmas characterized by higher viscosity and volatile contents. However, a huge spectrum of eruptive styles can characterize volcanoes where basaltic magmas are involved. Indeed, unusually explosive and unexpected eruptions have been observed in such contests. Example of basaltic volcanoes where Plinian/Subplinian events occurred in recent times and in the pasts are: the Plinian eruption of 122 BC at Mt. Etna, Italy (Coltelli et al., 1998); the 1974 AD Subplinian eruption at Volcan De Fuego, Guatemala (Llyod et al., 2014); the 1886 eruption of Tarawera, New Zeland (Sable et al., 2006); the ca. 2 ka Plinian eruption at Masaya, Nicaragua (Pérez et al., 2009). Less intense lava fountaining, although highly energetic if compared to the ordinary activity, have been observed in recent times at basaltic s.l. volcanoes: the exceptional paroxysmal activity at Mt. Etna occurred between 2011 and 2016 (e.g. Behncke et al., 2014; Viccaro et al., 2014, 2015; Cannata et al., 2018); the vigorous lava fountaining at Villarrica volcano (Chile) on 16 March 2015 (Romero et al., 2015); the 3 June 2018 eruption at Volcan de Fuego, with development of PDCs causing several fatalities (Pardini et al., 2018); the paroxysmal eruptions occurred at Stromboli volcano (Italy) during the summer of 2019 (Giudicepietro et al., 2020).

Nowadays, magmatic dynamics and triggering mechanisms of these unusual eruptive phenomena causing major source of hazard at basaltic volcanoes are, however, still poorly

understood. The unexpected character of these events makes difficult a proper interpretation of precursory signals available from monitoring systems, especially in open-system volcanoes characterized by almost persistent activity where such signals may be source of misunderstanding.

Estimation of accurate magma ascent rates is a challenge for the modern volcanology, being among the principal factors controlling the eruptive styles at basaltic volcanoes. In this regard, useful methods of geochronometry have been developed in recent times for investigating magma kinetics, involving diffusion processes of elements either in solid or in the fluid phase (e.g. Costa et la., 2008). Approaches based on the volatile diffusion in melt pockets partially enclosed within host crystals, a so called "embayment", are promising as powerful techniques allowing the determination of syn-eruptive magma ascent rates, being the method based on diffusion of elements interested in the final degassing process. This approach has been successfully applied for arc-volcanoes (e.g. Humpreys et al., 2008; Llyod et al., 2014), where intermediate to acid magmas are involved, as well as for some past eruptions at Kilauea volcano (Ferguson et al., 2016).

Aim of this study is the determination of ascent rates for magmas erupted during variably explosive eruptions occurred in recent times at Mount Etna through modeling of volatile diffusion in embayments of crystal found in tephra. Volatile gradients along melt embayments, can be quantified by different microanalytical techniques, including: Raman and FTIR spectroscopy for estimating the H_2O and CO_2 dissolved in the melt, and EMPA analyses for measuring S concentrations. The same techniques can be used for quantification of volatile in melt inclusions; in fact, a preliminary investigation on melt inclusions is needed in order to evaluate the parameters to be used in the diffusion modeling. Namely, estimation of ascent rates has been performed taking into consideration tephra emitted during: a) the mostly effusive flank eruption of December 24-27, 2018; b) the mid-intensity paroxysmal eruption occurred at

NSEC on February 19, 2013; c) the highly energetic paroxysm of December 3, 2015 occurred at VOR. Assessing the original volatile budgets of magmas and how their volatile load changes throughout the present configuration of the plumbing system is crucial to reconstruct the degassing dynamics and to identify causes leading to energetic vs. quiet eruptions.

2. METHODS OF ESTIMATION OF MAGMA ASCENT RATES

2.1. Ascent rates estimation: a brief summary

Different methods have been adopted in an attempt to estimate syn-eruptive magma ascent rates in various volcanic systems. Such approaches are focused on investigation of processes primarily controlled by ascent-driven decompression toward the surface. So, evaluation of specific parameters can be related directly or indirectly to the magma ascent rates.

One direct method is based on the calculation of the Mass Eruptive Rates (MER), which is a measure of the intensity of an explosive eruption (Pyle, 2000). Ascent rate may be derived from MER through the Hagen-Poiseuille law (Rutherford, 2008 and reference in), where conduit radius, magma mass flux, density, and viscosity must be determined for an ascending magma assumed to be a one-phase, laminar flow of a Newtonian fluid. This model has been used for the estimation of magma ascent rates for the 1980-1986 eruptive activity at Mt. St. Helens (Rutherford and Hill, 1993). However, some parameters, in particular the conduit radius, are generally unknow and assuming them constant may lead to not entirely negligible uncertainties in the calculation. This could explain the discrepancies between results obtained through this approach and those from other methods **(Figure 1**, from Rutherford, 2008).

An important process that affects significantly the ascending magma is the exsolution of volatiles driven by decompression. Volatile loss from the melt causes in turn changes in textural and compositional features of the mineral assemblage. Such effects can be analyzed in order to retrieve indirectly ascent rates by investigating kinetics of the texture development. A method involves analysis of reaction rims produced during the breakdown of hydrous crystals as a response of volatile loss during decompression (Rutherford and Hill, 1993; Browne and Gardner, 2006). Indeed, the kinetics of the reaction between the crystals and the volatile-

depleted melt are dependent from the decompression rates. Such reactions are complex functions of many parameters, including mineral and glass compositions, melt viscosity, and temperature (Rutherford, 2008) and calibrations have been determined only for dacitic to rhyolitic melts, using as case of study the 1980-1986 eruptions at Mt. St. Helens (Rutherford and Hill, 1993).

Volatile exsolution may enhances also groundmass crystallization in the ascending magma. Some studies on both natural and experimental products of the 1980-1986 Mt. St. Helens eruptions showed how magma ascent rates can be retrieved from analyses of the groundmass crystallization (Geschwind and Rutherford 1995). Although a clear relationship is observed between the crystallization of the interstitial melts and volatile loss during the decompression, the rates of the two processes are not necessarily the same. The composition affects significantly the rate of crystallization, being slower in high silica magma at given water concentrations (Rutherford, 2008). Moreover, nucleation of the microlites in crystal-poor magma can take much longer, whereas the presence of phenocrysts may serve as nucleation sites (Westrich et al., 1988; Rutherford 2008). Therefore, very high ascent velocity linked to intense explosive eruptions may inhibit crystallization of interstitial melts, given that these conditions are not suitable for the crystallization of microlites.

If a dense seismic network is present in active volcanic area, analysis of real-time seismicity may constitute another direct method for evaluating magma ascent. The Kilauea activity along the rift zones, the 1977 eruption at Krafla (Rutherford, 2008 and reference in) and the recent 2014 eruption in the Holuhraun region (Sigmundsson et al., 2015) are documented cases where the magma movements toward to the rift zones are well correlated with the migration of the earthquake hypocenters. Relationships between earthquakes and magma movements can be, however, ambiguous, as the surrounding rocks close to magmatic batches can behave either seismically or aseismically. Earthquakes can occur when magma

movements affect the surrounding rocks with brittle behavior already stressed by the regional tectonic, as observed during migration from lateral pathways of the central conduit. Generally, in open-systems volcanoes persistent movements of hot fluids occur along the central conduits, which inhibit the brittle failure of rocks.

Other methods consider the xenoliths transport from depth and effects of chemical reactions involving the exchange of elements between the mineral assemblage of xenoliths and the host liquid. The presence of xenoliths depends on the ability of magma to transport them, which is function of different factors (e.g. ascent velocity, the rheology of the magma, xenolith size and density; Rutherford 2008 and references therein).

Volcano	Observation	Explosive Ascent Rate (m/s)	Extrusive Ascent Rate (m/s)
Mt St Helens, Washington	Groundmass crystallization	1–3	0.01–0.02
Mt St Helens, Washington	Hornblende reaction rims	>0.18	0.004–0.015
Mt St Helens, Washington	Extrusion rate	1–2	0.005–0.0001
Mt St Helens, Washington	Seismicity	0.6	0.007–0.01
Pinatubo, Philippines	Groundmass crystallization	>0.2	0.002–0.05
Soufrière Hills, Montserrat	Hornblende reaction rims	>0.2	0.001–0.012
Soufrière Hills, Montserrat	Extrusion rate	>0.2	0.0001–0.02
Black Butte, California	Hornblende reaction rims and plagioclase growth	Not present	>0.1
Arenal Volcano, Costa Rica	Groundmass crystallization	0.05–0.9	<0.05
Chaitén, Chile	Extrusion rate	>0.5	0.02–0.5

Modified from Rutherford (2008).

Figure 1: *Magma ascent rates estimation by using different methods of investigations (Rutherford, 2008; Browne and Szramek, 2015).*

However, diffusion modeling provided some benefits in the understanding of the dynamics and kinetics of various magmatic processes and in recent years it revealed to be an exceptional tool for calculating syn-eruptive ascent rates. Approaches based on chemical

exchange of fast diffusivity elements, which offer the possibility to investigate timescales pertinent to the syn-eruptive magma ascent, will be illustrated in the next paragraph.

2.2. Diffusion chronometers

Perturbations on chemical and physical conditions of the magmatic system can trigger diffusive exchange of atoms between phenocrysts and surrounding melts in order to achieve a new equilibrium. If eruption occurs before equilibrium is fully attained, the diffusion process stops and the crystal preserves a compositional zonation, which represents a shot of a specific time since the beginning of diffusion. Compositional zonation measured in crystals can be therefore used as a record of magmatic processes taking place during pre-to-syn-eruptive stages of the magmatic evolution. Improvement of microanalytical techniques offered the possibility to better estimate the rates at which elements diffuse and so the timing of specific processes triggering diffusion. Different models have been developed during the last 20 years aimed at obtaining timescales of magma storage and transfer across the plumbing system, as well as recharge and mixing processes that anticipate an eruption [e.g. Zellmer (1999) for Ba-Sr in plagioclase; Costa and Chakraborty (2004) for Mg-Fe in olivine; Morgan et al. (2004) for Mg-Fe in clinopyroxene; Allan et al. (2013) for Mg-Fe in orthopyroxene). Estimation of syn-eruptive ascent rates through application of standard diffusion clocks is however not possible, since diffusivity of the above mentioned elements is unable to record any significant compositional variations during the short timescales accompanying the ascent-driven decompression (taking seconds, minutes, hours). In this regard, new diffusion clocks based on the investigation of compositional gradients of fast diffusivity elements or volatiles species in minerals and volcanic glass represent the frontier for constraining magma ascent rates.

Lithium is an example of fast diffusivity element. The very high mobility of Li does not allow to preserve any compositional zonation acquired during the growth of plagioclase crystals (Genereau and Clarck, 2010; Charlier et al., 2012; Giuffrida et al., 2018). The presence of gradients at the plagioclase rims have been attributed to diffusion toward the external melt as a response of gas phase separation from the melt upon eruption, leading to a rapid depletion of Li in the melt in turn causing decrease of the Li concentration in plagioclase. Very short timescales, on the order of minutes, have been estimated for some volcanic systems. Average ascent rates of 4-21 m/s have been derived for the Oruanui eruption (Taupo volcano, New Zealand) starting from 22 MPa (which corresponds a depth of 1 km below the surface) and with timescales of 125 to 720 s (Charlier et al., 2012). Similar results have been calculated for some lava fountaining episodes occurred at Mt. Etna during the 2011-2013 paroxysmal sequence, with timescales of maximum of 183 s from 40 MPa (corresponding to a depth of 2 km below the summit and an average velocity of 43 m/s; Giuffrida et al., 2018). These results are representative of kinetics relative to the late-stages of degassing process in syn-eruptive conditions, providing the velocity of an ascending magma within the last kilometers of the conduit during explosive eruptions.

Improvements of microanalytical investigations in terms of spatial resolution and accuracy (e.g. NanoSIMS) enabled to measure compositional profiles of volatile species inside olivine-hosted melt embayments or melt tubes (**Figure 2**). An embayment is an elongated pocket of melt hosted in a crystal. Unlike melt inclusions, the embayment is not fully enclosed into the host crystal but communicating with the external melt.

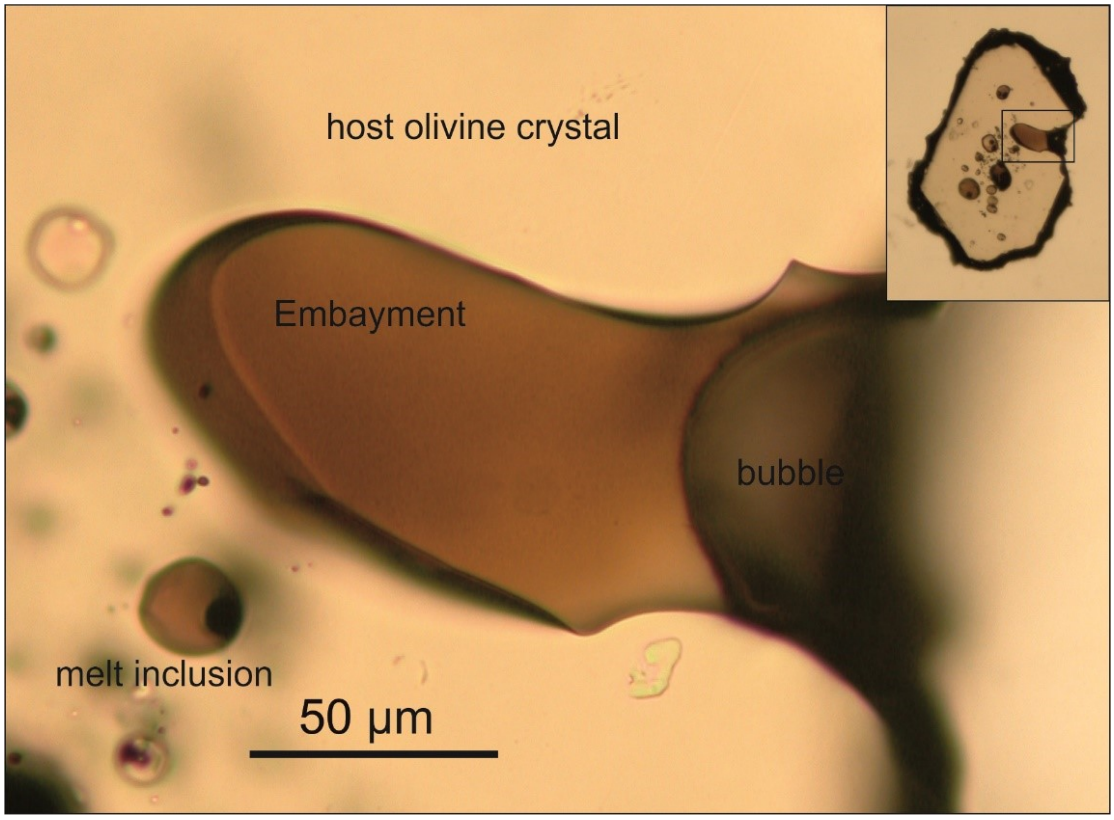

Figure 2: *An example of olivine-hosted melt embayment, found in tephra erupted during the paroxysmal eruption of 19 February 2013 at Mt. Etna.*

So, it is assumed that the melt inside the embayment maintains an equilibrium with the external melt, exchanging chemical elements during the evolution of the magma (**Figure 3a**), differently from melt inclusions which can (potentially) preserve the magma chemical features at the time of the entrapment. The presence of compositional gradients of volatile species measured along the embayment reflects diffusion process of volatile elements as a response of degassing the magma undergoes during ascent-driven decompression (Humpreys et al., 2008, Lloyd et al., 2014). Volatiles migrate from the inner part of the embayment toward its open side, forming a bubble in the surrounding melt. If the equilibrium is not reached before an incoming eruption, compositional gradients are preserved, and diffusion models can fix the timescales of magma decompression (**Figure 3b**). In this case, a basic assumption considers the decompression process as a function exclusively of the ascent from the storage area to the surface. Therefore,

the advantage of this petrological approach consists in the direct involvement of the considered elements in the degassing dynamics during ascent, offering the opportunity to investigate timescales pertinent to the syn-eruptive degassing process driven by the ascent.

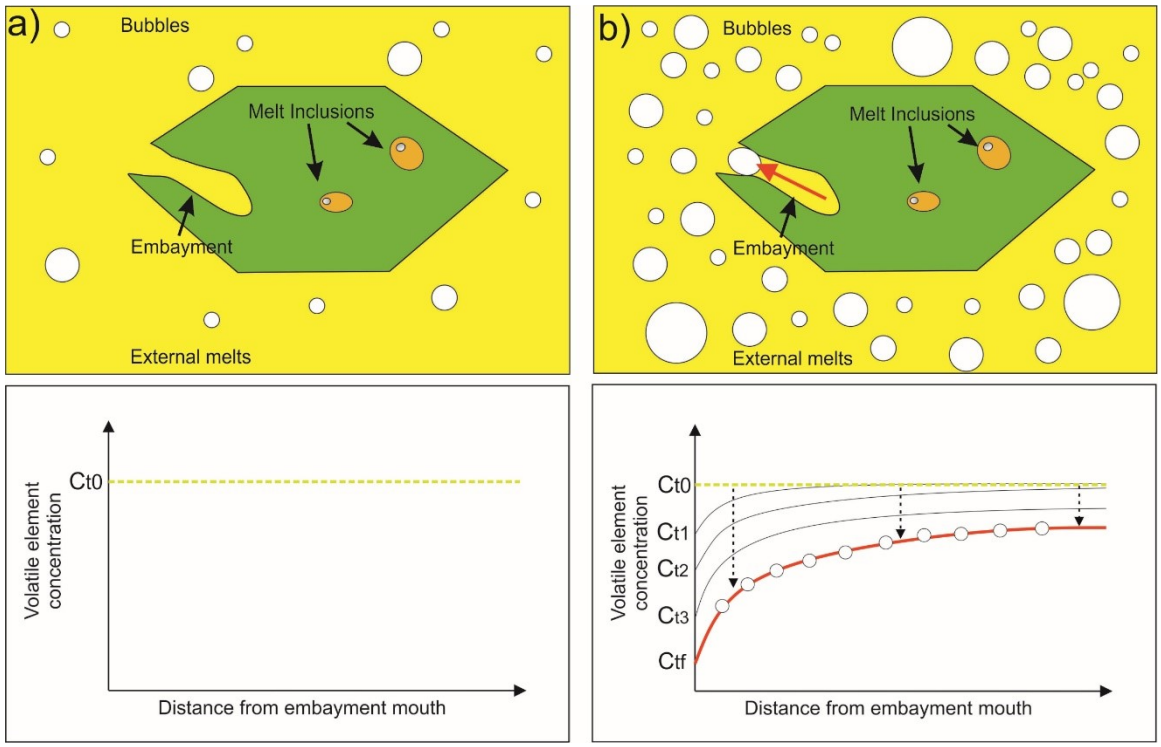

Figure 3: *Sketch showing volatile diffusion in an olivine-hosted melt embayment;* **a)** *at time* t_0, *before the ascent, the embayment is in equilibrium with the surrounding melt and the volatile concentration is assumed to be homogeneous along the tube;* **b)** *when ascent occurs, the decompression induces volatile elements to migrate towards the closest bubble; the concentration at the open side of the melt-tube will decrease over time and compositional gradients may be potentially preserved when diffusion stops.*

The main parameters for application of the diffusion model are: diffusion coefficients of each modeled volatile element, temperature, initial pressure (where ascent starts), final pressure (where diffusion process ends), initial and final concentrations of each volatile element. Such parameters can be constrained through petrological and geochemical techniques. In particular, analyses of olivine-hosted melt inclusions provide constraints on the degassing path of the H_2O-CO_2-S system, thus allowing the identification of original volatile contents in the magma before

the eruption and the depth corresponding to the beginning of the ascent. In this regard, diffusion modeling of multiple volatiles species can offer an estimation of magma ascent over a range of depths, which depends on the solubility of the modelled species. In this way, different ascent rates can be calculated as a function of the depth of the ascending magma (Lloyd et al., 2014). Major difficulty in the application of this technique concerns the research of embayments with specific features. Indeed, an embayment must be as possible as tube-shaped, crystal-free, long enough in order to get measurements of a compositional profile and with a vesicle in the melt at the embayment outlet, which indicates the presence of the bubble where volatiles migrated in during the diffusion. Although they are very common in olivine crystals, embayments are not exclusive of this mineral species, so their discovery can be extended to all kind of crystals present in tephra emitted during an explosive eruption.

Volatile diffusion in embayments has been used in some explosive eruptions involving closed system. The first attempt was made for the Orunaui eruption (Liu et al., 2007) analyzing water gradients in quartz-host embayments, with timescales of 1–7 kPa/s (~5–35 cm/s). Rates of 37-64 m/s have been estimated for the 1980 eruption at Mt. St. Helens (Humpreys et al., 2008) through water concentration in embayments found in plagioclase crystals. These results are very different if compared with those obtained from MER calculations, which gave 2-3 m/s (Geschwind and Rutherford, 1995). Both single-step and multi-steps ascent rates have been calculated for the 1974 sub-Plinian eruption occurred at Volcan De Fuego (Lloyd et al., 2014). Diffusion models using H_2O, CO_2 and S allowed to estimate in a single stage of ascent value of 0.3-0.5 MPa/s from a depth of ~10 km bsl, corresponding to timescale of 8-12 minutes. Application of the two steps modeling, allowed to improve best fit for CO_2 and S, with value of 0.05-0.3 MPa/s considering diffusion of CO_2 during the first step from ~220 to 145 MPa, whereas estimation of 0.3-0.5 MPa/s have been calculated for the second step from 145 MPa to the surface which considers mainly H_2O and S diffusion. Concerning more basic systems, past

eruptions of Kilauea Volcano (Hawaii) have been investigated (Ferguson et al., 2016), with ascent rates around 0.05-0.3 MPa/s for the typical Hawaiian fountains and higher rates of 0.45 MPa/s for the unusual explosive eruption related to the Keanakāko'I Layer 6 (c. 1650 CE).

Other approaches consider diffusion of water in nominally anhydrous minerals (basically, clinopyroxene and olivine; Le Voyer et al., 2014; Llyod et al., 2016; Barth et al., 2019). Various studies have been conducted for the determination of diffusion coefficients, depending on several factors (e.g. anisotropy, composition, structural defects, type of mechanism of diffusion of the H^+; e.g. Kohlstedt and Mackwell 1998; Demouchy and Mackwell 2003; Ferris et al., 2015). These experiments revealed high mobility of water in mafic crystals, which migrates toward the external melt as a response of decreasing water contents dissolved in melts induced by exsolution. Even in this case, initial conditions are constrained by studies of volatiles in olivine hosted-melt inclusions, in order to define the initial water content in the melt and partition coefficients of H_2O (mineral/liquid) for clinopyroxene or olivine. Results from diffusion modeling in clinopyroxene erupted during the 1974 eruption at Volcan De Fuego (Lloyd et al., 2016) are comparable with those obtained by using the embayment approach.

Re-equilibration of water dissolved in olivine-hosted melt inclusions with external melts can be also used for estimation of ascent rates. Water loss from melt inclusions can be estimated modeling the diffusion through olivine crystals, as described in the model by Qin et al. (1992). Many limitations affect this model, which considers a too idealized geometry for the host-crystal, i.e. crystal with spherical shape and the melt inclusion located in the center. Indeed, off center melt inclusions, closer to the crystal rim, re-equilibrate faster than the predicted model, whereas the presence of other melt inclusions can prevent re-equilibration (Lloyd e t al., 2013). Furthermore, other processes promoting water loss from melt inclusions (i.e. diffusive syn- and post-emplacement due to slow cooling; cf. Llyod et al., 2013) must be taken into account in this

approach, as well as the type of diffusivity of H^+ which is strongly anisotropic (Kohlstedt and Mackwell, 1998; Demouchy and Mackwell, 2003).

3. CASE OF STUDY: MT. ETNA VOLCANO

3.1. Why Mt. Etna volcano?

The approach based on volatile diffusion in melt-tubes has been successfully employed in the determination of magma ascent rates in closed-conduit volcanoes, with intermediate or acid compositions (Liu et al., 2007; Humpreys et al., 2008; Lloyd et al 2014). Results obtained from other different approaches are rather consistent between them, highlighting the robustness of such approaches. However, although the hypothesis that intense explosive eruptions are related to high magma ascent rates finds a general consensus in the scientific community, a true quantification of such relationship still need to be properly addressed. Investigations on a good number of cases for a unique volcanic system are missing. Up to date, magma ascent rates in open-system, persistently active volcanoes have not been fixed, especially for those systems where the ordinary Strombolian or effusive activity can shift suddenly toward unusual and unexpected highly explosive eruptions. Similar cases have been recently observed at some volcanoes (e.g. the 2015 eruption at Villarrica Volcano, Chile; the 2015-2016 paroxysmal eruptions at Mt. Etna, Italy; the 2018 eruption at Volcan De Fuego, Guatemala; the two paroxysms occurred during the summer 2019 at Stromboli, Italy).

This study is aimed at obtaining a spectrum of ascent rates related to eruptive events with different explosive intensity for a unique volcanic system. In this regard, Mt. Etna volcano has been chosen as case of study, being one of the most active and well monitored open conduit volcano over the world. Although the ordinary activity of Mt. Etna is generally Strombolian with effusion of lava flows, some violent manifestations have been recorded both in historical and recent times, involving basic and ultrabasic compositions in the most explosive records (Coltelli et al., 1998; Kamenetsky et al., 2007). Moreover, choice of a single volcano offers the

advantage to reduce the amount of variables affecting the final result, being unique/comparable the plumbing system geometry and the physical and chemical conditions of the erupted magmas (e.g. composition, temperature, pressure, viscosity and – at least in part – the volatile contents). In doing this, it is possible to quantify how differences in ascent rates can have in producing incredibly different eruptive styles starting from rather comparable magmatic conditions.

3.2. Volcanological background of Mt. Etna

Mt. Etna is the highest composite volcano in the continental Europe (~3340 m high), located on the eastern coast of Sicily, Italy. A complex geodynamic framework affects the regional tectonics, which is characterized by the convergence between the Euro-Asiatic and the African plates. Three main domains can be recognized in this area: 1) the Apennine-Maghrebian overthrust belt, which forms a complex duplex structure in the north-eastern Sicily; 2) the Hyblean Plateau at the south of the Etnean volcanic edifice, made up by a thick Mesozoic-Cenozoic carbonates sequence, interbedded with basic volcanic rocks dated from Upper Cretaceous; 3) the oceanic Ionian lithosphere, which represents a remnant of the Mesozoic Tethys ocean, separated by the continental crust by the a system of strike slip faults (the so called Malta Escarpment; Monaco et al., 1997; Doglioni et al., 2001).

The convergence is coupled with extensional stresses affecting the eastern Sicily, which are east-southeast/west-northwest oriented (Monaco et al., 1997). Such extension is responsible for the various volcano-tectonic active structures located on the different area of the volcanic edifice (**Figure 4**). The most active structures are located on the southern and northeastern flanks of the volcanic edifice, named respectively the South Rift and Northeast Rift. Along these tectonic alignments many flank eruptions occurred during the last 40 years, with major

frequency of events interesting the South Rift (e.g. 1983, 1985, 2001, 2002-03 eruptions; e.g. Frazzetta and Romano, 1984; Viccaro et al., 2006; Ferlito et al., 2012).

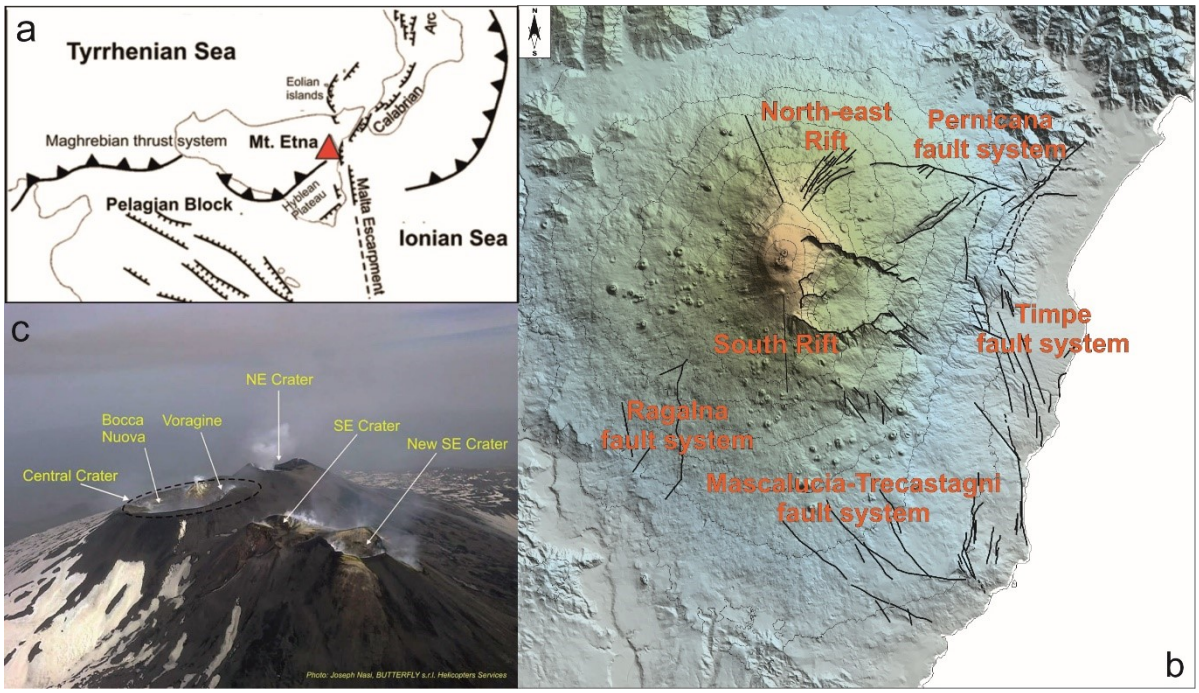

Figure 4: a) *Sketch of the geodynamic framework and regional active tectonic structures of south Italy (from Viccaro and Zuccarello, 2017);* **b)** *Morphotectonic map of Mt. Etna, with the main active tectonic structures localized on the volcanic edifice;* **c)** *Currently configuration of Etna summit, composed by different active craters.*

The active summit craters are located at the intersection of the two rifts, and are: 1) Voragine Crater (VOR), which represents the oldest central crater of the historic activity; 2) North East Crater (NEC), born in 1911 as subterminal vent and directly linked with the Northeast Rift; 3) Bocca Nuova (BN), born in the 1968 as pit crater and later joined with the central crater; 4) South East Crater (SEC), which is composed by two scoria cones: the first born during the 1971 eruption as pit crater, located on the direction southest-northwest respect to BN; the second scoria grown during the 2011-2013 paroxysmal sequence along the same direction and informally named New South East Crater (NSEC; Behncke et al., 2014).

The first volcanic manifestations date back to ~500 ka ago (Branca et al., 2011), with emission of sub-marine and then (~300 ka) subaerial tholeiitic lavas from fissural activity (Kamenetsky and Clocchiatti, 1996; Branca et al., 2011). During the "Timpe" phases (~220 ka), a change in composition characterized the erupted products which show transitional and then Na-alkaline affinities (Tanguy et al., 1997). Distinct central-conduit edifices started to develop since ~130 ka with more explosive activity (Branca et al., 2008) and emission of products compositionally more evolved. Construction of the Ellittico stratovolcano occurred between 57 and 15 ka, culminating with intense caldera-forming eruption/s (Branca et al., 2011). The present stage of activity, called "Mongibello Recente", started ~15 ka ago and is characterized by more effusive and moderate explosive activity, but episodes of sub-Plinian or Plinian episodes occasionally occurred in prehistoric and historic times (e.g. the 122 BC Plinian eruption, Coltelli et al., 1998). Since 1971 AD, the activity showed an increase of the explosive intensity and frequency of eruptions, with several cycles of lava-fountaining episodes at summit craters and explosive flank eruptions (Branca and Del Carlo, 2005). Such behavior of the recent activity has been accompanied by short-term variations in the compositions of the lava, which shifted from hawaiite to K-trachybasalt affinity, with more basic features than the historical products erupted before the year 1971 (Viccaro and Cristofolini, 2008). Major elements variations of the post-1971 products are coupled with enrichment of LILE (K, Cs, Ba, Rb) and radiogenic isotopic ratio $^{87}Sr/^{86}Sr$, whereas $^{143}Nd/^{144}Nd$ and $^{206}Pb/^{204}Pb$ showed gradual decrease (Viccaro and Cristofolini, 2008; Viccaro et al., 2011).

The presence of crystal xenoliths in some volcanic products led to some authors to invoke crustal contamination processes as the main cause in producing these changes (e.g. Clocchiatti et al., 1988). However, Viccaro and Cristofolini (2008) demonstrated that other processes than assimilation of the basement underling the volcanic edifice could effectively generate the geochemical variability observed between the pre and post 1971 volcanic products. Then,

different hypotheses have been advanced in an attempt to explain such changes. A first hypothesis considers a progressive involvement over time of a subduction-related fluids component in the genesis of the primary magma at Mt. Etna (Tornarini et al., 2001; Schiano et al., 2001). Such subduction-related fluid component should come from the Ionian slab through a tectonic window generated by strike slip segments located on the northern side of the Malta Escarpment, which allows upwelling of the asthenosphere below the subduction system favoring the uprise of fluids. An alternative idea for explaining the K-enrichment considers the role of supercritical fluids, which act as a carrier of alkali elements from the deeper portions of the plumbing system, enriching the shallower magmatic batches (Ferlito and Lanzafame, 2010). However, this hypothesis alone cannot explain all the short-term chemical variations observed in recent products. Finally, the idea of a heterogenous metasomatized mantle as source of the primary melts on Etna was discussed by several authors, who provided different evidence for chemical changes of the source (Armienti et al., 1989; Viccaro and Cristofolini, 2008; Viccaro et al., 2011; Correale et al., 2014; Viccaro and Zuccarello 2017). This hypothesis takes into account the short-term chemical variations which depend on proportions of the different portions of the source involved in the melting processes. Moreover, partial melting modeling provided a primary water content in primitive melts up to 2.5 wt.%, obtained from the contribution of hydrous phases (i.e. amphibole and phlogopite) plus water contents that can be derived from nominally anhydrous minerals involved in the partial melting (Viccaro and Zuccarello, 2017).

The latter hypothesis highlights how high water budgets can be inherited directly from the source, but dynamics of transfer, storage and degassing can affect significantly the amount of the final water content during ascent to the surface and, consequently, the eruptive style. This picture is well supported by data on volatile elements dissolved in olivine-hosted melt inclusions. Indeed, variable amounts H_2O and even CO_2 have been measured in olivine-hosted

melt inclusions from products erupted during both historical and recent eruptions at Mt. Etna. Unusual high compositions of H_2O and CO_2, up to 4.0-6.0 wt.% and ~4000-6000 ppm respectively, have found in magma which fed the Plinian eruption occurred at 4 ka (Kamenetsky et al., 2007; Gennaro et al., 2019). Such compositions reflect maximum pressure of entrapment at 500 MPa, i.e. at depth greater than 15 km b.s.l. indicating the presence of volatile-rich magmas in the deepest parts of the plumbing system. Products relative to the 2001-2007 eruptive period show variable compositions, with the highest H_2O and CO_2 contents measured for products of the 2001 eruption (up to 3.5 wt.% and ~4100 ppm, respectively; Metrich et al., 2004; Spilliaert et al., 2006a; 2006b; Collins et al., 2009; Moretti et al., 2018). These studies support the evidence of flushing by CO_2-rich fluids coming from the deeper levels of the plumbing system. Indeed, the presence of 98–99 wt.% of CO_2 in fluid inclusions hosted in high-Mg olivines (Fo_{92} mol%) from Mt. Maletto products (7 ka) suggests that CO_2 may be already exsolved at ~800 MPa (i.e., depth of 24 km; Condomines et al., 1995). Continuous infiltration of CO_2 toward the shallower levels is responsible of magma dehydration, occurring at nearly isobaric conditions. In this regard, a main magma ponding zone affected by substantial flushing of CO_2 were recognized at 170-200 MPa for the 2001 and 2002-2003 eruptions (Métrich et al., 2004; Spilliaert et al., 2006a). Therefore, re-equilibration of magma through the various levels of the plumbing system at different conditions can produce a large spectrum of total volatile budget. Variable proportions of H_2O and CO_2 also reflect modifications of phase equilibria and mineral textures. Experimental studies showed how flushing by CO_2-rich fluids can decrease the stability of plagioclase, associated to increase of clinopyroxene stability (Giuffrida et al., 2017), evidencing therefore how volatile flushing can play a key role in the chemical and physical magma evolution during ascent to the surface.

These findings support the idea that the release of a gas phase from volatile-rich magma ascending from the deeper sources may accumulate at shallower levels; such input of gas in the

shallow reservoir can promote overpressurization and then trigger intense explosive activity (Allard et al., 2003; 2005; Privitera et al., 2003; Aiuppa et al., 2007; Moretti et al., 2018). Alternatively, if primitive magmas ascend quickly through the plumbing system, they can retain most of their pristine volatile cargo, which in turn can potentially causes the overpressurization of the shallower portions of the plumbing system (Viccaro and Zuccarello, 2017). Interestingly, the most explosive volcanic manifestations at Etna over historical and recent periods just involved basic to ultrabasic magmas (Coltelli et al., 1998; Clocchiatti et al., 2004; Kamenetsky et al., 2007).

Assessing the kinetics of degassing processes during syn-eruptive magma ascent may provide useful clues in the understanding of how a persistent and relatively quiet volcanic activity can shift to intense behavior in open system volcanoes like Mt. Etna.

3.3. Description of the chosen eruptions as case-studies

Although the most explosive eruptions occurred in historical time (e.g. 122 BC and 3930 ka; Coltelli et al., 1998; Kamenetsky et al., 2007), some recent episodes from the post-2011 activity have been selected for this study chiefly for the possibility of integration of petrological data with those coming from geophysical signals acquired through the monitoring networks installed on the volcano. Furthermore, choice of eruptive events clustered in rather short time allows the evaluation of differences in magma ascent rates assuming comparable conditions/configurations of the plumbing system. The selected eruptions, with increasing explosive behavior, are: 1) the flank eruption of the December 24-27, 2018, which affected the eastern side of the volcanic edifice coupled with an intense seismic activity (Cannavò et al., 2019); 2) the lava fountaining episode of February 19, 2013, which is part of the 2011-2013 paroxysmal activity occurred at the New South East Crater (NSEC; Behncke et al., 2014;

Giuffrida and Viccaro, 2017); 3) the paroxysmal eruption occurred on December 3, 2015 at the Voragine Crater (VOR), which represents the most violent eruptive event at Mt. Etna over the last 20 years (Cannata et al., 2018).

3.3.1. 2011-2013 NSEC paroxysmal activity and the February 19, 2013 eruption.

Since the year 2011, a new cycle of paroxysmal activity occurred at the summit of the Etna (e.g. Behncke et al., 2014; Viccaro et al., 2013;2014). A total of 44 episodes of lava fountaining took place between January 2011 and December 2013, leading to the formation of a new scoria cone on the flank of the SEC, later renamed as the "New" South East Crater (NSEC; Behncke et al., 2014). Each paroxysmal episode has been characterized by generation of eruptive columns and lava flows (often rheomorphic) from the NSEC, generally direct towards to the Valle del Bove (**Figure 5**).

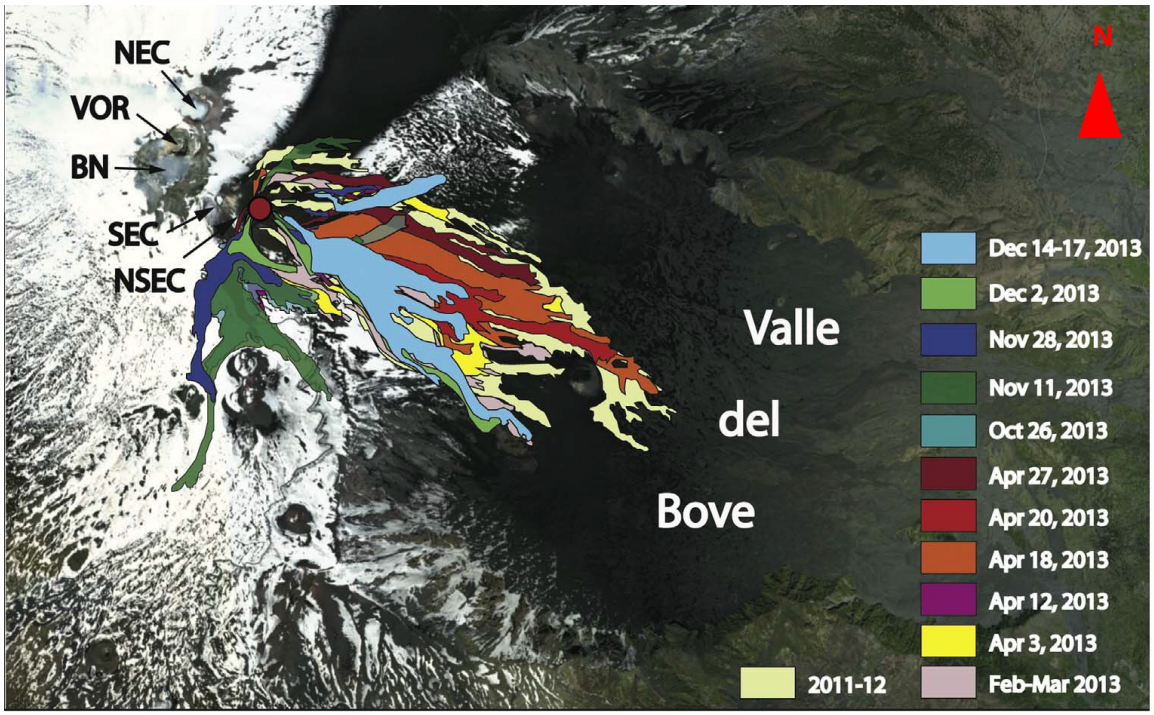

Figure 5: *Lava flow fields produced during the 2011-2013 paroxysmal activity at NSEC (Fig. 1c from Giuffrida and Viccaro, 2017).*

Ash emission generally from the NSEC (but sometimes with activation also of other summit craters) preceded the beginning of each episode, which had total duration generally ranging between 24 and 48 hours with development of different phases (Behncke et al., 2014): 1) incipient Strombolian activity, lasting hours to some days; 2) emission of lava flow from the crater or from vents opened on the flank of the NSEC (this phase is not observed for all episodes, e.g. the paroxysmal episode of November 23, 2013); 3) Increasing of intensity and frequency of the explosions, culminating in pulsating or continuous lava fountains, with heights of 500 - 1000 m above the crater, lasting some minutes to hours and feeding the emplacement of lava flows; 4) sudden decrease of lava fountaining followed by weak Strombolian activity or emission of ash and fragments of the conduit wall due to the drop of pressure inside the conduit; 5) passive extrusion of lava flow lasting for a few hours.

Based on the RMS pattern of volcanic tremor recorded by the permanent seismic network of the Istituto Nazionale di Geofisica e Vulcanologia–Osservatorio Etneo (INGV-OE), three types of lava fountaining episodes have been defined (Alparone et al., 2003; Viccaro et al., 2014): 1) ramp-shaped pattern, with gradual increase of the RMS signals, followed by a sudden decrease; 2) tower-shaped pattern, with a small initial gradual uprise of the RMS, followed by a sudden increase and then abrupt decrease; 3) bell-shaped pattern, which shows a symmetric shape with quick increase and decrease pattern. Generally, lava fountaining events with ramp- and tower-shaped patterns are associated with longer initial Strombolian phases and the overall intensity of the paroxysm is lesser than those with bell-shaped patterns, which show shorter duration but are more energetic. Disequilibrium textures recorded by plagioclase crystals coupled with their micro-compositional changes are well correlated with the type of paroxysmal activity observed (Viccaro et al., 2014), allowing to define two main processes acting as mechanism of triggering of the paroxysmal activity during 2011-2013.

Figure 6: *A typical lava fountaining episode occurred at NSEC during the 2011-2013 paroxysmal activity at Mt. Etna (episode of the November 15-16, 2013).*

In this regard, long-lasting paroxysms (ramp- and tower-shaped RMS pattern) are thought to be triggered by recharge of mafic and gas-rich magma, whereas injection of prevalent gas should control short-lasting paroxysms (bell-shaped RMS pattern). The February 19, 2013 paroxysmal episode is the first of 2013, after a rest of 10 months since the last paroxysmal activity occurred on 2012 at NSEC. A small PDC followed by confined lahars took place during this episode, with partial fracturing of the NSEC flank.

3.3.2. 2015-2016 VOR activity and the paroxysmal episode of the December 3, 2015.

The paroxysmal activity occurred at the Voragine Crater (VOR) on December 2015 was the most explosive over the last 20 years, with four episodes of lava fountaining in 3 days. The prelude of this activity started in the mid of October, with weak Strombolian activity at the

bottom of VOR, where lava shreds fell inside the crater and rarely they overcame the crater edges. Contemporaneously, a weak seismic activity affected the entire plumbing system, from 25 km bsl up to the shallow portions. An energetic LP event was recorded on November 1, 2015, with hypocenters localized under the summit (Cannata et al., 2018). Coupled with the deep seismic activity, a marked change in volcanic tremor RMS pattern was observed. The Strombolian activity increased slightly in energy at the end of November 2015 until the night of the December 2-3, when the first paroxysmal episode occurred. This powerful eruption produced a lava fountaining up to 2 km above the crater edge and an eruptive column ~15-km-high with triboelectric activity (**Figure 7**). A rheomorphic lava flow was emitted during the eruption, but it was entirely confined into the crater terrace. Other three episodes with similar dynamics took place on December 4-5, 2015, and then the activity shifted to the NSEC and NEC for a few days. No other lava fountaining occurred, but only Strombolian activity at NSEC coupled with emplacement of lava flows and small PDCs.

Figure 7: *The violent paroxysmal episode occurred during the early hours of the December 3, 2015, at VOR Crater (photo credit: Marco Restivo).*

Paroxysmal activity similar to December 2015 occurred at VOR on May 2016, but this sequence of paroxysms was characterized by minor energy with respect to the 2015 series. A multidisciplinary approach of investigation combining petrological and geophysical data (seismic and geodetic) has led to the definition of a modern picture of the Etnean plumbing system (Cannata et al., 2018). Specifically, the 2015 eruptions have been fed by magmas stored at intermediate-shallow levels of the plumbing system (160–30 MPa) that were pushed upward as a response of magma injections coming from the deepest storage zones into reservoirs located at 160 MPa. Diffusion modeling of olivine zoning suggested timescales within 1-2 months for these recharging processes, also in agreement with geophysical signals (seismic, infrasound and volcanic tremor; Cannata et al., 2018).

3.3.3. The flank eruption of the December 24-27, 2018

Since the VOR activity in May 2016, the volcanic edifice was affected by a remarkable ground deformation, characterized by an inflation pattern with a rather constant rate (Borzì et al., 2020). Interruption of the inflation cycle occurred during the February-April 2017 activity, when very short-lasting syn-eruptive deflation patterns were recorded. Viccaro et al. (2019) invoked a mechanism of self-feeding magma replenishment inside the plumbing system as a response of the depressurization caused by the violent paroxysmal activity at VOR during May 2016. Such magma replenishment process is responsible of the continuous pressurization of the reservoir located at ~5 km b.s.l. (Viccaro et al., 2019), although emissions of lava and tephra occurred during the 2017 activity and also during the modest eruption at NSEC on August 23-28, 2018. The replenishment process culminated on the flank eruption of the December 24-27, 2018. After months of weak Strombolian activity at the summit started on autumn of 2018, an intense seismic activity was recorded in the morning of the December 24, 2018, from the 9:30

AM. Contemporaneously, ash emission took place from BN and NEC. Suddenly, after the 12:00 AM, a new fracture opened at the base of the NSEC crater and propagated south-eastward for a length of 3 km composed by 3 segments. The highest segment of the fracture and BN crater fed Strombolian activity, with formation of an ash column spreading to east-southeast. Lava flows were emitted from all the three segments toward the Valle del Bove, with fronts reaching an altitude of 1650-1800 m asl. In the afternoon, the explosive activity decreased, whereas lava flows were emitted from the lowest segment until December 27, 2018. Then the activity was characterized by quiet ash and gas emission for about one week. Seismicity continued during and after the eruption and some events with magnitude greater than 4.0 M_L were recorded. The strongest event (4.8 M_L) shook the eastern side of the volcanic edifice during the night of December 26-27, producing several damages on buildings.

Figure 8: a) *Flank eruption of the December 24-27, 2018; photo taken at 12:20 PM of December 24, 2018 from Catania. The initial phase of the eruption was moderately explosive, with formation of an eruptive column spreading to southeast.* **b)** *Photo taken at 17:00 PM of December 24, 2018, from the south east flank of the volcano; explosive activity was characterized by Strombolian activity on the lowest portion of the fracture and ash emission from the BN crater.*

4. METHODS OF INVESTIGATION

4.1. Strategy of investigation

As already described, the approach based on volatile diffusion in melt tubes needs a preliminary study of olivine-hosted melt inclusions. Major and traces elements in melt inclusions provide insights on the chemical evolution of the melts, whereas measurements of volatile elements allow to assess the original pre-eruptive volatile budget. Solubility models (e.g. Newman and Lowenstern, 2002; Papale et al., 2006; Witham et al., 2012) will be used in order to track the degassing path of the system H_2O-CO_2-S in the three eruptive episodes selected, allowing to recognize the initial volatile concentrations prior the ascent and the associated pressure from which magma starts to ascent toward the surface.

An important question that is never treated on Mt. Etna volcano concerns the possibility that melt inclusions may be affected by water loss, which reflects in the re-equilibration of melt inclusions with lower H_2O than their original contents at time of entrapment. Such process has been extensively investigated through several experimental works (e.g. Portnyagin et al., 2008;2019; Gaetani et al., 2012), where exchange of H^+ between melt inclusions and external melts occurs in rapid timescales, depending by the mechanism of H^+ transport. The possible role of water loss must be evaluated carefully in order to avoid wrong interpretations of degassing models, which may lead to erroneous constraints of the initial conditions for the diffusion modeling and consequently to not correct estimation in ascent rates.

A novelty of this work is that new the data on volatile contents in melt inclusions relative to the recent activity post-2011 at Mt. Etna will be presented. Only data of melt inclusions analyzed in lavas emitted during a paroxysmal episode in April 2013 were published for the post-2011 period (Gennaro et al., 2019). However, it is likely that the investigated melt

inclusions have underwent extensively water loss because of the slow cooling during lava emplacement. In fact, data report very low water contents (< 0.3 wt.%). Therefore, the best strategy to assess volatile contents is to analyze melt inclusions entrapped in olivine crystals which can be found in small tephra (< 1.5 cm), in order to avoid as much as possible effect of water loss due to post-emplacement slow cooling (Llyod et al., 2013).

4.2. Samples preparation and microanalytical techniques

The samples relative to all the three eruptive episodes investigated for this study consist of ash and lapilli and have been collected in distal areas from the point of emission during the eruptions. They are representative of tephra emitted during the peak of the explosive activity. Pyroclasts emitted during the February 19, 2013 eruption have been collected 12 km far, east from the summit craters. Both ash and lapilli samples erupted during the December 3, 2015 paroxysm and ash samples emitted by the eruptive fracture of the December 24-27, 2018 flank eruption, have been collected about 8 km far away from the summit on the eastern flank of the volcano.

Each sample has been sieved with mesh smaller than 1.5 cm removing all clasts not passing the sieve, in order to avoid the possible effects of post-eruptive water lost, in according to Llyod et al., (2013). The fractions between 2 mm and 1.5 cm were lightly crushed and picked, while fractions smaller than 2 mm were sieved without crushing. Olivine crystals of 0.350 – 1.0 mm have been hand-picked from the clasts under binocular microscope. Then, they were mounted individually with Crystal Bond 509 and polished with silicon carbide paper (P1200 and P2400) and diamond paste (6 μm, 3 μm and 1 μm or 1/4 μm), until melt inclusions (MIs hereafter) and embayments were exposed. Almost all MIs from Etna contain bubbles and oxides, sometimes associated to small sulfide globule. Tube-shaped embayments with evidence

of a bubble at their open side were carefully inspected and chosen for further analyses. Crystals were removed from Crystal Bond 509 and cleaned with acetone for spectroscopy analyses. MIs bigger than 30 μm have been selected for the Fourier Transform Infrared Spectroscopy (FTIR) analyses. Raman analyses were performed on embayments and MIs not suitable for FTIR. Then, crystals were individually embedded in epoxy resin for EMPA and LA-IPCMS analyses on MIs in order to collect major elements, trace elements, S, Cl and F, whereas major element compositions of host olivine were collected through SEM-EDS analyses.

4.2.1. SEM-EDS analyses

Seventy-nine olivine crystals, containing MIs and melt embayments investigated in this study, have been analyzed. In situ microanalyses were performed using a Tescan Vega-LMU scanning electron microscope located at the Dipartimento di Scienze Biologiche, Geologiche ed Ambientali at the University of Catania. The microscope is equipped with an EDAX Neptune XM4–60 EDS micro-analyzer characterized by an ultra-thin Be window coupled with an EDAX WDS LEXS (wavelength dispersive low energy X-ray spectrometer) calibrated for light elements. Operative conditions of 20 kV accelerating voltage and ~2 nA beam current have been used for the analysis of major element abundances in olivines. Where core-to-rim transects were analyzed, spacing between each spot analysis was on the order of 5-9, whereas few spots (3-4) within 20 μm from the MIs were analyzed. Repeated analyses on SPI 02753-AB Serial KF certified standards (Fo-rich olivine) during the analytical runs provided precision for all measured elements of 3-5%. Accuracy is on the order of 5%.

4.2.2. FTIR spectroscopy

Water and CO_2 concentrations in MIs bigger than 30 μm have been determined by micro-FTIR spectroscopy, using a Bruker Vertex 70 spectrometer coupled with a Hyperion microscope system, at the Laboratoire Magmas et Volcans (Clermont-Ferrand, France). Spectra were collected using a Globar light source, a KBr beamsplitter, a MCT (Mercury-Cadmium-Tellurium alloy) detector cooled by liquid nitrogen, and the Bruker™ OPUS software (v. 5.0) for spectra acquisitions. Samples were placed on an IR-transparent CaF_2 disk, through which background measurements were taken before positioning the sample in the beam path. Spectra were collected at a spectral resolution of 4 cm^{-1} and setting the acquisitions on samples and background respectively at 600 and 200 scans. The beam size varied depending on the size of the inclusion and was minimum 30×30 μm for small inclusions. Analytical uncertainties for H_2O and CO_2 have been estimated at 9-15% and 10-18% of measured values respectively, depending on uncertainties of the extinction coefficient and measured thickness.

Olivine crystals were double-polished following the approach of Nichols and Wysoczanski (2007), avoiding a complete exposure of MIs on one of the polished surfaces. This approach has been chosen because it allows to overcome some difficulties related to the double-polishing preparation and minimize the risk of damaging the sample or losing it during the analytical session and thickness measurement. Moreover, since the inclusions analyzed show compositions rather depleted in CO_2 (see next chapter "Results"), the double-peak related to the antisymmetric stretch of CO_3^{2-} groups around 1430 cm^{-1} and 1520 cm^{-1} cannot be recognized in very thin samples, because it may be overwhelmed by the interference fringes on the spectra background. Thus, keeping a greater thickness avoids the presence of the fringes in the spectra and makes it possible to observe the CO_3^{2-} peaks. Another advantage that this technique offers is the possibility to analyze several inclusions hosted in a single olivine crystal, without double exposing each inclusion. Finally, thicker samples are easier to handle, prepare

and further analyze using other micro-analytical techniques, such as LA-ICPMS. On the other hand, measuring thickness of unexposed inclusions could be affected by greater uncertainties.

In this approach, it was necessary to collect also the spectrum of the host olivine nearby the inclusion, in order to quantify and subtract the olivine contamination from the inclusion spectrum, as well as estimating inclusions thickness. In this regard, a spectrum was first collected on the inclusion glassy area and, then, a second spectrum was taken on the host crystal close to the MI analyzed, carefully selecting an olivine volume free of inclusions in the beam path and keeping the same sample orientation because the intensity of the bands depends on the crystallographic orientation and on the thickness of the analyzed area (Nichols and Wysoczanski, 2007). The details of the spectra treatment will be better explained on the paragraph "Spectra treatment".

4.2.3. Raman spectroscopy

Water contents (wt.%) in embayments and in MIs that could not be analyzed by FTIR spectroscopy were determined at the Laboratoire Magma et Volcans (Clermont- Ferrand) using a Renishaw InVia confocal Raman micro-spectrometer equipped with a 532 nm diode laser (200mW output power), a Peltier-cooled CCD detector of 1024 × 256 pixels, a motorized XYZ stage and a Leica DM 2500 M optical microscope. A 100 × microscope objective was used in high confocality setting (slit aperture of 20 μm). The spectra were recorded from 100 to 1350 cm^{-1} for the alumino-silicate domain and from 2900 to 3800 cm^{-1} for the water domain using WiRE^{TM} 4.2 software, and acquisition time was set at 120 s and 240 s respectively for the alumino-silicate and water domains. The focus depth of the laser beam was set at 2 μm under the surface of the sample, which corresponds to the depth of maximum signal intensity in both water and alumino-silicate domains for glasses with basaltic compositions (Schiavi et al., 2018). In the spectra of few thin inclusions, olivine contamination was visible in the alumino-silicate

domain (peaks located near 822 and 855 cm^{-1}); in these cases, the laser was focused on the surface.

Figure 8: *Renishaw InVia Raman micro-spectrometer (Laboratoire Magmas et Volcans, Clermont-Ferrand, France)*

Profile compositions of H_2O have been measured along the central part of the embayments, from the inner toward the mouth of the melt tubes, with a spacing between each spot on the order of 5-8 µm. Glass standards used for the external calibration of Raman spectrometer (see the paragraph "Spectra Treatment") were analyzed several times during each session of analyses, in order to correct for the influence of the delivered energy on the band intensities (Schiavi et al., 2018). Analytical uncertainties are 5-8% of measured values.

4.2.4. Electron microprobe

Electron microprobe analyses (EMPA) have been carried out in two phases. A group of MIs and embayments were first analyzed at Dipartimento di Scienze della Terra, University of Milan, through JEOL JXA 8200 Superprobe equipped with five WDS-wavelength-dispersive

spectrometers, EDS, and cathodoluminescence detector. The radius of Rowland circle is 140 mm for spectrometers 1, 2 and 3, bearing LDE1, LDE2, LDEB, TAP, PET, and LiF crystals and 100 mm for spectrometers 4 and 5, bearing PETH and LIFH crystal. Major elements compositions, S and Cl in melt inclusions and embayments were collected thorough WDS spectrometers, setting 5 µm beam at 15 kV accelerating voltage and ~5 nA beam current.

A second group of MIs and few embayments of the DEC 2018 eruption have been analyzed at Laboratoire Magmas et Volcans (Clermont-Ferrand, France), using a WDS Cameca SxFiveTactis. The analytical conditions used for the collection of major elements were 15 kV accelerating voltage and 8 nA beam current with a beam diameter of 20 µm or 4 nA beam current and diameter of 10 µm in the case of smaller inclusions. For volatiles elements (S, CL, and F) have been used conditions of 15 kV accelerating voltage and 40 nA with variable beam diameter (10 to 20 µm). Volatile loss during the analysis is minimized by increasing the number of analysis (~5), using total counting time (peak and background) of 10 s for chlorine and sulfur and 60 s for fluorine. The beam was defocused for 20 s between each analysis, allowing the sample to cool down and so avoiding overheating which may lead to volatile loss. The average value calculated from the 5 measurements have been considered as the total volatile concentrations. Analytical uncertainties for major elements are on the order of 5% of measured values, for S and Cl are 5-10% while for F are 15-30%.

4.2.5. LA-ICP-MS

Trace elements on MIs have been collected at Laboratoire Magmas et Volcans (Clermont-Ferrand, France) using a Resonetics M-50 Excimer Ar/F (193 nm) laser ablation coupled with Thermofisher Element XR ICPMS. Samples were ablated under pure helium in the ablation cell at flow rate respectively of 700 ml/min, and nitrogen mixed to helium after the cell at flow rate of 6 ml/min. The fluency of the laser was of 2.8 J/cm^2 at repletion rate of 2 Hz. The dwell time

was 50 ms for each isotope and the beam size varied between 25 and 40 µm, depending from the inclusion size analyzed. The laser was calibrated using ^{44}Ca as internal standard.

Figure 10: *SXFive-TACTIS (CAMECA) microprobe (Laboratoire Magmas et Volcans Clermont-Ferrand, France).*

Figure 11: *Resonetics M-50 Excimer Ar/F laser ablation (Laboratoire Magmas et Volcans Clermont-Ferrand, France).*

4.3. Spectra treatment

4.3.1. Raman

Before Raman spectra treatment, inspection of the alumino-silicate domain allows to detect possible presence of magnetite (Fe_3O_4) nanolites in the glass, which may not be visible under optical microscope. Iron nanolites are highlighted by an intense peak near 690 cm^{-1} (**Figure 12**). It has been demonstrated that presence of iron nanolites in the glass affects the intensity of the water band located between ~2900 and 3800 cm^{-1} and may result in underestimating the water content of glass samples (Di Genova et al., 2017). The alumino-silicate spectral domain of many MIs revealed the presence of nanolites; glasses exhibiting a strong peak at 690 cm^{-1} have not been considered for quantification of water content by Raman analyses. More precisely, water contents of glass inclusions that showed a ratio between the height of the peak at 690 cm^{-1} and the height of the glass band at 966-990 cm^{-1} lower than 0.64 have been considered (**Figure 12**), after having verified that similar water contents were measured by FTIR on same inclusions (i.e. MIs having suitable size for FTIR analysis).

The background of the raw Raman spectra on suitable MIs was corrected using PeakFit package software (Jandel Scientific). Different approaches can be used for the background fitting, including linear baseline, cubic baseline or cubic spline baseline with at least three anchor points (e.g. Mercier et al., 2009; Behrens et al., 2006; Schiavi et al., 2018). Cubic baseline fittings using two or three anchor intervals were generally used and provided very similar results. A cubic baseline with three anchor intervals usually allowed to better subtract the background in the water domain of slightly fluorescing spectra, so preferentially it has been used.

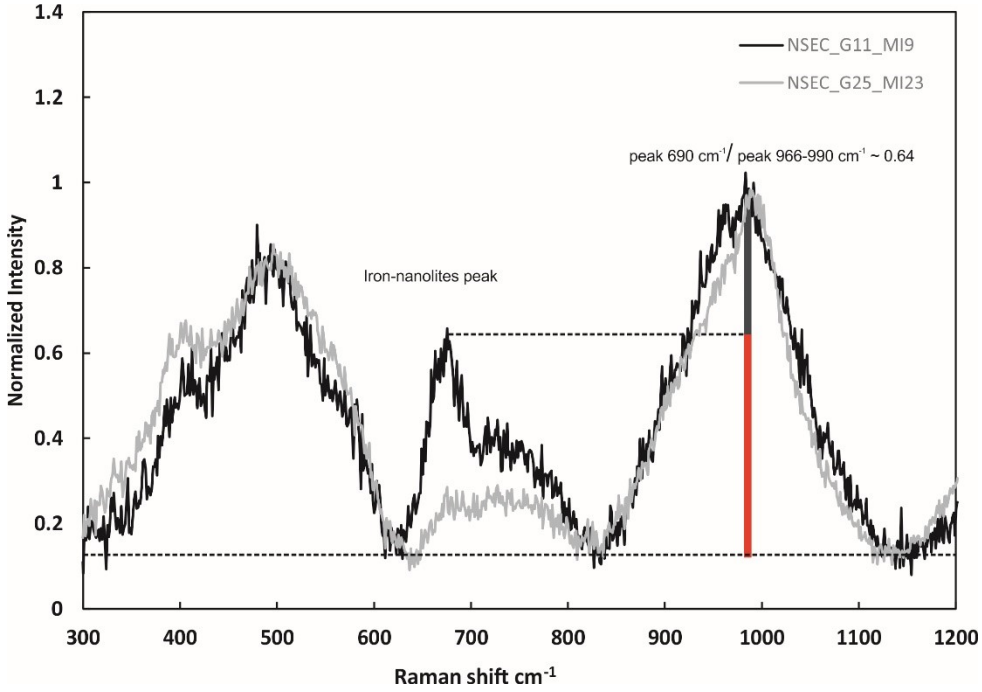

Figure 12: *Normalized Raman spectra in the alumino-silicate domain collected for a MI with iron-nanolites peak at 690 cm^{-1} (black line) and for iron nanolites-free MI (grey line). The ratio between the height of peak at 690 cm^{-1} and the height of the band at 966-990 cm^{-1} was calculated. Water concentrations measured in MIs and embayments by Raman spectroscopy were disregarded if this ratio was higher than 0.64.*

The anchor points were fixed at the extremities, specifically from 2980 to 3000-3008 and from 3725 to 3780 cm^{-1}, plus an intermediate narrow interval near 3100 cm^{-1} in the cubic baseline correction with three anchor points (**Figure 13**). After background subtraction, quantification of the water can be achieved through different methods based on either an internal or an external calibration (Schiavi et al., 2018 and reference therein). The internal calibration is based on the normalization of the water band to the intensity of bands located in the alumino-silicate region. Dissolved water contents are estimated by measuring the OH/Si ratio (i.e. the area ratio between the total water band and the total alumino-silicate band region), which can be defined measuring the total area of the bands considering either the entire region between 200 and 1250 cm^{-1}, the band located at high wavenumbers between 850 and 1250 cm^{-}

[1], or the band at low wavenumbers ranging from 200 to 650 cm^{-1} (Schiavi et al., 2018 and reference therein).

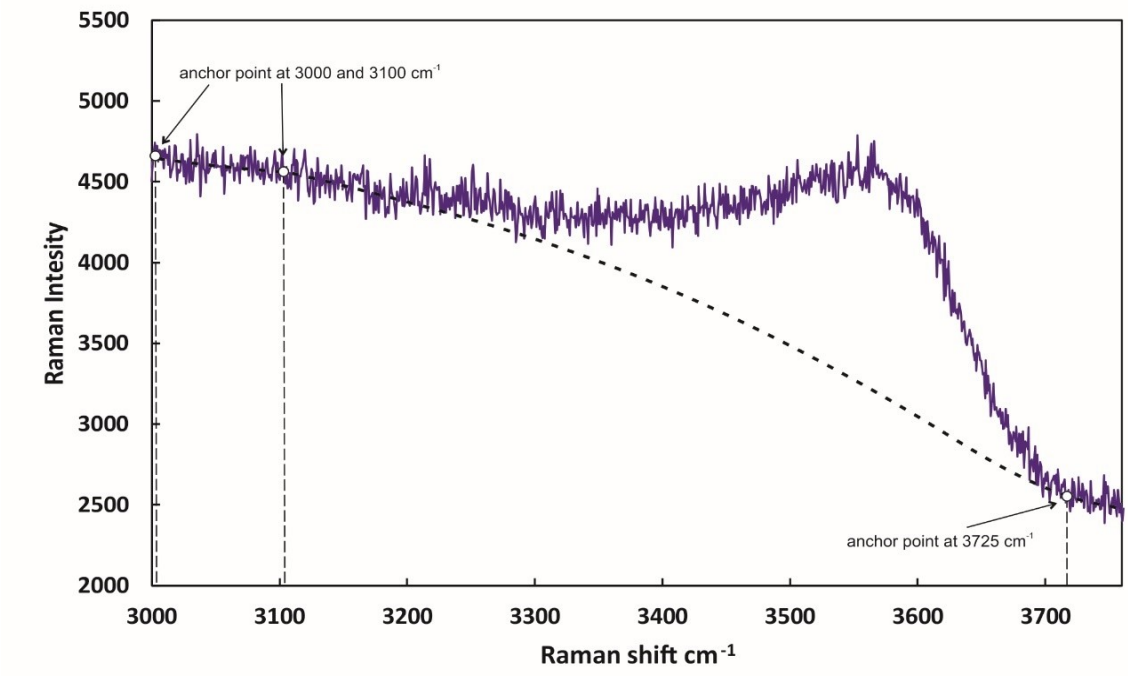

Figure 13: *Example of raw Raman spectrum in the water domain (VOR_G14_MI11); background correction (thick black dashed line) is obtained by subtracting a cubic polynomial function with two (near 3000 and 3700 cm^{-1}) or three anchor intervals (near 3100 cm^{-1}).*

Effects on Raman spectra due to instrumental and analytical conditions are removed through this type of calibration; however, internal calibration is affected by glass compositions and density, and oxidation state of iron (Di Genova et al., 2017; Schiavi et al., 2018). Several authors performed proper corrections in order to remove such effects and to define a single calibration over a large compositional range (e.g. Le Losq et al., 2012; Di Genova et al., 2017; Schiavi et al 2018). However, as stated before, the possible presence of oxide-nanolites affects the shape of the bands, so external calibration was more appropriate for water measurements. The internal calibration method was applied for water quantification only in few magnetite-free MIs and provided same results as the external calibration method (≤ 5% relative standard deviation).

External calibration consists in comparing the intensity of the band at 3570 cm^{-1} of the glass samples with the band intensities of reference glasses with known water contents. Measurements of the water band in reference glasses with variable amount of water allow to define an independent calibration line which correlates the band intensity (i.e., either the height or the area of the band normalized to acquisition time and laser power) and the H_2O concentration in wt.% (**Figure A1** from "Appendix"). So, measurements of band intensity in spectra of MIs with unknown water content can be referred to the defined calibration line (Schiavi et al., 2018 and reference in). Because the topology and width of the water band varies in spectra of glasses with different compositions (e.g. from basaltic to andesitic compositions) (Schiavi et al., 2018), area measurements have been preferred to measurements of the peak height. However, all glasses analyzed are basaltic in compositions, minimizing the effect related to the possible compositional variations. In the external calibration approach, effects related to the instrumental conditions cannot be removed, so measurements on reference glasses have been performed several times within a single session of analyses, in order to evaluate possible changing in the analytical conditions affecting Raman spectra. In case of such variations, a new calibration line must be defined for the following measurements.

4.2.2. FTIR spectra

As mentioned above, almost all MIs have been double-polished without a complete exposure of one of the sides of the inclusions as described in Nichols and Wysoczanski (2007), allowing to an easier and faster preparation of the samples and reducing the risks to damage or lose them. Two absorbance spectra have been collected for each measurement, in order to remove contamination of the olivine in the glass spectra. The evidence of olivine contamination is well observed in the Si-O bands in the range of 2000-1600 cm^{-1} on the inclusion spectra (**Figure 14**). The removal of the olivine contamination from the inclusion spectra and

measurement of the absorbance of the total H_2O and CO_3^{2-} were performed through Bruker™ OPUS software (v. 5.0).

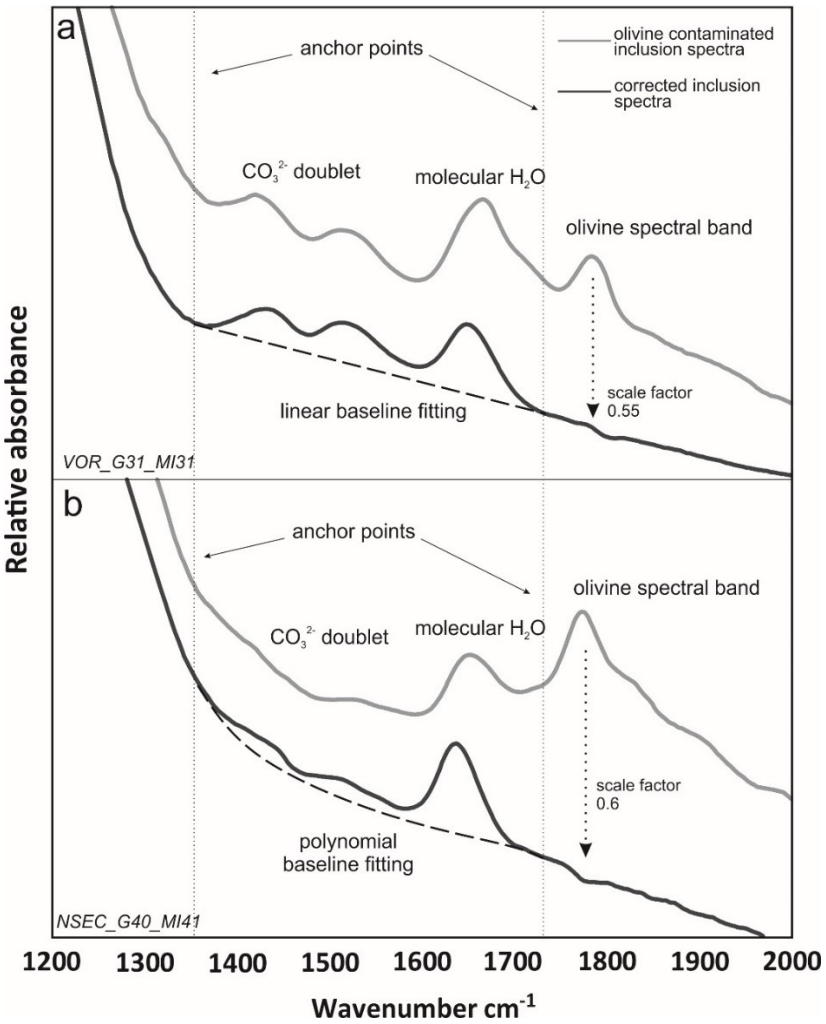

Figure 14*:* **a)** *linear and* **b)** *polynomial baseline fitting of corrected inclusion spectra (black solid line) from olivine-contaminated spectra (gray solid line), used for estimation of CO_2 dissolved in glass (double peaks at 1430 and 1520 cm^{-1}) by FTIR analyses. Small scale factors are estimated for relatively low intensity olivine band in the olivine-contaminated spectra.*

After the collection, raw spectra were corrected for the atmospheric compensation; then, the spectra of MIs that have not been double exposed were treated in order to remove contamination by the olivine host. In this regard, the intensities of the olivine spectra were

corrected for a scale factor and subtracted from the inclusion spectra until the olivine peaks disappeared completely or almost completely. This scale factor has been determined for each spectrum through OPUS software, by detecting the annihilation of the olivine peak at 1770 cm^{-1} or at 2000 cm^{-1} in inclusions spectra (**Figure 14**). An overestimation of a scale factor may lead to a formation of negative peaks in correspondence of the same bands.

Finally, from the obtained spectra is possible to calculate the absorbance of H_2O and CO_2. The height of the total OH peak at 3550 cm^{-1} was used to retrieve H_2O concentration, with an extinction coefficient of 62.8± 0.8 L/mol*cm (Mercier et al., 2010). CO_2 concentration was calculated considering the height of the carbonate peaks at 1420 cm^{-1} and 1520 cm^{-1} using extinction coefficients of 360 and 394 L/mol*cm, respectively (Shishkina et al., 2014). The heights of peaks have been measured from the baseline defined by linear fitting (Nichols and Wysoczanski, 2007) through OPUS software. Where the intensity of the CO_3^{2-} doublet was relatively low, a polynomial fitting was more suitable for the definition of the baselines and measurements of the height of peaks (**Figure 14**). The anchor points were fixed at ~1330 cm^{-1} and ~1730 cm^{-1} for CO_3^{2-}, whereas for H_2O were constrained at ~2500 cm^{-1} and ~3800 cm^{-1}. Thus, H_2O and CO_2 concentrations are obtained using the Beer-Lambert law:

$$c = MA/\rho d\varepsilon \quad (1)$$

where M is the molecular weight of H_2O or CO_2, A is the measured absorbance of the band of interest, ρ is the density of the hydrous basaltic glass, d is the thickness of the MI and ε is the molar extinction coefficient of the volatile species considered. In this regard, thickness of inclusions without olivine contamination must be determined from the total thickness of the samples, in order to retrieve the volatile contents.

The total thickness generally is measured through a digital displacement gauge, but measurements on small samples (<50 μm) can be affected by a significant error, and thin samples could be damaged or broken (von Aulock et al., 2014). In this study, the laser beam of

the micro-Raman spectrometer coupled with a Leica DM 2500 M optical microscope has been preferred for thickness measurements, using the high precision of the laser focus. Specifically, the laser was initially focused on the surface of the sample; then, the sample was moved along the vertical (*Z*) axis until the laser beam was focused on the surface of the sample holder. The displacement measured along *Z* corresponds to the total thickness of the samples, with an uncertainty of 2 μm. This approach was compared with the method described in Nichols and Wysoczanski (2007), where total thicknesses were estimated from the interferences fringes that appear on a reflectance FTIR spectrum collected on inclusions. The small differences between the two methods are inside the uncertainty, so the laser measurement approach has been validated, avoiding further measurements which require to collect reflectance spectra on inclusions.

The inclusion thickness can be calculated from the total thickness by determining the proportion of the olivine in the beam path of the contaminated inclusion spectra. This can be done measuring the bands between 2000 and 1600 cm^{-1} in both original pure olivine and olivine-contaminated inclusion spectra corrected for the atmospheric compensation. The inclusion thickness can be calculated following the equation:

$$t^{inc} = t^{ol+inc} - t^{ol+inc}\left(\frac{A^{ol+inc}_{2000-1600}\Big/_{t^{ol+inc}}}{A^{ol}_{2000-1600}\Big/_{t^{ol}}}\right) \quad (2)$$

where t is the thickness (cm), $A_{2000\text{-}1600}$ the absorbance of the olivine peaks between 2000 and 1600 cm^{-1}, ^{inc} is referred to inclusions without olivine contamination, ^{ol} is referred to pure olivine, $^{ol+inc}$ is referred to olivine contaminated inclusions (Nichols and Wysoczanski 2007). Once determined the inclusion thickness, it can be used in the Beer-Lambert law with the absorbance of the interested volatile specie and the volatile contents in the inclusion can be calculated.

Depending on the thickness of the sample analyzed and the relative amount of the volatile element considered, the OH band can become saturated and, thus, water concentration can be underestimated. In one sample from VOR 2015 products, the total OH band at 3550 cm^{-1} showed clear saturation (**Figure 15**); in this case, Raman spectroscopy was used for estimating H_2O content.

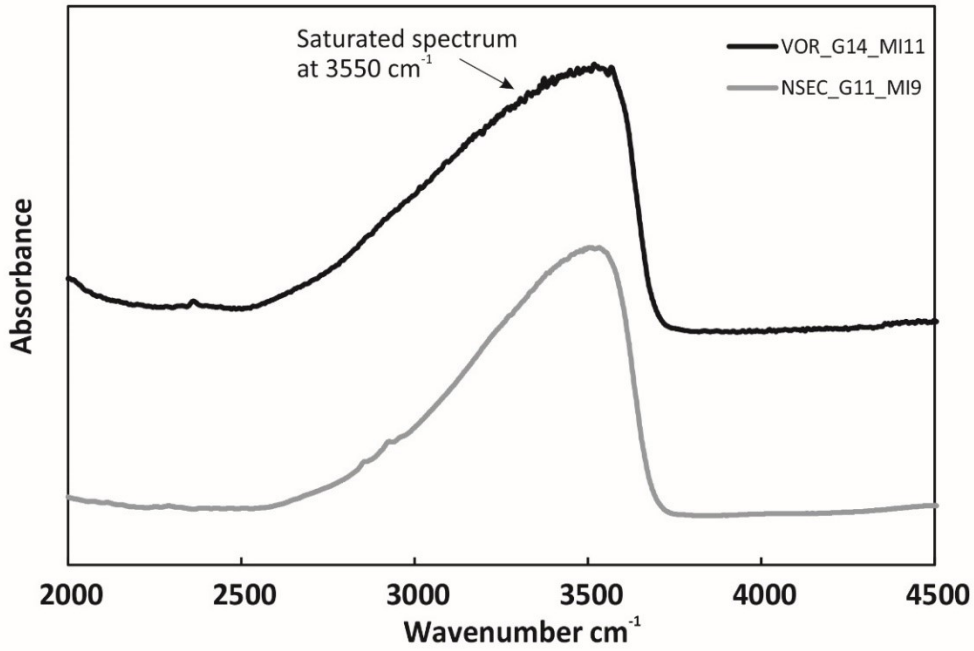

Figure 15: *Two examples of FTIR spectra in the water domain; the black line represents a saturated total OH peak at 3550 cm^{-1}, while the grey line spectrum displays a not saturated peak.*

5. RESULTS

5.1. Description of pyroclasts

Volcanic tephra with size ranging between 0.350 and 1 mm were analyzed under a binocular stereoscopic microscope and through the Tescan Vega-LMU scanning electron microscope. Juvenile fragments (sideromelane and tachylite), crystals and lithics constitute the components of the analyzed pyroclasts. In products erupted during the February 19, 2013 paroxysmal episode (NSEC 2013), sideromelane is the main component (46% of the total clasts observed, **Figure 16**) and lithics are rather abundant (~30%). Tachylite and sideromelane clasts are predominant in the December 3, 2015 (VOR 2015) products (respectively 55% and 35% of the total) and lithics are very rare (~5%). On the contrary, tephra samples erupted during the flank eruption of December 24-27, 2018 (DEC 2018), are characterized by a high number of lithics (~50%), which likely come from the different layers of volcanic edifice crossed by the dyke intrusion, whereas sideromelane and tachylite constitute together less than half of the total (respectively the 28% and 17%). Crystals represent less than 5% of all components and are constituted mainly by plagioclase and clinopyroxene. Olivine crystals are less common and in the DEC 2018 samples generally are present in the fraction smaller than 0.5 mm.

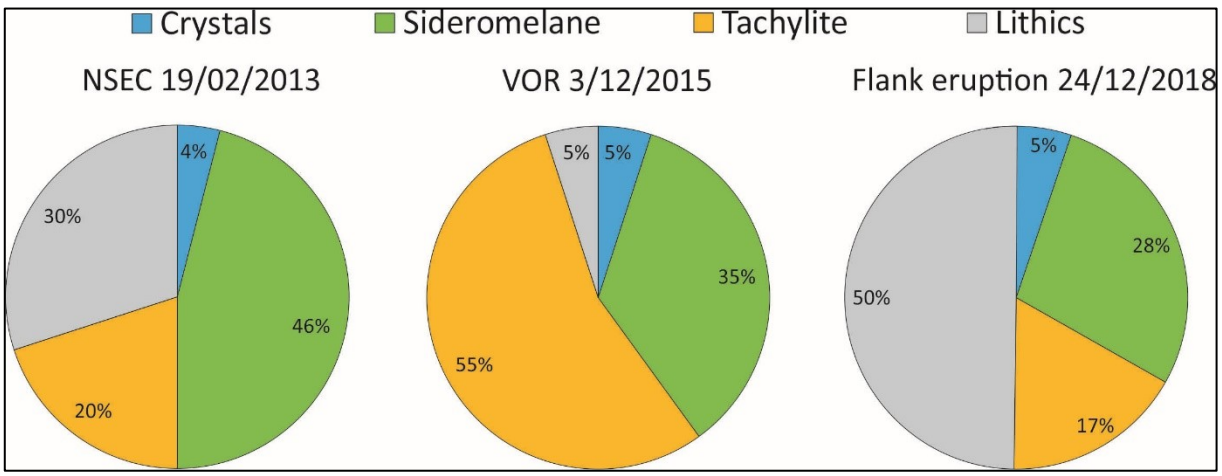

Figure 16: *Diagrams with relative percentages of clasts for all the selected eruptive episodes*.

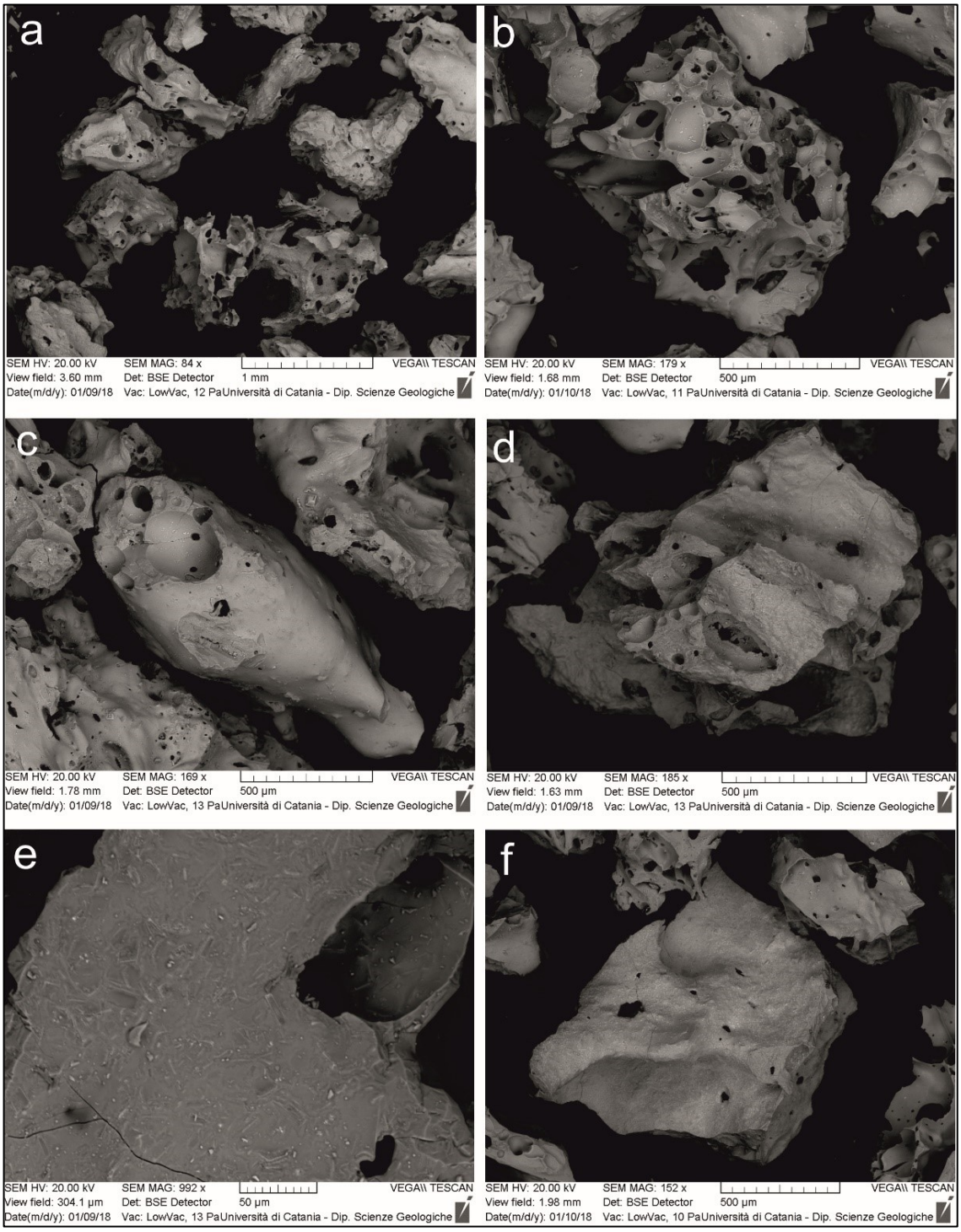

Figure 17: *BSE image showing some grains from VOR 2015 eruption* **(a)***; different types of clasts can be recognized:* **b)** *spongy morphology,* **c)** *fluidal morphology,* **d)** *blocky morphology,* **e)** *detail on blocky morphology clast, characterized by major crystallinity,* **f)** *lithic clast.*

Three types of external morphology have been recognized in the juvenile fragments (**Figure 17**): spongy, fluidal and blocky (cf. Pompilio et al., 2017). Both spongy and fluidal morphology are observed in sideromelane clasts of the VOR 2015 eruption, although spongy morphology is prevalent: these types of clasts show irregular shape and contain a high number of small spherical or elliptical vesicles, sometimes coalescent (**Figure 17b**). Fluidal morphology characterizes mainly sideromelane clasts of the NSEC 2013 and DEC 2018 products, which present elongated shape and smooth surface. Interconnected tubular vesicles are common and are responsible for the elongated shape of these clasts (**Figure 17c**). Both spongy and fluidal clasts are characterized by poor crystallinity. Blocky morphology has been observed mainly in tachylite clasts, which are affected by random oriented cracks and poor vesicularity (**Figure 17d**). Generally, a higher degree of crystallinity characterizes blocky clasts than the spongy and fluidal clasts, in which microlites of plagioclase are predominant (**Figure 17e**).

5.2. Textural and compositional features of olivine crystals

Olivine crystals containing MIs and embayments with size of 0.350 – 1 mm show euhedral to subhedral habitus and are often affected by fractures. Olivine compositions from all selected eruptions for this study range from Fo_{69} to Fo_{85}, with a peak between Fo_{79} and Fo_{82} (**Figure 18**). The highest concentration (Fo_{85}) is observed in the core of some olivines found in DEC 2018 products, although NSEC 2013 and VOR 2015 olivines show higher average compositions (Fo_{80} to Fo_{84}). Core-to-rim compositions measured along profiles in some olivine crystals reveal that rim compositions of NSEC 2013 and VOR 2015 eruptions show limited variability, ranging between Fo_{77} and Fo_{80}, whereas a wider compositional range is observed in rims of DEC 2018 olivine crystals, highlighting the existence of compositional zonation.

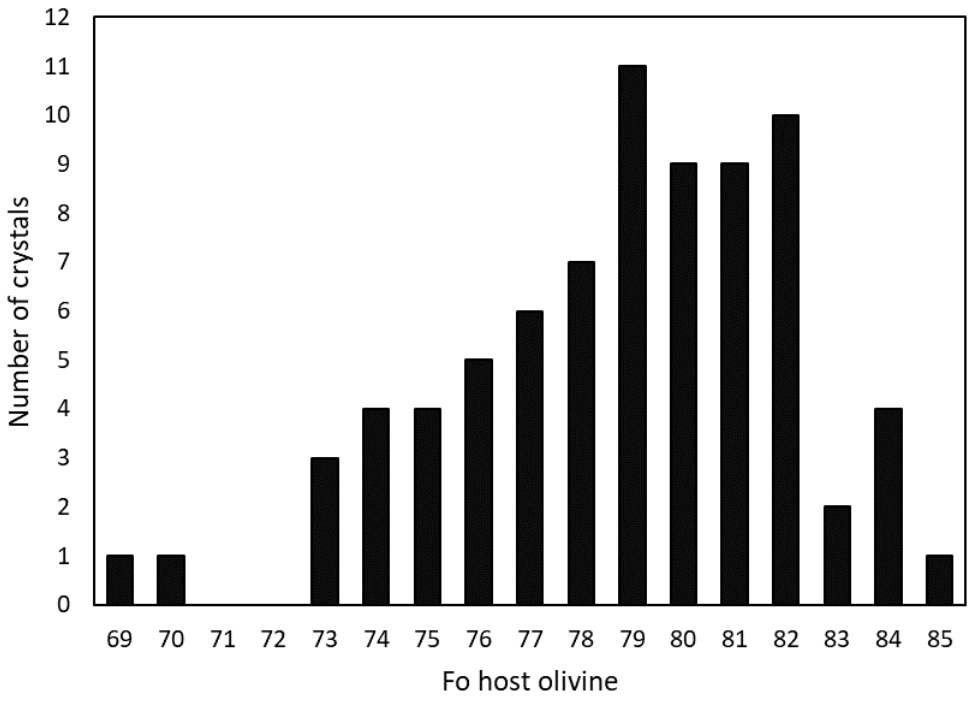

Figure 18: *Histograms showing the frequency relative to Fo compositions of host olivine crystals, measured close to the MIs and embayments.*

Normal zoning, which is the most common type of zonation, is generally observed in crystals with high forsterite content at core (Fo_{80-85}; **Figure 19a**), whereas olivines with lower concentration at core (Fo_{74-76}) display mainly reverse zoning pattern (**Figure 19b**). More complex zoning patterns have been also observed mainly in some olivine crystals with intermediate composition (Fo_{77-78}) from NSEC 2013 products and are characterized by a combination of reverse plus normal zoning (**Figure 19c**), whereas the opposite is very rare. Few crystals from NSEC 2013 and DEC 2018 products with composition between Fo_{75} and Fo_{78} show a homogeneous concentration from core to rim (**Figure 19d**).

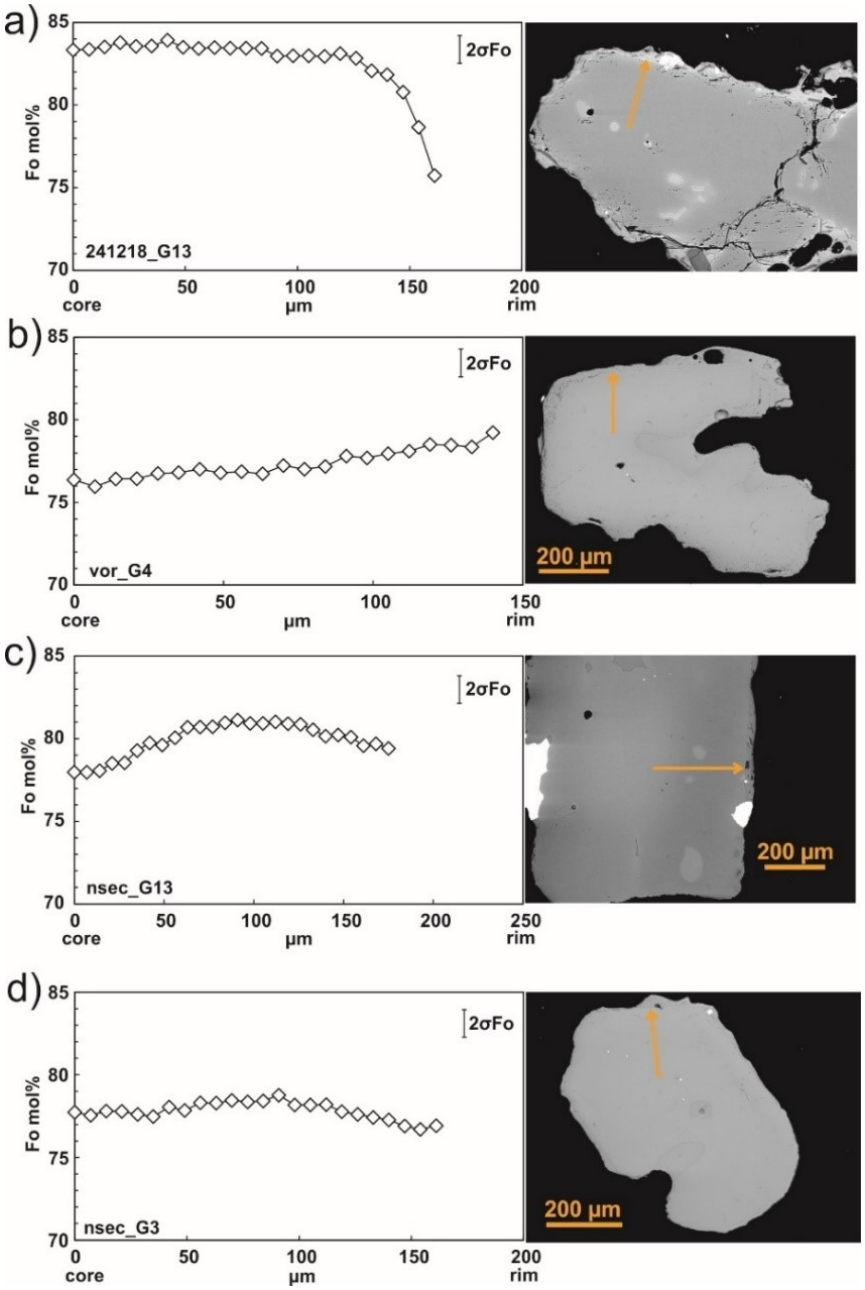

Figure 19: *Representative zoning patterns (***a)***: normal,* **b)***: reverse,* **c)** *complex,* **d)***: homogeneous) measured along core-to-rim profiles in host olivine crystals and their relative BSE images; orange arrows display the direction where compositional profiles have been collected.*

5.3. Description of Raman and FTIR spectra

The alumino-silicate domain of the Raman spectra, ranging from 200 to 1300 cm^{-1}, shows two main broad bands, located at 200-600 cm^{-1} (low-frequency band) and 850-1200 cm^{-1} (high-frequency band), and their topology (relative band intensities and band shape) depends on glass

structure, chemical composition and oxidation state. As expected, maximum peak positions of both low-frequency and high-frequency bands correspond to those generally measured in melts with basaltic compositions, respectively at 532 to 512 cm^{-1} and 966 to 990 cm^{-1} (**Figure 20**). Such bands are assigned to the different bridging and non-bridging T-O vibrations in the glass (Schiavi et al., 2018, and references therein). As stated in the previous chapter, the occurrence of magnetite nanolites produces a peak located at around 690 cm^{-1} (**Figure 20**). Furthermore, characteristic peaks at around 400 cm^{-1} and 990 cm^{-1} have been frequently observed (**Figure 20**), which are related to specific compositional features, as observed from MIs major element compositions (see next paragraph).

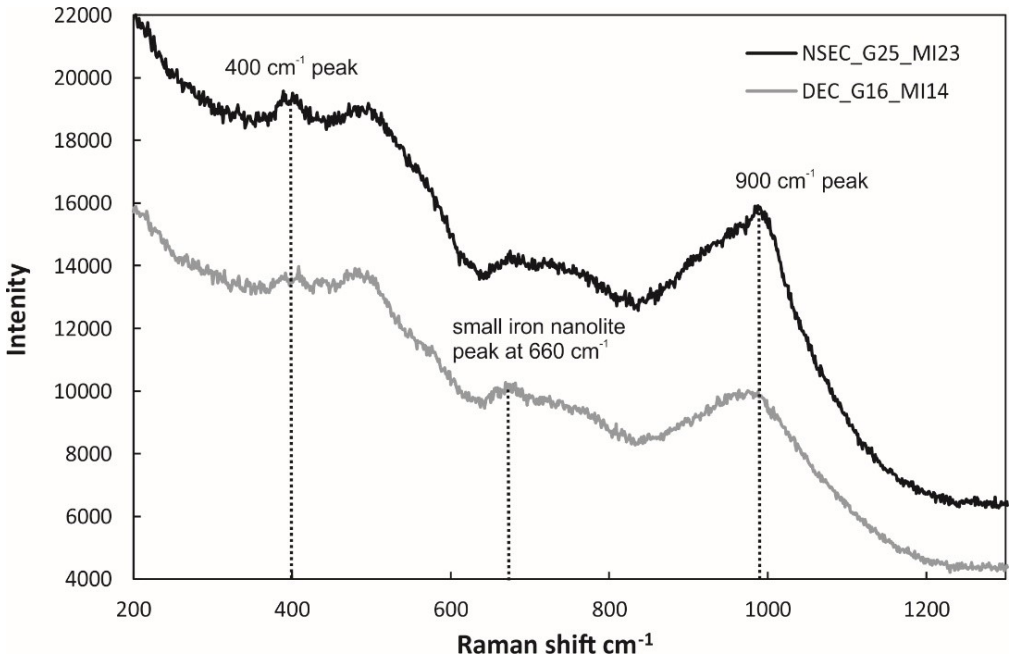

Figure 20: *Examples of raw Raman spectra in the alumino-silicate domain from 200 to 1300 cm^{-1} for two MIs. Characteristic peaks located at 400 and 990 cm^{-1} are observed, with the 990 cm^{-1} peak being visible only in the black spectrum. Such features are related to the presence of two types of MIs (see next paragraph).*

Glass matrix composition, water concentration, water speciation and strength of H-bonding affect the OH stretching vibration bands (from 3000 to 3800 cm^{-1}; **Figure 13**), which

show asymmetric shapes with a long tail on the lower wavenumber side. The maximum intensity of the band is found in the range of 3565–3582 cm^{-1}, as expected for basaltic compositions (Schiavi et al., 2018).

The absorbance FTIR spectra have been analyzed in the domain between 1000 and 4000 cm^{-1} (**Figure 21**). Glass inclusion spectra show a broad band centered at 3550 cm^{-1}, which contains the fundamental stretching vibrations of both molecular H_2O and OH^- groups (e.g., Stolper, 1982) and was used for quantification of total water concentrations in MIs; the bending mode of molecular H_2O is observed at 1640 cm^{-1}. The antisymmetric stretch of distorted CO_3^{2-} groups generate a doublet at around 1515 cm^{-1} and 1435 cm^{-1} (**Figure 20**) (Fine and Stolper, 1986). In the spectra of pure olivine, the bands of pure glass are absent, whereas a series of spectral bands between approximately 2000 and 1600 cm^{-1} are present and attributed to Si-O overtones (Fine and Stolper, 1986).

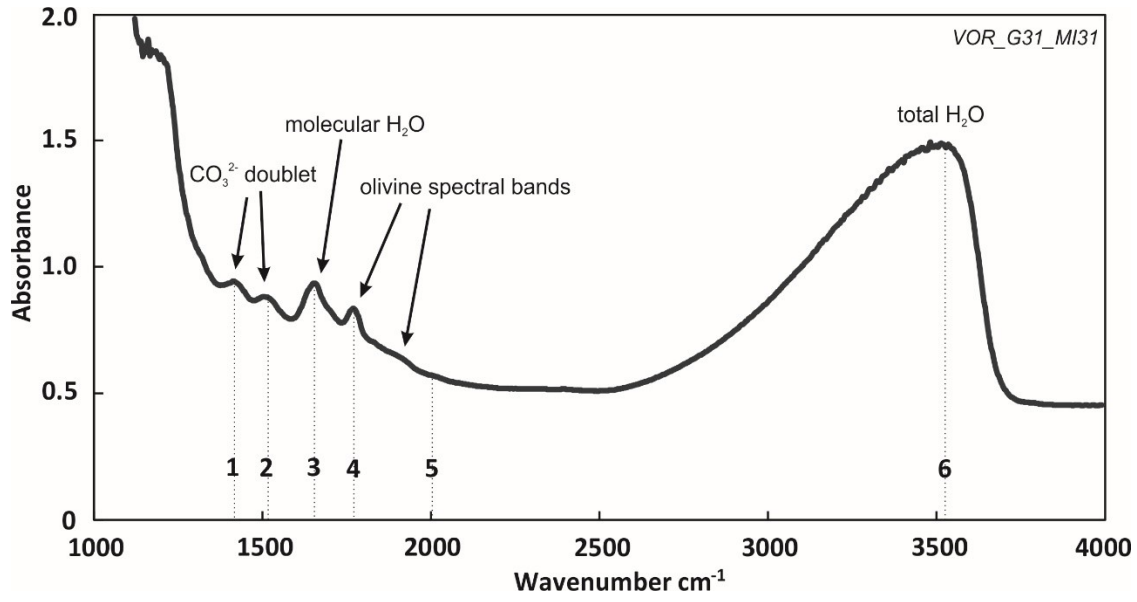

Figure 21: *Example of an olivine-contaminated inclusion transmittance FTIR spectrum (VOR 2015); 1, 2: CO_3^{2-} doublet peak (1420 and 1520 cm^{-1}); 3: molecular H_2O peak (1640 cm^{-1}); 4, 5: olivine spectral bands (from 1770 to 2000 cm^{-1}); 6: total H_2O band (3550 cm^{-1}).*

In olivine-contaminated inclusion spectra, H_2O and CO_3^{2-} bands are observed together with bands attributed to vibrations of the olivine lattice. No overlapping between CO_3^{2-} doublet and olivine spectral bands is observed, but the contamination from the olivine may cause a decrease in intensity of the CO_3^{2-} doublet and H_2O band height.

In some MIs, H_2O contents have been quantified using both Raman and FTIR analyses, in order to estimate the accuracy of the measurements and evaluate the effect of the presence of magnetite nanolites. The data show a good consistency between the two techniques (**Figure 22**); only in few cases Raman analyses underestimated H_2O contents because of the presence of magnetite nanolites. Therefore, preferentially H_2O quantification by FTIR analyses was chosen, except for the sample VOR_G14_MI11 (**Figure 15**), where FTIR spectra showed a strong saturation of the total OH peak.

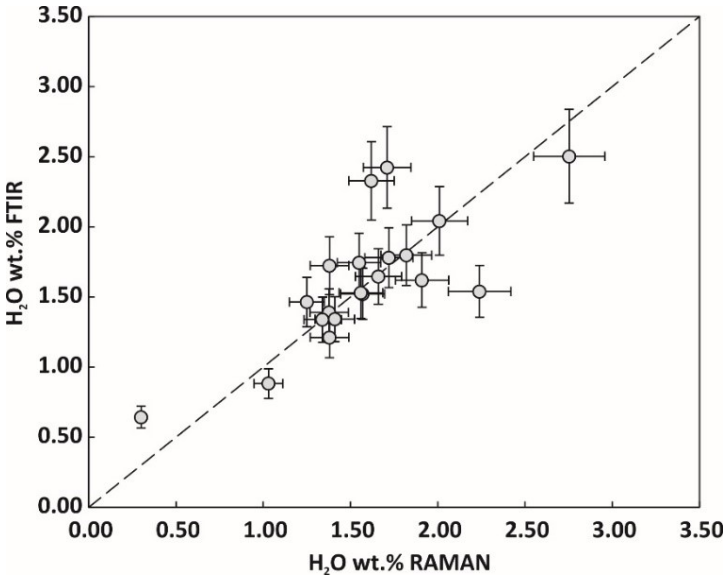

Figure 22: *Diagrams showing H_2O quantification in some MIs by both Raman and FTIR spectroscopy; measured compositions show very similar values close to the 1:1 dashed line (See measured compositions in **Table A1**).*

5.4. Compositions of olivine hosted-melt inclusions

5.4.1. MIs major elements compositions

A total of 71 MIs has been investigated for this study (24 from the NSEC 2013 eruption, 24 from the VOR 2015 eruption and 23 from the DEC 2018 eruption). The size of MIs analyzed ranges from 16 µm to 170 µm, with an average diameter of 50-60 µm. They show generally oval or elliptic shape and the color of the glass is dark to light brown. Some MIs are elongated or show irregular shape (**Figure 23**). Most of MIs contain a bubble and assuming elliptic and spherical shape for MIs and bubbles respectively, the bubble/MI volume ratio is calculated between 0.02 and 0.14, except very few inclusions which show higher value (maximum 0.33). Given the low ratio for most MIs, the bubbles are considered mainly as shrinkage bubbles, which are the result of a greater volume contraction of the silicate melt with respect to the hosting olivine during cooling (e.g. Wallace et al., 2015). Furthermore, many MIs contain oxide inclusions, which are often associated to small sulfide globules (**Figure 23**).

The compositions of host olivine crystals containing the investigated MIs range from Fo_{69} to Fo_{85}, and the most show value of Fo_{79-82}. Correction of major elements have been made taking into account the post-entrapment crystallization (PEC) on the wall of the inclusions through Petrolog3 (Danyushevsky and Plechov, 2011), a software developed for modeling fractional or equilibrium crystallization, reverse of fractional crystallization, and post-entrapment re-equilibration of MIs in olivine crystals. PEC calculation was performed using a K_d $[(FeO/MgO)_{olivine}/(FeO/MgO)_{melt}]$ of 0.3 for equilibrium partitioning of FeO and MgO between olivine and liquid in Etna basalt (Métrich and Clocchiatti, 1996) and assuming fO_2 at QFM buffer, based on MELTS calculations defined for tracking the evolution path of the magma erupted during the 2011-2013 paroxysmal series (Giuffrida and Viccaro, 2017) and corresponding to a ratio Fe^{3+}/Fe^{2+} of ~ 0.17-0.21.

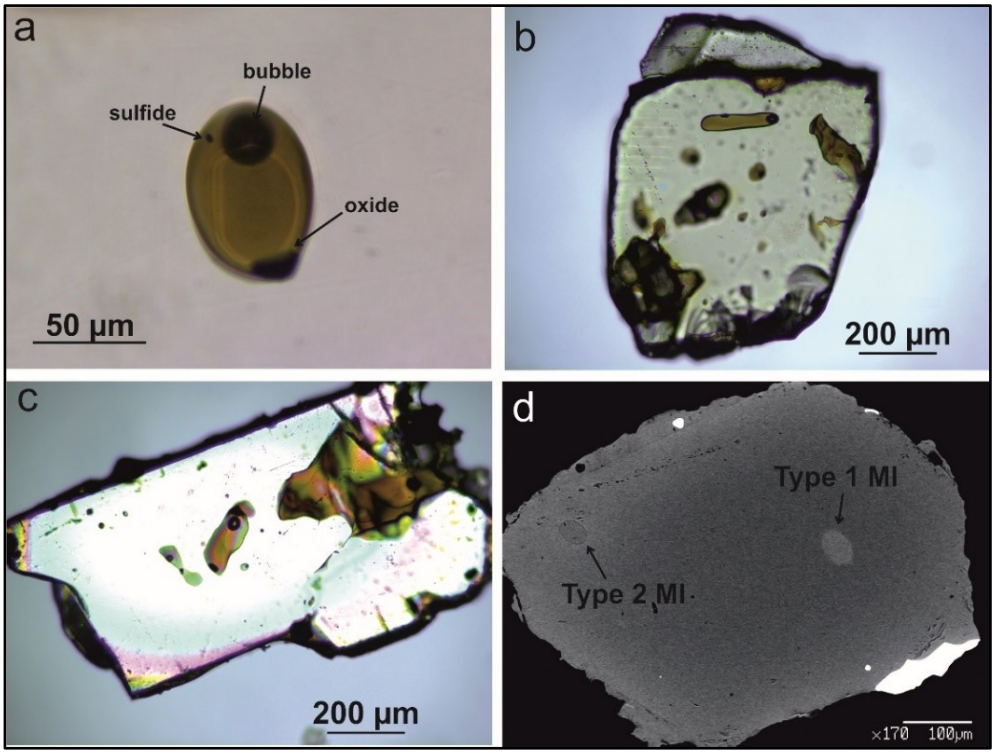

Figure 23: *Example of selected MIs:* **a)** *elliptic shape MI, containing bubble, sulfide and oxides (VOR 2015);* **b)** *elongated MI, off center located (NSEC 2013);* **c)** *irregular shape MI, center located (VOR 2013);* **d)** *BSE image of a olivine hosting the two types of MIs: type 2 is darker than type 1 and it is generally located closer to the rim of high Fo olivine crystals.*

The calculation is carried step by step, where small percentages of olivine with the MI composition is added until the equilibrium composition with the host olivine adjacent to the MI is reached. Forsterite composition of the host olivine required for the calculation is constrained by considering an average value from 3-4 SEM-EDS spot analyses taken at distance from the inclusion less than 20 µm. FeO_{tot} must be constrained in the calculation, in order to consider Fe loss processes during the re-equilibration induced by the crystallization on the walls of inclusions (Danyushevsky et al., 2000). Generally, FeO measured from bulk rock compositions are used, but this will produce the same FeO value for all MIs. So, MIs have been grouped on the basis of the Fo content of the host olivine, following the approach of Giuffrida and Viccaro (2017), where have been recognized at least 5 olivine population: 1) Fo_{83-85}; 2) Fo_{79-82}; 3) Fo_{77-78}; 4) Fo_{75-76}; 5) Fo_{72-73}. The highest value of FeO measured in MIs correlated to each olivine

population has been considered for the correction. Values of PEC% generally are lower than 8%, except in some cases where the maximum value is 14%.

Corrected MIs for PEC effects from all the three selected eruptive episodes have similar major element compositions and display a general trend concordant with an ordinary evolution path for basaltic liquids (s.l.). However, diagrams in **Figure 24** highlight how MIs compositions seems to be clustered in two different groups, especially considering some elements like SiO_2, CaO, and alkali. Using the SiO_2 concentration as classification criterium, the MIs can be grouped in two types on the base of major element compositions (**Figure 24**). Type 1 MIs are more basic and show SiO_2 ~42.7-45.7 wt.%, Na_2O+K_2O ~5.1-6.2 wt.%, CaO ~9.9-12.5 and wt.%, Mg# ~55-62. Type 2 MIs are more evolved, displaying SiO_2 ~46.5-51.2 wt.%, Na_2O+K_2O ~6.2-8.3 wt.%, CaO ~6.1-9.7 and wt.%, Mg# ~ 48-54. Generally, type 1 MIs have been found entrapped in olivine crystals with Fo_{79-85}, whereas the type 2 are more common in olivine crystals with Fo_{69-78} (**Figure 24h**). Few inclusions from NSEC 2013 and VOR 2015 show intermediate featured between the two types of MIs; for example, the VOR_G6_MI2 sample shows SiO_2 ~46.50 wt.% and can be classified as type 2, with Fo composition measured close to the inclusions at 74 mol%, but alkali and CaO concentrations are more similar to type 1 MIs. Where both types of MIs have been measured in the same olivine crystal, type 2 MIs are off center located and closer to the crystal rim (**Figure 23d**). Furthermore, very low SiO_2 contents, up to 42.7 wt.%, characterize the type 1 MIs (**Figure 24**). Such strong depleted concentrations in SiO_2 is an odd feature for volcanic rocks erupted in historic and recent times at Mt. Etna. It is worth to note that differences in major and minor element compositions (e.g., Ca and S contents) between the two types of MIs are highlighted even by the spectral differences observed in the alumino-silicate domains of the Raman spectra. In particular, almost all type 1 MIs display two pronounced peaks centered at 400 and 990 cm^{-1}, whereas in few type 2 MIs only the peak at 400 cm^{-1} is observed (**Figure 20**).

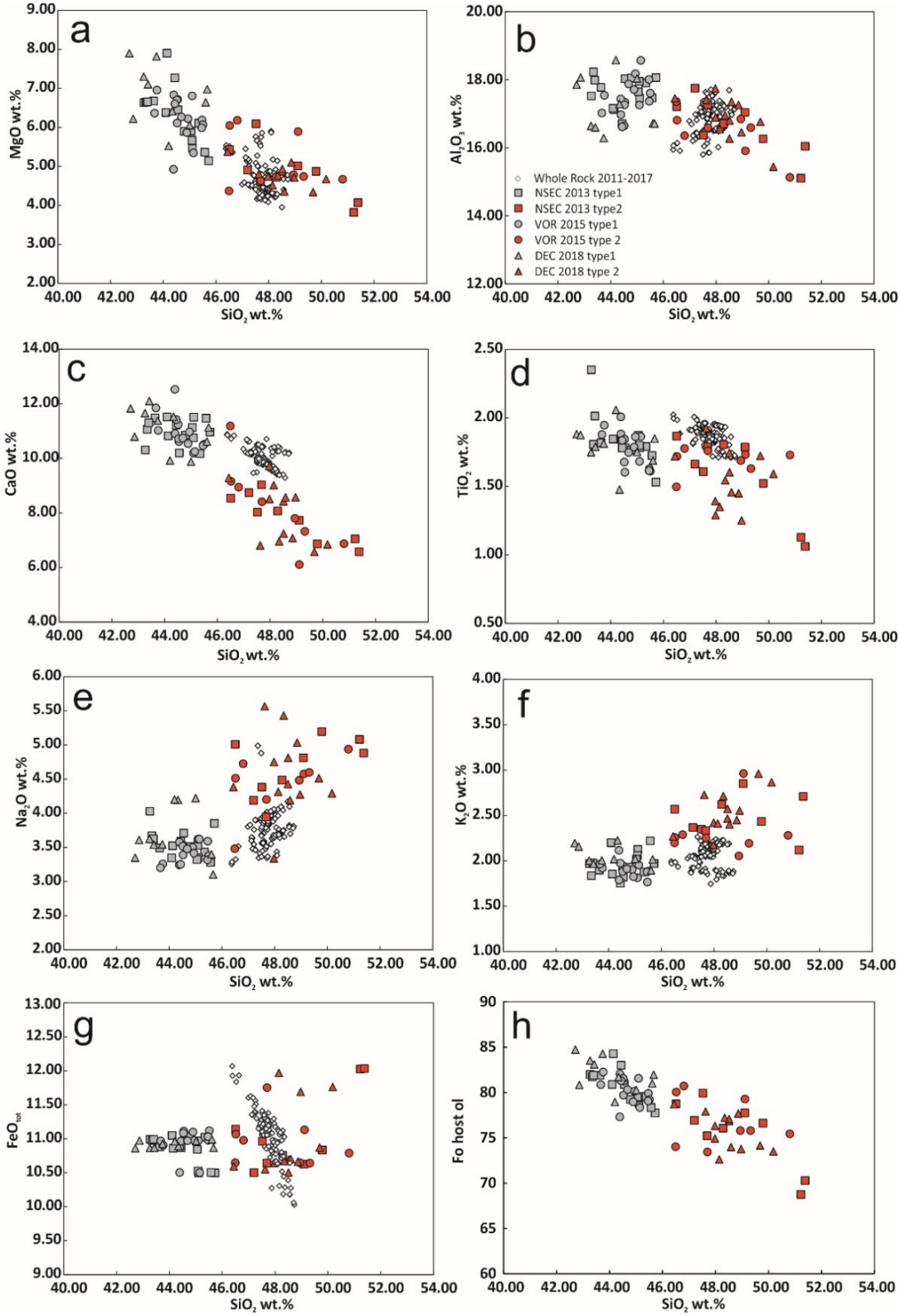

Figure 24: *PEC corrected major elements compositions vs. SiO_2, used as index differentiation, in selected MIs from the three eruptive episodes of the post-2011 activity at Mt. Etna. Type 1 and type 2 MIs are distinguished on the base of color (light grey and red respectively), whereas symbols recognize the eruptive episode (square: NSEC 2013; circle: VOR 2015; triangle: DEC 2018). White diamonds are whole rock compositions emitted during 2011-2017 activity (data from Viccaro et al., 2014; 2019).*

5.4.2. MIs volatiles compositions

Water contents measured on MIs found in recent products erupted at Mt. Etna range between 0.40 and 2.40 wt.% (**Figure 25**). NSEC 2013 MIs display a narrow compositional range, with water contents from 1.00 to 1.60 wt.% for most of the analyzed MIs. Differently, VOR 2015 and DEC 2018 samples are characterized by a greater variability. In this regard, contents on the order of ~2.00 wt.%, have been observed more frequently in type 1 MIs of VOR 2015, where the mean average value is higher than the other two eruptions. High contents were found also in a few MIs of type 1 of DEC 2018 (up to 2.40 wt.%). However, a clear correlation with the two types of MIs is not observed. Indeed, some of type 1 MIs of DEC 2018 entrapped in high Fo olivine (>Fo_{80}) occasionally show very low H_2O contents, up to 0.47 wt.% (**Figure 25d**), when higher contents are expected since MIs entrapped in high Fo olivine should be representative of more primitive and undegassed melts. Poor correlation is observed with SiO_2 concentrations, as both low and high H_2O compositions are found in undersaturated SiO_2 type 1 MIs (**Figure 25b**), especially for DEC 2018 samples. A negative correlation can be recognized with K_2O, which can be used as differentiation index thanks to its high incompatibility in olivine crystals (**Figure 25c**). Such correlation is an indication of degassing coupled to crystallization, with higher water contents in less evolved MIs.

FTIR measurements revealed a general low budget of CO_2 (46-849 ppm) dissolved in the melt for the post-2011 products (**Figure 25a**), if compared to concentrations found in other recent eruptions (~4000 ppm in MIs from 2001 and 2002-2003 activity; Métrich et al., 2004; Spilliaert et al., 2006a). The highest CO_2 contents were measured in type 1 MIs from VOR 2015 samples, with a maximum concentration of 849 ppm. On the contrary, NSEC 2013 MIs display very low CO_2 contents in the range 46 - 165 ppm, except for one MI showing CO_2 at 355 ppm. MIs from DEC 2018 products display slight enrichment in CO_2 at very low water contents and generally higher contents are observed in type 1 MIs.

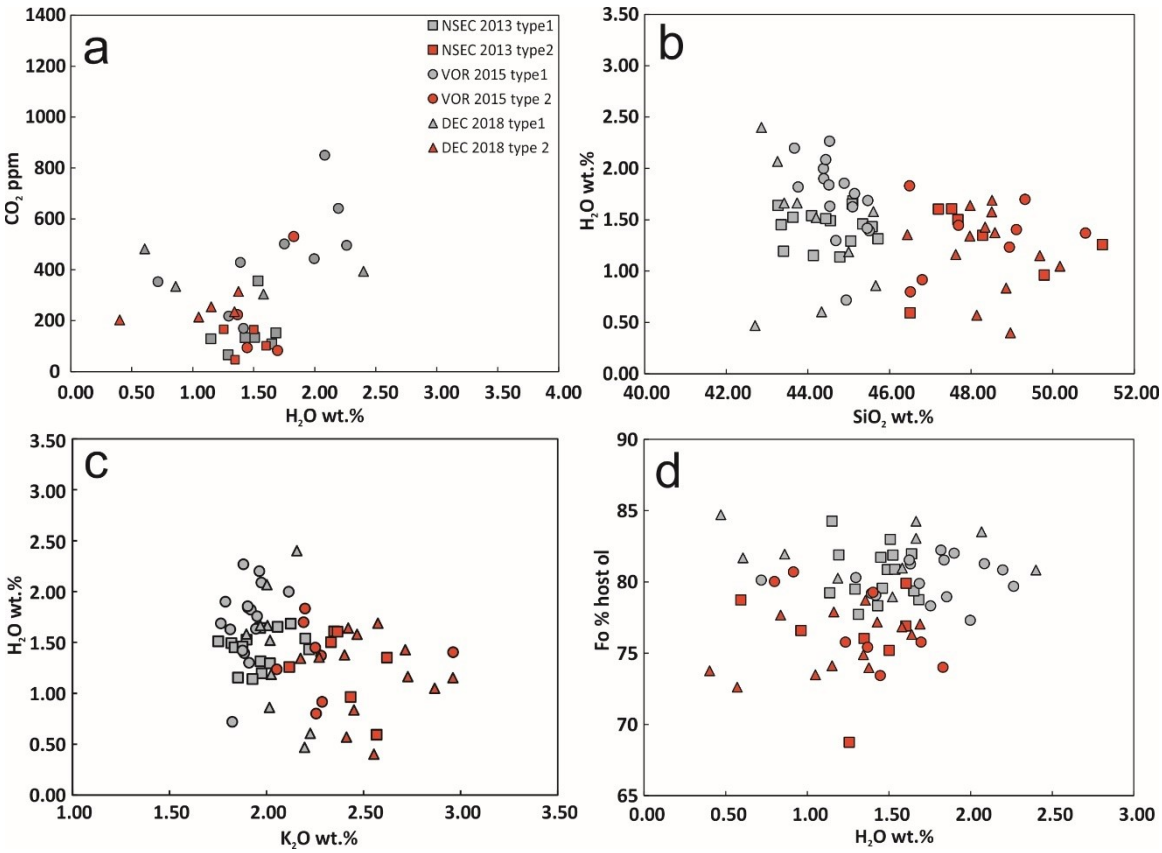

Figure 25: *H_2O compositions plotted against CO_2, SiO_2, K_2O and Fo% host olivine measured in selected MIs from the post-2011 activity at Mt. Etna.*

Sulfur (S, 172-3072 ppm), Chlorine (Cl, 870-3423 ppm) and Florine (F, 670-1546 ppm) concentrations are rather comparable for all the three eruptive episodes (**Figure 26**). The highest S content (~3072 ppm) is measured in type 1 MI from VOR 2015 products; type 2 MIs generally show concentrations lower than 1500 ppm, except the sample VOR_G6_MI2 having content of 2634 ppm, being more pertinent with values found for type 1 MIs. The K_2O vs S diagram displays a trend of constant decrease for S, where a variation in the slope characterizes the transition from type 1 to type 2 MIs.

Concerning Cl, both types of MIs are characterized by fairly comparable compositions, except for a few samples where high Cl value (~3423 ppm) have been measured. Differently, F is higher in type 2 than type 1 MIs. Such observation suggests that magma erupted in the three

selected eruptions from the post 2011 activity did not experience significant degassing for these two volatile species.

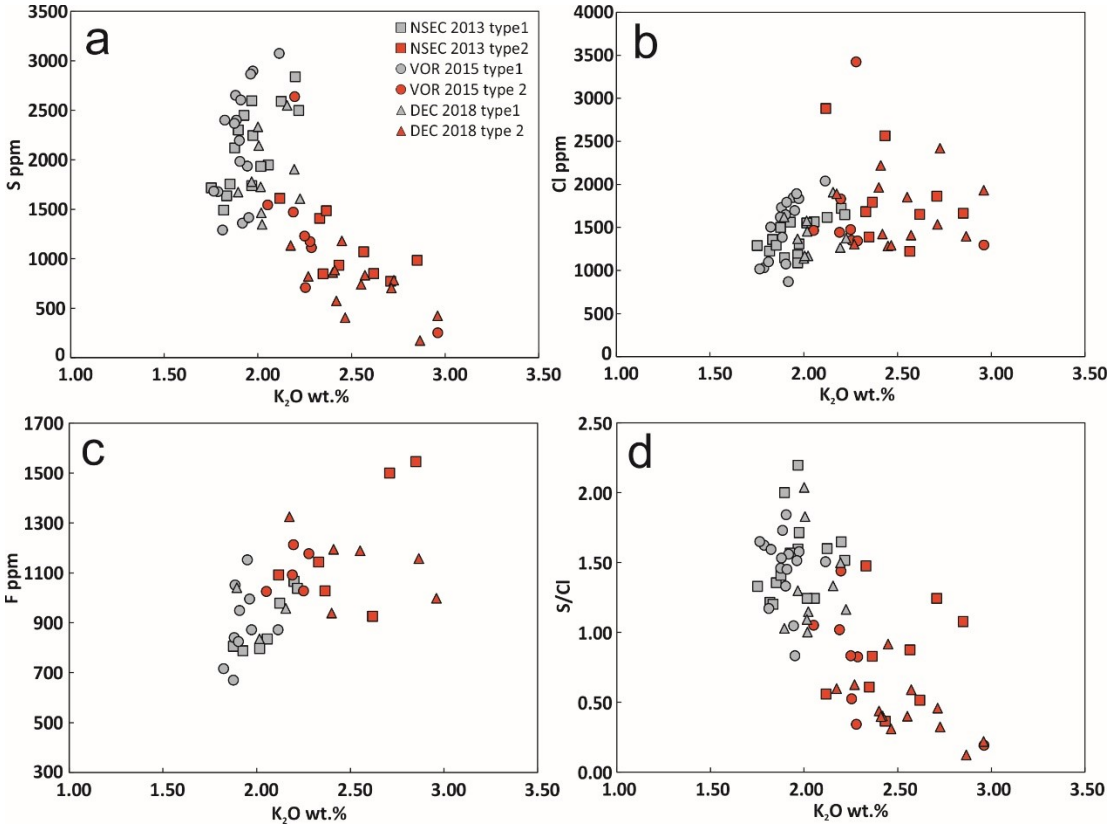

Figure 26: *S, Cl, F and S/Cl ratio plotted against K_2O, used as index of differentiation.*

5.4.3. MIs traces elements compositions

MIs from the recent post-2011 activity show similar trace elements compositions for all the three eruptive episodes, as inferred from major elements. Type 1 MIs from products of the three considered eruptions show rather comparable concentrations for LILEs, HFSEs and REEs. Type 2 MIs generally display trace element concentrations higher than type 1 MIs, also covering wider compositional ranges. An anomaly is observed for two MIs from DEC 2018 products, which have been classified as type 2 from major elements but display trace elements compositions more consistent to type 1 MIs.

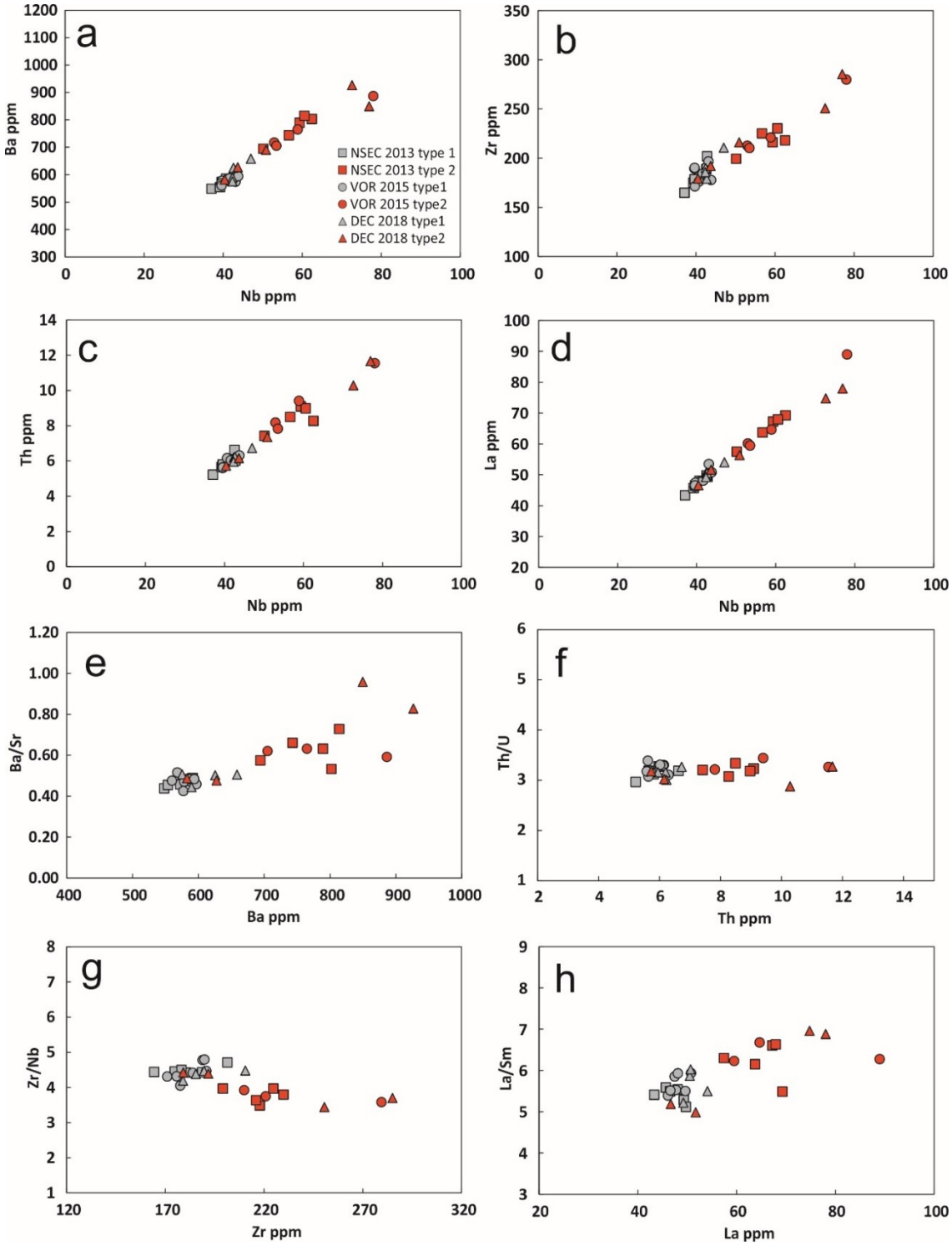

Figure 27: *Diagrams showing the variation of selected trace elements plotted against Nb together with selected incompatible trace element ratios.*

Ratios involving variably incompatible trace elements allow to investigate on the nature of possible variations of the geochemical signatures. No substantial differences affect MIs of

the recent products (**Figure 27**), suggesting they have origin from the same parental magma. Small differences can be observed in some ratios from the type 1 to type 2 transition. Specifically, the type 1 MIs display lower La/Sm and LREE/MREE and higher Zr/Nb compared to type 2 MIs, whereas the Ba/Sr ratio shows a progressive increase within the type 2 MIs series. Such variations may be correlated to crystallization and fractionation processes of specific mineral phases.

5.5. Compositions of olivine-hosted melt embayments

5.5.1 Embayments major elements compositions

A total of 15 embayments has been selected for this study: 5 from NSEC 2013 products, 6 from VOR 2015 products and 4 from DEC 2018 products. Tubular-shaped embayments are the more common, but few samples display a narrower neck close to the open side or more irregular shape. A vesicle at the open side of the tube evidence the occurrence of a bubble exchanging elements with the melt inside the embayment during ascent. The size ranges between 49 and 144 μm, with longer embayments more common on NSEC 2013 and VOR 2015 products than in DEC 2018.

PEC effects on major elements compositions are not considered, since volatiles in embayments are the main objects of interest in this study. Major elements compositions are consistent with type 2 MIs, suggesting that the melt filling the embayments is almost the same trapped in the evolved MIs hosted in low Fo olivines. In fact, rim compositions of olivine crystals containing melt tubes, which are assumed to be in equilibrium with the external melt before the eruption, range between Fo_{74} and Fo_{77}, occasionally showing Fo_{79} mol%. Such observations support the idea that the formation of embayments may have occurred during the late stages of magma evolution.

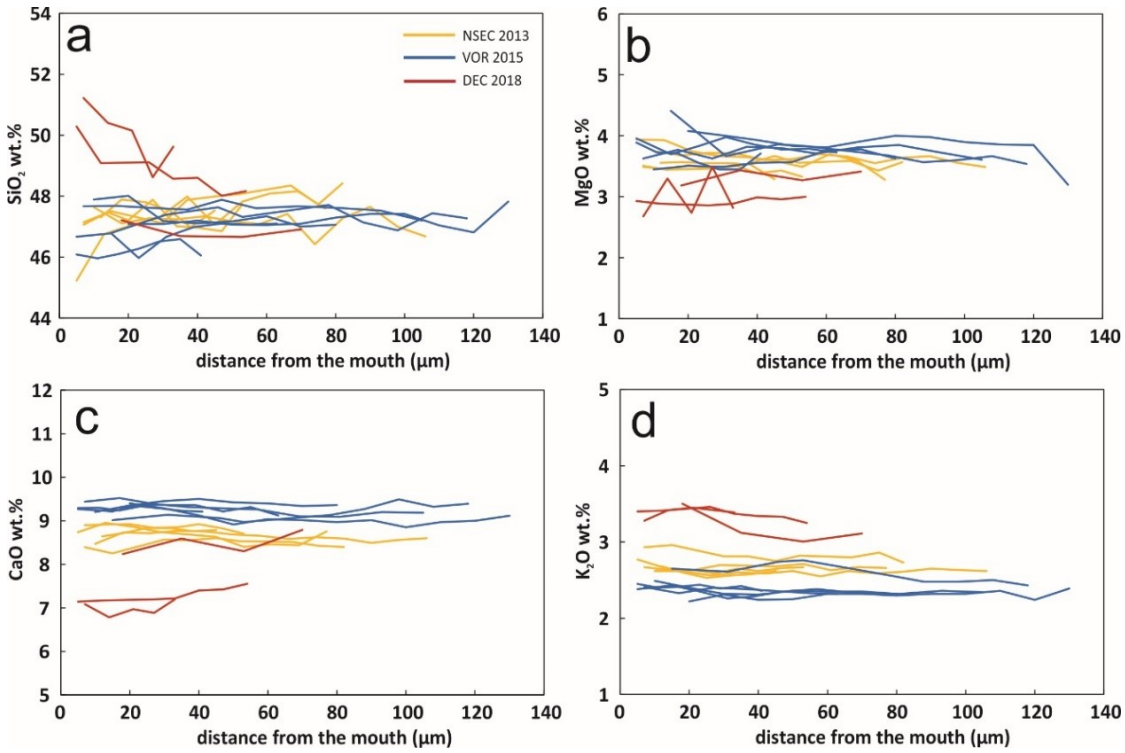

Figure 28: *Selected major elements variations in melt-embayments found in products of the post-2011 activity at Mt. Etna, in function of the distance from the mouth of embayments.*

Two of the four selected embayments from DEC 2018 products are characterized by slightly more evolved compositions (SiO_2 ~48.5-49.0 wt.%; **Figure 28**) compared to the other analyzed embayments (SiO_2 ~47.0-48.0 wt.%). Compositions along the tubes are rather constant for what concerns all major elements. Only SiO_2 display slight increase at the last outermost 30-40 µm in a few samples. An exception is represented by one embayment from NSEC 2013 (NSEC_emb1) which displays a marked decrease of SiO_2 (up to 45.2 wt.%).

5.5.2. Embayments volatile elements compositions

As for major elements, profile compositions of H_2O, S and Cl have been measured along the median axis of each embayment analyzed in this study. Unfortunately, no CO_2 data are available because average sizes of embayments were not suitable for FTIR analyses.

Raman analyses on embayments highlight the presence of H_2O compositional gradients, where the concentrations progressively decrease toward to the open side of the tubes (**Figure 29**). The NSEC 2013 and VOR 2013 samples show compositions in the range of 0.85-1.33 wt.% and 1.14-1.72 wt.%, respectively, in the interior of embayments. Higher contents are observed for VOR 2015 embayments, except for the sample VOR_ emb2 which shows lower concentration (~0.9 wt. %; **Figure 29g**) respect to other samples of the same eruption. On the contrary, marked lower concentrations are observed for the DEC 2018 samples, with compositions of 0.3-0.7 wt.%. It is worth to note that the highest H_2O compositions for each eruptive episode are observed in the longest embayments, indicating that the diffusive volatile loss affected more extensively the shorter embayments. The shape of gradients is different between each eruptive episode selected for this study. VOR 2015 embayments are characterized by a plateau with rather constant compositions, followed by steep variations in the last 30-40 μm from the end of the melt tubes, up to ~0.2-0.5 wt.%. Differently, more gradual variations can be observed in the NSEC 2013 embayments, starting from 50-70 μm from the open side of tubes. The DEC 2018 embayments display gently gradients, reaching contents of 0.1-0.3 wt.% at end of the tubes.

Sulfur concentrations along the embayments obtained through EMP analyses reveal similar inferences for H_2O compositions. Measurements in the interior of embayments evidence that VOR 2015 samples are characterized by slightly higher concentrations, on the order of 734-1392 ppm, than the NSEC 2013 products, which show values in the range of 626-1142 ppm, except for one sample characterized by very low S content (NSEC_emb3, ~153-260 ppm). As expected, the DEC 2018 products show lower concentrations in the range of 543-965 ppm. Sulfur concentrations generally decrease at the end of the embayments, with values lower than 500 ppm showing presence of compositional gradients, although in few of the analyzed samples clear and regular gradients cannot be recognized.

Chlorine concentrations in embayments are comparable with those measured in MIs. As observed for S concentrations, no clear gradients have been observed for Cl in embayments selected for this study. NSEC 2013 and VOR 2015 display similar compositions, in the range of 992 – 1721 ppm, with an average value of 1400 ppm. MIs from the DEC 2018 eruption are characterized by higher values, between 1420-2143 ppm.

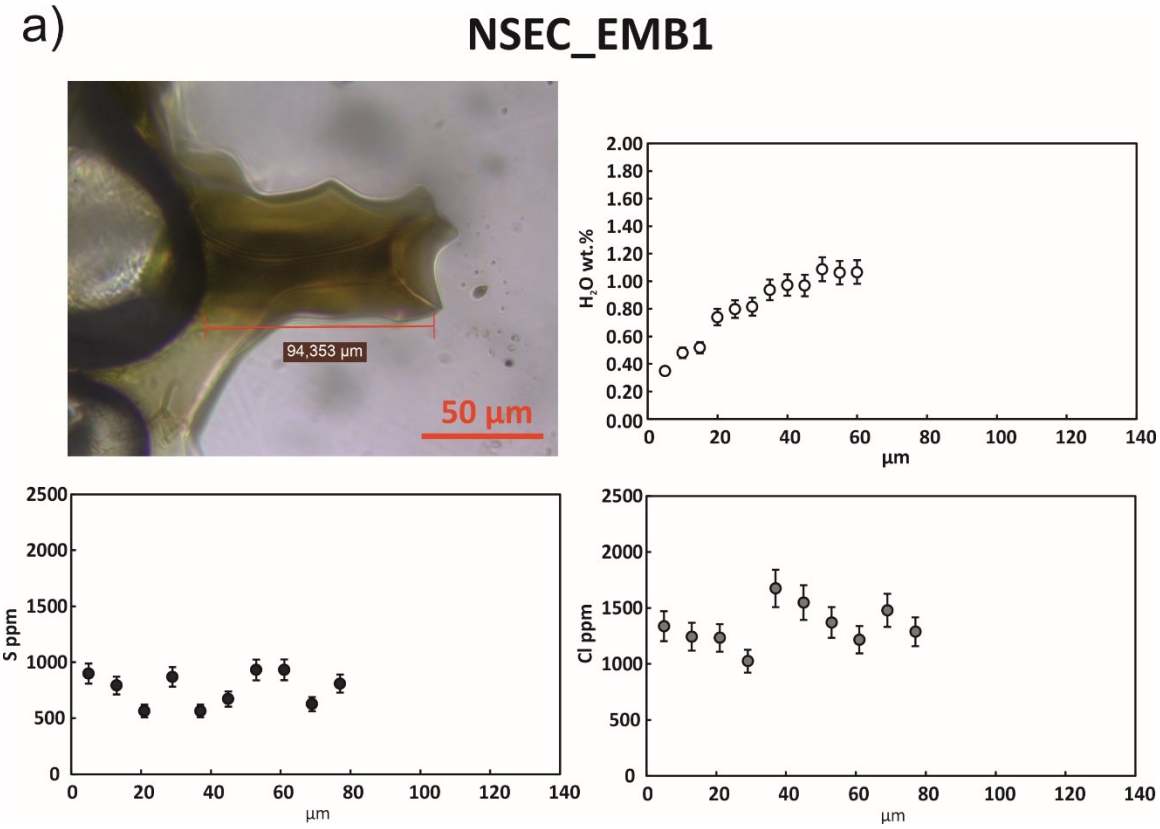

b)

NSEC_EMB2

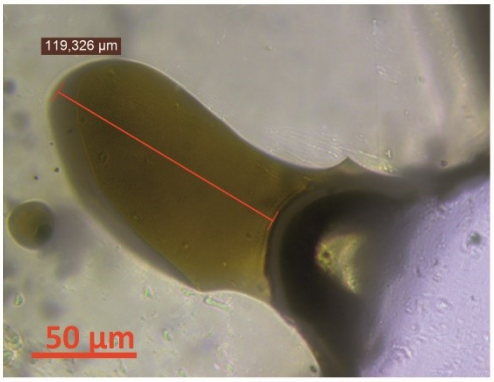

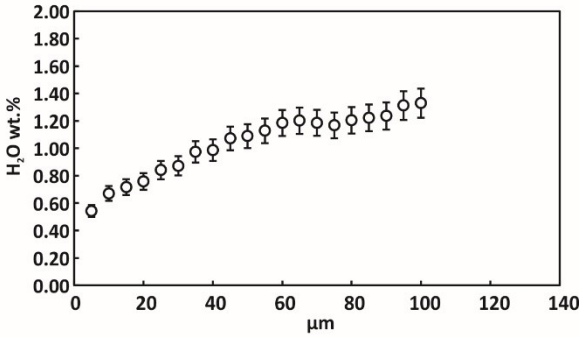

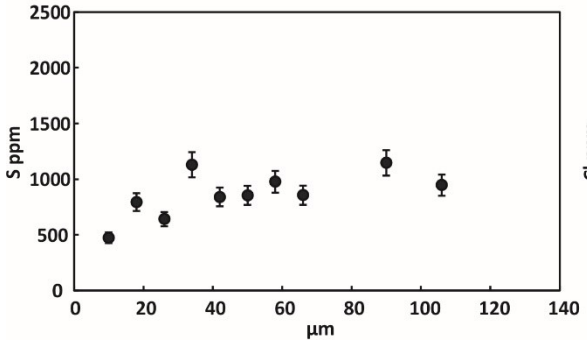

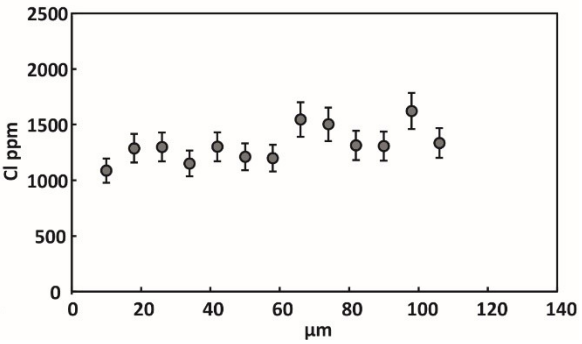

c)

NSEC_EMB3

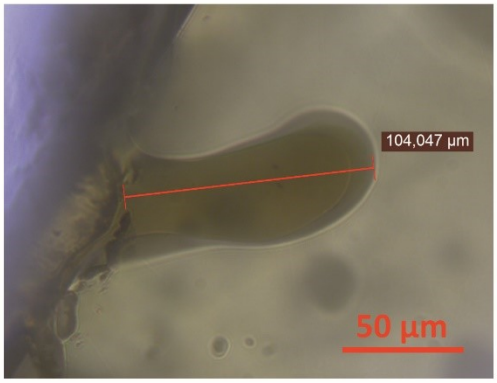

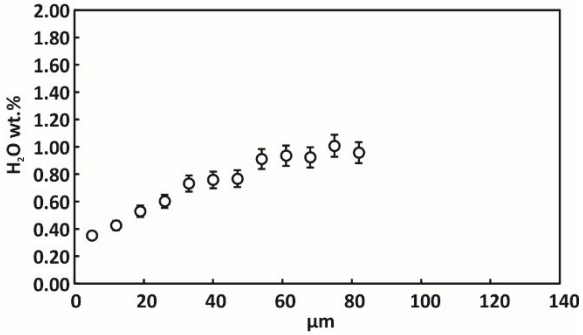

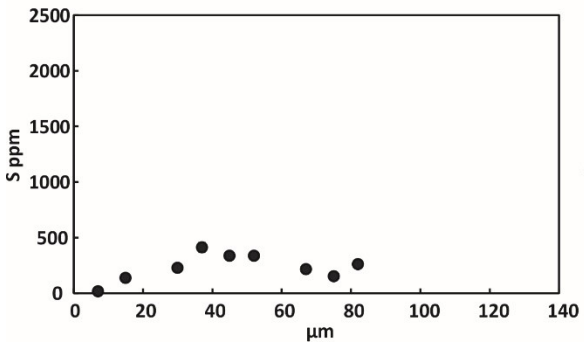

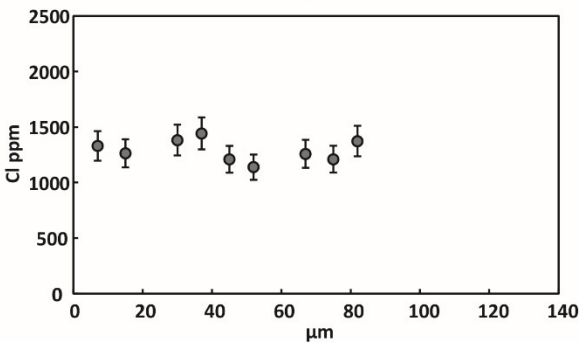

d) NSEC_EMB4

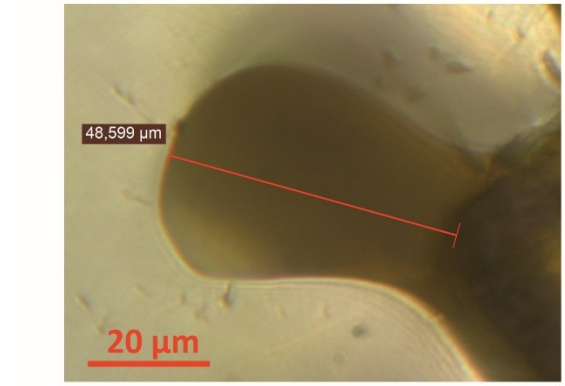

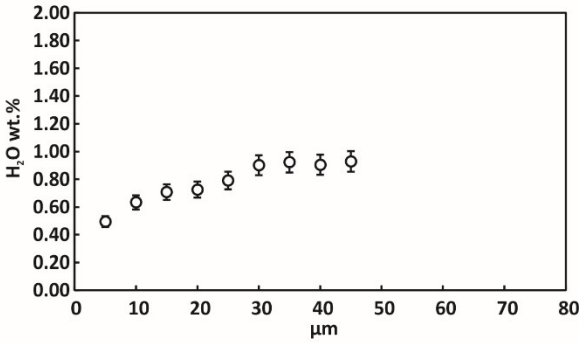

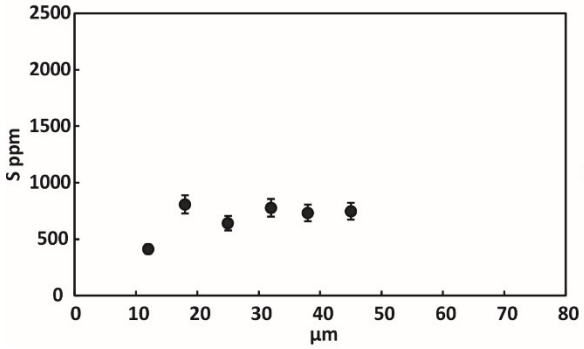

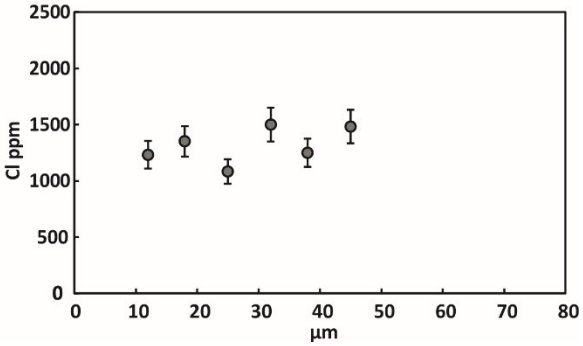

e) NSEC_EMB5

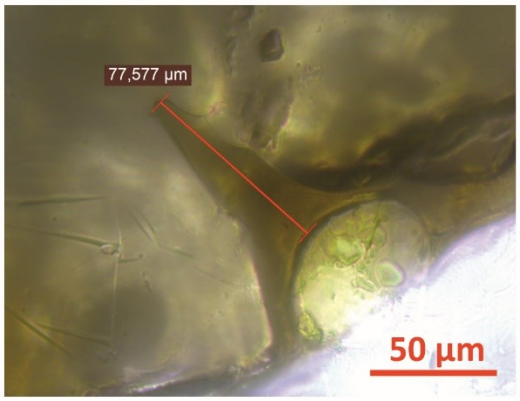

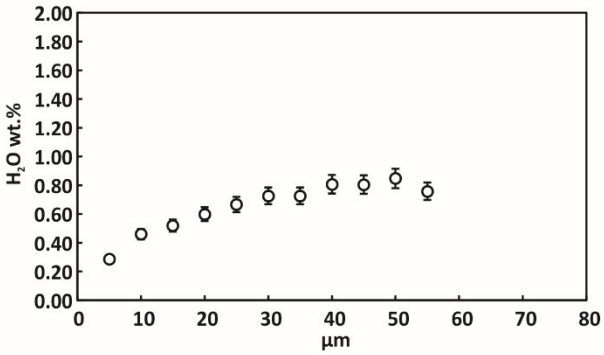

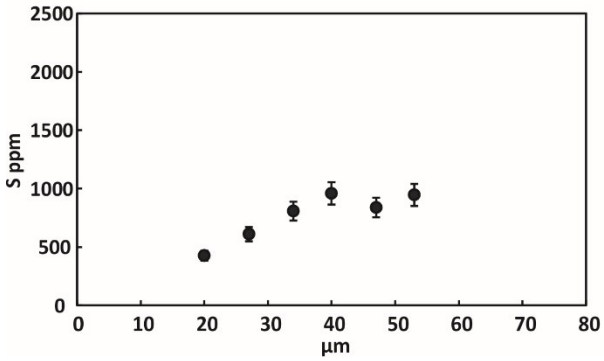

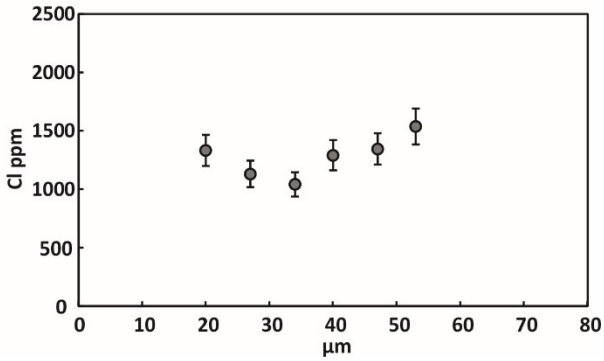

f)

VOR_EMB1

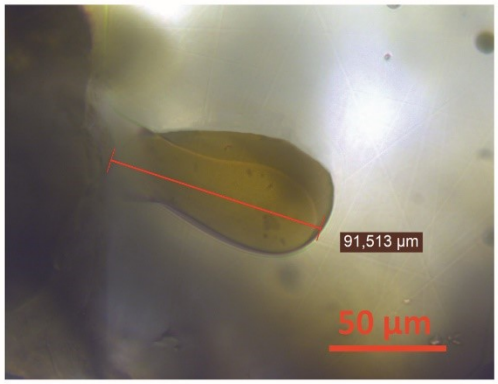

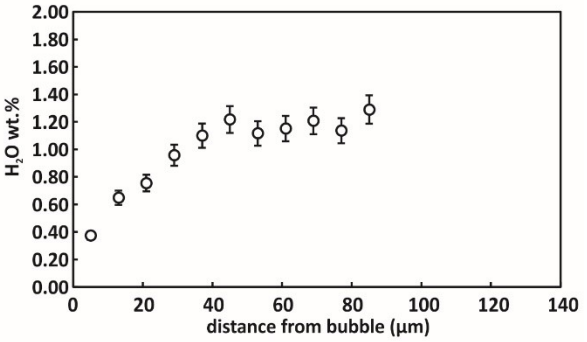

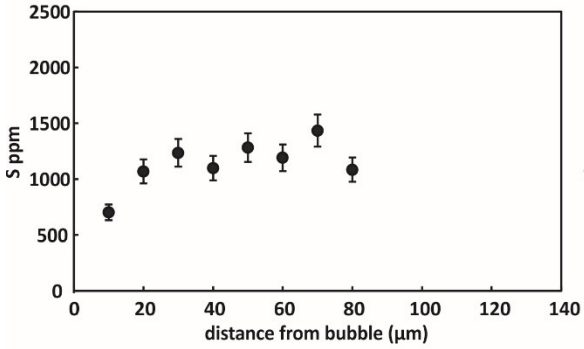

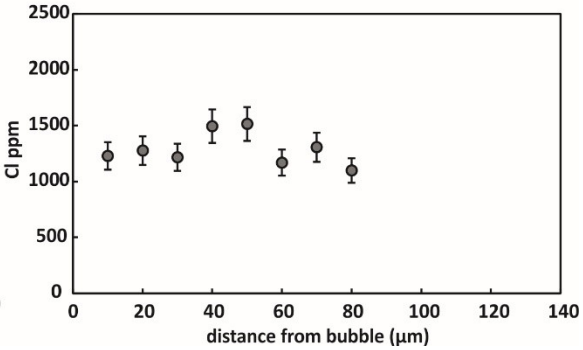

g)

VOR_EMB2

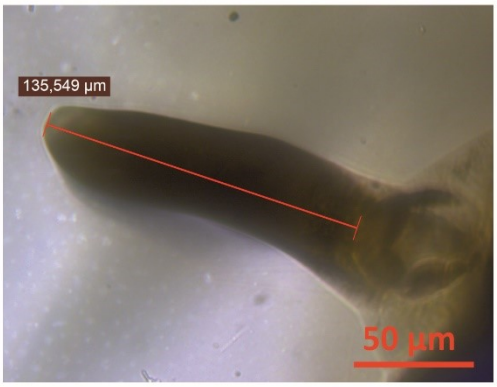

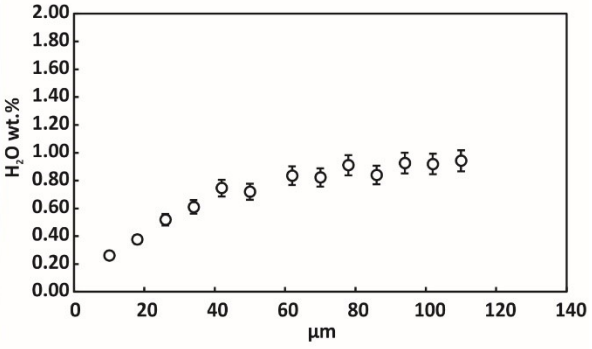

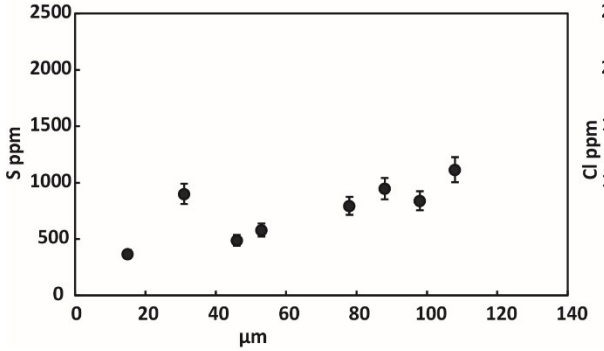

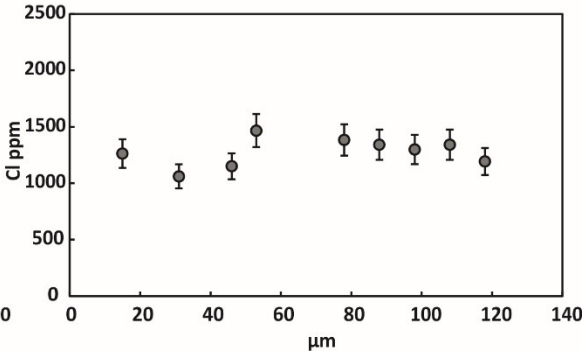

h) VOR_EMB3

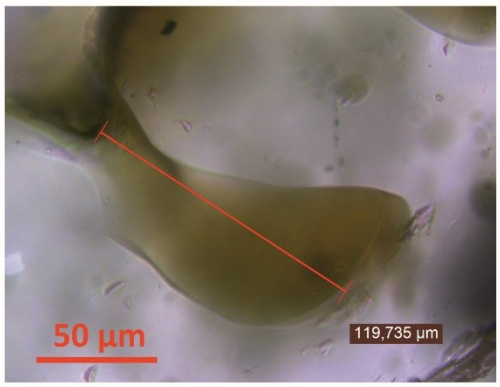

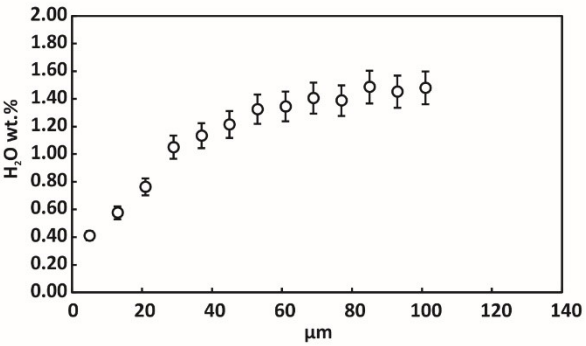

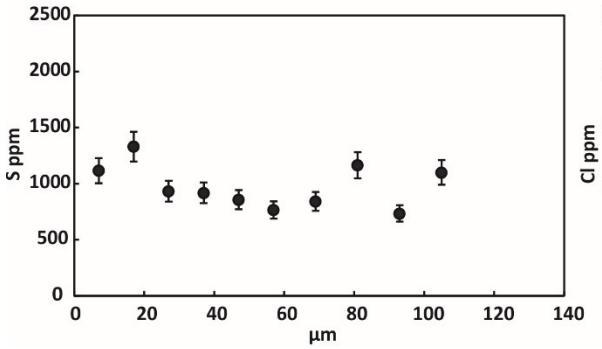

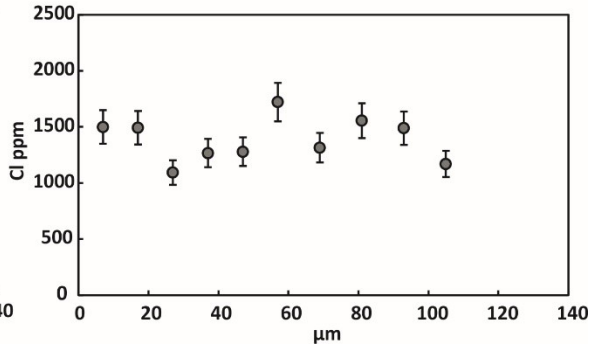

i) VOR_EMB4

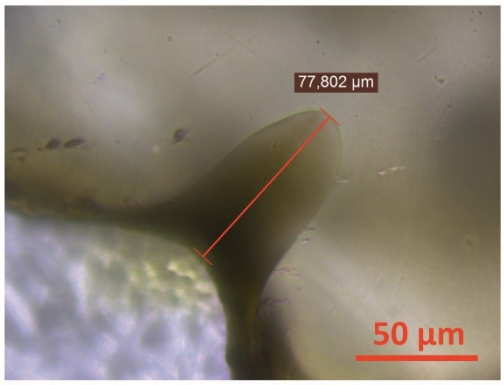

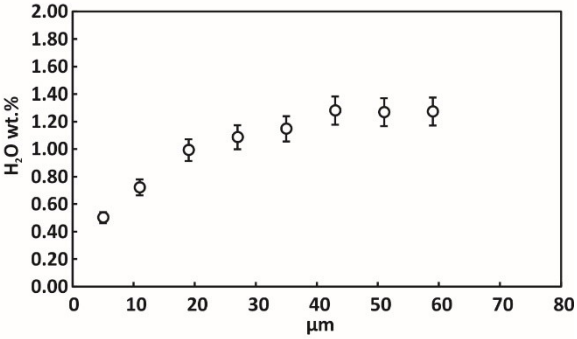

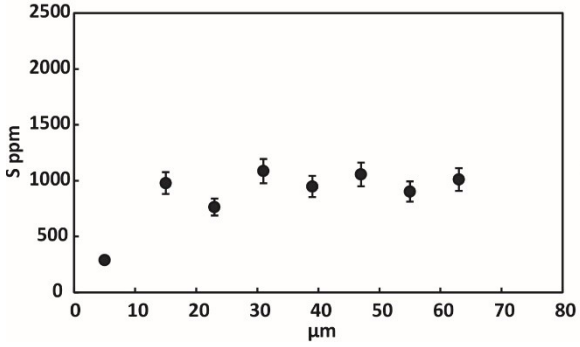

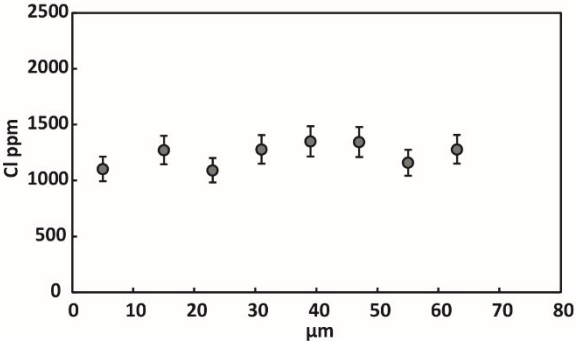

j) VOR_EMB5

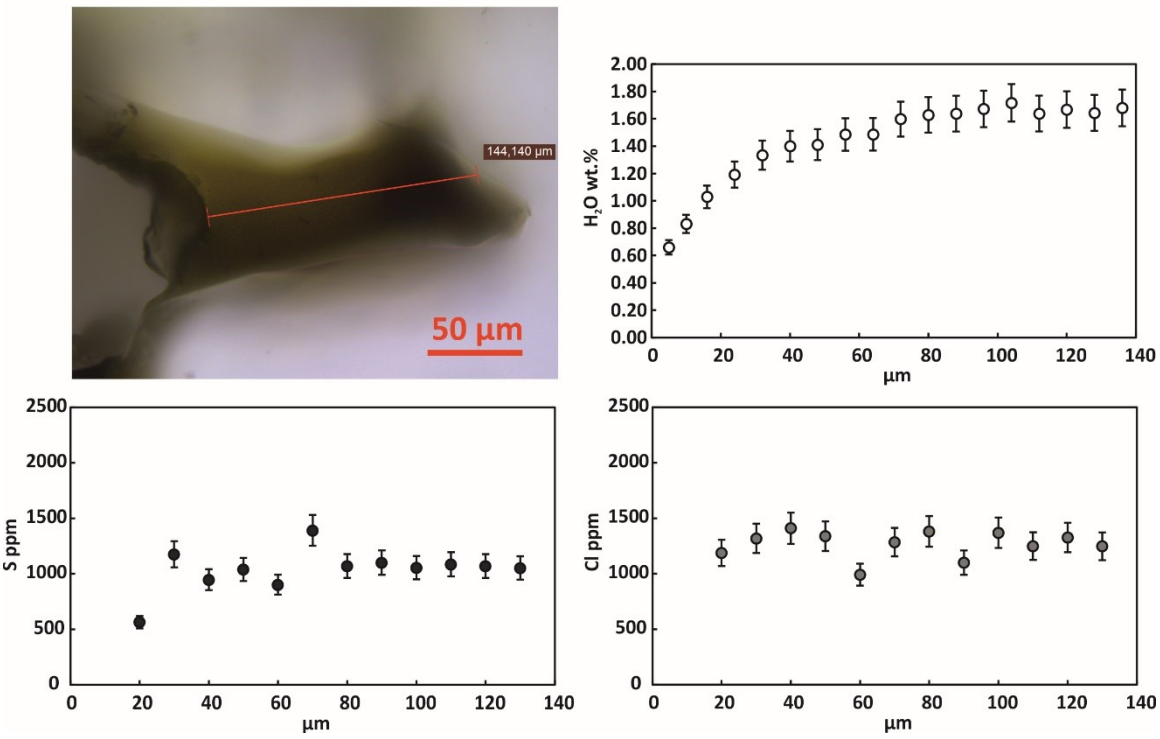

k) VOR_EMB6

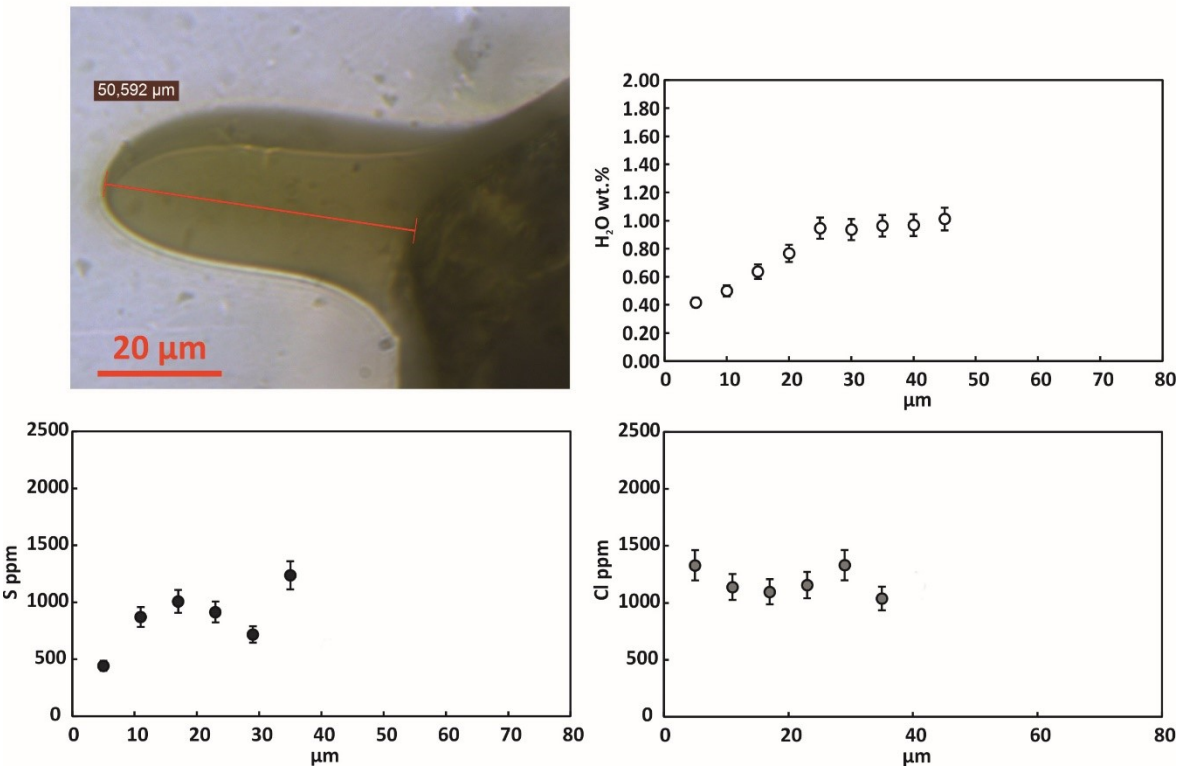

l) **DEC_EMB1**

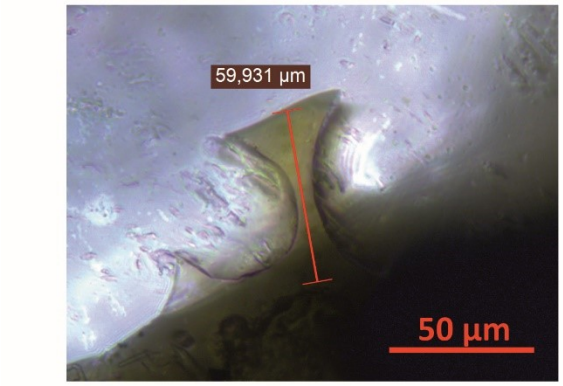

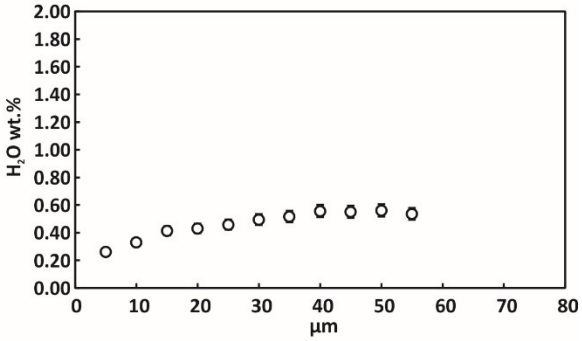

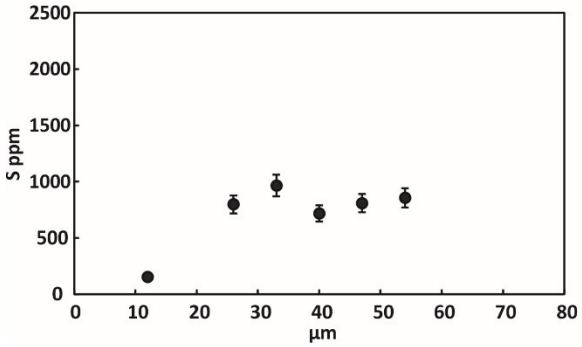

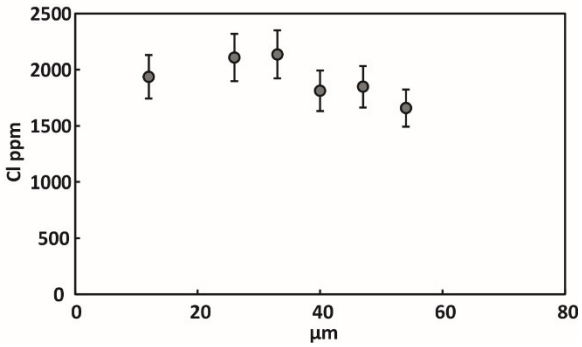

m) **DEC_EMB2**

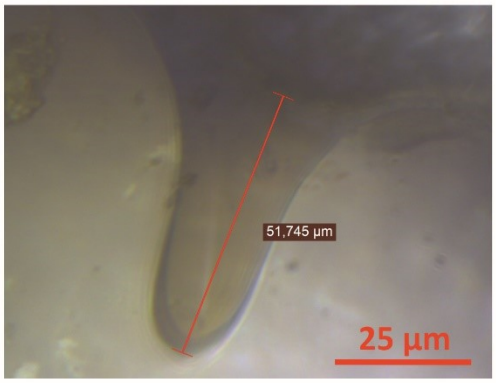

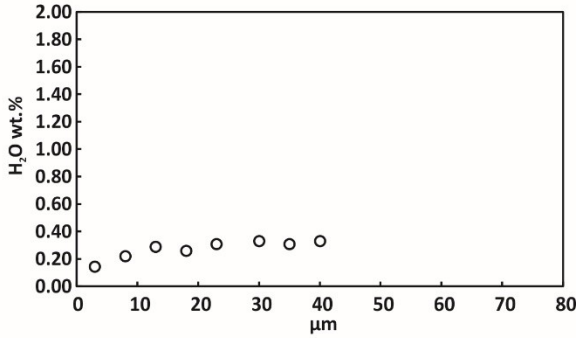

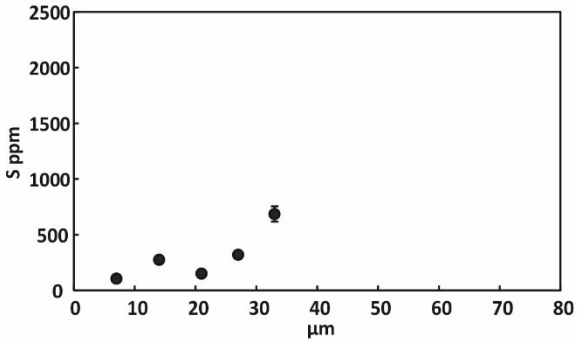

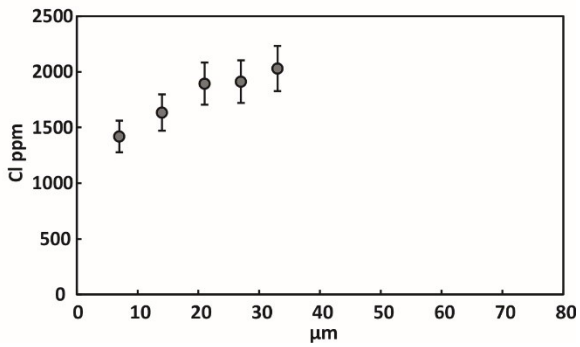

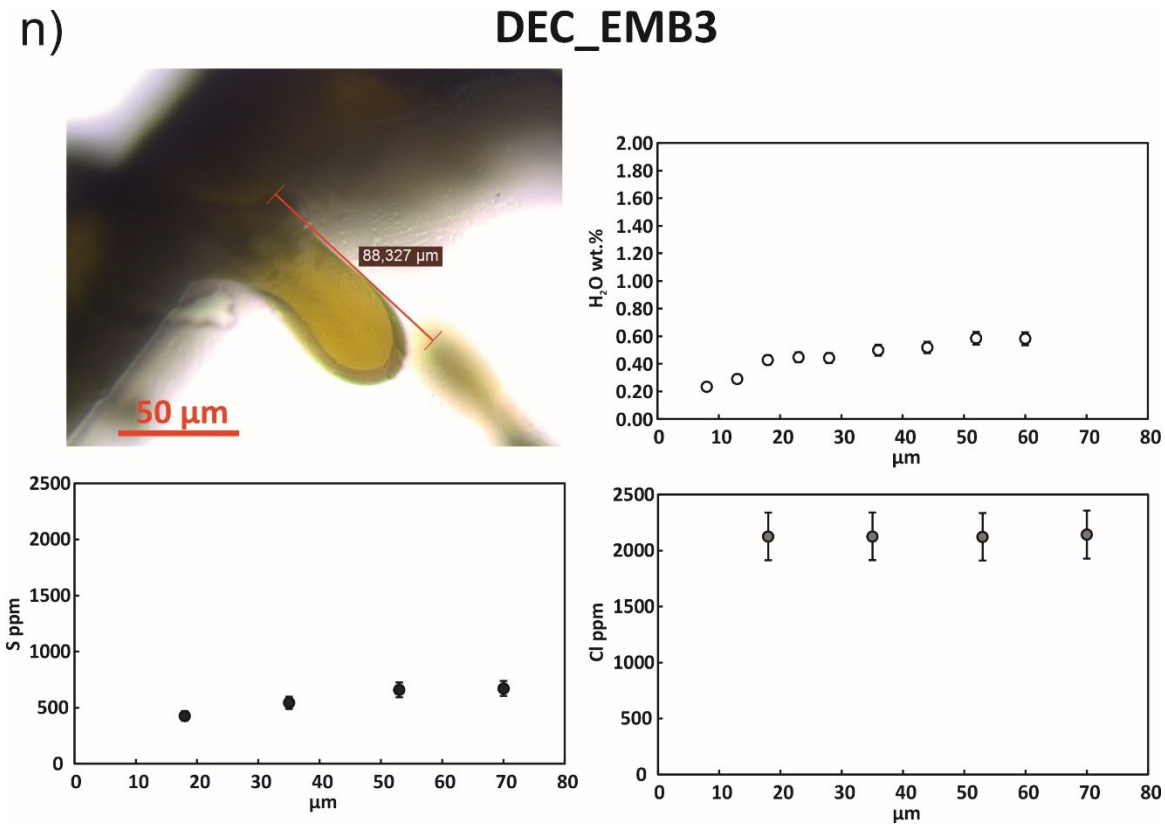

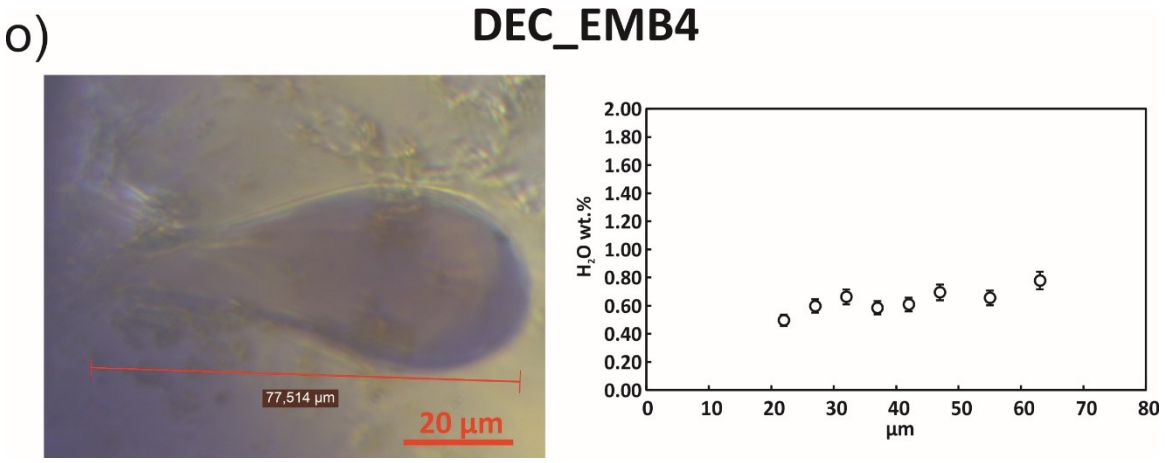

Figure 29: *Diagrams showing H_2O, S, Cl compositional profiles along olivine-hosted melt embayments selected for this study. For the sample DEC_emb4 **(o)** only H_2O profile has been measured, whereas S and Cl compositions were measured on two spot analyses in the interior of embayments by EMPA (**Table A5e**). Embayments images are taken under optical microscope.*

6. CONSTRAINING DEGASSING PATH THROUGH MELT INCLUSIONS DATA

6.1. Chemical evolution of measured MIs and degassing model

6.1.1. Differentiation processes affecting MIs

Major elements of MIs from all the three selected post-2011 eruptions display a compositional range comparable with those analyzed for the 2001-2007 period. The more evolved type 2 MIs are similar to those analyzed for the period 2004-2007 (Collins et al., 2009) and represent the melt resulting from differentiation processes of the magmas entrapped in type 1 MIs, which have compositions close to those analyzed in the 2001 and 2002-2003 products (Métrich et al., 2004; Spilliaert et al., 2006a). In fact, MIs closer to the crystal rim show type 2 compositions, suggesting that entrapment occurred during late stages of crystal growth in a more evolved magma, a feature also supported by the olivine composition measured close to the MIs where Fo is generally lower than 79 mol.%.

Thermodynamic modeling was performed by rhyolite-MELTS (Gualda et al., 2012; Ghiorso and Gualda, 2015) in order to testify this, allowing to track the differentiation path for the post-2011 MIs considering a melt in presence of a fluid phase composed by H_2O and CO_2, on the base of solubility model of Ghiorso and Gualda (2015). The most primitive inclusion among those analyzed for this study (Mg# ~59.5), which is entrapped in Fo_{84-85} olivine, has been selected as starting composition for the modeling. K_2O and H_2O evolution provides the effect of degassing coupled with melt differentiation, using K_2O as differentiation index. In this regard, K_2O was fixed at 1.75 wt.%, which is the lowest content measured in post-2011 MIs, whereas the highest water content measured is 2.40 wt.%. Several simulations have been performed using different conditions of T, P and fO_2 in order to find those values to fit the observed data.

Starting pressure has been selected at P = 400 MPa, simulating magma differentiation during the last 13-15 km bsl, after the early stage of evolution at deeper conditions. Indeed, olivine with core compositions of Fo_{90-92}, which are assumed to be the first mineral phase crystallizing from melts with primary compositions (Kamenetsky et al., 2007; Gennaro et al., 2019), are absent in the selected post-2011 products, where analyzed MIs are entrapped in olivine with Fo content lower than 85 mol% that have crystallized at pressure lower than 500 MPa (Giuffrida and Viccaro 2017; Gennaro et al., 2019). A good best-fit on measured major elements in MIs (exception is made for Al_2O_3 and TiO_2; **Figure 30**) has been obtained using as initial temperature 1160°C and final temperature at 1072°C, in agreement with direct temperature measurements made on lava flow from vents (in the range 980-1080°C; Calvari et al., 1994). However, the whole spectrum of olivine populations found in recent products erupted at Mt. Etna, from Fo_{69} to Fo_{85}, has not been reproduced by thermodynamic models. Olivine composition is strongly controlled by fO_2. Using QFM buffer (D'Orazio et al., 1998; Giacomoni et al., 2014; Giuffrida and Viccaro 2017), which provides a more reliable fitting, a narrower range of olivine compositions is predicted from rhyolite-MELTS simulations, from Fo_{76} to Fo_{81}, while using more oxidized conditions, as NNO buffer (Kamenetsky and Clocchiatti, 1996; Gennaro et al., 2019) only Fo_{81-82} olivine are reproduced at very low pressure (< 31 MPa). Redox changing in real systems (e.g. due to degassing, Moussallam et al., 2016) cannot be included in thermodynamic modeling, so the modeling at constant redox cannot fully predict the evolution.

On the other hand, the anomalous low silica concentration used for the modeling (~42.7 wt.%) may be responsible for such discrepancies between the results of the simulation and the observed data. In fact, measured SiO_2 compositions in the most primitive rocks found at Mt. Etna (e.g. 3930 B.P. eruption Kamenetsky et al., 2007; Mt. Maletto lava, Kamenetsky and Clocchiatti, 1996) range between 45.8-47.6 wt.%. Using these compositions as starting melt,

rhyolite-MELTS provides an evolution path controlled by crystallization of mineral phases which causes only an increase of the SiO_2 in the residual melts. So, fractional crystallization processes on known primitive melts from Mt. Etna are not able to reproduce such low SiO_2 compositions observed in MIs from the post-2011 activity.

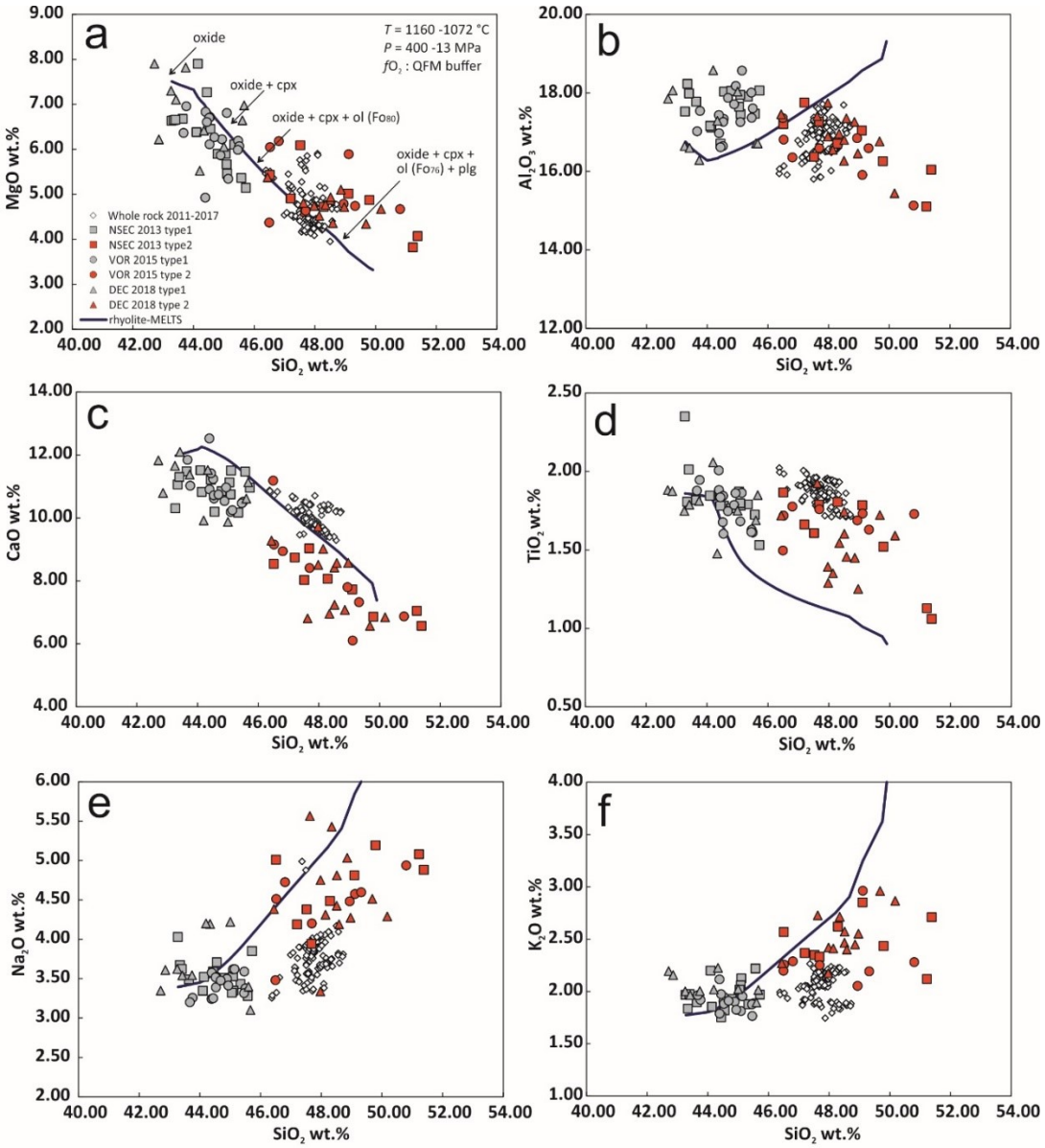

Figure 30: *Rhyolite-MELTS modeling with the best fit (blue line) for major elements of MIs, using the most basic MI composition as starting melt at initial conditions of T =1160 °C, P = 400 MPa and fO_2: QFM buffer. Iron-oxides and clinopyroxene are the first mineral phases which crystallize from the melt; olivine (Fo_{81}) starts to crystallize at 270 MPa, while crystallization of plagioclase occurs at late stage of magma differentiation (<50 MPa).*

Previous MI datasets showed similar silica depletion features (42-43 wt.% SiO_2), like in Mt. Maletto lava (15 ka; Kamenetsky and Clocchiatti, 1996), Mt. Spagnolo lava (Gennaro et al., 2019) and 1997-99 products (Moretti et al., 2018). Gennaro et al. (2019) advanced an explanation for such strong SiO_2 depletion recorded in some MIs. They invoke a possible assimilation of evaporitic rocks belonging to the Late Messinian Gessoso-Solfifera Formation (Lentini, 1982) as the cause of the SiO_2 depletion. This formation is rather widespread in Sicily and so it is possible that a layer of this rocks may be present under the volcano edifice. The authors observed that MIs from Mt. Spagnolo lava contain very huge amount of dissolved S (~ 4238 ppm), higher than those measured for 3930 B.C. products (<3351 ppm), Despite the low pressure of MIs entrapment (< 150 MPa). Such high S contents may be also derived from assimilation of evaporitic rocks, which in turn causes an increase of the oxidation state coupled with decreasing SiO_2. However, trace elements in post-2011 MIs do not provide any clues about a possible role of evaporitic assimilation, and this process may occur at shallow levels of the plumbing system at the boundary between the volcanic edifice and the sedimentary basement ca. 2-3 km below the summit craters. So, only MIs entrapped in low Fo olivine could provide evidence of S enrichment due to assimilation, whereas for the post-2011 products low SiO_2 are measured in MIs trapped in olivine with intermediate to high Fo contents (Fo_{80} to Fo_{85}), crystallizing at deeper pressures (300-600 MPa), as inferred by previous thermodynamic modeling (Giuffrida and Viccaro, 2017). Furthermore, MIs from post-2011 activity show a maximum S concentration (~3072 ppm) lower than measured values in MIs selected from Mt. Spagnolo lava and occasionally are observed small sulfide globules in some inclusions, which are indication that melts were possibly sulfide-saturated at more reduced conditions, contrary to the supposed relative higher state of oxidation for Mt. Spagnolo lavas (Gennaro et al., 2019).

The heterogeneity of mantle source may play a role in generating such low silica contents in primary magma. As stated by some authors, the mantle source beneath Mt. Etna is likely composed by a metasomatized lherzolite bearing hydrous phases plus a garnet pyroxenite, which may be in the form of veins intruded into the spinel lherzolite (Correale et al., 2014; Viccaro and Zuccarello, 2017). Primary melts obtained by partial melting modeling for the Ellittico ages, historic and recent products, have SiO_2 contents between 45.0 and 47.0 wt.% (Viccaro and Zuccarello, 2017), comparable with compositions of the most primitive rocks and MIs found in the 3930 B.C. rocks (Kamenetsky et al., 2007, Gennaro et al., 2019) and Mt. Maletto (Kamenetsky and Clocchiatti, 1996). Any possible mixing processes of primary magma with the more evolved ones at progressively shallower levels of the plumbing system may induce only an increase of SiO_2 compositions.

6.1.2. Constraining trapping pressure and degassing path

The new data on olivine-hosted MIs relative to the post-2011 activity at Mt. Etna reveal a rather low budget for the main volatile components (H_2O and CO_2). Predicted trapping pressure for each pair H_2O-CO_2 data measured in MIs have been calculated through the VOLATILECALC program (Newman and Lowenstern, 2002), fixing an average value of SiO_2 ~46.5 wt.%, which is used as compositional parametrization in order to consider the dependence of CO_2 solubility from the melt (Dixon et al., 1997). The maximum trapping pressure is estimated at 136 MPa for a MI relative to the VOR 2015 eruption, containing H_2O and CO_2 at 2.09 wt.% and 849 ppm, respectively. Differently, all MIs from the NSEC 2013 eruption provide trapping pressure lower than 100 MPa and the lowest pressure has been estimated at 25 MPa for some MIs from NSEC 2013 and DEC 2018 products. Almost all the MIs samples analyzed for the post-2011 activity follow a degassing path between 136 MPa and the surface (**Figure 31**), which was previously defined by Spilliaert et al., (2006a) for MIs of the 2002-03

eruption. Such degassing path has been defined as a closed-system with a presence of exsolved volatile phase between 2 and 8 wt.% and initial H_2O and CO_2 respectively of ~2.20-2.90 wt.% and 1050-1140 ppm, starting from 170-200 MPa. A ponding zone was inferred at these pressures, where magma undergoes a substantial flushing of CO_2-rich gas phase (e.g. Métrich et al., 2004; Spilliaert et a., 2006a). This suggests that eruptions of the post-2011 activity may be fed by magmas which have experienced significant flushing during the storage at 200 MPa prior to the MIs entrapment. Following the density model made by Corsaro and Pompilio (2004), where a relation between the depth and lithostatic pressure have been defined on the basis of the lithostratigraphy of the basement underlying the volcano, the corresponding depth is estimated at ~5-6 km b.s.l., in agreement with ground deformation data which constrained sources at similar range of depths for the recent post-2011 activity (Cannata et al., 2015, 2018; Viccaro et al., 2016, 2019).

Some DEC 2018 MIs and one inclusion from the VOR 2015 products fall outside of the degassing path, displaying a relative slightly CO_2 enrichment at low water contents (<1.00 wt.%). This observation evidences that flushing process may act also at shallow levels of the plumbing system (25-70 MPa), as advanced by Collins et al., (2009) for magmas erupted during the 2004-2007. So, MIs of the DEC 2018 samples may represent a residual magma of the 2015-2017 activity which has been re-equilibrated with a CO_2-rich gas phase at shallower depth. However, CO_2 flushing may be not exclusively responsible for depletion in H_2O observed in MIs. In fact, some depleted H_2O contents have been found in type 1 MIs entrapped in intermediate to high Fo olivine (Fo_{80-85}), which crystallize at greater depth than those predicted from degassing model (e.g. Giuffida and Viccaro, 2017; Gennaro et al., 2019). Other processes may be responsible for such depletion in H_2O concentrations in type 1 MIs. In particular, the role of water loss will be discussed on the next paragraph.

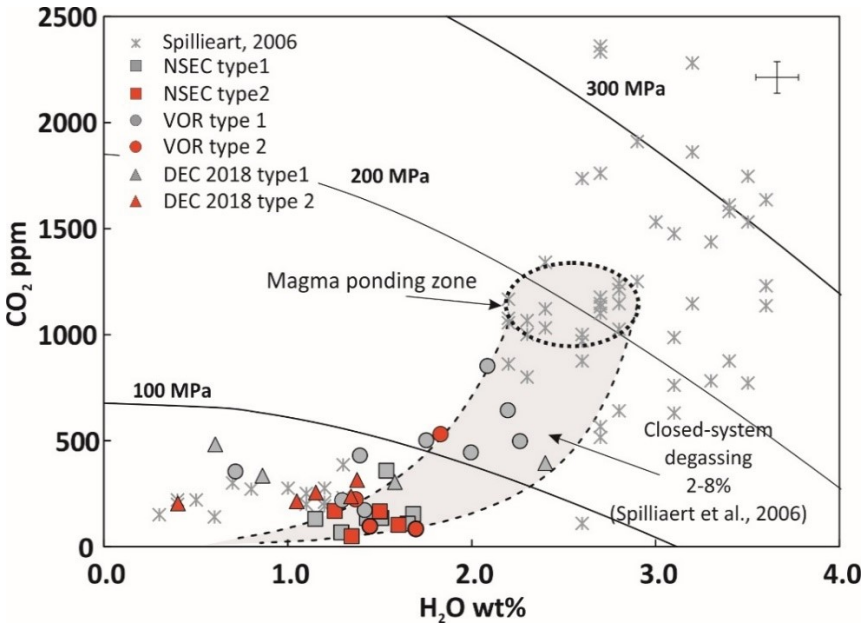

Figure 31: *H_2O and CO_2 compositions measured in MIs. Isobars were calculated at different temperature, taking into account the effect of melt differentiation: T=1150°C at 300 MPa, T=1140°C at 200 MPa, T=1130°C at 100 MPa. MIs from post 2011- activity follow a similar path modeled by Spilliaert et al. (2006a) on MIs from 2002-03 (closed-system degassing model with 2-8% of initial gas from a pressure of ~200 MPa). Few type 1 MIs suggest possible occurrence of CO_2 flushing at shallow level (~50 MPa). The error bars indicate the largest uncertainties related to the highest H_2O and CO_2 measured compositions.*

S compositions are comparable with those measured for recent eruptions (e.g. the 2002-03 eruption, Spilliaert et al., 2006b; **Figure 30**). H_2O-S data suggest trapping pressure for post-2011 MIs lower than ~140 MPa, which corresponds to the pressure of initial sulfur exsolution defined by Spilliaert et al., (2006b). S degassing in basaltic systems are not only depending by decompression, but also strongly controlled by the redox state of the systems. In fact, sulfide saturation is reached at more reduced conditions, and precipitation of sulfide is responsible of an early S depletion in melts. Differently, higher S content dissolved in melts are favored by more oxidized state. A weak depletion of sulfur characterizes type 2 MIs of DEC 2018 samples, following a trend between the degassing of S in sulfide-undersaturated melt and that in presence of sulfide-saturated melt (**Figure 32**; Spilliaert et al., 2006b). This is testified by the occasional occurrence of small globule of sulfide in some MIs. CO_2 flushing may control changing in the

state of redox, explaining either moderately high (~3072 ppm) or low S contents in post-2011 samples.

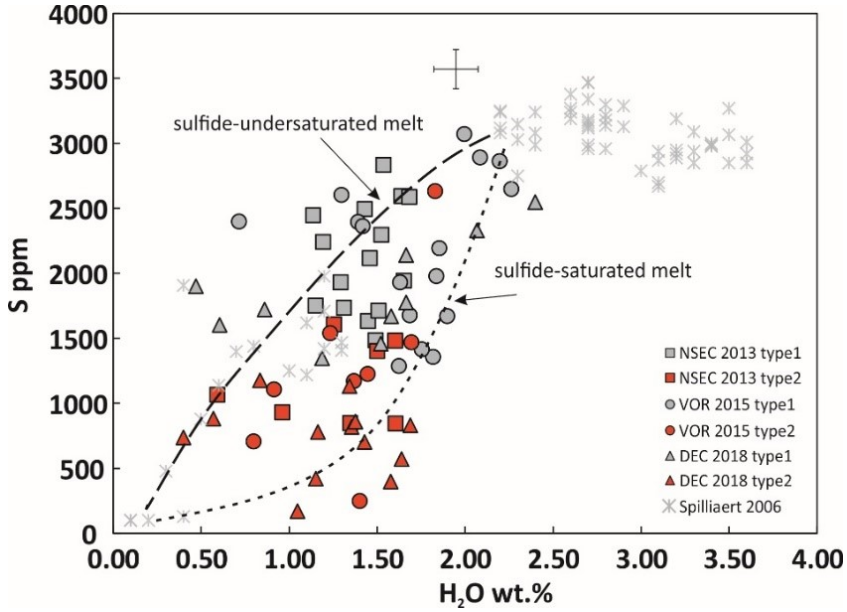

Figure 32: *H_2O and S compositions measured in MIs from post-2011 activity. The thick dashed line represents the H_2O-S degassing path in a sulfide-undersaturated melt erupted in lateral eruptions, whereas the thin dashed line is the evolution of sulfide-saturated melt (modified from Spilliaert et al., 2006b). Data of 2002-03 eruption data are reported for comparison (Spilliaert et al., 2006b).*

6.2. Evidence of volatile loss in MIs from post 2011-activity

6.2.1. Assessing CO_2 lost in shrinkage bubbles

Recent studies have demonstrated the importance of taking into account the contribution of shrinkage bubbles in the estimation of bulk CO_2 in MIs (e.g. Hartley et al., 2014; Wallace et al., 2015; Moore et al., 2015,2018; Tucker et al., 2019; Hanyu et al., 2020). Shrinkage bubbles formation is dependent by a combination of several factors, including PEC, thermal contraction of melt and host olivine, and water loss from MIs (Maclennan, 2017; Moore et al., 2015). In

this regard, a large fraction, up to 90%, of the total CO_2 dissolved in the melt may be lost to the bubble because of its very low solubility in alkaline melts (Wallace et al., 2015; Tucker et al., 2019). Therefore, dissolved concentrations measured in the melt will provide underestimated values of pressure through any solubility model, and such low concentrations may reflect achievement of the melt-bubble equilibrium at MI quenching rather than the trapping pressure. An attempt to pristine bulk CO_2 considering the contribution from the shrinkage bubbles allow therefore to calculate more reliable trapping pressures, although for H_2O-rich like those erupted at Mt. Etna this effect is expected to have a minor influence than in H_2O-poor systems (Wallace et al., 2015).

The concentration of CO_2 in a bubble can be calculated as: $\phi \times \rho_v / \rho_{melt}$, where ϕ is volume fraction of the bubble in the melt inclusion, ρ_v is the density of fluid CO_2 phase in the bubble and ρ_{melt} is the melt density (Tucker et al., 2019). The density of fluid CO_2 phase is function of the distance between the two peaks referred as "Fermi Diad", which can be detected in Raman spectra in the domain between 1200 and 1400 cm^{-1} (Kawakami et al., 2003). Alternatively, approaches based on equation of states allow to infer the amount of CO_2 that would have been lost in the bubble at given pressure and temperature (Wallace et al., 2015; Moore et al., 2018; Tucker et al., 2019). Both approaches require to know the volume of MI, where generally ellipsoidal shape with axis c = b is assumed. The difficult in determining accurately the third axis, together with the irregular shape observed in some MIs constitute the main source of uncertainty in the calculation of amount of CO_2 restored in the bubble (Tucker et al., 2019; Hanyu et al., 2020).

For this study an equation of state-based approach has been employed for restoration of the original CO_2 concentrations, although this approach may lead to great uncertainties, up to 50% (Moore et al., 2015; Tucker et al., 2019). This approach has been chosen because: i) many bubbles were accidentally not preserved during exposition of MIs for spectroscopy analysis; ii)

bubble reconstruction by Raman microtomography require rather long time of analyses and data treatment (Venugopal et al 2020). Therefore, original bulk CO_2 compositions can be restored knowing the H_2O and CO_2 contents dissolved in the MI glass using: 1) VOLATILECALC (Newman and Lowenstern, 2002) to determine the saturation pressure and CO_2 mol% in the vapor phase in equilibrium with the entrapped liquid, and 2) a modified Redlich-Kwong equation of state (Kerrick and Jacobs, 1981) to calculate the molar volume of the H_2O-CO_2 mixture in the vapor phase. The effect of thermal expansion of the bubble due to melt contraction during cooling is considered by calculating the bubble volume (vol% of the inclusion, Wallace et al., 2015) before the eruption, which depends mainly on the difference between the trapping temperature (up to 1220 °C in a MI trapped in high Fo olivine, estimated by Petrolog3 software during PEC correction) and the pre-eruptive temperature (~1080 °C; Calvari et al., 1994) for each MI. Results suggest that a percentage between 28 and 70% of the total CO_2 is stored in the bubbles, with the highest total CO_2 concentration of 2134 ppm estimated for a MI from the VOR 2015 products.

Using CO_2 restored compositions, the deepest pressure estimated by VOLATILECALC is ~250 MPa for a MI from VOR 2015 products and a closed-system degassing with initial gas phase from 0 to 5% has been modeled by starting from this pressure (**Figure 33**). However, variable H_2O-CO_2 compositions still highlight the possible occurrence of CO_2 flushing in the upper part of the plumbing system (<130 MPa), as well as the role of water loss must be taken into account for the H_2O depletion in type 1 MIs. Furthermore, rhyolite-MELTS modeling performed using restored CO_2 compositions (constraining the initial pressure at 250 MPa from the degassing model) do not show, on the whole, any substantial change from solutions obtained using measured MIs data. In fact, the calculation provides only a slightly higher Fo olivine composition at QFM buffer (~Fo_{82}), but low Fo olivines (< 76 mol %) still are not reproduced.

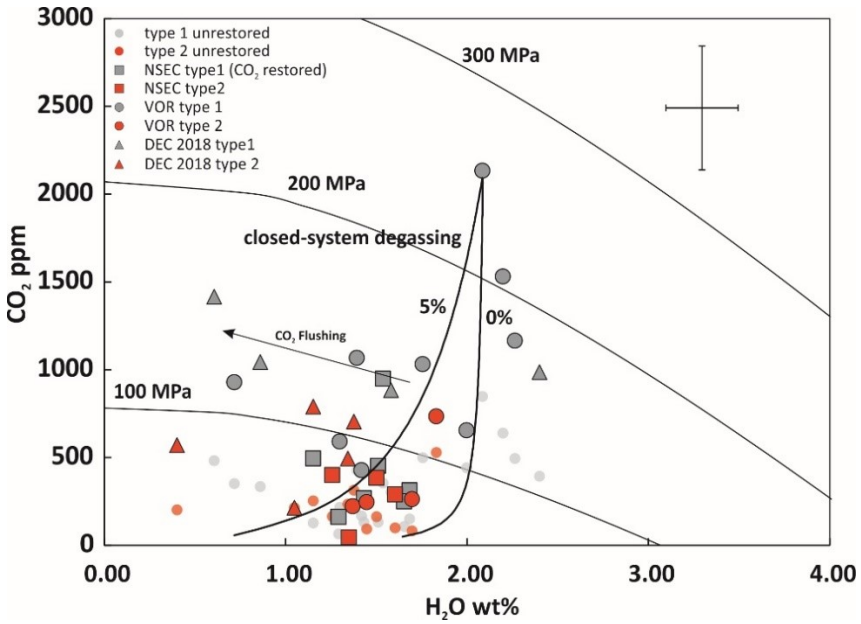

Figure 33: *Diagrams showing restored bulk CO_2 compositions compared to measured compositions. Closed-systems degassing models with initial gas phase from 0 to 5% are defined starting from a pressure of 250 MPa with H_2O= 2.09 wt.% and restored CO_2 = 2134 ppm. The greater error bar on CO_2 takes into account the error propagation in the calculation of restored bulk CO_2 compositions.*

6.1.1. Diffusive water loss

As stated above, anomalous low H_2O contents (~0.47–1.20 wt.%) have been measured in some type 1 MIs entrapped in intermediate to high Fo olivine (Fo_{80-85}), indicating low trapping pressure for the analyzed MIs during crystallization of such olivine populations (<130 MPa), also considering CO_2 correction. These results are partly in contrast with thermodynamic models which indicate deeper crystallization conditions (300-600 MPa; cf. Giuffrida and Viccaro, 2017). A large variability in water contents (ΔH_2O ~2 wt.%) characterizes MIs entrapped in olivine with similar Fo content, indicating that olivines crystallized in melts with similar compositions but variable amounts of water (**Figure 34a**). Analogous considerations can be advanced observing H_2O-MgO or H_2O-K_2O variations (**Figure 34b**), whereas some MIs of both types are characterized by coupled decreasing of H_2O and SiO_2 (**Figure 34c**).

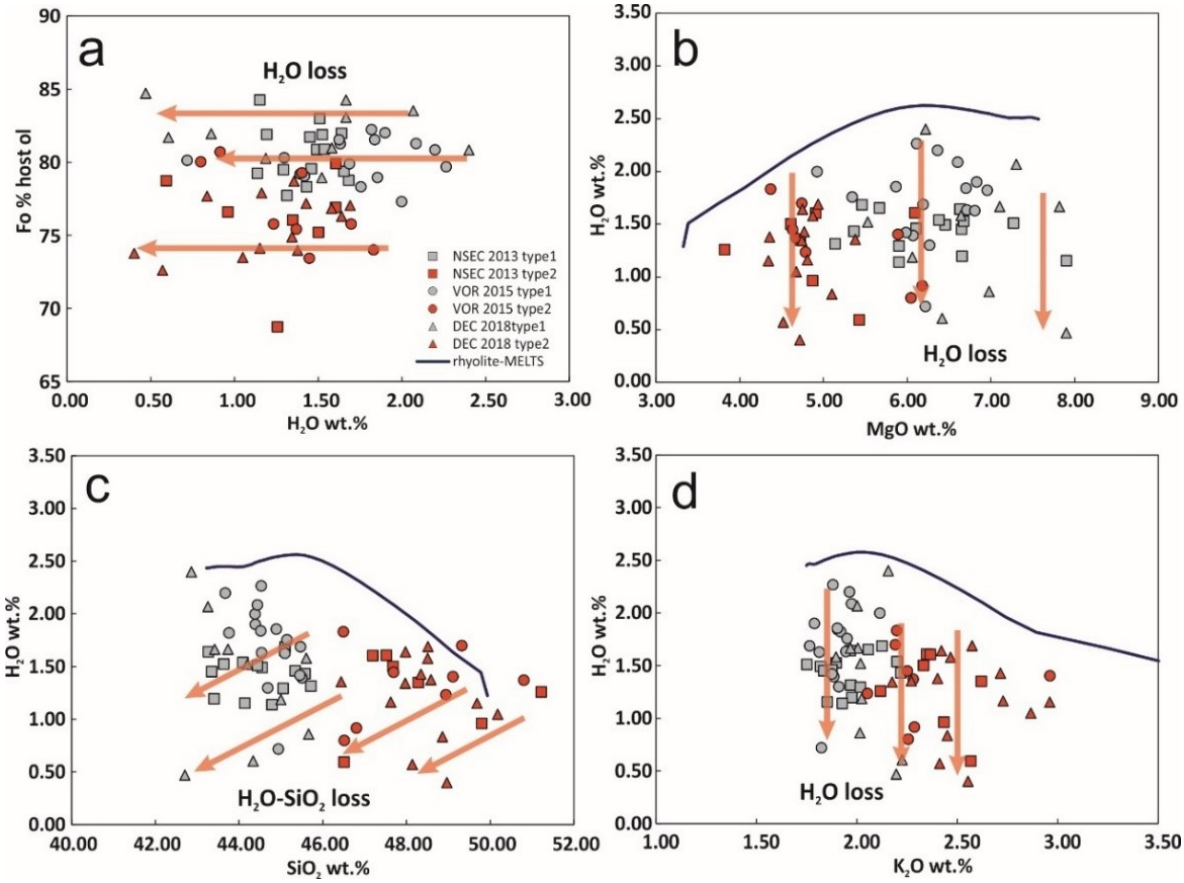

Figure 34: *Diagrams showing evidence of H_2O loss for MIs from the post 2011 activity at Mt. Etna, highlighted by red arrows; in* **c)** *H_2O loss is coupled with SiO_2 decreasing in some MIs.*

Furthermore, predicted H_2O concentrations from thermodynamic modeling are much higher than those observed in MIs. The sole volatile flushing of CO_2-rich gas phase cannot explain such variability. If flushing is the only responsible for water depletion in type 1 MIs, enrichment in CO_2 should be also noted in the CO_2-S diagrams for same type 1 MIs at very low S content. In this regard, only few type 1 MIs show weak enrichment in CO_2 at moderately high S content (**Figure 35**).

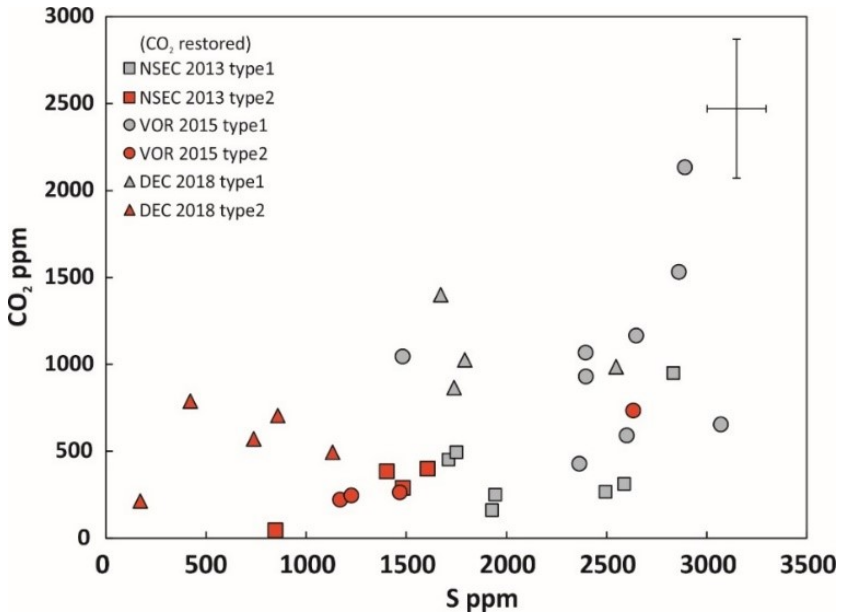

Figure 35: *S compositions plotted against restored CO_2. Weak CO2 enrichment is observed in few type 1 MIs, which are, on the whole, concordant with the main degassing path.*

Thus, H_2O-depleted compositions in MIs of the post-2011 activity can be attributed to diffusive water loss, a process commonly observed during experimental studies on MIs (e.g. Portnyagin et al., 2008; 2019; Gaetani et al., 2012; Lloyd et al., 2013). Post-emplacement slow cooling can be excluded because of the small size of tephra (<1.5 cm) from which were selected olivine, assuming almost instant cooling during the ejection in the air (Llyod et al., 2013). However, MIs can experience water loss during the ascent as a response of the syn-eruptive degassing and the diffusion can be used for constraining ascent rates (Llyod et al., 2013). On the other hand, post-entrapment water loss in MIs during pre-eruptive magma dynamics within the plumbing system cannot be ruled out.

Several studies were focused on the investigation of the spatial and temporal configuration of the recent plumbing system of Mt. Etna (e.g. Kahl et al., 2015; Viccaro and Giuffrida 2017; Cannata et al., 2018). These studies provided a very complex configuration of the plumbing system, characterized by distinct magmatic environments with specific *P-T-f*O_2 conditions and melt compositions where magma storage and crystallization occur (Giuffrida

and Viccaro et al., 2017). Connections between magmatic environments can be deducted from the Mg-Fe zonation of olivine crystals, whereas diffusion modeling can provide temporal information of storage, transfer and/or recharge processes (Costa et al., 2008; Giuffrida and Viccaro, 2017; Cannata et al., 2018). During the transfer from the deeper area of the plumbing system magma starts to exsolve a gas phase, as a function of the solubility of each volatile element. For Etna magmas, water saturation is generally reached starting from 400 MPa (Armienti et al., 2013; Mollo et al., 2015), depending from the initial volatile contents inherited from the source and melt compositions. Depletion of water dissolved in the external melt due to the degassing process coupled to the flushing may lead to a new re-equilibrium of MIs, reflecting into the decrease of original water contents by diffusion of H^+ through the olivine lattice. The timing of pre-eruptive dynamics may play a crucial role. Indeed, if magma reaches shallower depth quickly, it may retain most of its volatile budget, whereas long time of storage at intermediate to shallow levels of the plumbing system enables the progressive depletion of volatiles from the melts. Water loss in post-2011 samples seems to affect both type MIs with major effects on some type 1 MIs. Thus, an attempt to reconstruct the original water contents is necessary in order to better constrain the degassing path model coupled with the differentiation and fix more reliable initial conditions for the volatile diffusion model in embayments (see next chapter).

Many experimental studies demonstrated that hydroxyl group can be incorporated in olivine crystals as point defects. Quantification of H^+ diffusivity have been attained through cycles of hydration and dehydration, resulting in water gain and loss, respectively, in MIs hosted in olivine. Essentially, two main mechanisms of protons (H^+) transport have been described. The first involves proton-polarons exchange, where redox reactions occur between H^+ and polaron on ferric iron atoms occupying the octahedral sites at temperature lower than

<1000 °C (Mackwell and Kohlstedt 1990; Kohlstedt and Mackwell 1998; Gaetani et al., 2012). The diffusion is strongly anisotropic, with fastest diffusion process parallel to [100] axes:

$$D_{[100]} > D_{[001]} >> D_{[010]}$$

Diffusivity of hydrogen through proton-polaron mechanism is independent from the hydrogen concentration in the olivine, but limited by the amount of polaron in olivine, which depends on the iron concentrations. Indeed, experiments demonstrated that proton-polaron diffusion is slower in iron-free olivine (Demouchy and Mackwell 2003).

The second mechanism considers the incorporation of proton in metal vacancy defects in olivine (Kohlstedt and Mackwell 1998; Demouchy and Mackwell 2003,2006). This type of diffusion is favored at higher temperature and shows a different anisotropy from the proton-polaron:

$$D_{[001]} > D_{[010]} > D_{[100]}$$

The diffusivity related to the proton-metal vacancies is independent by iron contents but slower than proton-polaron mechanism, consistent with some experimental studies where concentration in MIs olivine changed of several weight % in 2 days (Portnyagin et al., 2008). The incorporation of hydrogen may concern silicon-vacancies defects, characterized by lower diffusivity (Padron-Navarta et al., 2014). The dominant mechanism depends by different parameters, such as silica activity, amount of Fe and some trace elements, temperature and oxygen fugacity (e.g. Portnyagin et al., 2019 and reference in).

A recent experimental study revealed that the mechanism of incorporation of proton H^+ in metal vacancies is independent from the pre-existing defects in olivine structure (Portnyagin et al., 2019). In the experiments, SiO_2-undersatured MIs entrapped in high-Fo olivines from Klyuchevskoy Volcano were subjected to cycles of hydration and rehydration considering as external matrix a basaltic glass or SiO_2-MgO free fluid. In the case of basaltic glass matrix, the results highlighted a concordant behavior of H_2O and SiO_2 contents in MIs, showing a coupled

enrichment of both elements during the olivine hydration in glass matrix. Instead, the reversal experiment showed that the process is reversible. The possible reactions occurring on the interface between the crystal and the MIs leading to incorporation of water in the olivine structure during the rehydration are:

$$2H_2O + SiO_2 \rightarrow H_4SiO_4 \quad (3)$$

$$H_2O + SiO_2 + MgO \rightarrow MgH_2SiO_4 \quad (4)$$

$$H_2O + Fe_2O_3 + 2SiO_2 \rightarrow 2FeHSiO_4 \quad (5)$$

These reactions are supposed to create (or destruct) metal-vacancies during crystallization (or dissolution) of olivine at interface with the melts, Despite pre-existing defects in the olivine lattice, in order to explain the high amount of water exchange in the MIs. Indeed, during experiments in MgO and SiO_2-free fluid matrix such reactions do not occur, and results show marked minor degree of water enrichment during rehydration, likely due to limited incorporation of H_2O in the olivine lattice. Such findings were able to explain why MIs in island-arc volcanic rocks, which normally are characterized by SiO_2-saturated compositions, show SiO_2-undersatured features (Portnyagin et al., 2019, and reference in).

Results of these experiments provide a possible explanation of the both low H_2O and SiO_2 contents measured in some of MIs of the post-2011 activity at Mt. Etna. Unfortunately, the experiments have been carried out only for olivine crystallized in Ti depleted and relatively oxidized calc-alkaline melts, suggesting that effects of dehydration in MIs of different compositions (e.g., alkaline magma) require further investigations. Until now, no experimental studies have been conducted on olivine crystallized from alkaline melts, which means that data useful for disambiguation of the possible mechanism of H^+ incorporation and transport for Etnean olivines are not available.

However, some clues from post-2011 MIs data may suggest that H^+ transport by metal-vacancies could effectively work for Etna compositions. Natural olivines crystallized in Etna magmas are generally water depleted, so FTIR spectra collected on pure olivine do not show peaks in the domain between 3000 and 3700 cm^{-1} related to the various point defects occupied by hydroxyl in olivine lattice. for the spectrum of an olivine from VOR 2015 eruption, which displays the presences of a broad band centered near 3160-3170 cm^{-1} and a peak at 3220-3240 cm^{-1} (**Figure 36**). These characteristic bands are attributed to H^+ position in point defects associated to metal vacancies, (M1 for 3160 cm^{-1} and M2 for 3220 cm^{-1}; Lemaire et al., 2004; Berry et al., 2005; Portnyagin et al., 2019), whereas the other bands related to Si vacancies, Ti point defects and Fe^{3+} point defects are missing.

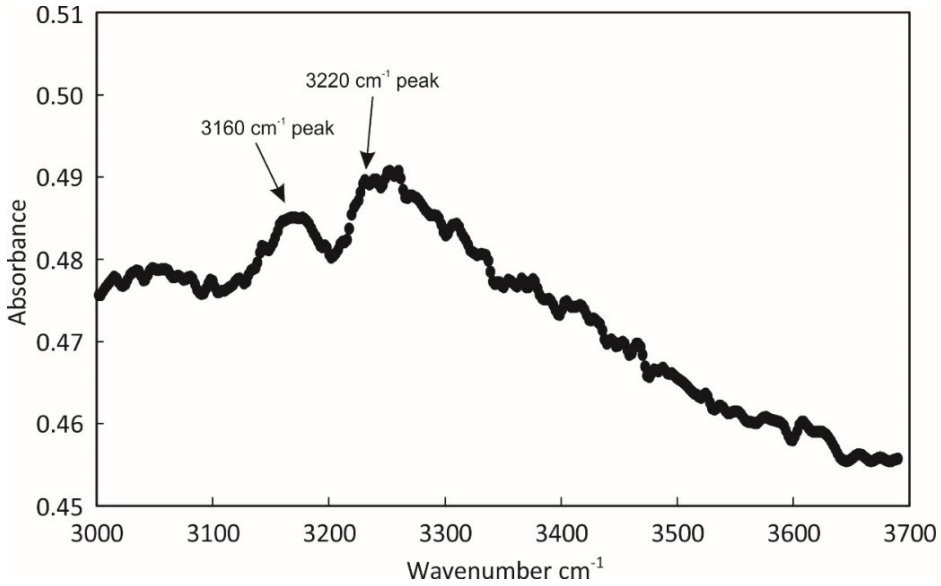

Figure 36: *FTIR spectrum between 3000 and 3700 cm^{-1} on pure olivine crystal from VOR 2015 eruption, where the peaks at around 3160 and 3220 cm^{-1} corresponds to H^+ position in point defects associated to metal vacancies.*

Two factors may have allowed the detection of water in this olivine crystal: FTIR measurement was performed very close to the MI and probably along the orientation of maximum absorbance of water in olivine. These results support the hypothesis that diffusion of

H^+ in olivine crystallized in Etna melts occurs by metal-vacancy defects. In the H_2O-SiO_2 diagrams concordant variations in some Mis are observed, where water decreases in accordance with silica, a feature particular evident for DEC 2018 MIs (**Figure 34c**). Thus, the correlation between the low H_2O and SiO_2 coupled with the characteristic bands of H^+ in metal-vacancies suggests that the process described in Portnyagin et al. (2019) may really occur in Etna MIs, although experimental data are necessary in order to prove it. On the basis of this assumption, restoration of both H_2O and SiO_2 contents before the diffusive water loss has been performed for MIs of the post-2011 activity at Mt. Etna.

The approach for the restoration of original H_2O and SiO_2 in MIs consists in the calculation of the normative mineral components (Jd, Lc, CaTi-Ts, CaTs, Di, Ol, Qz) from each MI composition, following the scheme of Falloon and Green (1987); the same is done for bulk rock compositions used as pristine SiO_2 composition. If the Si-saturation index of the MI is lower than the bulk rock index, percentage of SiO_2 will be added until the Si-saturation index of MI matches that of the bulk rock, otherwise no recalculation is performed. Then, the MI composition will be normalized and corrected for PEC calculation, which represents the following step after the H_2O-SiO_2 recalculation. Two bulk rock compositions with SiO_2 = 46.4 wt.% and 48.5 wt.%, representing respectively the most basic and the more evolved K-trachybasalts within the 2011-2013 series (Viccaro et al., 2014), are used for restoration of type 1 and 2 MIs found in the 2013 products. Two bulk rock compositions with SiO_2 = 47.5 wt.% and 48.7 wt.% from the 2015-2017 products (Viccaro et al., 2019) for type 1 and 2 MIs from 2015 and 2018 products.

Results of the recalculation display a lower average percentage of SiO_2 added (~2.1-2.9 %) to the melt in type 2 MIs than in type 1 MIs (~3.5-7.0 %), reflecting a lower degree of re-equilibration for the more evolved MIs. In some cases, type 2 MIs were characterized by higher Si-saturation index than the bulk rock, so they were not corrected. Moreover, NSEC 2013 and

VOR 2015 MIs show lower average percentage than DEC 2018. This suggests that MIs DEC 2018 suffered more extensively water loss, in agreement with previous observations on H_2O-SiO_2 data. Finally, MIs recalculated with high SiO_2% added to the melt composition are associated with higher PEC correction, although a great variability characterizes such correlation (**Figure 37**). This correlation highlights the evidence that crystallization on the MIs wall may be controlled also by the extent of water loss, leading to the formation of new metal vacancies which migrate from the MIs exchanging Fe and Mg.

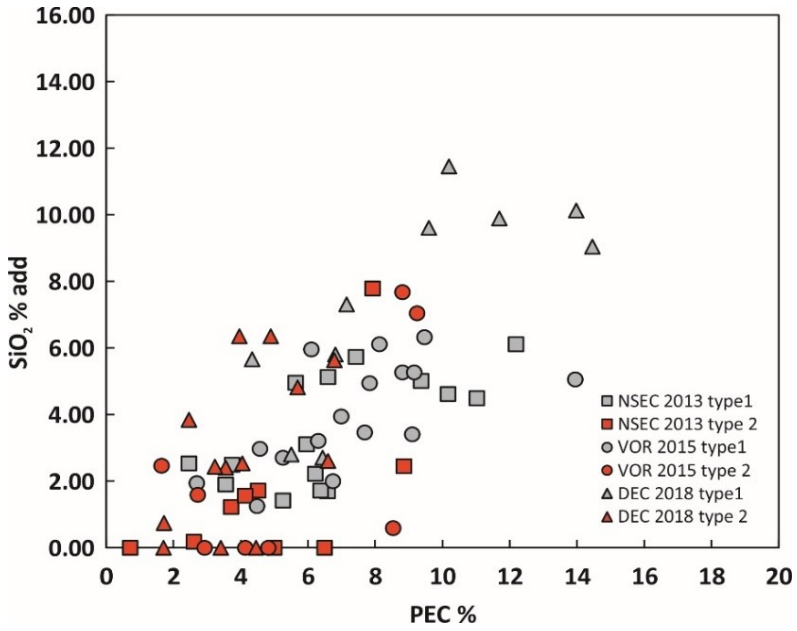

Figure 37: *Diagram showing linear correlation between the percentage of SiO_2 added to MIs for restoring the original compositions, following the approach of Portnyagin et al. (2019), and PEC% recalculated on restored MIs.*

Therefore, such findings support the hypothesis that H^+ incorporation in olivine structure from the MIs through new metal-vacancies created by the reactions described in Portnyagin et al., (2019), causes the coupled depletion of SiO_2-H_2O in MIs.

The amount of H_2O to be restored depends on the stoichiometry ratio $\Delta H_2O/\Delta SiO_2$ in function of reactions (3), (4) and (5) which occur at the MIs wall. In Portnyagin et al. (2019)

the stoichiometry ratio used for Klyuchevskoy Volcano was defined on the basis of molar proportions of H_2O and SiO_2 exchanged between olivine and MIs during the experiments. As stated before, no experiments are available for Etna olivines. So, in absence of experimental data, we used an intermediate molar proportion ($\Delta H_2O/\Delta SiO_2$=1) among those defined by Portnyagin et al. (2019) for restoring H_2O compositions as a function of the percentage of SiO_2 added to MIs. Using the highest ratio $\Delta H_2O/\Delta SiO_2$ = 2, the maximum H_2O restored content is estimated at ~6 wt.% and such high water content seems to be inappropriate for recent products, considering that restored bulk CO_2 contents of the post-2011 activity are lower than those measured in very primitive MIs from the 3930 B.C. eruption (~4000-6000 ppm, Kamenetsky et al., 2007; Gennaro et al., 2019) correlated with this H_2O concentration. On the contrary, ratio of 0.5 will bring little modifications to the analyzed dataset. Indeed, using the ratio $\Delta H_2O/\Delta SiO_2$ = 1, restored MIs show a maximum water content comparable with those measured for the 2001 and 2002-2003 eruptions (between 3.5 and 4.09 wt.%, see next paragraph). This inference suggests that in the deep levels of the plumbing system the magma may potentially contain up to 4.0 wt.% of water and part of this volatile load is lost during the progressive transfer upward to shallower levels.

6.3. Modeling on restored MIs compositions

The highest restored H_2O has been obtained for DEC 2018 eruption at 4.09 wt.%, whereas NSEC 2013 and VOR 2015 show respectively maximum contents of 3.00 and 3.58 wt.%. Restored H_2O-CO_2 MIs compositions allowed to estimate deeper trapping pressures. In fact, the highest pressure calculated through VOLATILECALC software is ~320 MPa for a MI from VOR 2015 products with H_2O at 3.26 wt.% and CO_2 at 2122 ppm (recalculated after PEC correction on restored H_2O-SiO_2 compositions), in agreement with thermodynamic modeling

(see below in this section). However, closed-system degassing model with variable initial gas phase (from 0 to 4%), defined using the mentioned H_2O and CO_2 compositions, cannot reproduce all restored MIs data (**Figure 38**).

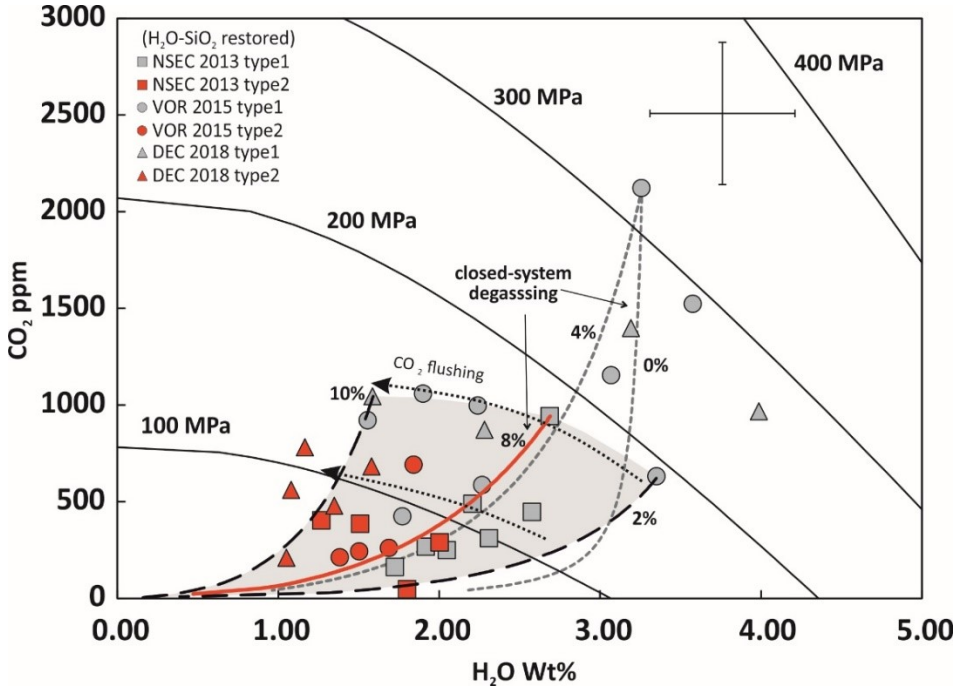

Figure 38: *H_2O-CO_2 composition in restored MIs for H_2O-SiO_2 loss and bulk CO_2 restored. The highest trapping pressure is calculated at 320 MPa, where closed system degassing with 0 to 4% of initial gas phase are represented with dashed light grey line. Evidence of CO_2 flushing is observed at pressures lower than 200 MPa, highlighted by the grey area. The greater error bar on H_2O takes into account the error propagation on measured compositions from the calculation in restoring original H_2O contents, considering a variation of ±0.1 respect to the $\Delta H_2O/\Delta SiO_2$ used.*

The variable proportions of H_2O-CO_2 at lower pressure (<200 MPa) suggest that the occurrence of CO_2 flushing in the upper part of the plumbing system between 200 and 50 MPa cannot be entirely excluded (Collins et al., 2009). The MI composition with H_2O at 2.69 wt.% and CO_2 at 942 ppm from 180 MPa can be used as an intermediate solution for the degassing model at pressure lower than 200 MPa.

SiO_2 on restored MIs ranges between 45.23 wt.% and 51.46 wt.% (compositions normalized after PEC correction) and type 1 MIs show a silica contents comparable with the most basic rocks found in historical and recent times. Negligible differences characterize the other major elements of the recalculated post-2011 MIs. Furthermore, improvements of thermodynamic modeling have been achieved through a two step modeling, using the restored SiO_2-H_2O MIs compositions (**Figure 39**). Initial conditions of T =1160°C, P = 320 MPa (constrained from the degassing model), fO_2 at the QFM buffer, restored H_2O at 4.09 wt.% and CO_2 at 2122 ppm have been fixed for the first step, ending at T = 1110°C and P = 190 MPa. The initial melt composition for the second step was fixed starting from the last melt obtained in the first step, then constraining T = 1110°C, P = 190 MPa, fO_2 at the QFM buffer and changing H_2O at 2.69 wt.% and CO_2 at 942 ppm, in order to take into account the effect of CO_2 flushing at 170-200 MPa (**Figure 37**). The final T was fixed at 1074°C and pressure close to the surface conditions. Crystallization of olivine (~4%) is the only parameter controlling the evolution of the melt in the first step, and olivine composition changes from Fo_{83} to Fo_{80}. During the second step (starting from 190 MPa), crystallization of olivine (from Fo_{79} to Fo_{70} at last step of simulation, corresponding to a pressure of 13 MPa) is followed by clinopyroxene (132 MPa), oxides and plagioclase during the very late stages of evolution (<50 MPa), for a total of ~57% crystallization of an assemblage constitute by 7% of olivine, 23% of clinopyroxene, 22% of plagioclase and 5% of oxides.

The transition from type 1 to type 2 MIs occurs during the crystallization of clinopyroxene which starts to crystallize at 132 MPa in a melt in equilibrium with Fo_{78} olivine, in agreement with the olivine compositions measured close to type 2 MIs. Trace elements support such inferences, indeed the small differences in ratios like Zr/Nb and La/Sm between the two types of MIs can be controlled chiefly by crystallization and fractionation of clinopyroxene. Moreover, field observations allowed to verify the presence of a mush made by clinopyroxene

crystals deposited on the summit crater edges after the VOR 2015 eruptions. All these considerations support that a proper correction on MIs compositions was obtained using the Portnyagin calculation.

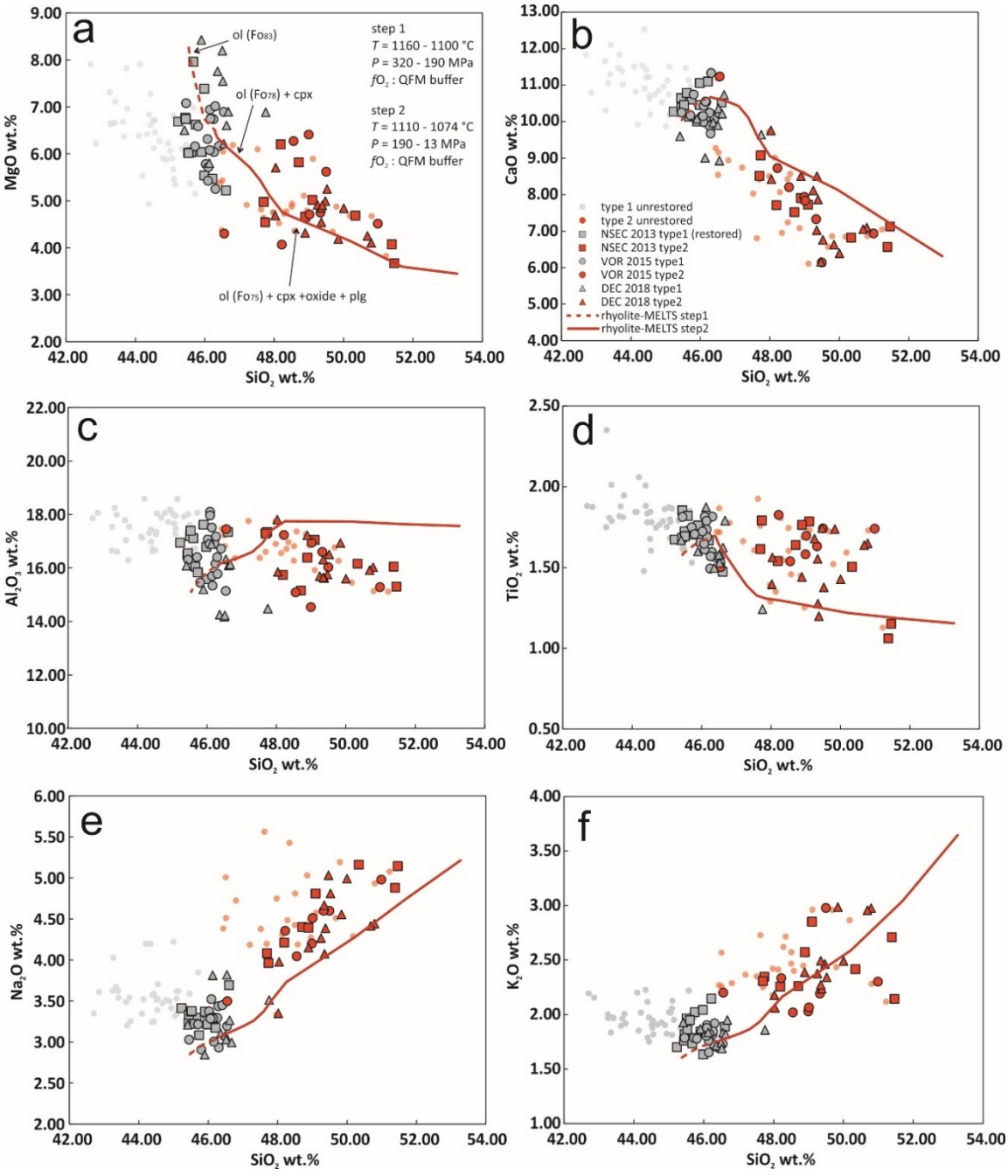

Figure 39: *Major elements MIs corrected for H_2O-SiO_2 loss and rhyolite-MELTS modeling, performed in two steps: 1) T =1160°C, P = 320 MPa, and fO_2 = QFM buffer, Fo_{83} to Fo_{80} olivine are reproduced; 2) T =1110°C, P = 190 MPa, and fO_2 = QFM buffer, Fo_{79} to Fo_{70} olivine are reproduced. Not corrected MIs for H_2O-SiO_2 loss were reported for comparison.*

The highest S content after PEC correction on restored MIs is ~2900 ppm from VOR 2015 eruption. However, a weak dispersion of S-H_2O affects the restored data (**Figure 40**). Two reasons can explain such dispersion on water in restored MIs. The first reason can be related to the constant bulk rock compositions used for the recalculation of SiO_2-H_2O loss in MIs, which can lead to underestimation or overestimation as a function of the real Si-saturation index of MIs prior to the entrapment. On the other hand, only metal-vacancies diffusion is assumed in the evaluation of water loss in the recalculation of Portnyagin et al. (2019).

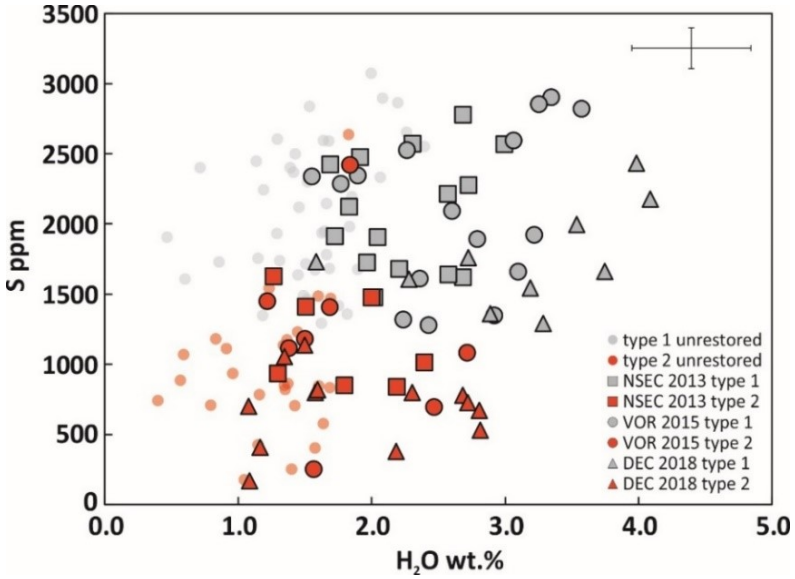

Figure 40: *H_2O and S compositions in MIs corrected for H_2O-SiO_2 loss. Unrestored MIs are reported for comparison.*

Occurrence of H^+ proton-polaron diffusion during syn-eruptive magma ascent at lower temperature cannot be excluded, leading to further water loss that is not possible to estimate in absence of experimental data. Llyod et al. (2013) inferred H^+ diffusion coefficient in olivine from the 1974 eruption at Volcano De Fuego through the Qin et al (1992) model, and they obtained diffusion coefficients consistent to the proton-polaron mechanism, resulting in timescales of diffusion in the order of 10-20 minute. They attributed this timing to the syn-eruptive magma ascent in the conduit.

Water loss induced by syn-eruptive ascent can be indicated by an inverse correlation between the percentage of H_2O re-equilibrium and MI size, where faster re-equilibration affects MI of small size (Llyod et al., 2013). Percentage of re-equilibrium can be calculated as $(H_2O_{predicted} - H_2O_{measured})/(H_2O_{predicted} - H_2O_{matrix})*100$, where average H_2O matrix is estimated at 0.2 wt.%. However, a weak inverse correlation is observed for MIs from selected eruption of the post-2011 activity at Mt. Etna (**Figure 41**), suggesting therefore that MIs water loss is the result of a coupled effect induced by syn-eruptive ascent and degassing during storage. Moreover, re-equilibration of MIs depends also on the distance of MI from the rim of crystal: assuming the same size, a MI closer to the rim will re-equilibrate faster than a MI located in the center of the host olivine, making tricky the sole evaluation of syn-eruptive ascent in MIs re-equilibration.

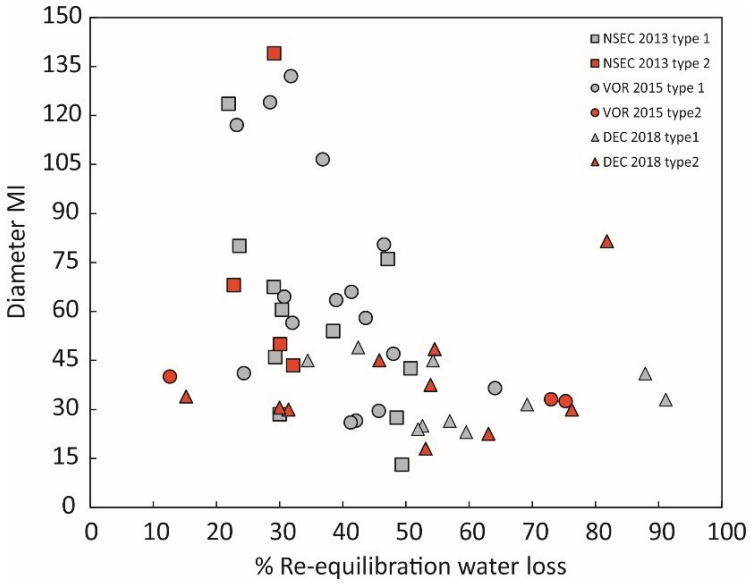

Figure 41: *Re-equilibration of water in MI due to water loss vs. diameter of MIs, calculated as* $(D_{max}+D_{min})/2$*, where D is diameter. A weak inverse correlation is observed, so syn-eruptive ascent cannot alone explain the water loss observed in MIs from post-2011 activity at Mt. Etna.*

6.4. S degassing modeling

S solubility and degassing in basaltic system is dependent by the melt composition, pressure and redox state. No direct measurements of Fe^{3+}/FeO_{tot} are available for the post-2011 MIs, so effects of the oxidation state of the magma during its ascent to surface cannot be evaluated. However, S degassing path can be defined using the balance calculation model of Spilliaert et al. (2006b). The model is not constrained for fO_2 and it provides calculation of bulk partition coefficients (D) of S for both open-system and closed-system conditions. The same calculation can be done also for Cl and F. In open-system conditions, the exsolved volatile species is lost from the magma during degassing and the dissolved volatile element X_i can be modeled following the Rayleigh law:

$$C = C_i \times f^{(D-1)} \quad (6)$$

where C_i is the initial concentration of the volatile element dissolved in the melt, f is the melt fraction and D is the bulk partition coefficient of the volatile element considered. The melt fraction is estimated using K_2O as differentiation index, considering its high incompatibility in olivine crystals. Specifically, f is calculated as K_2O_0/K_2O, where K_2O_0 is the initial content of K_2O assumed in the most primitive MI.

Closed-system degassing is constrained considering the continuous re-equilibration of the gas phase with the melt, and the concentration can be calculated using the batch fractionation model:

$$C = C_i / (D + (1-\alpha_0) f) \quad (7)$$

In this case C_i is the total element considering vapor + melt and α_0 is the percentage of volatile phase constituted by H_2O and CO_2 that may be present before the initial exsolution (S is assumed to be not exsolved in the initial gas phase). The bulk coefficient is calculated as:

$$D = \alpha K_d^{vap\text{-}melt} \quad (8)$$

where $K_d^{vap\text{-}melt}$ is the vapour-melt partition coefficient and α is the volatile mass fraction accumulated during each step of degassing, calculated as:

$$\alpha = \alpha_0 + [(X_{0\_H2Omelt} / f) - X_{H2Omelt}] \quad (9)$$

where $X_{0\_H2Omelt}$ and $X_{H2Omelt}$ are the dissolved water contents in melts respectively at initial conditions and during each differentiation step defined by f. $X_{H2Omelt}$ values are defined from the K_2O-H_2O covariation calculated through rhyolite-MELTS simulations. Fitting of the calculations is performed through least squares minimization using S and K_2O compositions as *Ln*S and *Ln*K_2O, allowing to better constrain the model considering a more linear variation between S and K_2O. Then, the calculated S is used to define the degassing path in H_2O-S system.

Using *Ln* is possible to observe that type 1 MIs are more clustered, while type 2 MIs display a strong inverse correlation, suggesting that S degassing affect more extensively type 2 MIs. In accordance with the closed-system modeling defined for H_2O-CO_2, batch fractionation model has been used in order to define S degassing. Considering unrestored MIs H_2O-SiO_2 data, rhyolite-MELTS model has not provided a good fit for K_2O-H_2O (**Figure 34d**), where higher H_2O contents have been calculated from the thermodynamic model, due to water loss recorded in MIs. The effect in H_2O-S system is a shifted degassing path with respect to the MIs data (**Figure 42**).

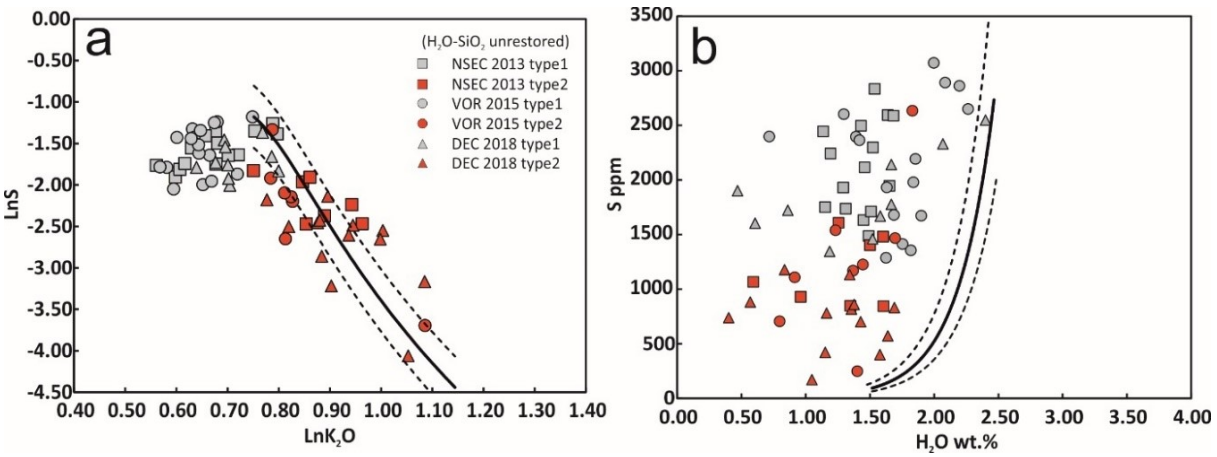

Figure 42: *S degassing model on unrestored MIs for H_2O-SiO_2 loss, plotted in LnS vs LnK_2O and S vs H_2O, calculated through the approach of Spilliaert et al. (2006b); the model is performed by least squares minimization on LnS-LnK_2O data; in S-H_2O system the degassing model does not reproduce MIs because of the effect of water loss. The black line is the best-fit model and dashed lines represent the variance on S respect to the best fit model.*

In the case of restored MIs, the K_2O-H_2O covariation is provided by thermodynamic simulation performed by rhyolite-MELTS (**Figure 43**). The closed-systems degassing for S is constrained at melt fraction of 85%, corresponding to K_2O = 1.92 wt.% and H_2O = 2.70 wt.%, which is closed to the composition used to constrain the intermediate H_2O-CO_2 degassing path on corrected MIs starting from a pressure of ~180 MPa and with an initial volatile phase of 8%. The estimated bulk partition coefficient *D* increase progressively from 0 to 32 (**Figure 44**).

S bulk partition coefficients *D* calculated using post-2011 MIs are within the range defined in Spilliaert et al. (2006b) for 2002-2003 eruption at Mt. Etna (D_s ~0-60). Obtained D_s are comparable with values calculated for monogenetic volcanoes in central Mexico (Johnson et al., 2010), but lower than other Central American volcanoes (35-110; e.g. Sisson and Layne 1993; Llyod et al., 2013). From the modeling on restored H_2O-SiO_2 compositions, sligh deeper pressure of initial exsolution of S has been constrained (180 MPa) than the value (140 MPa) previously defined by Spilliaert et al. (2006b). Such difference in the estimated pressures can be likely due to the volatile compositions of MIs from the 2002-2003 eruptions, which have not

been corrected for diffusive water loss. In fact, water loss cannot be excluded for products of the past eruptions, and evaluation of the loss degree could provide different conditions of degassing in the H_2O-CO_2-S system, thus possibly constraining a higher pressure of initial S exsolution also for the 2002-2003 products.

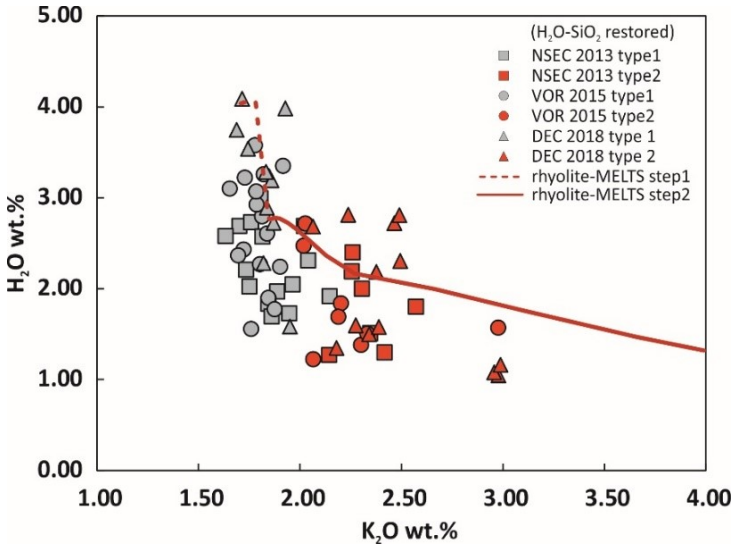

Figure 43: *H_2O vs. K_2O compositions in restored MIs for H_2O-SiO_2 correction and rhyolite-MELTS best fit model.*

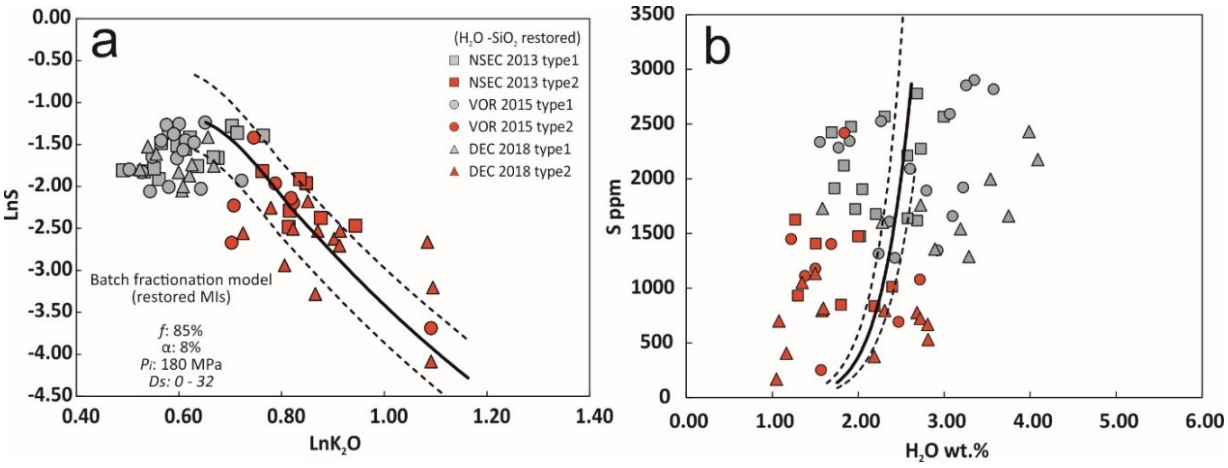

Figure 44: *S degassing model on restored MIs for H_2O-SiO_2 correction, plotted in LnS vs LnK_2O and S vs. H_2O, calculated through the approach of Spilliaert et al. (2006b); the model is performed by least squares minimization on LnS-LnK_2O data. The best fit is calculated at melt fraction (f) of 85%, with initial gas phase (α) of 8% (from H_2O-CO_2 degassing) at pressure of 180 MPa. The black line is the best-fit model and dashed lines represent the variance on calculated S respect to the best fit model.*

7. VOLATILE DIFFUSION MODELING IN MELT-EMBAYMENTS

7.1. Diffusion modeling: approach

7.1.1. Fixing initial, final conditions and diffusion coefficients

Parameters for constraining the volatile diffusion modeling along olivine-hosted melt embayments are: 1) initial conditions prior to the ascent, including pressure, temperature and volatile concentrations; 2) concentrations of volatile elements at the end of diffusion; 3) diffusion coefficients of each volatile element modeled. Microanalyses along olivine-hosted melt embayments highlight clear H_2O compositional gradients in all the analyzed samples, with a decreasing of compositions observed in the last 30-60 μm of the tubes. Differently, some samples display irregular compositional gradients for sulfur, probably due to the lower S diffusivity which produces less pronounced gradients in the last 20 μm, and those suitable for diffusion modeling were selected. Finally, Cl does not display compositional gradients and measurements of CO_2 are not available. This means that the volatile diffusion modeling for Mt. Etna embayments from post-2011 activity has been applied for water and sulfur.

Embayments are assumed to be in continuous exchange of elements with the external melt, whose evolution has been constrained through thermodynamic and degassing models on MIs. Such models can be therefore assumed valid also for embayments. Major element compositions measured in embayments are comparable with those observed in type 2 MIs (**Figure 45**). In rhyolite-MELTS modeling, the transition from type 1 to type 2 MIs were constrained between 90-130 MPa in restored MIs at temperature lower than 1100°C. Thus, the last embayments re-equilibration with the external melt prior to ascent may have occurred between the surface and 130 MPa. This agrees with degassing models, where trapping pressure for type 2 MIs were estimated at values lower than 130 MPa.

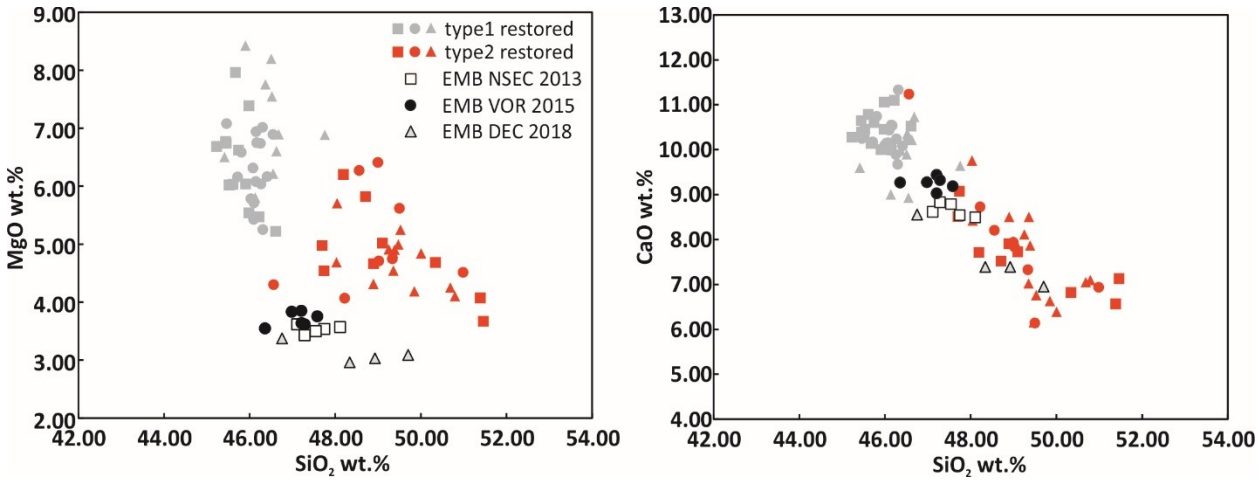

Figure 45: *Selected major elements measured in melt embayments from the selected post-2001 eruptions compared to major elements in restored MIs. Embayments display lower MgO concentrations than MIs because effects of PEC are not considered in embayments.*

Both initial pressures and concentrations for the diffusion modeling on each embayments can be constrained from degassing models, assuming a degassing equilibrium of embayments consistent with that defined for MIs. The basic assumption considers that sulfur is characterized by lower diffusivity than H_2O, allowing to preserve potentially its original concentrations in the interior of embayments (Llyod et al., 2014). Solutions relative to H_2O-CO_2 and H_2O-S systems for restored MIs can be combined considering H_2O as the intermediary between the two degassing models. Thus, assuming that the concentration of S in the interior of embayments is representative of its original value before ascent, the relative H_2O initial concentration estimated through balance calculation method of Spilliaert et al. (2006b) can be constrained as initial concentration for the diffusion modeling (**Figure 46**). Finally, the respective initial pressure P_0 is defined from VOLATILECALC modeling in the H_2O-CO_2 system. Observing H_2O vs. S diagrams, a few embayments overlap H_2O contents in some MIs (restored for H_2O-SiO_2 loss) but, as stated above, recalculation for H_2O-SiO_2 loss does not take into account the

possible further water loss during syn-eruptive ascent, making not suitable the use of such compositions as initial concentrations (**Figure 46**).

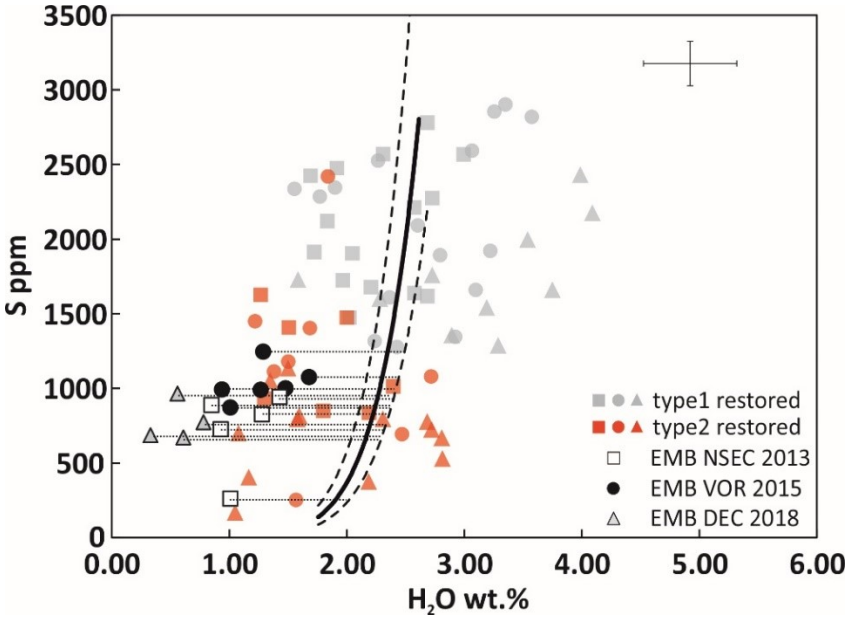

Figure 46: *S-H_2O compositions measured in the interior embayments, plotted with MIs restored compositions; assuming that S measured in embayments correspond to the original values before the magma ascent, respective H_2O values in the degassing path at same S concentrations are used as initial concentrations for H_2O diffusion modeling.*

Assuming that the melt inside the embayment undergoes equilibrium degassing concordant with those defined through MIs, H_2O variation defined in the degassing model is used for determining the concentration at the melt-bubble boundary. In the case of restored MIs, the intermediate solution of degassing modeling at 190 MPa, calculated at H_2O ~2.69 wt.% and CO_2 ~942 ppm with an initial volatile content of 8 wt.%, was used in the determination of H_2O in the external melt during the ascent. Final H_2O concentrations are constrained in a range between 0.1 and 0.3 wt.%, as measured in some spots on the surrounding melts, corresponding to final pressure of 1-2 MPa.

Diffusion coefficient is a critical parameter strongly influencing the modeling. Estimation of diffusion coefficient is based on the Arrhenius law and is chiefly function of temperature,

pressure and melt compositions. Assuming isothermal condition during the magma ascent, a constant temperature of 1080°C was fixed for the modeling, corresponding to the average value estimated in the calculation of residual liquids by rhyolite-MELTS simulations with comparable compositions to those measured in embayments. In the case of magma with mafic to intermediate compositions, pressure has a minor influence on H_2O diffusivity, and it can be neglected. Thus, H_2O diffusivity is estimated following the equation defined experimentally by Zhang et al. (2007):

$$D_{H_2O} = C_{H_2O} exp\left(-8.56 - \frac{19110}{T}\right) \quad (10)$$

where C_{H2O} is the concentration of water in wt.%, D_{H2O} the water diffusion coefficient in m^2/s and T is temperature in K. This equation has been developed for basaltic melts, but the influence of variations in melt compositions on D_{H2O} is not considered. In particular, the degree of melt polymerization strongly affects the water diffusivity, which results in a factor of 10 greater in basalts with respect to andesites (Zhang and Ni, 2010). Lloyd et al. (2013) parametrized the effect of melt compositions on Fuego embayments using the NBO/T ratio. These embayments were zoned for what regards major element compositions, so they have estimated the dependence of diffusivity on NBO/T as a function of the distance from the bubble. Embayments investigated in this study are not zoned for major elements and the correction can consider a single value of NBO/T, representative for all the length of each embayment. Embayments from all the three eruptions investigated in this study are characterized by similar major elements concentrations, corresponding to K-trachybasaltic compositions. So, using the calculation of Mysen and Richet (2005), an average value of NBO/T ~0.56 ± 0.03 has been estimated for Mt. Etna melt embayments, which is an intermediate value between basalt and andesitic compositions (Llyod et al., 2013). The parametrization (**Figure 47**) was performed by defining a linear relationship between NBO/T and LogD_{H2O} at temperature of 1080°C and H_2O = 2.3

wt.%, corresponding to the highest H_2O initial concentration estimated for Etna embayments (constrained from degassing models on restored MIs), using a basaltic composition from Zhang et al. (2007), and an andesitic composition from Behrens et al. (2004). The resulting D_{H_2O} for NBO/T = 0.56 is lower than the diffusivity calculated through the equation (10) in a factor of 0.29. The same factor is obtained at lower H_2O concentrations. Thus, D_{H_2O} can be estimated by multiplying the equation (10) by 0.29 (±0.03), in order to include the influence of melt polymerization, corresponding to a value of Log$D$ ~ -10.03 (± 0.06).

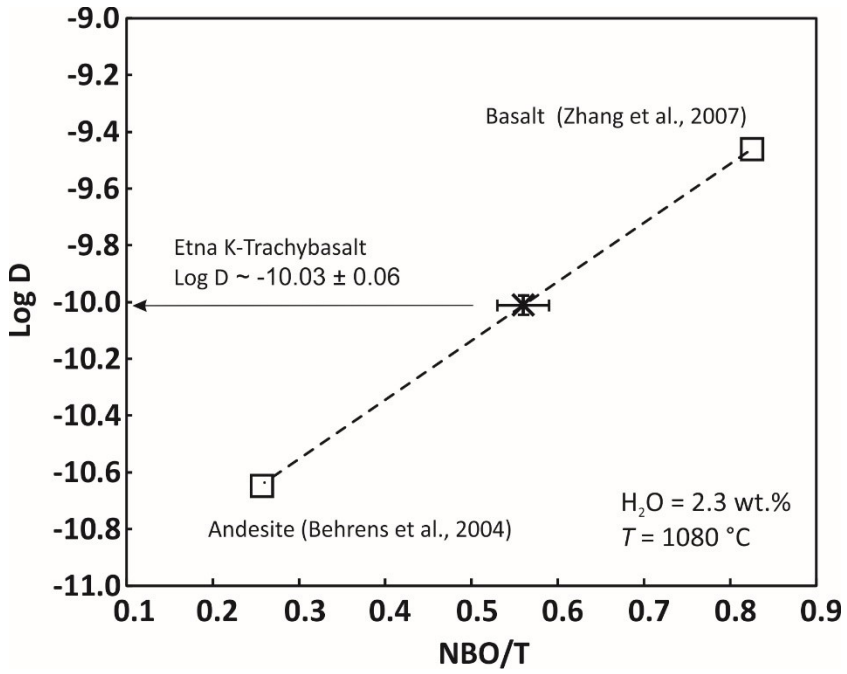

Figure 47: *Parametrization on H_2O diffusion coefficient for Mt. Etna K-trachybasalt compositions, using a basalt from Zhang et al. (2007) and an andesite from Behrens et al. (2004) at H_2O 2.3 wt.% and T 1080°C. A linear relationship is defined between LogD and NBO/T, resulting as:*

LogD =2.07857×NBO/T - 11.194.

Diffusivity of S is dependent not only on the temperature and composition, but also on the oxygen fugacity, which affects the sulfur speciation in the melt. Indeed, changing from oxidizing to reducing conditions leads to an increase by about 2.5 orders of magnitude in diffusivity (Zhang et al., 2007). Such dependence makes difficult to develop a general equation

for defining S diffusivity. However, based on experiments on Etna and Stromboli melts, D_S have been defined for basaltic liquid under reducing conditions, taking into account the dependence from H_2O concentration (Freda et al., 2005; Zhang et al., 2007):

$$D_S = exp\left(-8.21 - \frac{27692 - 651.6C_{H_2O}}{T}\right) \quad (11)$$

Occasional occurrence of small sulfide globules in MIs from recent eruptions selected for this study suggests rather reduced conditions, making the equation (11) suitable for calculating S diffusivity for Mt. Etna melts.

7.1.2. Development of the numerical model

Olivine-hosted melt embayments chosen for this study are mostly tubular-shaped and compositional profiles are measured parallel to the elongated direction from the interior toward to the mouth. Although their volumes are developed over three dimensions, the one-dimensional diffusion has been used for modeling the concentration profile, based on the second Fick's law (Crank, 1975):

$$\frac{\partial C(x,t)}{\partial t} = D\frac{\partial^2 C(x,t)}{\partial x^2} \quad (12)$$

where C and D are respectively the concentration and the diffusion coefficient relative to the volatile element modeled. The partial differential equation describes the variation of the volatile concentration as a function of time t at each point along the x direction. In the case of water, the diffusion coefficient is dependent from the concentration of the volatile element [from the equation (10)], so the equation (12) becomes:

$$\frac{\partial C(x,t)}{\partial t} = \frac{\partial D}{\partial x} \cdot \frac{\partial C(x,t)}{\partial x} + D\frac{\partial^2 C(x,t)}{\partial x^2} \quad (13)$$

Taylor series expansion provides a discrete numerical form of the differential equation (13). Using the finite differences approach, the equation (13) can be rewritten as:

$$C_{i,j+1} = C_{i,j} + \left(\left(\frac{D_{i+1,j} - D_{i-1,j}}{2\Delta x} \right) \left(\frac{C_{i+1,j} - C_{i-1,j}}{2\Delta x} \right) + D_{i,j} \left(\frac{C_{i+1,j} - 2C_{i,j} + C_{i-1,j}}{\Delta x^2} \right) \right) \cdot \Delta t \quad (14)$$

where the subscripts *i* and *j* refer respectively to space and time coordinates of each grid point, Δx is the spatial step in μm between each point of the diffusion profile and Δt is the temporal step in seconds (s) between each calculation of the diffusion profile over time (Crank, 1975; Costa et al., 2008). Both Δx and Δt must be determined in order to satisfy the Courant condition, a dimensionless parameter which defines the stability of the numerical development of the differential equation (Costa et al., 2008). The Courant condition is defined as:

$$r = D \frac{\Delta t}{(\Delta x)^2} \quad (15)$$

and the condition is fulfilled for $r < 0.5$.

The absence of compositional gradients in major elements measured from interior to the open side of tubes indicates that during the ascent the melt inside the embayments did not interact with melts of different compositions. Thus, the embayments can be considered under equilibrium with the external melt prior to the ascent and the initial volatile concentrations are assumed to be homogenous throughout the tubes:

$$C_{x,0} = C_{melts}(P_0) \quad (16)$$

where $C_{x,0}$ is the initial volatile concentration at each point of the embayment and C_{melts} is the concentration on the external melt at pressure P_0 from which the magma starts to ascend toward the surface.

Only exchange of mass from the interior of embayment to the bubble growing at end of the tube is assumed during the diffusion. The interface between the melt and the bubble at the

outlet of embayment is defined as the boundary of the diffusion (x = 0). A Dirichlet boundary condition is constrained at this point:

$$C_{0,t} = C_{melt}(P, t) \quad (17)$$

where $C_{0,t}$ is the concentration specified at interface bubble-melt at given time t and pressure P during the ascent, which will change in accordance to variation of volatiles in the surrounding melt as a function of the pressure-dependent degassing model (**Figure 48**).

Differently, zero-flux is assumed in the interior of embayment adjacent to the host olivine crystal, and no exchange or growth with the host olivine is assumed. Thus, a Neumann condition is specified at the opposite side of the embayment, of length L measured from the bubble:

$$\partial C_{L,t}/\partial x = 0 \quad (18)$$

setting for each time j: $C_{n,j} = C_{n-1,j,}$ where n is the total number of the spatial grid points along the direction x. The diffusion simulation ends assuming instant cooling of the magma at pressure P_f close to the surface conditions. The final concentration is constrained by measuring volatile contents on spots in the glass surrounding the host crystals:

$$C_{0,t_f} = C_{melt}(P_f, t_f) \quad (19)$$

Temperature is kept constant during the estimation of diffusion coefficient, simulating an isothermal diffusion during the ascent before reaching the surface. Thus, decompression rate is the only free parameter allowed to change in the simulation and represents the target to achieve through the diffusion modeling. A single stage approach is performed, since both initial exsolution of H_2O (after dehydration caused by CO_2 flushing) and S are constrained at similar pressure (180 MPa on restored MIs). Starting from the initial pressure P_0, the simulation works through an iterative scheme where at each step j of the modeled pressure decreases as a function of dP/dt (MPa/s) and the temporal step Δt:

$$P_j = P_{j-1} - \frac{dP}{dt} * \Delta t \quad (20)$$

During decompression, the concentration of volatiles at embayment outlet will change as a function of their solubility and of the pressure calculated at each step of the simulation, according to the pressure-dependent degassing model (**Figure 47**).

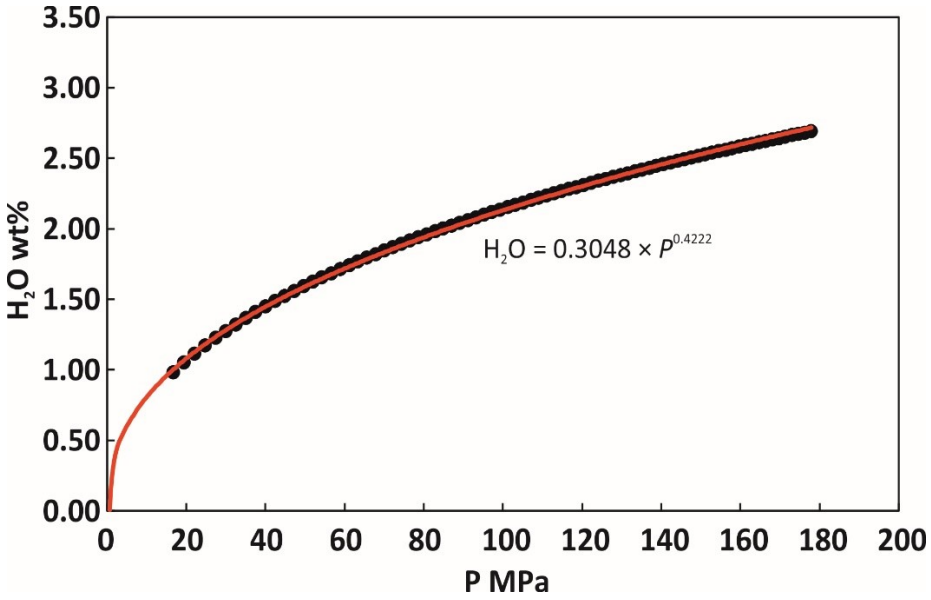

Figure 48: *Variation of H_2O in function of the pressure calculated by VOLATILECALC for the degassing path with initial H_2O=2.69 wt.%, starting at pressure of ~180 MPa. H_2O concentration at outlet embayment for each step of decompression can be predicted using the equation: $H_2O = 0.3048 \times P^{0.4222}$.*

Assuming same initial conditions, variations in *dP/dt* affect the shape of modeled gradients. Many simulations are performed changing progressively *dP/dt* within a defined range and the best fit is determined by modeling the water, since its diffusivity is better characterized than sulfur and provides more accurate results. The best fit on measured data have been defined by minimizing the parameter χ^2:

$$\chi^2 = \sum_{i=1}^{n} \frac{(C_i - y_i)^2}{{\sigma_i}^2} \quad (21)$$

where C_i is the concentration of water at i position in the compositional profile, y_i is the modeled water concentration by equation (14) and σ_i is the uncertainty associated to the measured concentration (estimated at 8% by Raman spectroscopy). Once determined the best fit, the time and velocity can be calculated as:

$$t = \frac{P_i - P_f}{dP/dt} \tag{22}$$

$$v = \frac{1}{t}\left(\frac{P_i - P_f}{\rho g}\right) \tag{23}$$

where g is the gravitational acceleration (9.81 m/s^2) and ρ is the density of a magma, considering a mean value of 2.65 g/cm^3 for a melt with ~2% of water dissolved in the melt (extrapolated from Fig. 2 in Corsaro and Pompilio, 2004).

Uncertainties on calculated timescales depend on: i) analytical uncertainties on the H_2O compositional profile measured through Raman; ii) uncertainties on initial conditions (temperature, initial pressure and initial concentration) used for running diffusion simulations and calculation of D_{H_2O}. The equation (21) used for minimization of χ^2 takes into account the weight of uncertainties for each spot measured, enhancing measurements with lower uncertainties in the calculation of the best fit model. Uncertainties on initial H_2O concentration are determined through S degassing model showed in **Figure 46** for restored H_2O-SiO_2 MIs. However, variations on initial H_2O concentration reflect proportional variations on the initial pressure defined in the H_2O-CO_2-S system described above, resulting in the same value of ascent rate obtained from the best fit model. Thus, uncertainties on modeling are evaluated considering temperature variations in the calculation of D_{H_2O}, by defining $\Delta T = \pm 6$°C from the value constrained by thermodynamic modeling (~1080°C), which corresponds to the range of temperature in equilibrium with Fo compositions measured in olivine hosting melt embayments. Uncertainty on the calculated NBO/T (0.56 ±0.03) produces a variation of the

correction factor (0.29), used in the calculation of D_{H_2O}, of ±0.03, resulting in a decreasing/increasing of the H_2O diffusivity at lower/higher values of the correction factor.

7.2. Results of volatile diffusion modeling

The approach described above allows the estimation of a constant decompression rate for each embayment compositional profile modeled, assuming that the decompression is driven only by magma ascent through the conduit. It is reasonable that syn-eruptive ascent velocity from the reservoir to the surface in natural systems is not constant, so estimation provided by diffusion modeling can be considered as average values recorded by each embayment investigated in this study.

Volatile diffusion modeling is performed using the degassing path defined for CO_2-H_2O-SiO_2 restored MIs for constraining the initial conditions. VOR 2015 embayments are characterized by the highest values of starting pressures, ranging from 112 to 120 MPa, corresponding to 4.2–4.5 km below summit craters. Instead, NSEC 2013 and DEC 2018 embayments were fixed at similar range of initial pressures, between 101–110 MPa and 97–110 MPa respectively (~3.7–4.2 km below summit craters). An exception is represented by the NSEC_emb6, where the lower S content measured in the embayment interior (average ~412 ppm) corresponds to a pressure of 84 MPa (3.1 km below summit). These range of depth correspond to a portion of the conduit between the shallowest reservoir located at ~1.5-2.0 km below the summit, inferred by location of the sources of volcanic tremor during non-eruptive periods or before to an oncoming eruption (Patanè et al., 2013, Viccaro et al., 2016) and the reservoir located at 150-200 MPa inferred by geodetic and petrological data (Viccaro et al., 2016; Cannata et al., 2018). Initial H_2O concentrations for NSEC 2013, VOR 2015 and DEC 2018 embayments are constrained respectively in the range of 1.99–2.23 wt.%, 2.23–2.31 wt.% and 2.12–2.23 wt% (**Figure 49**).

Minimization of the χ^2 is performed through a script code using the programming language Python and allows to find the best fit model by varying *dP/dt* for each simulation in defined ranges (between 0.1-1.0 MPa/s for calculated high rates and 0.01-0.1 for low rates). Estimated χ^2 values suggest that acceptable best fits have been obtained for each model, considering a significance level at 5%. Few samples are characterized by relatively high χ^2, possibly due to the more irregular H_2O gradients modeled. For example, the sample VOR_emb3 (**Figure 49h**) displays a more irregular H_2O profile composition toward the open side of embayment, likely due to a narrow neck of the tube which may cause change in the diffusivity of the water with respect to that predicted from one-dimensional numerical approaches. Therefore, diffusivity is strongly dependent by the embayment shape (deGraffenried and Shea, 2020) and more reliable results from one dimensional diffusion are obtained for tubular-shaped embayments.

On the whole, results from volatile diffusion modeling are concordant with the expected increase in ascent rates as explosivity of eruptions increases. In fact, the most powerful VOR 2015 eruption displays the highest calculated decompression rates, in the range between 0.34 MPa/s and 0.57 MPa/s (average ~0.46 ± 0.13 MPa/s), corresponding to a total duration of 3-6 minutes. NSEC 2013 eruption is characterized by rates from 0.11 MPa/s to 0.41 MPa/s (average ~0.22 ± 0.12 MPa/s), with associated timescales of 4-14 minutes. DEC 2018 eruption displays low decompression rates, in a range of 0.017 MPa/s to 0.075 MPa/s (average ~0.043 ± 0.027 MPa/s), corresponding to timescales of 23-96 minutes. Average ascent rates expressed as velocity in m/s are calculated in the order of 9.6 ± 4.6 m/s for NSEC 2013, 17.9 ± 5.0 m/s for VOR 2015 and 1.6 ± 1.0 m/s for DEC 2018. An outlier is represented by the sample VOR_emb2 which gives an ascent rate of 0.044 MPa/s (~42 minutes; **Figure 49g**). In fact, this sample has lower H_2O concentration measured in the interior with respect to other VOR 2015 embayments but at similar S concentrations, suggesting a similar initial pressure as defined for other

embayments for running the diffusion modeling. This sample also displays a progressive decrease of S from the interior to the embayment outlet, indicating that a lower ascent rate enabled major loss by diffusion of S and H_2O toward the external melt.

Concerning S modeling on other embayments, some samples display a good fit at same ascent rates estimated from H_2O diffusion modeling, while samples with irregular profile compositions are characterized by less accurate fitting.

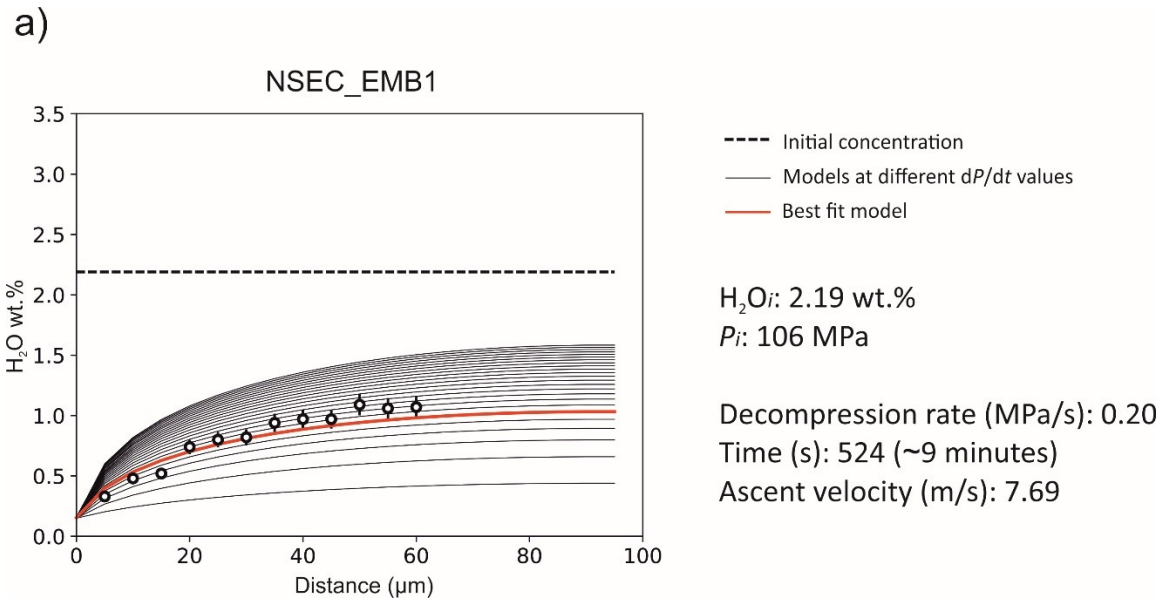

b)

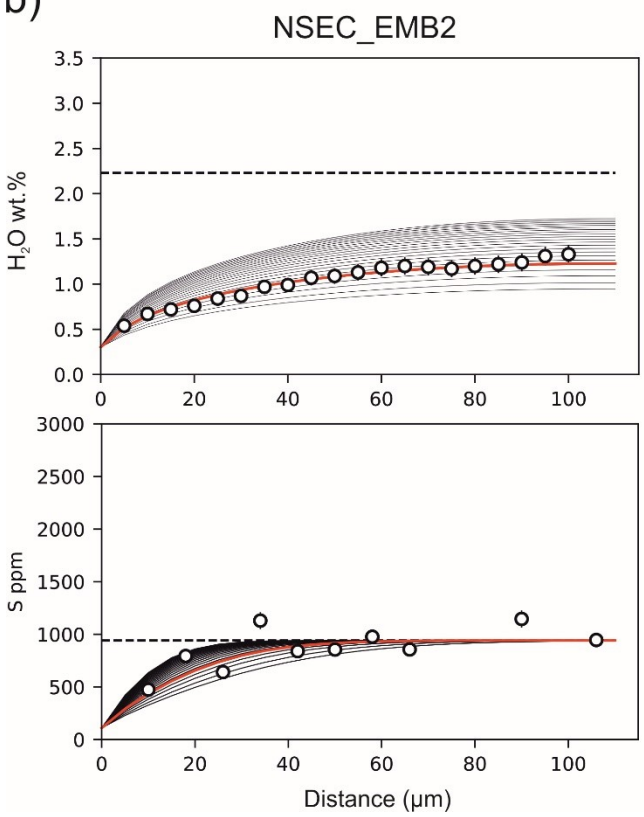

H_2O_i: 2.23 wt.%
S_i: 942 ppm
P_i: 110 MPa

Decompression rate (MPa/s): 0.26
Time (s): 415 (~7 minutes)
Ascent velocity (m/s): 10.00

c)

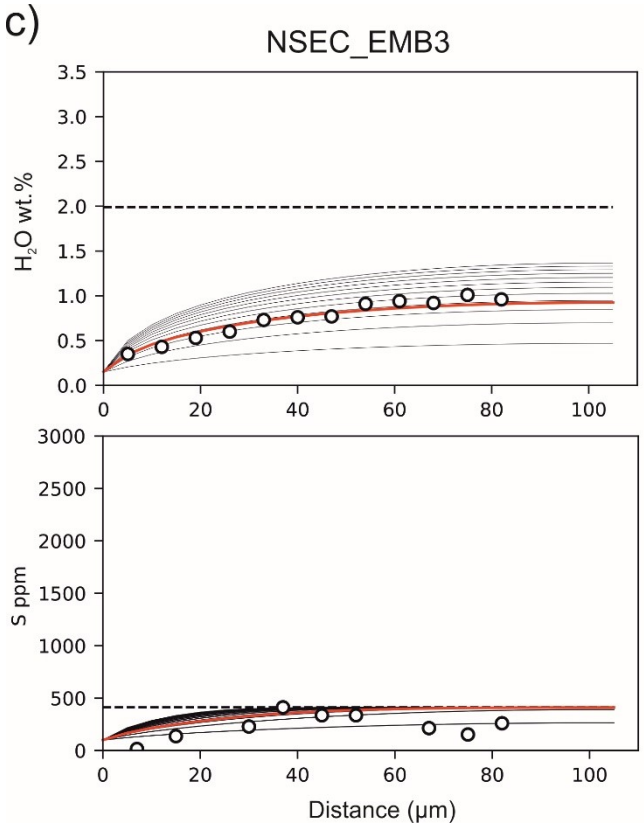

H_2O_i: 1.99 wt.%
S_i: 412 ppm
P_i: 84 MPa

Decompression rate (MPa/s): 0.11
Time (s): 754 (~13 minutes)
Ascent velocity (m/s): 4.23

d)

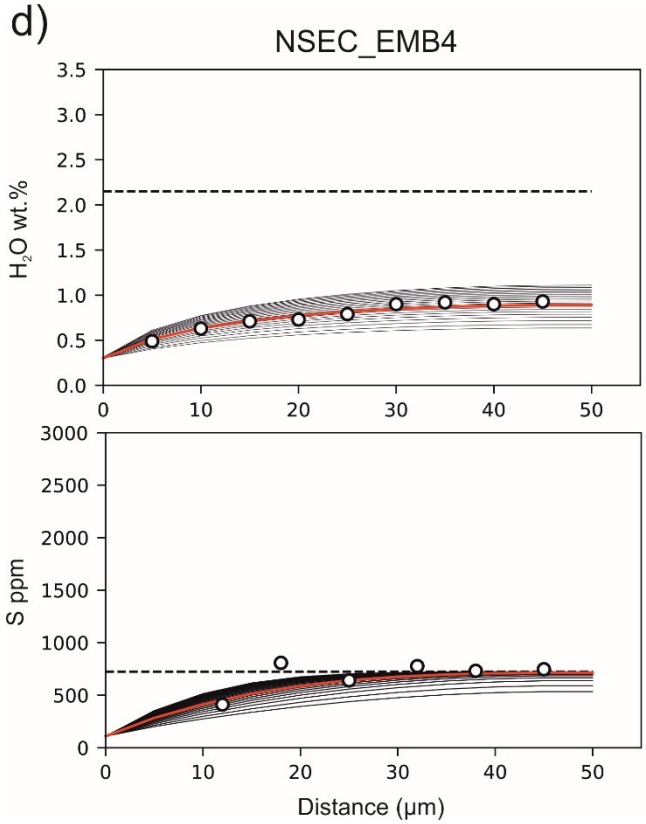

H_2O_i: 2.15 wt.%
S_i: 724 ppm
P_i: 101 MPa

Decompression rate (MPa/s): 0.41
Time (s): 241 (~4 minutes)
Ascent velocity (m/s): 15.77

e)

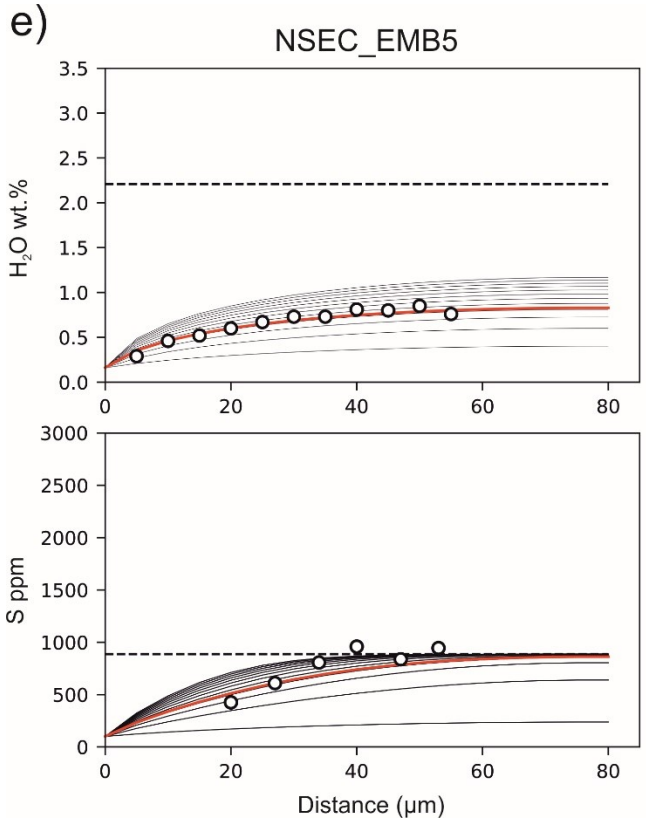

H_2O_i: 2.21 wt.%
S_i: 888 ppm
P_i: 108 MPa

Decompression rate (MPa/s): 0.13
Time (s): 823 (~14 minutes)
Ascent velocity (m/s): 5.00

f)

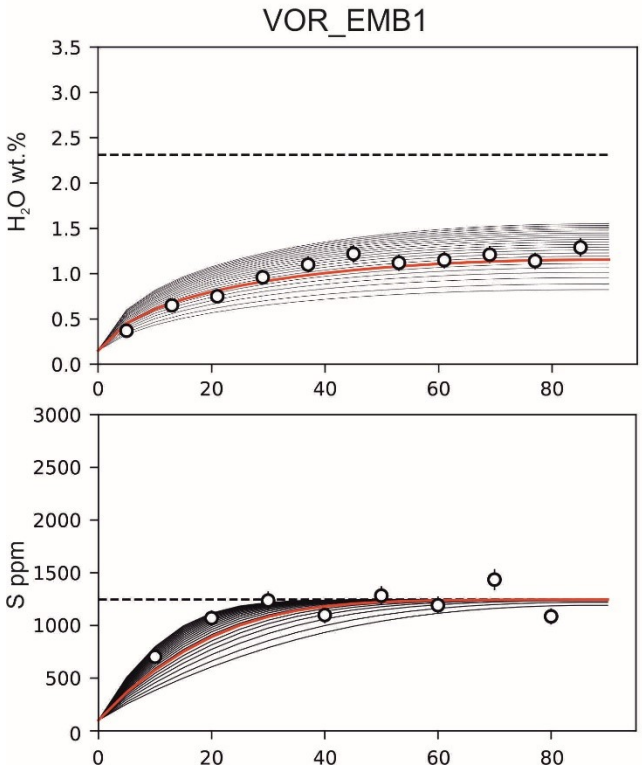

H_2O_i: 2.31 wt.%
S_i: 1245 ppm
P_i: 120 MPa

Decompression rate (MPa/s): 0.34
Time (s): 330 (~6 minutes)
Ascent velocity (m/s): 13.07

g)

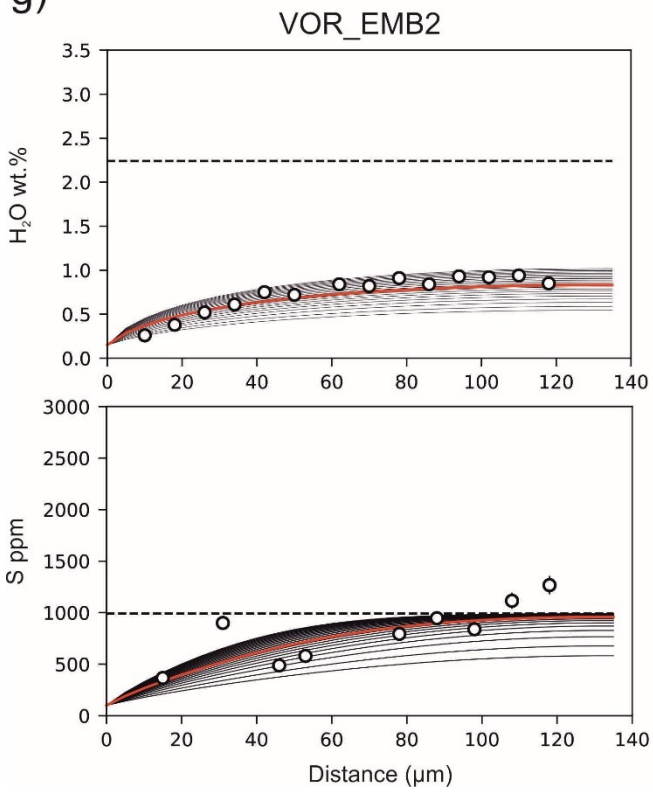

H_2O_i: 2.24 wt.%
S_i: 992 ppm
P_i: 112 MPa

Decompression rate (MPa/s): 0.044
Time (s): 2523 (~42 minutes)
Ascent velocity (m/s): 1.69

h)

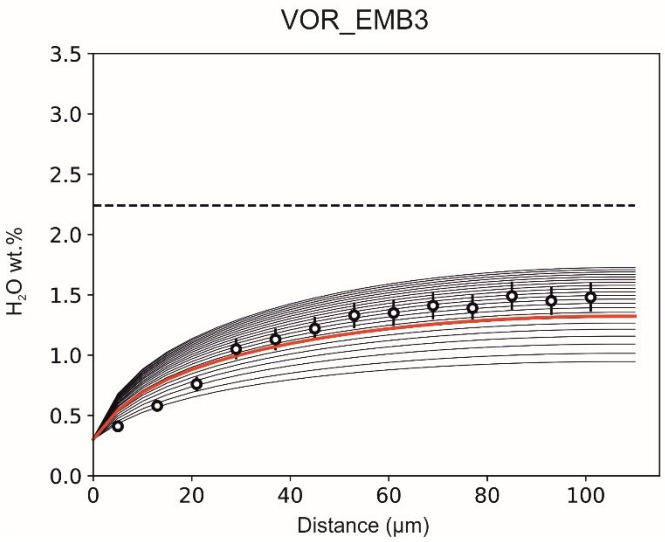

H_2O_i: 2.24 wt.%
S_i: 999 ppm
P_i: 112 MPa

Decompression rate (MPa/s): 0.34
Time (s): 323 (~5 minutes)
Ascent velocity (m/s): 13.07

i)

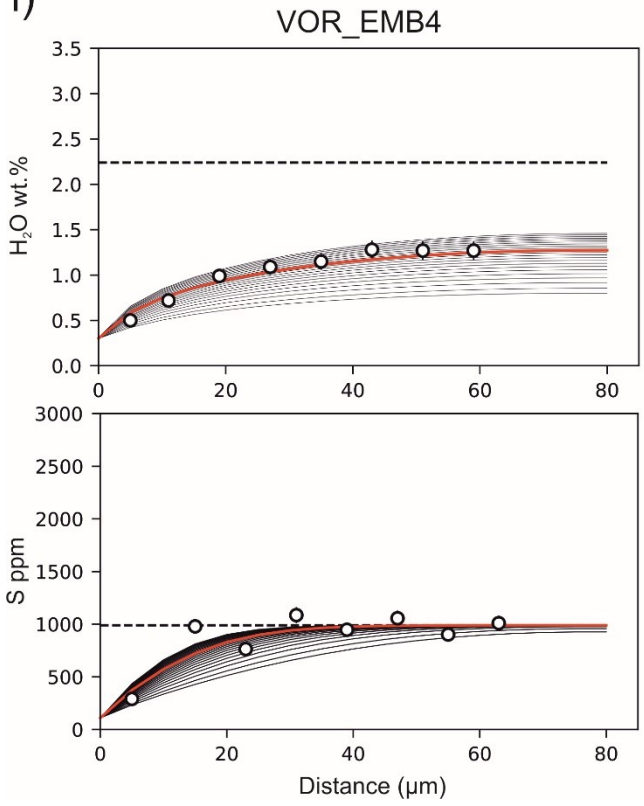

H_2O_i: 2.24 wt.%
S_i: 989 ppm
P_i: 112 MPa

Decompression rate (MPa/s): 0.57
Time (s): 193 (~3 minutes)
Ascent velocity (m/s): 21.93

j)

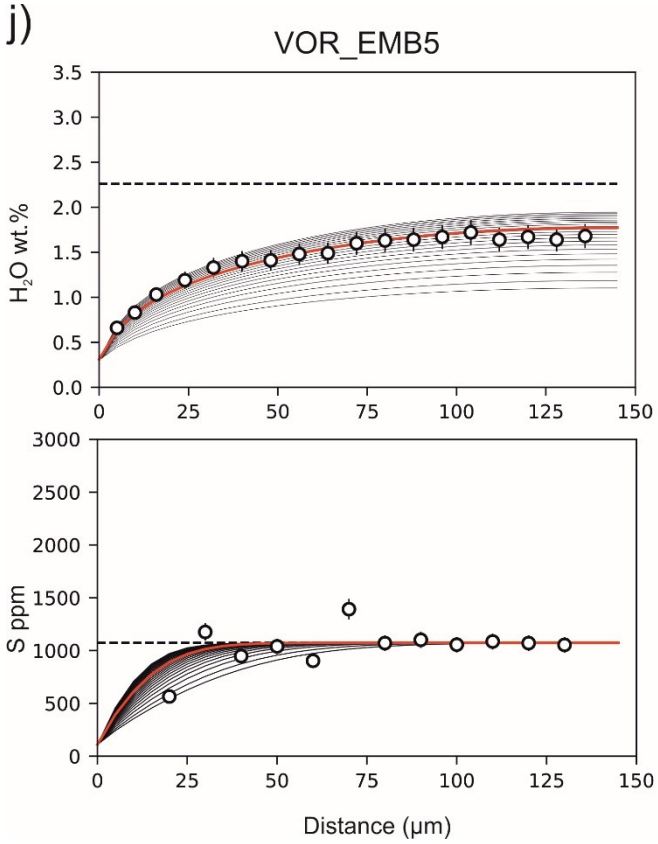

H_2O_i: 2.26 wt.%
S_i: 1073 ppm
P_i: 114 MPa

Decompression rate (MPa/s): 0.57
Time (s): 197 (~3 minutes)
Ascent velocity (m/s): 21.93

k)

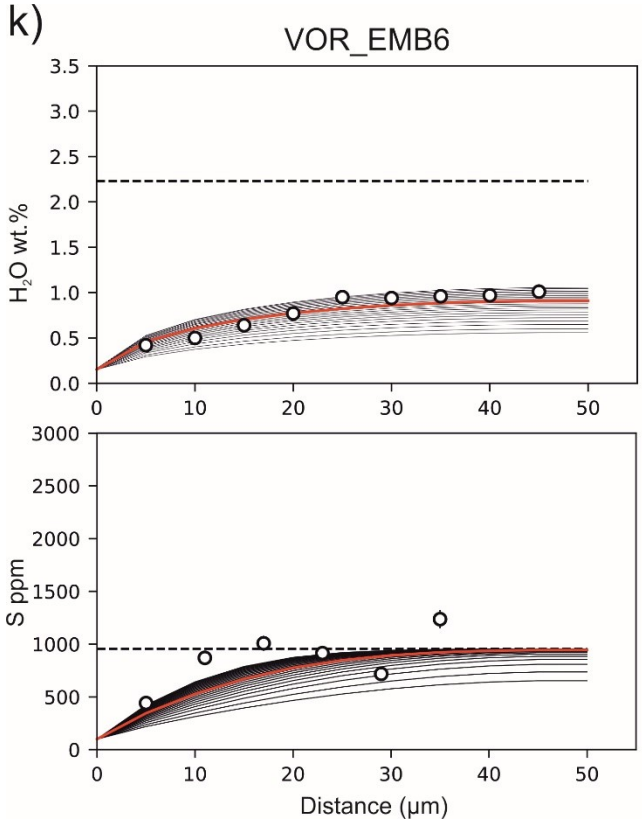

H_2O_i: 2.23 wt.%
S_i: 956 ppm
P_i: 110 MPa

Decompression rate (MPa/s): 0.48
Time (s): 227 (~4 minutes)
Ascent velocity (m/s): 18.46

l)

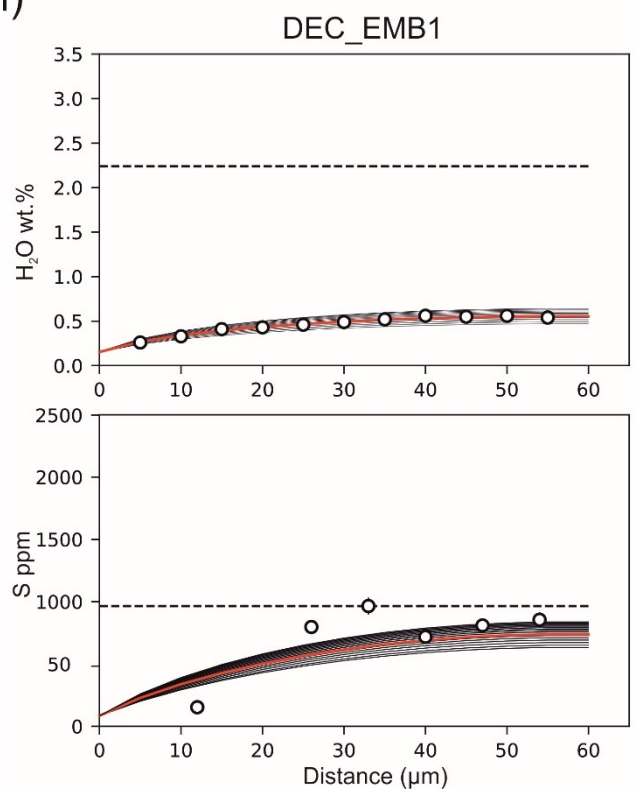

H_2O_i: 2.23 wt.%
S_i: 965 ppm
P_i: 110 MPa

Decompression rate (MPa/s): 0.055
Time (s): 1981 (~33 minutes)
Ascent velocity (m/s): 2.11

m)

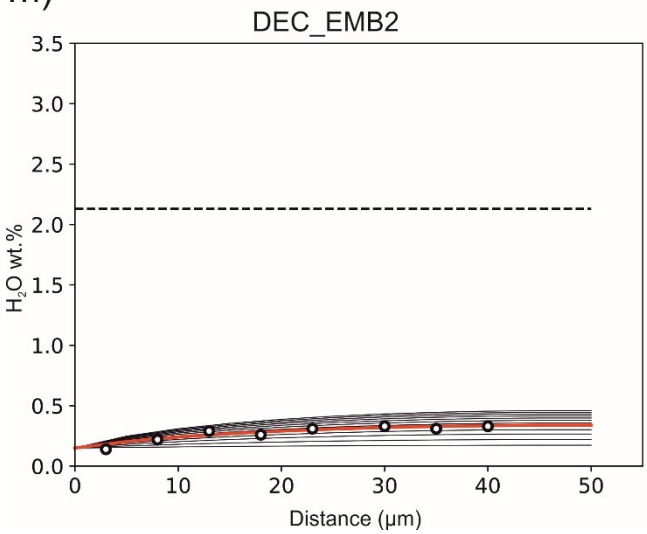

H_2O_i: 2.13 wt.%
P_i: 99 MPa

Decompression rate (MPa/s): 0.017
Time (s): 5765 (~96 minutes)
Ascent velocity (m/s): 0.65

n)

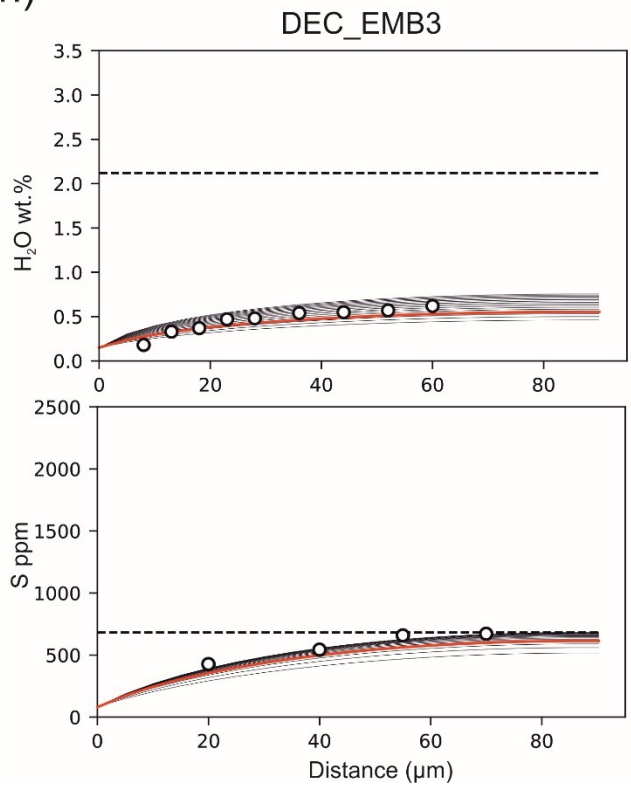

H_2O_i: 2.12 wt.%
S_i: 671 ppm
P_i: 97 MPa

Decompression rate (MPa/s): 0.024
Time (s): 3999 (~67 minutes)
Ascent velocity (m/s): 0.92

o)

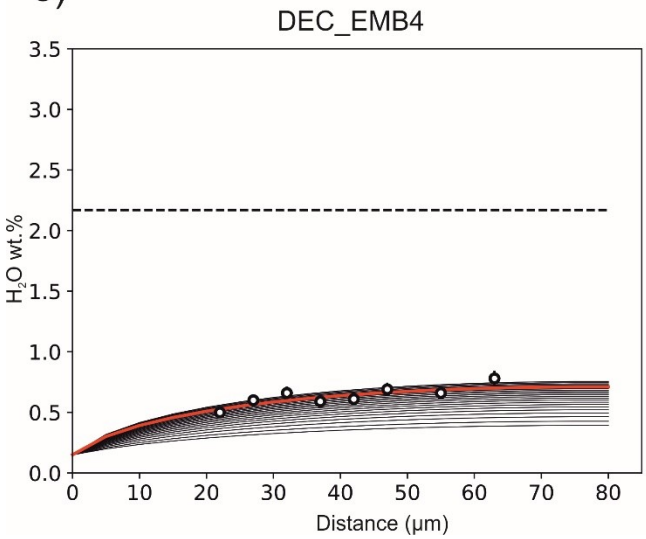

H_2O_i: 2.17 wt.%
P_i: 103 MPa

Decompression rate (MPa/s): 0.075
Time (s): 1360 (~23 minutes)
Ascent velocity (m/s): 2.86

Figure 49: *Results from volatile diffusion modeling along melt-embayments found in the selected eruptions from the post-2011 activity at Mt. Etna. S diffusion is modeled for samples displaying more regular decrease of S toward the open side. Red line represents the best fit model corresponding to the estimated dP/dt by χ^2 minimization, starting from fixed initial P_i and H_2O_i (black dashed line; T_i = 1080°C for each model); black thin lines represent each simulation for different dP/dt values defined in the range used for minimizing χ^2 at same fixed conditions (**Table A7**).*

8. VOLCANOLOGICAL IMPLICATIONS FROM DIFFUSION MODELING

8.1. Syn-eruptive ascent vs. degassing in determining magma dehydration

Thermodynamic and degassing models provided insights on the evolution of the two types of MIs analyzed from the selected eruptions of the post-2011 activity. Extensive crystallization of olivine and clinopyroxene may be induced by degassing coupled with CO_2-flushing processes, occurring throughout a vertical column at pressure lower than 200 MPa. Here, basic melts, entrapped as type 1 MIs in Fo_{80-85} olivine, differentiate to more evolved compositions, recorded in type 2 MIs and hosted in less Fo olivine (< Fo_{78}). Compositional variations from core (~Fo_{80-85}) to rim (~Fo_{79-77}) observed in normally zoned olivines, which are the more common analyzed in this study, reflect changing compositions of the surrounding melts in equilibrium with olivine rims, in agreement with evolution of MIs entrapped during crystal growing. This portion of the plumbing system is considered the region of neutral buoyancy for Mt. Etna (Corsaro and Pompilio, 2004), where continuous magma replenishment is responsible for the ground deformation sources modeled for the various eruptive period of the post-2011 activity (Cannata et al., 2015, 2018; Viccaro et al., 2016, 2019). As advanced by Plank et al. (2013) for mafic magma erupted in arc volcanic systems, such portion of the plumbing system may work as a "filter", where H_2O-rich magmas coming from depth reach the H_2O saturation, generally estimated at 4 wt.% at 200 MPa, and start to lose H_2O. The effect of flushing causes further dehydration, resulting in lower H_2O composition dissolved in the melts at 200 MPa (2-3.5 wt.%) for Etna magmas. Depletion of water from the melt causes re-equilibration of MIs already entrapped in high Fo olivine, whereas MIs enclosed in olivine with lower Fo during further ascent will record amounts of water lower than 2 wt.%.

The recalculation based on the model of Portnyagin et al. (2019) suggests that the pre-eruptive total volatile budget of Etna magmas inherited during their evolution in the deep

portions of the plumbing system is similar for the recent and past activity at Mt. Etna (e.g. 2001 and 2002-03 eruptions; Métrich et al., 2004; Spilliaert et al., 2016a). Different degassing conditions during magma storage in the upper part of the plumbing system and kinetics of transfer toward the surface determine the final volatile contents. Indeed, although the volatile evolution recorded in both type of MIs from the recent activity simulates a closed-system degassing, a substantial load of volatile can be lost during magma ascent. Prolonged magma storage at pressure lower than 200 MPa may enhance water loss from the melts, resulting in pre-eruptive H_2O content < 2.5 wt.%.

On the other hand, magma ascent leads to further magma dehydration. Slower magma ascent promotes efficiently the dehydration, as observed for the low-intensity flank eruption of December 24-27, 2018. Conversely, minor water loss observed in MIs found in products of the paroxysmal eruptions occurred in February 2013 and December 2015 may be related to fast magma transfer, enabling to retain part of the initial water content with consequent triggering of more explosive eruptions. This is well supported by calculation of magma ascent rates by modeling volatile diffusion along melt embayments. The modeling highlighted how different rates of ascent for magmas with similar physical and chemical conditions are linked to modifications of the final explosive intensity. The magma erupted during the flank eruption of December 24-27, 2018 was characterized probably by higher water load before the eruption, than the magma involved in paroxysmal episodes of the February 19, 2013 and December 3, 2015 as inferred by the recalculation of original H_2O before the loss, producing, however, a low energy explosive activity compared to the two lava fountains episodes because of slower magma ascent (~0.017-0.076 MPa/s). On the contrary, very high decompression rates have been obtained for the powerful lava fountaining occurred on December 3, 2015 (~0.33-0.57 MPa/s), which are greater of ~0.20 MPa/s than those estimated for the lava fountain of February 19, 2013 (~0.11-0.41 MPa/s).

8.2. Comparison with other ascent rates estimation

Results obtained by modeling of volatile diffusion in embayments are, on the whole, consistent with previously estimated rates for eruptions with comparable explosivity (e.g. Lloyd et al., 2014; Fergusson et al., 2016; Giuffrida et al., 2018). Ascent velocities estimated in this study for the intense eruptions of February 19, 2013 and December 3, 2015 at Mt Etna are within the range estimated by Li diffusion modeling on plagioclase (Giuffrida et al., 2018). Timescales of 10 – 183 s, corresponding to ascent rates of 4 – 64 m/s, were obtained for some lava fountaining episodes from the 2011-2013 paroxysmal series at NSEC. Higher rates estimated by Li modeling for some lava fountains than those calculated by volatile diffusion in embayment can be related to the different strategy for constraining the initial conditions and the different approach used in the calculation of the modeled gradients. Initial pressures for all the eruptive episodes investigated by Li diffusion were constrained at 40 MPa, corresponding to the inferred magma reservoir located under 1.5 – 2 km below the summit craters through seismic data (e.g. Patanè et al., 2013; Viccaro et al., 2016). Moreover, the modeled gradients were calculated through analytical solution using a one-dimensional model of diffusion in a semi-infinite solid, where final concentrations were fixed at constant values. Therefore, the progressive decreasing of the Li in the melt during the ascent at surface was not considered in the simulations, resulting in a faster diffusive relaxation of Li gradients.

Volatile modeling in embayments for estimation of ascent velocities of the sub-Plinian eruption occurred at Volcan de Fuego on 1974 (Llyod et al., 2014) and for Keanakakoi Layer 6 (c. 1650 CE; Ferguson et al., 2016) provided rates of 0.32 – 0.47 MPa/s and ~0.45 MPa/s respectively. These values are within the range estimated for the intense lava fountaining occurred at VOR on December 3, 2015 (0.34 – 0.57 MPa/s) (**Figure 49**). Despite slightly higher values have been calculated for the 2015 eruption at Mt. Etna than for the 1974 eruption at Volcan de Fuego, the greater explosive intensity of the Volcan De Fuego eruption can be due

to: i) higher melt polymerization than Etna melts, close to an andesitic composition (Llyod et al., 2014), resulting in an increase of magma viscosity; ii) higher initial H_2O contents dissolved in the magma before the ascent (~4.1-4.2 wt.%, Llyod et al., 2014) than those estimated for Mt. Etna (~2.5 wt.%), which may be responsible for a major overpressurization during the exsolution induced by the decompression.

Analogous results have been obtained also from experimental works focused on the relationship between magma fragmentation and rapid groundmass crystallization in highly explosive basaltic eruptions (e.g., Arzilli et al., 2019). This study demonstrated how strong undercooling at fast decompression rates leads to formation of skeletal plagioclase with swallow-tailed textures as microcrystal in the groundmass. Rapid crystallization causes in turn an increase of viscosity of about one order of magnitude. Such dramatic variations in viscosity is observed in a range of decompression rates between 5 and 50 m/s, comparable with rates obtained by modeling volatile diffusion in embayments for the selected paroxysmal episodes of the February 2013 and December 2015 activities investigated in this study (respectively ~9.6 and ~17.9 m/s).

On the contrary, calculation of ascent rates on Mt. Etna from a combination of clinopyroxene-liquid thermobarometers and crystal size distribution theory (Armienti et al., 2013), provided very low values, on the order of 10 mh^{-1}. However, these rates are correlated for magma ascending in the deeper part of the plumbing system (> 6 km) and may represent a measure of magma supply in reservoirs located in deep zones of the plumbing system, perhaps independent from the shallowest dynamics (Armienti et al., 2013).

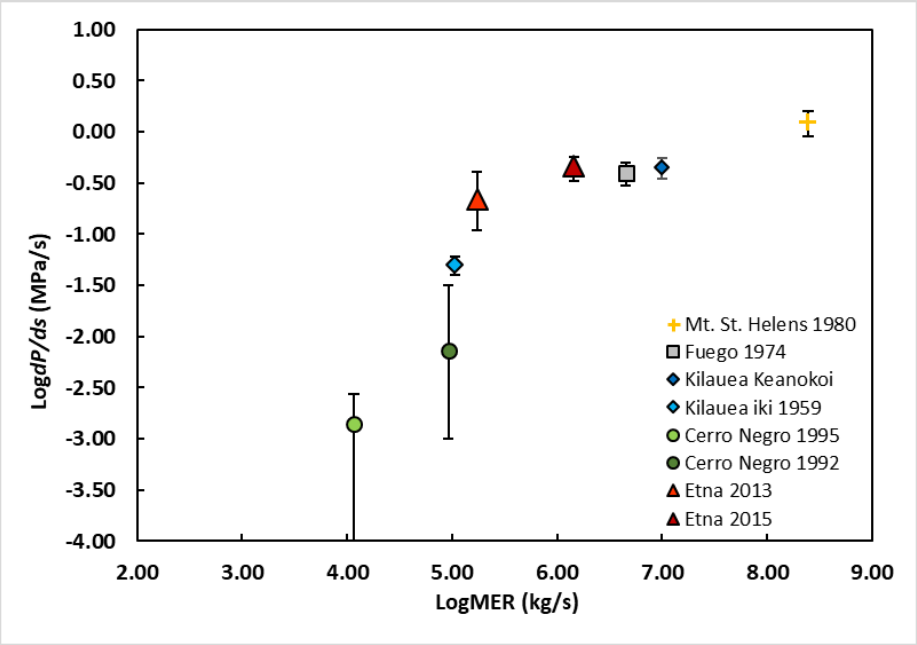

Figure 50: *Diagram showing decompression rates vs. MER (in Log) calculated for lava fountaininig episodes (NSEC 2013 and VOR 2015) investigated in this study (for the December 2018 eruption there are no data about MER) and for other eruptions with variable explosivity in other volcanoes. Data are from: Humphreys et al.,2008 (Mt. St. Helens); Llyod et al., 2014 (Fuego); Richter et al., 1970; Ferguson et al., 2016 (Kilauea Iki, Kilauea Keanokoi); Pioli et al., 2009; Barth et al., 2019 (Cerro Negro).*

8.3. Cross-check with monitoring data

Depths assumed for the beginning of magma ascent are between the shallowest reservoir located 1-2 km below the summit craters and the pressurizing source estimated by ground deformation data at 4-7 km bls (Cannata et al., 2018; Borzì et al., 2020). Specifically, estimated depths are in the range of 84-110 MPa (~0.2 km asl – 0.9 km bsl) and 112-120 MPa (~0.9–1.2 km bsl) respectively for the February 19, 2013 and December 3, 2015 eruptions. These are consistent with source depths estimated by strainmeters data, which recorded negative strain changes of the summit area during the lava fountaining episodes caused by sources located at 0 and 1.5 km bsl, respectively, for the paroxysmal series occurred at NSEC during the 2011-2013 activity (Bonaccorso et al., 2013) and for the paroxysmal activity at VOR on 3-5 December 2015 (Bonaccorso and Calvari, 2017). A slightly deeper overpressurization of the

source feeding lava fountains occurred at VOR during December 2015 may constitute the driving force for the higher decompression rates estimated for this eruption than for the eruptive episode of February 19, 2013. These results agree with estimation of the Mass Eruption Rates (MER) obtained by remote sensing techniques (Freret-Lorgeril et al., 2018). Average values of 1.45×10^6 kg/s and 1.72×10^5 kg/s (**Figure 50**) have been obtained respectively for the VOR 2015 and NSEC 2013 eruptions by using a Doppler Radar. The higher MER of the VOR 2015 eruption can be related to slightly higher conduit radius than the NSEC 2013 eruptive episodes, where values of ~3 m and ~1 m have been respectively calculated by taking into account the conservation of mass, expressed as $Q = \rho u A$ (Barth et al., 2019), where Q is the Mass Eruptive Rates (kg/s), ρ is the density of the multiphase fluid composed by magma and gas, u is the ascent velocity (m/s) and A is the the cross-sectional conduit area (m^2). Higher conduit radius may allow more efficient syn-eruptive degassing leading in turn to increase of the MER and decompression rate.

Timescales provided by diffusion modeling are representative of the total duration of the ascent from the moment when each olivine crystal hosting melt embayments has been incorporated into the ascending multiphase flow throughout the conduit at depths inferred by degassing models. The longer time estimated for the VOR_emb2 could be related to a portion of the magma ascending during the increasing of the Strombolian activity before the paroxysmal phase at lower velocity and incorporated then in the lava fountaining. Such observation is consistent with the timing detected through an approach based on infrasound data for the December 3, 2015 paroxysmal episode (Ripepe et al. 2018). Indeed, an early warning signal was detected about 30 minutes before the onset of the paroxysmal phase, comparable with the total duration of ascent recorded by the VOR_emb2 sample (~42 minutes). Alternatively, the olivine crystal could have been incorporated in the portion of the multiphase flow at contact with the wall, characterized by lower velocities due to the friction. As well as,

the longer timescales of total ascent calculated for the flank eruption for the December 24-27, 2018 are consistent with timing of the seismic sequence on the flank of the volcano, started a couple of hours before the opening of the fracture at base of the NSEC (Alparone et al., 2020).

8.4. The role of the syn-eruptive ascent in the eruptive dynamics

Two main models describing dynamics of explosive eruptions in basaltic systems exist in literature (e.g. Parfitt, 2004): 1) the rise speed dependent (RSD) model and 2) the collapsing foam (CF) model (**Figure 51**).

The RSD model assumes homogeneous two-phase flow composed by magma and gas. This two-phase flow may result in a single fluid phase behavior when rise speed of gas bubble is the same of the rise speed of the magma. Nucleation and growth of bubbles occurs through diffusion of volatile induced by decompression during magma uprising and fragmentation occurs when a large bubble volume fraction (60–95%) is reached. The jet of the mixture made by gas and magma may accelerate after fragmentation due to reduction of the wall friction, resulting in a continuous flow when reaches the vent at surface, typical of Hawaiian lava fountain. This mechanism is proposed to describe also Plinian eruptions, with the difference that erupted material is very fine compared to coarser products which generally are emitted during Hawaiian lava fountain (Parfitt, 2004). On the contrary, a higher speed rise of bubbles with respect to the melt within the conduit allows coalescence and segregation of the gas bubble, resulting in Strombolian explosions.

In the CF model, proposed for the first time by Vergniolle and Jaupart (1986), melt and gas are considered two separated phases, not constituting a homogenous flow as described in the RSD model. In this model, gas bubbles are assumed to move independently from the magmatic column and accumulate at the top of the storage area. Accumulation of the bubbles

leads to formation of a foam layer. When such foam layer becomes unstable, it collapses and gas bubbles coalesce forming a gas pocket rising to the vent (Parfitt, 2004). Discrete events of collapsing foam lead to Strombolian activity, whereas an instantaneous foam collapse generates lava fountaining activity. The CF model implies that the gas phase is already exsolved at depth and accumulates at shallow levels.

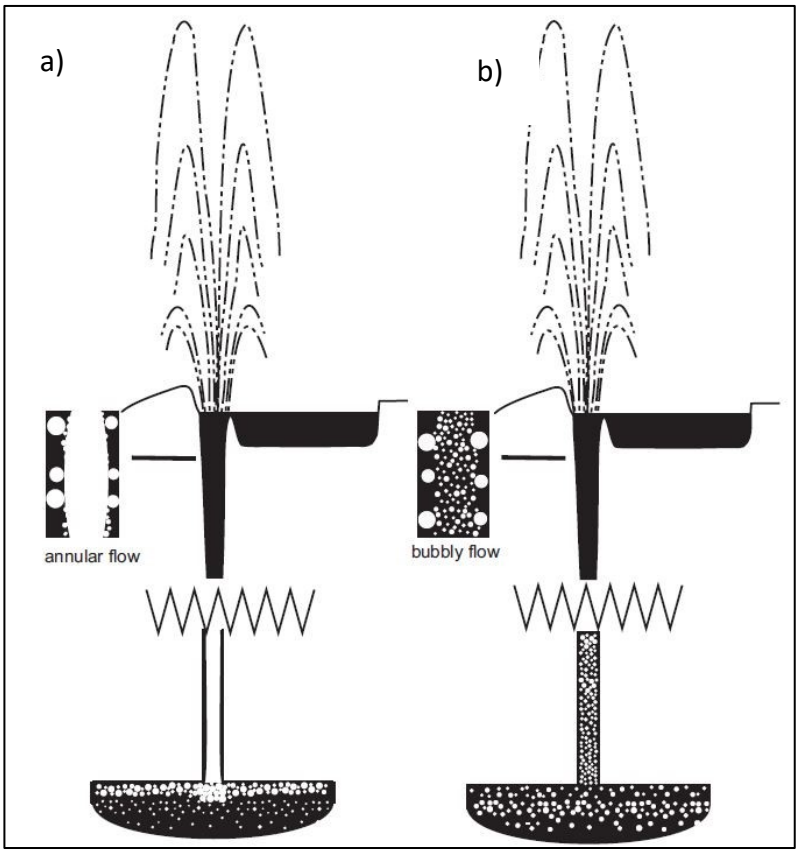

Figure 51: *Cartoon showing a representation of **a)** collapsing foam model and **b)** rise speed dependent model (from Houghton and Goonermann, 2008).*

Geochemical and geophysical studies focused on the past paroxysmal activity at Mt. Etna revealed that CF model is more appropriate in the generation of explosive activity (e.g. Alparone et al., 2003; Privitera et al., 2003; Allard et al., 2003, 2005). Interesting results have been obtained from a spectroscopic investigation on the gas plume during a lava fountaining episode from the paroxysmal series at SEC during 1999-2000 (Allard et al., 2005). Measurements of gas compositions during the sustained lava fountaining phase highlighted the

presence of a separated gas phase, characterized by higher CO_2/S and S/Cl than the normal emission during quiet activity which could not be produced by the syn-eruptive degassing. These authors inferred that such gas layer was accumulated at depth of 1.5 km below the summit, causing overpressurization of the degassed and partly crystallized magma body residing in the shallowest storage area.

However, results obtained by volatile diffusion modeling in embayments point out an important contribution from syn-eruptive degassing and its kinetics in determining the intensity of explosive activity. These inferences are consistent with observation of the nature of tephra erupted during the selected post-2011 eruptions, as well from past paroxysmal activity (Polacci et al., 2006). In fact, the occurrence of syn-eruptive degassing is testified by the presence of high vesiculated and microlites-poor sideromelane clasts emitted during the February 19, 2013 and December 3, 2015 paroxysmal episodes. In particular, tephra from the most intense lava fountaining of 3 December 2015 are characterized by spongy-shaped sideromelane clasts with a high density number of small vesicles, which means high nucleation rates induced by fast magma decompression rate. Furthermore, the less evolved compositional features of sideromelane clasts (Polacci et al., 2006) indicate the involvement of more basic and undegassed magma intruded in the shallowest reservoir occupied by the residual and degassed magma, represented by tachylite clasts. In this regard, geophysical data showed a deepening of volcanic tremor sources during the climax of paroxysmal episodes, likely related to the activation of deeper levels of the plumbing system (Alparone et al., 2003). Such observation is concordant with results obtained by measurements of the SO_2 flux during the paroxysmal episodes occurred at VOR on 3-5 December 2015 (D'Aleo et al., 2019). A total amount of 21000 ± 2730 tons of SO_2 injected into the atmosphere has been estimated, which is inferred to be generated by a magma volume of ∼1.9 ± 0.3 Mm^3, much smaller than the 5.1–12 Mm^3 erupted volume. D'Aleo et al. (2019) proposed that a small fraction of undegassed magma were

emplaced in the shallowest reservoir during the paroxysmal episodes, while most of the erupted magma underwent extensive degassing during the previous weeks, consistent with the relative high abundance of tachylite clasts in products emitted during the December 3, 2015 eruption (Pompilio et al., 2017).

Therefore, depressurization of the shallowest reservoir located at ~30 MPa during the pre-paroxysmal phases may induce ascent of deeper and less degassed magma, residing in the portion of plumbing system comprises between the two reservoirs located at 30 MPa and 150-200 MPa. As advanced by Polacci et al. (2006), a combination of the two distinct styles of degassing determines the dynamics of explosive activity at basic and open-system volcanoes. In this regard, the syn-eruptive nucleation and growth of bubbles in the melt play an important role during the peak of lava fountaining, enabling a more efficient magma fragmentation. Since the rates of bubble nucleation and growth are controlled by the magnitude of decompression, faster kinetics of magma ascent strongly control the magma fragmentation and the final intensity of the explosive style, as inferred from volatile diffusion modeling in embayments.

9. CONCLUDING REMARKS

The present study investigated the role of magma ascent rates in determining the explosive intensity in open conduit volcanoes, where basaltic magmas are involved. In this regard, Mt. Etna has been selected as case study, offering the possibility of examining a wide spectrum of eruptive styles, from Strombolian activity during a lateral eruption up to intense paroxysmal activity. Selected eruptive episodes with different explosivity from the recent post-2011 activity allowed to get insights into kinetics of magma ascent, evaluating if differences in ascent rates influence the eruptive styles considering similar physical and chemical conditions of the plumbing system and magmas involved. The approach used for determining magma ascent rates is based on volatile diffusion in olivine-hosted melt embayments. Fixing initial conditions for running the diffusion model requires a preliminary study on olivine-hosted melt inclusions. Indeed, examination of melt inclusions is necessary for quantifying the potential magma volatile budget immediately before the eruption. Melt inclusion data revealed that a substantial load of water is lost from the melt. Water loss can be induced by degassing, coupled to CO_2 flushing during storage at shallow levels of the plumbing system, at pressure below than 200 MPa (~6-7 km bsl), determining thus a lower final pre-eruptive water load (< 2.5 wt%) than the inferred initial budget (~ 4.0 wt.%). Volatile loss can be also induced by syn-eruptive decompression within the conduit during magma ascent toward the surface. Restoration of original volatile contents is crucial for constraining reliable parameters used for running diffusion simulations.

Results from volatile diffusion modeling demonstrated how the different explosivity of eruptions fed by magma with similar physical and chemical conditions is positively correlated with ascent rates. Small differences in estimated decompression rates between the December 3, 2015 and February 19, 2013 eruptions, in the order of 0.20 – 0.30 MPa/s, reflect a major

explosivity observed for the paroxysmal event occurred at Voragine Crater on December 2015. Conversely, decompression rates estimated for the low-energy flank eruption occurred on Christmas 2018 (0.017 – 0.075 MPa/s) are characterized by one order of magnitude smaller than intense lava fountaining activities (0.11 – 0.57 MPa/s). Results also support the prominent contribution of syn-eruptive degassing of the residual volatile dissolved in the melt, in addition to accumulation of the gas phase coming from depth causing overpressure of the shallow reservoir. This study demonstrates how magma ascent rates play a key role in determining the final explosivity at Mt. Etna. Very short timescales of ascent, on the order of 3 to 15 minutes, are peculiar of the intense lava fountaining during the episodes of February 19, 2013 and 3 December 2015.

Finally, as stated in some experimental works this study highlights the importance of evaluating possible processes affecting the original compositions of MIs. Particular attention must be payed to the role of water loss in MIs for a proper interpretation and reconstruction of the original magma water contents and degassing processes during the ascent.

APPENDICES

Table A1: Measured major and volatile elements in melt inclusions found in products erupted during February 19, 2013, December 3, 2015 and December 24-27, 2018 eruptions at Mt. Etna.

Table A2: Measured major and volatile elements in melt inclusions found in products erupted during February 19, 2013, December 3, 2015 and December 24-27, 2018 eruptions at Mt. Etna corrected for PEC and original CO_2 content by estimating the amount of CO_2 in shrinkage bubbles.

Table A3: Major and volatile elements of melt inclusions found in products erupted during February 19, 2013, December 3, 2015 and December 24-27, 2018 eruptions at Mt. Etna corrected for H_2O-SiO_2 loss and PEC.

Table A4: Trace elements compositions (ppm) of melt inclusions found in products erupted during February 19, 2013, December 3, 2015 and December 24-27, 2018 eruptions at Mt. Etna.

Table A5: Major elements, S and Cl compositions measured along melt-embayments from products erupted during February 19, 2013, December 3, 2015 and December 24-27, 2018 eruptions at Mt. Etna.

Table A6: H_2O compositions measured by Raman spectroscopy along olivine-hosted melt embayments found in products erupted during February 19, 2013, December 3, 2015 and December 24-27, 2018 eruptions at Mt. Etna.

Figure S1: example of external calibration lines used for H_2O quantification by Raman spectroscopy in olivine hosted-melt embayments from VOR 2015 products.

Table A7: whole rock compositions used for H_2O-SiO_2 loss correction on melt inclusions found in products erupted during February 19, 2013, December 3, 2015 and December 24-27, 2018 eruptions at Mt. Etna.

Table A8: Results from volatile diffusion modeling along melt-embayments

Table A1: Measured major and volatile elements in melt inclusions found in products erupted from post-2011 activity at Mt. Etna

	NSEC 2013 type 1 MI										
Sample	NSECG13MI11	NSECG18MI16	NSECG20MI18	NSECG22MI20	NSECG24MI22	NSECG25MI23	NSECG29MI27	NSECG32MI30	NSECG41MI42	NSECG26MI24	NSECG44MI47
SiO_2 wt%	44.3	43.1	42.9	42.9	45.34	44.2	43.9	42.7	44.3	45.7	44.9
TiO_2 wt%	1.85	2.58	1.88	1.86	1.54	1.91	2.00	2.09	1.98	1.89	1.82
Al_2O_3 wt%	18.7	19.2	19.0	18.2	18.16	17.9	18.6	18.7	18.4	18.9	17.8
FeOt wt%	11.0	9.28	10.5	10.9	10.49	9.78	9.34	10.1	9.38	9.99	9.99
MnO wt%	0.23	0.15	0.17	0.16	0.17	0.13	0.11	0.15	0.15	0.21	0.19
MgO wt%	4.27	2.93	4.47	4.71	4.35	4.18	4.64	4.44	4.30	4.53	4.44
CaO wt%	10.6	11.3	11.5	11.7	11.02	12.0	11.7	11.7	12.4	10.7	11.8
Na_2O wt%	3.85	4.42	3.82	3.57	3.87	3.85	3.82	3.76	3.59	3.62	3.42
K_2O wt%	1.89	2.16	1.91	1.94	1.98	1.88	2.01	2.05	2.36	1.98	2.17
P_2O_5 wt%	0.64	1.08	0.68	0.52	0.63	0.65	0.59	0.58	0.61	0.57	0.70
Total	97.3	96.2	96.9	96.5	97.6	96.5	96.8	96.2	97.5	98.1	97.2
H_2O wt% Raman	1.55	1.80	1.51			1.91		1.24	1.66	1.54	
H_2O wt% FTIR				1.56	1.32	1.62	1.25		1.65		1.72
CO_2 ppm						141	137		384		156
Cl ppm	1291	1331	1442	1205	1107	1372	1390	1395	1861	1588	1668
S ppm	1567	2923	1730	2408	1766	1822	1884	2389	3064	2236	2668
F ppm									1152	852	1008
Mg#[a]	44.95	39.82	47.08	47.59	46.50	47.25	51.01	47.95	48.97	48.74	48.25
Fo% host ol	80.85	81.96	81.70	81.86	77.71	82.98	84.25	81.87	80.86	79.53	78.74

	NSEC 2013 type 1 MI				NSEC 2013 type 2 MI						
Sample	NSECG28MI26	NSECG42MI43	NSECG17MI15	NSECG21MI19	NSECG7MI33	NSECG27MI25	NSECG40MI41	NSECG43MI43	NSECG45MI49	NSECG47MI51	NSECG11MI9
SiO_2 wt%	45.2	44.6	44.4	44.2	47.5	46.0	51.1	51.6	47.2	48.7	48.0
TiO_2 wt%	1.87	1.94	1.83	1.71	1.71	1.92	1.14	1.10	1.81	1.86	1.86
Al_2O_3 wt%	18.7	18.3	18.7	17.3	17.4	17.7	15.3	16.6	17.5	17.8	17.2
FeOt wt%	9.63	9.15	9.87	10.12	9.42	10.4	11.4	10.2	10.0	8.59	9.30
MnO wt%	0.21	0.20	0.25	0.18	0.18	0.24	0.20	0.24	0.21	0.11	0.17
MgO wt%	4.29	4.48	4.26	4.07	3.62	3.74	3.40	3.20	3.61	3.29	3.55
CaO wt%	11.2	11.5	11.2	11.4	8.54	8.78	7.12	6.81	9.14	8.05	8.31
Na_2O wt%	3.67	3.44	3.64	3.25	4.66	5.15	5.13	5.06	3.99	5.01	4.62
K_2O wt%	2.14	2.09	2.00	2.20	2.50	2.64	2.14	2.81	2.36	2.97	2.70
P_2O_5 wt%	0.65	0.59	0.66	0.62	0.80	0.74	0.78	0.83	0.82	0.79	0.88
Total	97.5	96.3	96.9	95.1	96.3	97.3	97.66	98.4	96.6	97.1	96.6
H_2O wt% Raman	1.38	1.41	1.18		1.71	0.61		1.38	1.57	0.93	1.38
H_2O wt% FTIR	1.72	1.34		1.42			1.27		1.52		1.39
CO_2 ppm	112	69		136			168		169		48
Cl ppm	1639	1641	1649	1694	1510	1258	2936	1863	1736	1664	1730
S ppm	2037	2041	2583	2565	917	1099	1637	768	1445	980	887
F ppm	874	843	832	1067			1111	1500	1178	1546	970
Mg#[a]	48.28	50.67	47.51	45.62	44.61	43.05	38.53	39.72	43.04	44.53	44.48
Fo% host ol	79.35	79.47	79.21	78.31	79.90	78.71	68.73	69.73	75.19	76.19	76.02

	NSEC 2013 type 2 MI		VOR 2015 type 1 MI								
Sample	NSECG31MI29	NSECG13MI120	VORG12MI9	VORG16MI13	VORG18MI15	VORG18MI16	VORG18MI17	VORG19MI18	VORG24MI23	VORG13MI100	VORG10MI7
SiO_2 wt%	49.3	46.4	44.3	44.3	45.1	44.7	44.3	43.7	44.0	44.9	45.3
TiO_2 wt%	1.55	1.68	1.69	2.00	1.80	1.67	1.76	2.17	2.05	1.97	1.70
Al_2O_3 wt%	16.6	17.9	18.3	18.0	18.5	17.8	17.5	19.6	17.8	18.4	18.6
FeOt wt%	10.3	9.41	9.74	9.84	9.54	10.5	10.3	9.42	9.31	9.31	9.24
MnO wt%	0.19	0.19	0.22	0.13	0.15	0.13	0.19	0.17	0.13	0.20	0.13
MgO wt%	3.45	3.84	4.56	4.29	4.29	4.25	4.49	2.50	3.97	4.30	4.22
CaO wt%	6.99	8.83	11.2	11.6	10.9	10.8	11.8	12.3	12.8	11.5	11.1
Na_2O wt%	5.29	4.23	3.72	3.80	3.87	3.68	3.69	3.63	3.31	3.62	3.56
K_2O wt%	2.48	2.39	2.05	1.90	1.94	1.81	2.00	2.14	2.16	2.01	1.99
P_2O_5 wt%	0.92	0.73	0.64	0.65	0.70	0.58	0.69	0.64	0.57	0.61	0.68
Total	97.01	95.6	96.3	96.5	96.75	95.9	96.7	96.3	96.0	96.8	96.5
H_2O wt% Raman	0.98	1.62	1.72	2.02	1.74	1.73	1.93	2.03	2.01	1.71	
H_2O wt% FTIR									2.04	2.42	1.47
CO_2 ppm		104							459	532	460
Cl ppm	2666	1858	1987	1120	1197	1071	1146	1002	2118	1861	1489
S ppm	966	1537	2077	1818	1401	1766	2111	1562	3187	2848	2576
F ppm		1066							905	904	1130
Mg#[a]	41.27	46.07	49.53	47.75	48.52	45.97	47.84	35.74	47.23	49.17	48.92
Fo% host ol	76.57	76.90	81.25	82.00	81.52	79.87	81.52	82.22	77.28	79.67	79.18

	VOR 2015 type 1 MI							VOR 2015 type 2 MI			
Sample	VORG14MI11	VORG8MI6	VORG31MI31	VORG25MI24	VORG10MI70	VORG22MI21	VORG22MI210	VORG9MI6	VORG20MI19	VORG23MI22	VORG32MI32
SiO_2 wt%	44.7	44.7	43.4	44.9	44.6	45.0	44.4	50.1	46.7	47.0	51.0
TiO_2 wt%	1.97	1.85	1.99	1.89	1.66	1.97	1.83	1.90	1.83	1.88	1.79
Al_2O_3 wt%	17.8	18.3	18.0	18.8	18.5	19.2	18.7	17.5	17.9	17.3	15.7
FeOt wt%	8.87	10.1	9.62	10.2	9.42	9.85	9.87	8.93	10.5	10.5	10.0
MnO wt%	0.12	0.10	0.17	0.29	0.11	0.18	0.25	0.20	0.27	0.22	0.32
MgO wt%	4.67	4.48	3.93	4.54	4.30	4.13	4.26	3.14	3.41	3.76	3.31
CaO wt%	12.3	10.9	12.6	10.4	10.8	11.6	11.3	6.70	9.74	9.46	7.11
Na_2O wt%	3.49	3.62	3.39	3.67	3.41	3.61	3.64	5.02	4.80	5.00	5.11
K_2O wt%	2.12	1.97	2.08	1.98	1.93	1.93	2.00	3.25	2.40	2.42	2.36
P_2O_5 wt%	0.58	0.62	0.61	0.58	0.59	0.62	0.66	0.90	0.74	0.69	0.96
Total	96.6	96.7	95.7	97.3	95.3	98.1	96.9	97.6	98.3	98.2	97.7
H_2O wt% Raman	2.24	1.92	1.62	1.72	1.25	0.76		1.54	0.85	0.97	
H_2O wt% FTIR	1.54		2.33	1.78	1.46		1.36				1.42
CO_2 ppm	920		692	511	179	376	231				232
Cl ppm	1987	1726	2048	1736	1720	1612	1913	1439	1454	1437	3571
S ppm	3134	2297	3097	1445	2510	2567	2774	275	760	1185	1221
F ppm	945	864	1077	1178	711	766	1012				1228
Mg#[a]	52.44	48.13	46.14	48.34	48.90	46.78	47.51	42.43	40.48	42.95	40.74
Fo% host ol	81.26	78.93	80.83	78.31	79.03	80.12	80.29	79.25	80.02	80.68	75.40

	VOR 2015 type 2 MI				DEC 2018 type 1 MI						
Sample	VORG26MI25	VORG6MI2	VORG7MI4	VORG7MI3	DECG4MI1	DECG8MI5	DECG13MI11	DECG14MI12	DECG15MI13	DECG20M18	DECG22MI20
SiO_2 wt%	48.4	45.4	49.1	48.4	44.4	44.4	42.5	42.8	43.3	42.9	42.3
TiO_2 wt%	1.86	1.47	1.68	1.71	1.56	1.80	1.81	2.03	1.98	1.90	2.04
Al_2O_3 wt%	17.5	17.1	17.1	17.1	18.3	18.5	17.2	18.3	17.8	17.6	19.4
FeOt wt%	9.51	10.3	9.02	9.80	9.66	10.6	10.1	10.9	9.68	9.77	9.81
MnO wt%	0.32	0.15	0.20	0.23	0.17	0.12	0.12	0.26	0.11	0.19	0.13
MgO wt%	3.80	3.97	3.55	3.75	4.51	4.07	5.19	4.38	3.79	4.26	4.35
CaO wt%	8.89	10.99	7.55	7.90	12.2	10.2	12.1	9.78	12.4	12.9	12.8
Na_2O wt%	4.44	3.42	4.74	4.54	4.43	4.34	3.75	4.14	3.87	3.76	3.63
K_2O wt%	2.38	2.16	2.26	2.08	2.35	2.08	2.07	1.99	2.19	2.09	2.38
P_2O_5 wt%	0.80	0.60	0.94	1.16	0.75	0.62	0.58	0.57	0.63	0.65	0.75
Total	97.9	95.5	96.1	96.6	98.2	96.7	95.4	95.2	95.8	96.0	97.6
H_2O wt% Raman	1.56	1.82	1.55		0.30	1.22	2.14	1.50	1.82	1.77	0.51
H_2O wt% FTIR	1.53	1.80	1.75	1.25	0.64						
CO_2 ppm	99	534	86		515						
Cl ppm	1557	1847	1516	1515	1473	1232	1181	1487	1275	1447	1364
S ppm	1295	2657	1542	1592	1716	1416	2407	1491	2333	1879	2046
F ppm	1086	1223	1147	1060							
Mg#[a]	45.58	45.56	45.23	44.55	50.27	45.44	52.76	46.50	45.88	48.56	50.22
Fo% host ol	73.41	73.99	75.76	75.76	81.68	80.25	83.50	78.94	84.25	83.06	84.70

	DEC 2018 type 1 MI			DEC 2018 type 2 MI							
Sample	DECG34MI34	DECG32MI32	DECG33MI33	DECG5MI2	DECG8MI6	DECG9MI7	DECG11MI9	DECG16M14	DECG17MI15	DECG21MI19	DECG10MI8
SiO_2 wt%	43.8	44.5	44.3	48.8	45.6	48.6	46.8	48.6	47.4	48.7	51.0
TiO_2 wt%	2.00	1.72	1.89	1.51	1.75	1.79	1.92	1.67	1.29	1.61	1.70
Al_2O_3 wt%	19.2	17.0	17.1	18.0	17.8	16.7	17.4	17.5	16.9	17.7	16.5
FeOt wt%	10.3	9.83	10.2	9.88	10.1	10.0	10.1	9.46	10.6	9.47	9.66
MnO wt%	0.31	0.11	0.09	0.19	0.18	0.20	0.15	0.16	0.27	0.18	0.18
MgO wt%	4.92	4.88	4.42	3.19	3.68	3.89	4.03	3.52	3.97	3.58	3.14
CaO wt%	11.5	10.8	11.4	7.37	9.44	8.64	6.79	7.54	8.51	7.25	7.31
Na_2O wt%	3.84	3.46	3.17	5.24	4.46	4.54	5.55	5.01	4.75	5.66	4.58
K_2O wt%	2.30	1.93	2.06	2.55	2.31	2.53	2.72	2.68	2.42	2.83	3.06
P_2O_5 wt%	0.62	0.62	0.59	0.96	0.79	0.86	1.09	0.84	0.67	0.86	0.99
Total	98.7	94.8	95.1	97.6	96.1	97.8	96.4	97.0	96.8	97.8	98.1
H_2O wt% Raman	2.78		1.03	0.87	1.38	1.62	1.16	1.76	1.64	1.49	
H_2O wt% FTIR	2.55	1.61	0.88								1.12
CO_2 ppm	413	321	358								230
Cl ppm	2005	1713	1691	1360	1365	1332	2471	1486	1446	1610	1501
S ppm	2672	1761	1848	1247	854	413	797	875	582	736	185
F ppm	1005	1098	896								1243
Mg#[a]	50.83	51.79	48.50	40.36	43.30	44.89	45.59	43.82	43.91	44.21	40.55
Fo% host ol	80.82	80.97	81.93	77.67	78.70	76.83	77.88	77.04	76.29	77.17	73.47

	DEC 2018 type 2 MI				
Sample	DECG31MI31	DECG42MI42	DECG43MI43	DECG44MI44	DECG35MI35
SiO_2 wt%	48.6	47.7	50.2	47.1	47.5
TiO_2 wt%	1.28	1.45	1.81	1.39	1.35
Al_2O_3 wt%	16.8	17.3	17.6	17.7	16.5
FeOt wt%	9.99	9.90	8.64	10.2	11.7
MnO wt%	0.26	0.24	0.19	0.26	0.33
MgO wt%	3.97	3.84	3.39	3.93	3.84
CaO wt%	8.77	8.53	6.90	9.70	9.01
Na_2O wt%	4.37	4.17	4.74	3.33	4.31
K_2O wt%	2.61	2.39	3.11	2.17	2.41
P_2O_5 wt%	0.68	0.58	1.11	0.51	0.62
Total	97.4	96.0	97.7	96.3	97.6
H_2O wt% Raman			1.38	1.34	
H_2O wt% FTIR	0.41	1.37	1.21	1.34	0.57
CO_2 ppm	211	320	268	240	
Cl ppm	1927	2002	2044	1932	2258
S ppm	768	875	446	1156	897
F ppm	1237	957	1055	1353	1215
Mg#[a]	45.44	44.83	45.15	44.63	40.77
Fo% host ol	73.75	73.97	74.12	74.89	72.60

[a] Mg# is calculated considering $Fe^{3+}/Fe^{2+} = 0.20$

Table A2: Major and volatile elements corrected for PEC and restored CO_2 in melt inclusions found in products erupted from post-2011 activity at Mt. Etna

	NSEC 2013 type 1 MI										
Sample	NSECG13MI11	NSECG18MI16	NSECG20MI18	NSECG22MI20	NSECG24MI22	NSECG25MI23	NSECG29MI27	NSECG32MI30	NSECG41MI42	NSECG26MI24	NSECG44MI47
SiO_2 wt%	44.6	43.3	43.4	43.6	45.7	44.4	44.1	43.4	44.1	45.3	45.1
TiO_2 wt%	1.78	2.35	1.81	1.82	1.53	1.78	1.84	2.01	1.85	1.79	1.78
Al_2O_3 wt%	18.0	17.5	18.2	17.8	18.1	16.7	17.1	18.0	17.2	17.9	17.5
FeOt wt%	11.0	11.0	11.0	10.9	10.5	10.9	10.9	11.0	11.1	11.0	10.5
MnO wt%	0.22	0.14	0.16	0.16	0.17	0.12	0.10	0.14	0.14	0.2	0.19
MgO wt%	6.45	6.63	6.65	6.68	5.14	7.27	7.90	6.66	6.38	6.11	5.46
CaO wt%	10.2	10.3	11.1	11.5	11.0	11.2	10.8	11.3	11.5	10.2	11.5
Na_2O wt%	3.71	4.03	3.67	3.49	3.85	3.59	3.52	3.62	3.35	3.43	3.35
K_2O wt%	1.82	1.97	1.84	1.90	1.97	1.75	1.85	1.98	2.20	1.88	2.13
P_2O_5 wt%	0.62	0.98	0.65	0.51	0.63	0.61	0.54	0.56	0.57	0.54	0.69
Total	98.4	98.2	98.4	98.3	98.5	98.3	98.7	98.7	98.3	98.4	98.2
H_2O wt%	1.49	1.64	1.45	1.53	1.31	1.51	1.15	1.19	1.54	1.46	1.68
CO_2 ppm						132	128		355		151
Cl ppm	1225	1181	1361	1149	1089	1289	1292	1309	1722	1502	1618
S ppm	1487	2593	1633	2297	1737	1712	1751	2241	2835	2115	2588
F ppm									1066	806	978
XCO_2						0.31	0.44		0.53		0.29
***P* sat. MPa**						38	27		61		47
CO_2 rest. ppm[a]						453	494		949		312
Mg#[b]	54.42	55.35	55.18	55.53	50.27	57.59	59.46	55.29	54.25	52.97	51.79
Fo% host ol	80.85	81.96	81.70	81.86	77.71	82.98	84.25	81.87	80.86	79.53	78.74
PEC %	5	11	6	5	2	9	10	6	7	5	3

	NSEC 2013 type 1 MI				NSEC 2013 type 2 MI						
Sample	NSECG28MI26	NSECG42MI43	NSECG17MI15	NSECG21MI19	NSECG7MI33	NSECG27MI25	NSECG40MI41	NSECG43MI43	NSECG45MI49	NSECG47MI51	NSECG11MI9
SiO_2 wt%	45.1	45.1	44.8	45.6	47.5	46.5	51.2	50.8	47.7	48.6	48.3
TiO_2 wt%	1.80	1.87	1.77	1.73	1.61	1.87	1.13	1.05	1.79	1.77	1.81
Al_2O_3 wt%	18.0	17.6	18.1	17.5	16.4	17.2	15.1	15.9	17.3	16.9	16.7
FeOt wt%	10.5	10.8	11.0	10.5	11.0	11.1	12.0	11.7	10.6	10.9	10.8
MnO wt%	0.20	0.19	0.24	0.18	0.17	0.23	0.20	0.23	0.21	0.11	0.17
MgO wt%	5.67	5.90	5.90	5.36	6.09	5.43	3.82	3.85	4.61	4.71	4.72
CaO wt%	10.8	11.1	10.9	11.5	8.03	8.54	7.05	6.53	9.03	7.66	8.07
Na_2O wt%	3.53	3.32	3.51	3.28	4.38	5.01	5.08	4.85	3.94	4.77	4.48
K_2O wt%	2.06	2.02	1.93	2.22	2.35	2.57	2.12	2.69	2.33	2.83	2.62
P_2O_5 wt%	0.63	0.57	0.64	0.63	0.75	0.72	0.77	0.80	0.81	0.75	0.85
Total	98.2	98.5	98.7	98.4	98.2	99.2	98.5	98.4	98.3	99.1	98.5
H_2O wt%	1.65	1.29	1.14	1.43	1.61	0.59	1.26	1.32	1.50	0.89	1.35
CO_2 ppm	107	65		132			165		164		46
Cl ppm	1566	1552	1562	1647	1390	1222	2884	1863	1685	1664	1651
S ppm	1945	1930	2445	2495	844	1067	1608	768	1403	980	847
F ppm	835	797	788	1038			1092	1500	1143	1546	926
XCO_2	0.24	0.24		0.34			0.55		0.46		no bubble
***P* sat. MPa**	41	25		36			38		46		-
CO_2 rest. ppm[a]	251	161		268			400		384		46
Mg#[b]	52.49	52.74	52.26	51.33	53.33	50.58	40.41	41.11	47.51	49.73	48.02
Fo% host ol	79.35	79.47	79.21	78.31	79.90	78.71	68.73	69.73	75.19	76.19	76.02
PEC %	5	5	5	3	8	5	2	4	3	6	5

	NSEC 2013 type 2 MI		VOR 2015 type 1 MI								
Sample	NSECG31MI29	NSECG13MI120	VORG12MI9	VORG16MI13	VORG18MI15	VORG18MI16	VORG18MI17	VORG19MI18	VORG24MI23	VORG13MI100	VORG10MI7
SiO_2 wt%	49.8	47.2	44.5	44.4	45.1	45.5	44.5	43.8	44.4	44.5	45.5
TiO_2 wt%	1.52	1.66	1.60	1.88	1.68	1.63	1.68	1.95	2.01	1.84	1.61
Al_2O_3 wt%	16.3	17.8	17.3	17.0	17.3	17.4	16.6	17.5	17.4	17.3	17.6
FeOt wt%	10.8	10.5	11.1	10.9	11.0	11.0	11.0	10.9	10.5	11.1	11.1
MnO wt%	0.19	0.19	0.21	0.12	0.14	0.13	0.18	0.15	0.13	0.19	0.12
MgO wt%	4.87	4.91	6.71	6.83	6.81	6.19	6.70	6.96	4.93	6.11	6.07
CaO wt%	6.86	8.74	10.6	10.9	10.2	10.5	11.2	11.0	12.5	10.7	10.5
Na_2O wt%	5.19	4.19	3.53	3.58	3.62	3.59	3.52	3.26	3.24	3.39	3.38
K_2O wt%	2.43	2.37	1.95	1.79	1.81	1.77	1.91	1.92	2.12	1.88	1.89
P_2O_5 wt%	0.90	0.72	0.61	0.61	0.65	0.57	0.66	0.57	0.56	0.57	0.65
Total	98.9	98.2	98.2	98.0	98.2	98.2	98.0	98.0	97.8	97.6	98.5
H_2O wt%	0.96	1.60	1.63	1.90	1.63	1.69	1.84	1.82	2.00	2.27	1.39
CO_2 ppm		100							442	495	428
Cl ppm	2565	1793	1849	1030	1100	1018	1075	870	2041	1731	1386
S ppm	930	1482	1932	1673	1288	1679	1980	1356	3072	2649	2397
F ppm		1028							872	841	1052
XCO_2		0.31							0.45	0.41	0.63
***P* sat. MPa**		41							88	106	62
CO_2 rest. ppm[a]		290							655	1165	1067
Mg#[b]	48.51	49.21	55.11	56.12	55.69	53.44	55.50	56.38	49.63	53.01	52.63
Fo% host ol	76.57	76.90	81.25	82.00	81.52	79.87	81.52	82.22	77.28	79.67	79.18
PEC %	4	4	7	8	8	5	6	13	4	7	7

	VOR 2015 type 1 MI							VOR 2015 type 2 MI			
Sample	VORG14MI11	VORG8MI6	VORG31MI31	VORG25MI24	VORG10MI70	VORG22MI21	VORG22MI210	VORG9MI6	VORG20MI19	VORG23MI22	VORG32MI32
SiO_2 wt%	44.4	44.9	43.7	45.2	45.5	44.9	44.7	49.1	46.5	46.8	50.8
TiO_2 wt%	1.84	1.79	1.88	1.86	1.61	1.86	1.75	1.73	1.72	1.78	1.73
Al_2O_3 wt%	16.6	17.7	17.0	18.6	18.0	18.2	17.9	15.9	16.8	16.4	15.1
FeOt wt%	11.0	11.1	11.0	10.5	11.0	11.0	11.0	11.1	11.1	11.0	10.8
MnO wt%	0.11	0.10	0.16	0.29	0.11	0.17	0.24	0.18	0.25	0.21	0.31
MgO wt%	6.61	5.87	6.37	5.34	5.99	6.22	6.27	5.89	6.05	6.18	4.67
CaO wt%	11.4	10.5	11.8	10.2	10.5	11.0	10.7	6.10	9.15	8.94	6.87
Na_2O wt%	3.25	3.50	3.20	3.62	3.32	3.41	3.48	4.57	4.51	4.72	4.94
K_2O wt%	1.97	1.90	1.96	1.95	1.88	1.82	1.91	2.96	2.26	2.29	2.28
P_2O_5 wt%	0.54	0.60	0.58	0.57	0.57	0.59	0.63	0.82	0.70	0.65	0.93
Total	97.8	98.0	97.6	98.1	98.4	99.1	98.5	98.4	99.0	98.9	98.4
H_2O wt%	2.09	1.86	2.20	1.76	1.42	0.72	1.30	1.40	0.80	0.92	1.37
CO_2 ppm	849		640	500	169	351	217				222
Cl ppm	1834	1647	1892	1698	1620	1506	1794	1297	1351	1344	3423
S ppm	2892	2192	2862	1413	2365	2397	2602	248	706	1108	1170
F ppm	872	824	995	1152	670	716	949				1177
XCO_2	0.58		0.49	0.54	0.40	0.85	0.50				no bubble
***P* sat. MPa**	130		116	83	39	38	39				-
CO_2 rest. ppm[a]	2134		1532	1032	429	930	592				222
Mg#[b]	55.17	51.96	54.33	51.09	52.41	53.57	53.78	52.27	53.05	53.86	47.69
Fo% host ol	81.26	78.93	80.83	78.31	79.03	80.12	80.29	79.25	80.02	80.68	75.40
PEC %	8	5	8	2	6	7	6	10	7	7	4

	VOR 2015 type 2 MI				DEC 2018 type 1 MI						
Sample	VORG26MI25	VORG6MI2	VORG7MI4	VORG7MI3	DECG4MI1	DECG8MI5	DECG13MI11	DECG14MI12	DECG15MI13	DECG20M18	DECG22MI20
SiO_2 wt%	47.7	46.5	49.3	48.9	44.3	45.0	43.3	44.2	43.7	43.4	42.7
TiO_2 wt%	1.76	1.50	1.63	1.69	1.48	1.75	1.75	2.06	1.81	1.79	1.88
Al_2O_3 wt%	16.6	17.4	16.6	16.9	17.3	18.0	16.6	18.6	16.3	16.6	17.9
FeOt wt%	11.8	10.7	10.6	10.7	10.9	11.0	10.9	11.0	10.9	10.9	10.9
MnO wt%	0.30	0.15	0.19	0.23	0.16	0.12	0.12	0.26	0.10	0.18	0.12
MgO wt%	4.63	4.37	4.74	4.79	6.42	6.06	7.30	5.53	7.82	7.11	7.90
CaO wt%	8.41	11.2	7.32	7.80	11.5	9.87	11.7	9.92	11.4	12.1	11.8
Na_2O wt%	4.20	3.48	4.60	4.48	4.19	4.22	3.62	4.20	3.54	3.54	3.35
K_2O wt%	2.25	2.20	2.19	2.05	2.23	2.02	2.00	2.02	2.01	1.97	2.20
P_2O_5 wt%	0.76	0.61	0.91	1.13	0.71	0.60	0.56	0.58	0.58	0.61	0.69
Total	98.4	98.0	98.1	98.6	99.2	98.7	97.8	98.3	98.2	98.2	99.4
H_2O wt%	1.45	1.83	1.70	1.23	0.61	1.19	2.07	1.52	1.67	1.67	0.47
CO_2 ppm	94	529	82		482						
Cl ppm	1474	1831	1443	1466	1377	1171	1143	1457	1170	1369	1268
S ppm	1226	2634	1468	1540	1604	1346	2330	1461	2142	1777	1901
F ppm	1028	1212	1092	1026							
XCO_2	0.35	0.63	0.25		0.92						
***P* sat. MPa**	35	106	42		48						
CO_2 rest. ppm[a]	247	735	264		1417						
Mg#[b]	45.39	46.23	48.09	48.30	54.87	53.12	57.82	51.08	59.25	57.22	59.52
Fo% host ol	73.41	73.99	75.76	75.76	81.68	80.25	83.50	78.94	84.25	83.06	84.70
PEC %	5	1	5	3	6	5	6	2	11	8	10

	DEC 2018 type 1 MI			DEC 2018 type 2 MI							
Sample	DECG34MI34	DECG32MI32	DECG33MI33	DECG5MI2	DECG8MI6	DECG9MI7	DECG11MI9	DECG16M14	DECG17MI15	DECG21MI19	DECG10MI8
SiO_2 wt%	42.9	45.6	45.7	48.9	46.4	48.5	47.6	48.5	48.0	48.4	50.2
TiO_2 wt%	1.88	1.69	1.85	1.45	1.72	1.75	1.93	1.60	1.29	1.54	1.59
Al_2O_3 wt%	18.1	16.7	16.7	17.3	17.5	16.3	17.4	16.8	16.9	17.0	15.4
FeOt wt%	11.0	11.0	10.9	10.7	10.6	10.5	10.6	10.7	10.7	10.7	11.8
MnO wt%	0.29	0.11	0.09	0.18	0.18	0.20	0.15	0.15	0.27	0.17	0.17
MgO wt%	6.22	6.64	6.98	5.10	5.38	4.87	4.81	4.94	4.75	4.77	4.67
CaO wt%	10.8	10.6	11.1	7.08	9.28	8.42	6.81	7.24	8.51	6.95	6.85
Na_2O wt%	3.61	3.40	3.10	5.03	4.38	4.43	5.56	4.81	4.75	5.43	4.29
K_2O wt%	2.16	1.90	2.02	2.45	2.27	2.47	2.73	2.57	2.42	2.71	2.87
P_2O_5 wt%	0.60	0.61	0.58	0.92	0.78	0.84	1.09	0.81	0.67	0.83	0.93
Total	97.4	98.3	99.0	99.0	98.5	98.2	98.7	98.1	98.2	98.4	98.8
H_2O wt%	2.40	1.58	0.86	0.84	1.36	1.58	1.16	1.69	1.64	1.43	1.05
CO_2 ppm	394	304	334								214
Cl ppm	1912	1624	1578	1286	1307	1292	2422	1412	1424	1538	1399
S ppm	2548	1670	1724	1179	818	401	781	831	573	703	172
F ppm	958	1041	836								1158
XCO_2	0.34	0.48	0.79								no bubble
***P* sat. MPa**	104	57	39								-
CO_2 rest. ppm[a]	986	885	1044								214
Mg#[b]	53.76	55.14	56.56	49.82	51.28	49.29	49.04	49.05	48.26	48.48	45.59
Fo% host ol	80.82	80.97	81.93	77.67	78.70	76.83	77.88	77.04	76.29	77.17	73.47
PEC %	5	5	6	5	4	3	2	5	2	4	7

	DEC 2018 type 2 MI				
Sample	DEC G31MI31	DEC G42MI42	DEC G43MI43	DEC G44MI44	DEC G35MI35
SiO_2 wt%	49.0	48.6	49.7	48.0	48.1
TiO_2 wt%	1.25	1.46	1.72	1.39	1.35
Al_2O_3 wt%	16.5	17.4	16.8	17.7	16.6
FeOt wt%	11.7	10.7	10.9	10.6	12.0
MnO wt%	0.25	0.24	0.18	0.26	0.33
MgO wt%	4.72	4.36	4.34	4.74	4.52
CaO wt%	8.58	8.57	6.57	9.72	9.01
Na_2O wt%	4.27	4.19	4.51	3.34	4.31
K_2O wt%	2.55	2.40	2.96	2.18	2.41
P_2O_5 wt%	0.67	0.58	1.06	0.51	0.62
Total	99.4	98.5	98.7	98.5	99.2
H_2O wt%	0.40	1.38	1.15	1.34	0.57
CO_2 ppm	203	314	254	236	
Cl ppm	1853	1965	1935	1893	2221
S ppm	738	859	422	1132	882
F ppm	1189	939	998	1325	1195
XCO_2	0.94	0.65	0.69	0.60	
***P* sat. MPa**	28	61	47	50	
CO_2 rest. ppm[a]	572	705	791	495	
Mg#[b]	45.83	45.95	45.70	47.75	44.41
Fo% host ol	73.75	73.97	74.12	74.89	72.60
PEC %	4	2	5	2	2

[a] restored CO_2 compositions are obtained by adding to the composition dissolved in the melt the amount stored in the bubble, calculating the mass fraction in the vapor phase at $P_{sat.}$ through VOLATILECALC program and considering a pre-eruptive bubble volume of 0.47-2.37 % of the inclusions, calculated as $0.0612 \times (T_{trapping} - T_{pre\text{-}eruption})$.

[b] Mg# is calculated considering Fe^{3+}/Fe^{2+} = 0.16-0.22 from Petrolog3 calculation (QFM buffer).

Table A3 Major and volatile elements corrected for PEC and restored H_2O-SiO_2-CO_2 in melt inclusions found in products erupted from post-2011 activity at Mt. Etna

	NSEC type 1 MI										
Sample	NSECG13MI11	NSECG18MI16	NSECG20MI18	NSECG22MI20	NSECG24MI22	NSECG25MI23	NSECG29MI27	NSECG32MI30	NSECG41MI42	NSECG26MI24	NSECG44MI47
SiO_2 wt%	45.3	45.4	45.2	45.4	46.6	46.0	45.7	45.5	45.7	45.9	46.0
TiO_2 wt%	1.72	2.17	1.67	1.69	1.47	1.66	1.73	1.85	1.71	1.76	1.71
Al_2O_3 wt%	17.4	16.1	16.9	16.5	17.3	15.6	16.0	16.5	15.8	17.6	16.8
FeOt wt%	10.9	10.5	10.5	10.5	10.4	10.6	10.5	10.5	10.9	10.8	10.4
MnO wt%	0.22	0.13	0.15	0.15	0.17	0.11	0.10	0.14	0.14	0.20	0.18
MgO wt%	6.55	6.71	6.68	6.76	5.21	7.38	7.96	6.73	6.62	6.04	5.53
CaO wt%	9.83	9.47	10.3	10.7	10.5	10.5	10.1	10.4	10.6	10.0	11.1
Na_2O wt%	3.57	3.70	3.41	3.24	3.69	3.35	3.29	3.33	3.09	3.37	3.22
K_2O wt%	1.75	1.81	1.70	1.76	1.89	1.63	1.74	1.82	2.02	1.85	2.04
P_2O_5 wt%	0.60	0.95	0.63	0.49	0.61	0.58	0.53	0.54	0.55	0.54	0.67
Total	97.8	96.9	97.2	97.1	97.9	97.3	97.7	97.3	97.2	98.0	97.5
H_2O rest. wt%[a]	2.02	3.00	2.69	2.73	1.97	2.58	2.21	2.57	2.69	1.84	2.31
CO_2 ppm						127	122		348		150
Cl ppm	1214	1169	1347	1137	1080	1233	1237	1291	1687	1505	1605
S ppm	1474	2567	1616	2273	1722	1637	1676	2211	2777	2119	2568
F ppm									1044	807	970
CO_2 rest. ppm[b]						447	489		942		311
Mg#[c]	54.93	56.62	56.31	56.64	50.79	58.55	60.42	56.54	55.32	53.26	52.30
Fo% host ol	80.85	81.96	81.70	81.86	77.71	82.98	84.25	81.87	80.86	79.53	78.74
PEC %	6	12	7	6	2	10	11	7	9	5	4
% SiO_2 add[d]	3.11	6.12	5.13	4.96	2.54	4.62	4.50	5.73	5.01	1.43	2.50

	NSEC type 1 MI				NSEC type 2 MI						
Sample	NSECG28MI26	NSECG42MI43	NSECG17MI15	NSECG21MI19	NSECG7MI33	NSECG27MI25	NSECG40MI41	NSECG43MI43	NSECG45MI49	NSECG47MI51	NSECG11MI9
SiO_2 wt%	45.5	45.6	45.5	46.2	48.2	48.7	51.5	50.8	47.7	49.5	48.9
TiO_2 wt%	1.72	1.82	1.69	1.67	1.54	1.64	1.15	1.05	1.79	1.72	1.76
Al_2O_3 wt%	17.2	17.1	17.4	16.9	15.7	15.1	15.3	15.9	17.3	16.4	16.4
FeO wt%	10.9	10.9	11.0	10.5	10.9	11.1	11.6	18.3	10.5	10.6	10.5
MnO wt%	0.20	0.19	0.23	0.17	0.16	0.20	0.20	0.23	0.21	0.09	0.16
MgO wt%	6.02	6.03	6.01	5.47	6.20	5.82	3.66	3.85	4.54	4.62	4.66
CaO wt%	10.3	10.8	10.5	11.1	7.71	7.52	7.13	6.53	9.08	7.41	7.90
Na_2O wt%	3.37	3.22	3.38	3.17	4.21	4.40	5.14	4.85	3.96	4.61	4.39
K_2O wt%	1.97	1.95	1.86	2.15	2.26	2.26	2.14	2.69	2.35	2.73	2.57
P_2O_5 wt%	0.60	0.55	0.61	0.59	0.73	0.68	0.73	0.80	0.82	0.73	0.84
Total	97.8	98.1	98.2	97.9	97.7	97.4	98.5	98.4	98.3	98.4	98.0
H_2O rest. wt%[a]	2.05	1.73	1.69	1.92	2.19	2.40	1.27	1.32	1.51	1.60	1.80
CO_2 ppm	104	64		131			167		165		46
Cl ppm	1532	1537	1547	1633	1376	1158	2915	1863	1690	1664	1652
S ppm	1903	1911	2422	2474	836	1012	1625	768	1407	980	847
F ppm	817	790	780	1029			1103	1500	1147	1546	927
CO_2 rest. ppm[b]	249	161		267			402		385		46
Mg#[c]	52.90	53.11	52.73	51.72	53.79	52.11	40.27	41.11	47.39	47.69	48.12
Fo% host ol	79.35	79.47	79.21	78.31	79.90	78.71	68.73	69.73	75.12	76.16	76.02
PEC %	7	6	6	4	9	8	1	4	3	6	5
% SiO_2 add[d]	1.71	1.72	2.22	1.90	2.45	7.79	0.00	0.00	0.18	2.76	1.72

	NSEC 2013 type 2 MI		VOR 2015 type 1 MI								
Sample	NSECG31MI29	NSECG13MI120	VORG12MI9	VORG16MI13	VORG18MI15	VORG18MI16	VORG18MI17	VORG19MI18	VORG24MI23	VORG13MI100	VORG10MI7
SiO_2 wt%	50.3	47.7	46.3	46.2	46.3	46.4	46.6	45.5	46.3	45.7	46.3
TiO_2 wt%	1.50	1.61	1.49	1.74	1.60	1.56	1.53	1.81	1.82	1.75	1.57
Al_2O_3 wt%	16.2	17.3	16.2	15.7	16.4	16.7	15.1	16.3	15.8	16.4	17.2
FeOt wt%	10.4	10.5	10.6	10.5	10.6	10.6	10.6	10.6	10.5	10.8	10.9
MnO wt%	0.18	0.18	0.19	0.11	0.14	0.12	0.17	0.14	0.11	0.18	0.12
MgO wt%	4.68	4.97	6.73	6.94	7.01	6.16	6.89	7.08	5.25	6.16	6.03
CaO wt%	6.82	8.51	9.89	10.1	9.68	10.1	10.2	10.3	11.3	10.2	10.2
Na_2O wt%	5.16	4.08	3.29	3.30	3.44	3.45	3.20	3.03	2.93	3.22	3.30
K_2O wt%	2.42	2.31	1.82	1.65	1.72	1.70	1.73	1.79	1.92	1.79	1.85
P_2O_5 wt%	0.89	0.69	0.60	0.64	0.53	0.65	0.59	0.50	0.57	0.62	0.54
Total	98.5	97.8	97.1	96.8	97.4	97.5	96.6	96.9	96.5	96.8	98.0
H_2O rest. wt%[a]	1.30	2.00	2.80	3.10	2.43	2.37	3.22	2.92	3.35	3.07	1.90
CO_2 ppm		100							418	484	419
Cl ppm	2567	1781	1808	1021	1089	975	1043	862	1927	1694	1355
S ppm	931	1473	1890	1658	1275	1607	1921	1344	2900	2592	2344
F ppm		1022							823	822	1028
CO_2 rest. ppm[b]		289							631	1154	1058
Mg#[c]	47.91	49.50	56.11	57.23	57.07	54.02	56.74	57.38	50.82	53.75	52.97
Fo% host ol	76.57	76.90	81.25	82.00	81.52	79.87	81.52	82.22	77.28	79.67	79.18
PEC %	4	4	8	9	9	5	8	14	6	8	7
% SiO_2 add[d]	1.22	1.57	4.95	5.27	3.41	2.71	6.11	5.06	5.96	3.47	2.00

	VOR 2015 type 1 MI							VOR 2015 type 2 MI			
Sample	VORG14MI11	VORG8MI6	VORG31MI31	VORG25MI24	VORG10MI70	VORG22MI21	VORG22MI210	VORG9MI6	VORG20MI19	VORG23MI22	VORG32MI32
SiO_2 wt%	46.2	46.0	45.8	46.1	46.1	46.1	46.1	49.5	48.6	49.0	51.0
TiO_2 wt%	1.69	1.72	1.71	1.82	1.61	1.79	1.65	1.74	1.54	1.58	1.74
Al_2O_3 wt%	15.3	17.1	15.4	18.1	18.0	17.5	16.9	16.0	15.1	14.5	15.3
FeOt wt%	10.6	10.6	10.6	10.4	10.4	10.4	10.6	10.7	10.8	10.6	10.5
MnO wt%	0.10	0.10	0.14	0.27	0.10	0.17	0.22	0.19	0.23	0.18	0.31
MgO wt%	6.75	5.78	6.58	5.43	5.71	6.08	6.31	5.61	6.27	6.41	4.51
CaO wt%	10.5	10.2	10.8	9.99	10.4	10.6	10.2	6.14	8.20	7.94	6.93
Na_2O wt%	3.01	3.37	2.91	3.52	3.30	3.29	3.29	4.60	4.05	4.20	4.98
K_2O wt%	1.82	1.84	1.78	1.90	1.88	1.76	1.80	2.98	2.02	2.03	2.30
P_2O_5 wt%	0.56	0.57	0.52	0.56	0.59	0.62	0.57	0.82	0.67	0.63	0.92
Total	96.6	97.2	96.3	98.1	98.1	98.3	97.6	98.3	97.4	97.1	98.4
H_2O rest. wt%[a]	3.26	2.61	3.58	2.24	1.77	1.56	2.27	1.57	2.47	2.72	1.38
CO_2 ppm	837		630	465	163	342	210				211
Cl ppm	1808	1571	1863	1579	1565	1467	1741	1309	1323	1308	3250
S ppm	2852	2090	2818	1315	2284	2336	2524	251	691	1079	1111
F ppm	860	786	980	1072	647	697	921				1118
CO_2 rest. ppm[b]	2122		1522	997	423	921	585				211
Mg#[c]	56.26	52.54	55.65	51.49	52.66	54.21	54.56	52.18	54.37	55.29	46.83
Fo% host ol	81.26	78.93	80.83	78.31	79.03	80.12	80.29	79.25	80.02	80.68	75.40
PEC %	9	5	9	3	4	6	7	9	9	9	4
% SiO_2 add[d]	5.27	2.98	6.33	1.94	1.26	3.21	3.94	0.59	7.05	7.68	0.00

	VOR 2015 type 2 MI				DEC 2018 type 1 MI						
Sample	VORG26MI25	VORG6MI2	VORG7MI4	VORG7MI3	DECG4MI1	DECG8MI5	DECG13MI11	DECG14MI12	DECG15MI13	DECG20M18	DECG22MI20
SiO_2 wt%	48.2	46.6	49.3	49.0	47.8	46.5	46.4	46.1	46.5	46.5	45.9
TiO_2 wt%	1.83	1.50	1.63	1.70	1.24	1.58	1.50	1.87	1.58	1.53	1.60
Al_2O_3 wt%	17.2	17.4	16.6	16.9	14.5	16.3	14.3	16.9	14.2	14.2	15.2
FeOt wt%	10.5	10.5	10.7	10.5	10.5	10.6	10.5	10.8	10.5	10.5	10.5
MnO wt%	0.31	0.15	0.19	0.23	0.13	0.11	0.10	0.24	0.09	0.16	0.10
MgO wt%	4.07	4.30	4.74	4.71	6.88	6.22	7.75	5.80	8.20	7.54	8.42
CaO wt%	8.73	11.23	7.32	7.84	9.65	8.93	9.98	9.01	9.90	10.4	10.1
Na_2O wt%	4.36	3.50	4.60	4.51	3.51	3.82	3.11	3.82	3.08	3.03	2.85
K_2O wt%	2.33	2.20	2.19	2.07	1.86	1.83	1.72	1.84	1.74	1.69	1.87
P_2O_5 wt%	0.78	0.62	0.88	1.11	0.67	0.57	0.52	0.54	0.54	0.58	0.65
Total	98.3	98.0	98.1	98.6	96.7	96.6	95.8	97.0	96.3	96.1	97.1
H_2O rest. wt%[a]	1.50	1.84	1.69	1.22	3.19	3.29	4.09	2.89	3.54	3.75	2.73
CO_2 ppm	90	486	78		463						
Cl ppm	1417	1681	1379	1379	1323	1121	1068	1353	1091	1278	1173
S ppm	1179	2418	1403	1448	1541	1289	2176	1357	1996	1659	1760
F ppm	988	1113	1044	965							
CO_2 rest. ppm[b]	243	691	260		1398						
Mg#[c]	44.88	46.69	48.05	48.16	57.16	54.32	59.89	52.33	61.10	59.28	61.70
Fo% host ol	73.41	73.99	75.76	75.76	81.68	80.25	83.50	78.94	84.25	83.06	84.70
PEC %	3	2	5	3	10	7	10	4	14	12	14
% SiO_2 add[d]	1.59	2.47	0.00	0.00	11.45	5.80	9.61	5.67	9.04	9.89	10.13

	DEC 2018 type 1 MI			DEC 2018 type 2 MI							
Sample	DECG34MI34	DECG32MI32	DECG33MI33	DECG5MI2	DECG8MI6	DECG9MI7	DECG11MI9	DECG16M14	DECG17MI15	DECG21MI19	DECG10MI8
SiO_2 wt%	45.4	46.6	46.7	49.5	48.0	49.3	49.5	49.4	49.4	50.0	50.8
TiO_2 wt%	1.67	1.62	1.79	1.38	1.56	1.68	1.75	1.55	1.20	1.43	1.65
Al_2O_3 wt%	16.1	16.1	16.1	16.5	15.9	15.7	15.8	16.3	15.6	15.6	16.0
FeOt wt%	10.6	10.6	10.5	10.7	10.6	10.4	10.3	10.3	10.5	10.3	10.5
MnO wt%	0.26	0.10	0.08	0.18	0.17	0.18	0.13	0.15	0.25	0.16	0.17
MgO wt%	6.50	6.60	6.89	5.25	5.70	4.91	4.99	4.85	4.90	4.84	4.10
CaO wt%	9.61	10.2	10.7	6.77	8.42	8.12	6.16	7.02	7.87	6.39	7.10
Na_2O wt%	3.21	3.27	3.00	4.81	3.98	4.27	5.04	4.67	4.39	4.99	4.45
K_2O wt%	1.93	1.82	1.95	2.34	2.06	2.38	2.47	2.50	2.24	2.49	2.98
P_2O_5 wt%	0.57	0.58	0.55	0.89	0.73	0.82	1.03	0.79	0.64	0.80	0.95
Total	95.9	97.6	98.3	98.3	97.2	97.6	97.1	97.5	97.0	97.0	98.7
H_2O rest. wt%[a]	3.99	2.28	1.59	1.50	2.68	2.19	2.72	2.31	2.81	2.81	1.09
CO_2 ppm	376	292	335								209
Cl ppm	1825	1559	1582	1238	1242	1212	2249	1352	1316	1465	1366
S ppm	2432	1603	1729	1135	777	376	725	796	529	670	168
F ppm	914	999	838								1131
CO_2 rest. ppm[b]	968	872	1045								209
Mg#[c]	55.34	55.69	57.10	50.31	52.38	49.70	50.23	49.40	49.11	49.45	45.23
Fo% host ol	80.80	80.97	81.93	77.67	78.70	76.83	77.88	77.04	76.29	77.17	73.47
PEC %	7	6	6	7	7	4	4	5	3	6	3
% SiO_2 add[d]	7.32	2.81	2.71	2.61	5.63	2.41	6.36	6.36	2.44	4.82	0.00

	DEC 2018 type 2 MI				
Sample	DECG31MI31	DECG42MI42	DECG43MI43	DECG44MI44	DECG35MI35
SiO_2 wt%	50.7	48.9	49.8	48.0	49.4
TiO_2 wt%	1.64	1.44	1.74	1.40	1.28
Al_2O_3 wt%	15.9	17.2	16.9	17.8	15.6
FeOt wt%	10.7	10.5	10.5	10.5	11.6
MnO wt%	0.17	0.23	0.19	0.26	0.31
MgO wt%	4.25	4.31	4.19	4.69	4.54
CaO wt%	7.05	8.51	6.64	9.76	8.51
Na_2O wt%	4.42	4.15	4.56	3.35	4.08
K_2O wt%	2.96	2.39	2.99	2.18	2.28
P_2O_5 wt%	0.94	0.57	1.04	0.50	0.60
Total	98.7	98.3	98.7	98.5	98.2
H_2O rest. wt%[a]	1.08	1.58	1.17	1.35	1.60
CO_2 ppm	192	291	244	219	
Cl ppm	1754	1821	1860	1758	2055
S ppm	699	797	406	1052	816
F ppm	1126	871	960	1231	1106
CO_2 rest. ppm[b]	561	682	781	478	
Mg#[c]	45.62	46.05	45.59	47.73	45.02
Fo% host ol	73.75	73.97	74.12	74.89	72.60
PEC %	4	2	4	2	2
% SiO_2 add[d]	2.53	0.74	0.00	0.00	3.85

[a] restored H_2O is given by the measured contents plus the amount calculated in function of the % SiO_2 added to the MI, considering a moral ratio $\Delta H_2O/\Delta SiO_2=1$.

[b] restored CO_2 compositions are calculated as in table 2 before H_2O loss, then corrected for PEC after restoration for H_2O-SiO_2.

[c] Mg# is calculated considering Fe^{3+}/Fe^{2+} = 0.16-0.22 from Petrolog3 calculation (QFM buffer).

[d] % SiO_2 add corresponds to the amount of SiO_2 added until the Si-saturation index of MI matches that of the bulk rock taken as reference for pristine value; then the whole composition of each MI is normalized and corrected for PEC.

Table A4: Trace elements compositions in melt inclusions found in products erupted from post-2011 activity at Mt. Etna

	NSEC 2013 type 1 MI						
Sample	NSECG24MI22	NSECG25MI23	NSECG26MI24	NSECG28MI26	NSECG29MI27	NSECG41MI42	NSECG42MI43
Li7	7.34	4.57	6.9	6.49	4.95	6.84	63.04
Sc	18.0	28.3	25.7	27.1	24.2	30.8	24.8
Ti	9228	11557	11810.83	10619	11679	12210	11292
V	237	337	348.95	302	351	356	337
Cr	<10.99	<10.87	11.79	<5.33	<9.35	7.74	<19.28
Co	40.93	33.17	42.03	33.15	34.17	34.35	55.57
Ni	27.59	13.88	19.59	20.94	24.55	25.42	79.54
Rb		47.6	47.9	52.3			
Sr	1254	1240	1245	1219	1252	1211	1203
Y	21.9	24.1	24.0	23.7	23.6	26.9	25.3
Zr	164	181	178	175	178	202	189
Nb	37.1	40.8	41.0	39.3	39.6	42.8	42.6
Cs	0.67	0.79	0.798	0.79	0.83	0.96	1.18
Ba	548	586	603	554	573	592	581
La	43.4	48.1	48.2	45.7	46.5	49.3	49.7
Ce	87.1	98.2	95.7	90.5	94.2	98.7	100.0
Pr	9.8	10.9	10.7	10.2	10.3	11.2	10.9
Nd	39.9	44.1	42.6	41.5	41.7	45.2	44.3
Sm	8.01	8.68	8.52	8.18	8.47	9.33	9.71
Eu	2.48	2.59	2.55	2.48	2.44	2.77	2.63
Gd	5.90	7.17	6.59	6.18	7.20	7.81	7.27
Tb	0.77	0.88	0.87	0.89	0.84	0.97	0.87
Dy	4.71	5.08	4.98	5.08	5.06	6.04	5.54
Ho	0.8	0.98	0.909	0.88	0.92	0.98	0.99
Er	2.34	2.7	2.41	2.39	2.59	2.70	2.26
Tm	0.26	0.32	0.31	0.32	0.31	0.38	0.34
Yb	1.66	1.97	2.023	1.97	2.07	2.27	2.27
Lu	0.26	0.3	0.282	0.28	0.28	0.31	0.30
Hf	3.40	3.76	3.83	3.88	4.03	4.35	3.88
Ta	1.79	1.88	1.84	1.86	1.91	1.95	2.16
Pb	5.27	6.47	6.47	5.81	5.92	6.57	7.31
Th	5.22	5.98	5.90	5.65	5.81	6.02	6.63
U	1.76	1.83	1.883	1.77	1.86	1.84	2.08

NSEC 2013 type 2 MI						
Sample	NSECG11MI9	NSECG40MI41	NSECG43MI43	NSECG45MI49	NSECG47MI51	NSECG13MI120
Li7	10.71	12.82	13.36	7.75	7.71	8.47
Sc	15.5	13.9	10.5	13.8	15.5	19.4
Ti	11095	6352	6044	11019	11580	11148
V	273	232	156	291	263	293
Cr	<5.84	<9.29	<5.76	7.24	<4.99	7.29
Co	30.12	28.45	24.24	29.39	26.07	33.15
Ni	5.6	5.59	3.81	6.16	11.47	12.36
Rb						56.97
Sr	1125	1506	1250	1210	1119	1135
Y	27.6	44.4	32.3	25.7	27.8	25.6
Zr	225	218	216	199	230	204
Nb	56.7	62.5	59.4	50.2	60.6	51.2
Cs	1.14	0.68	1.04	0.84	1.14	0.99
Ba	743	802	789	694	814	698
La	63.7	69.3	67.2	57.5	67.9	57.9
Ce	123.7	138.7	128.9	112.0	131.2	113.4
Pr	13.2	15.2	13.8	12.0	13.9	12.4
Nd	52.1	60.5	53.5	48.1	54.8	48.6
Sm	10.36	12.62	10.18	9.12	10.24	9.28
Eu	2.84	3.28	2.95	2.68	3.00	2.69
Gd	7.33	9.96	7.86	6.74	8.13	7.25
Tb	0.99	1.39	1.06	0.92	1.01	0.93
Dy	5.79	8.62	6.48	5.37	5.97	5.25
Ho	1.02	1.66	1.11	0.9	1.02	0.99
Er	2.81	4.84	3.29	2.65	2.79	2.62
Tm	0.38	0.71	0.49	0.36	0.39	0.35
Yb	2.35	4.63	2.8	2.06	2.24	2.00
Lu	0.35	0.68	0.43	0.28	0.32	0.30
Hf	4.46	4.53	4.17	4.01	4.48	4.32
Ta	2.67	2.78	2.66	2.20	2.71	2.34
Pb	7.72	5.5	7.62	6.96	8.44	7.73
Th	8.50	8.27	9.09	7.42	8.98	7.61
U	2.54	2.69	2.81	2.32	2.82	2.44

VOR 2015 type 1 MI									
Sample	VORG8MI6	VORG10MI7	VORG13MI100	VORG14MI11	VORG22MI21	VORG25MI24	VORG31MI31	VORG10MI70	VORG22MI100
Li7	5.28	4.13	7.52	7.01	6.54	7.16	7.36	6.12	4.42
Sc	20.6	19.6	26.6	32.9	26.6	21.7	33.9	25.2	28.4
Ti	11352	10672	11965	12096	12085	11231	12051	11192	11261
V	340	301	339	352	378	337	349	316	343
Cr	12.87	<6.04	9.85	<11.25	12.77	<8.29	18.79	3.15	7.48
Co	37.4	33.8	34.0	35.2	43.2	36.4	33.3	38.6	39.3
Ni	17.6	21.0	20.1	25.7	38.6	20.7	27.0	22.3	29.0
Rb			51.8					49.4	50.4
Sr	1229	1361	1301	1101	1214	1230	1179	1360	1167
Y	23.1	22.8	25.7	25.1	24.3	23.2	25.9	25.6	24.4
Zr	176	171	191	189	184	178	190	187	182
Nb	40.7	39.7	42.7	39.6	41.7	43.8	39.6	42.6	40.4
Cs	0.91	0.83	0.83	0.71	0.78	0.7	0.75	0.82	0.82
Ba	578	577	597	568	587	594	560	647	586
La	47.8	47.4	49.6	46.1	48.1	50.8	46.6	52.8	46.5
Ce	95.0	93.7	99.1	91.9	95.6	99.5	93.7	104.8	95.0
Pr	10.2	10.3	11.0	10.5	10.9	11.2	10.5	11.6	10.6
Nd	40.6	41.9	45.0	43.6	43.5	43.8	43.3	46.2	42.7
Sm	8.64	8.11	9.02	8.55	8.11	8.55	8.45	9.01	8.92
Eu	2.40	2.48	2.63	2.76	2.72	2.55	2.59	2.67	2.50
Gd	6.83	6.27	7.28	7.09	7.17	6.58	6.81	7.19	6.91
Tb	0.77	0.83	0.97	0.99	0.96	0.77	0.90	0.94	0.90
Dy	4.72	5.03	5.55	5.42	4.91	5.14	5.41	5.39	5.34
Ho	0.92	0.88	0.98	0.94	0.79	0.89	0.95	1.00	0.95
Er	2.25	2.37	2.56	2.50	2.65	2.32	2.47	2.48	2.36
Tm	0.33	0.30	0.33	0.25	0.38	0.31	0.36	0.34	0.31
Yb	1.91	1.78	1.82	2.29	1.43	1.83	2.05	2.09	2.02
Lu	0.30	0.26	0.27	0.31	0.31	0.26	0.29	0.30	0.28
Hf	3.68	3.63	4.25	4.05	4.10	3.72	4.13	4.04	4.01
Ta	1.81	1.90	1.96	1.92	1.92	1.90	1.84	1.95	1.84
Pb	6.24	6.35	6.02	6.00	6.33	6.22	5.57	7.00	6.24
Th	6.15	5.64	6.12	5.59	6.03	6.30	5.62	6.16	5.79
U	1.86	1.83	1.86	1.76	1.82	2.03	1.66	1.94	1.79

VOR 2015 type 2 MI				
Sample	VORG6MI2	VORG7MI4	VORG26MI25	VORG32MI32
Li7	10.71	7.34	10.56	11.41
Sc	29.5	13.8	18.0	14.0
Ti	9186	9974	10936	10280
V	230	192	279	179
Cr	<5.37	<4.93	<5.90	<6.67
Co	32.5	25.1	28.9	24.5
Ni	18.0	2.92	7.73	7.39
Rb	56.4			
Sr	1179	1211	1137	1499
Y	25.9	25.7	25.8	42.1
Zr	199	221	210	280
Nb	42.8	58.9	53.5	78.1
Cs	0.87	0.83	0.9	0.83
Ba	616	765	705	886
La	50.4	64.6	59.5	89.0
Ce	101.8	127.4	115.6	179.3
Pr	11.5	13.6	12.6	19.6
Nd	45.7	53.0	49.0	77.7
Sm	9.78	9.68	9.55	14.19
Eu	2.80	2.84	2.67	3.42
Gd	7.85	7.11	7.03	10.42
Tb	1.00	0.89	1.01	1.47
Dy	5.10	5.00	5.42	8.22
Ho	0.98	0.94	0.93	1.44
Er	2.58	2.79	2.65	4.52
Tm	0.33	0.34	0.37	0.55
Yb	1.80	2.34	2.15	4.39
Lu	0.27	0.35	0.32	0.60
Hf	4.27	4.53	4.32	5.48
Ta	1.95	2.85	2.54	3.43
Pb	6.31	6.73	7.20	7.01
Th	5.94	9.40	7.82	11.55
U	1.97	2.73	2.43	3.54

	DEC 2018 type 1 MI				DEC 2018 type 2 MI					
Sample	DECG4MI1	DECG14MI12	DECG33MI33	DECG34MI34	DECG10MI8	DECG16M14	DECG31MI31	DECG44MI44	DECG17MI5	DECG43MI43
Li7	9.19	11.45	5.75	4.66	9.73	14.71	10.18	12.19		
Sc	20.9	15.5	29.2	31.5	16.1	4.4	14.2	16.2	18.3	14.6
Ti	9389	13121	11514	11434	10899	10701	7442	8181	8678	10367
V	271	402	361	341	232	245	299	215	330	217
Cr	<10.79	<18.02	18.3	50.94	<10.28	<27.61	<4.74	10.28	7.65	<1.98
Co	35.5	35.8	38.1	36.1	29.4	33.2	29.7	38.8	31.2	26.3
Ni	29.0	18.6	31.2	20.3	15.6	15.5	8.1	21.9	9.1	10.0
Rb				65.5			61.9		68.0	67.2
Sr	1302	1326	1244	1136	887	1118	1318	1198	1451	983
Y	27.8	25.2	23.8	24.8	32.3	29.3	34.7	25.3	35.7	30.3
Zr	211	190	179	186	285	251	192	179	230	260
Nb	47.0	42.4	42.7	42.3	77.0	72.7	43.7	40.4	55.1	66.0
Cs	0.96	0.87	1.08	0.90	1.33	1.47	1.00	0.81	1.19	1.22
Ba	658	590	625	575	850	926	627	583	768	872
La	54.1	50.5	50.6	49.2	78.0	74.8	51.7	46.7	62.8	74.6
Ce	107	97	100	97	150	148	105	94	128	143
Pr	11.9	11.4	11.3	10.8	15.8	15.6	12.0	10.6	14.1	15.3
Nd	50.3	46.3	44.8	44.6	60.7	62.0	49.4	41.9	56.6	60.2
Sm	9.83	8.60	8.40	9.42	11.3	10.7	10.4	9.0	11.3	11.1
Eu	2.94	2.36	2.69	2.54	2.91	3.34	3.00	2.64	3.19	3.06
Gd	8.72	6.55	7.07	7.04	8.89	8.21	8.25	6.62	9.02	8.38
Tb	1.05	1.02	0.86	0.98	1.15	0.96	1.22	0.83	1.19	1.09
Dy	5.82	5.82	5.22	5.04	6.72	5.64	7.32	5.34	7.03	6.33
Ho	1.04	0.99	0.83	0.96	1.26	1.07	1.28	0.92	1.28	1.13
Er	2.89	2.75	2.29	2.47	3.01	2.99	3.55	2.47	3.45	3.13
Tm	0.35	0.36	0.30	0.38	0.53	0.45	0.47	0.32	0.50	0.42
Yb	2.05	2.07	1.89	2.28	2.82	2.23	3.05	2.04	3.25	2.59
Lu	0.34	0.26	0.27	0.25	0.39	0.33	0.44	0.33	0.47	0.37
Hf	4.30	4.04	3.80	4.05	5.49	4.84	4.18	3.88	4.91	5.24
Ta	1.98	2.06	1.81	1.93	3.78	3.17	1.98	1.79	2.49	3.08
Pb	5.12	6.70	8.37	6.58	9.58	10.23	5.12	4.78	7.90	9.57
Th	6.73	6.20	6.23	5.95	11.7	10.3	6.16	5.73	7.75	10.4
U	2.06	1.96	2.07	1.88	3.56	3.57	2.03	1.80	2.60	3.19

Table A5 Major elements, S and Cl compositions measured along melt-embayments found in products erupted from post-2011 activity at Mt. Etna

	SiO_2 wt%	TiO_2 wt%	Al_2O_3 wt%	FeO wt%	MgO wt%	MnO wt%	CaO wt%	Na_2O wt%	K_2O wt%	P_2O_5 wt%	S ppm	Cl ppm	µm
NSEC_EMB1_1	47.6	1.93	17.4	9.91	3.28	0.12	8.75	5.27	2.66	0.81	809	1288	77
NSEC_EMB1_2	48.2	1.84	17.3	10.0	3.59	0.25	8.44	5.24	2.67	0.74	626	1479	69
NSEC_EMB1_3	48.1	1.85	17.5	10.1	3.70	0.20	8.46	5.20	2.63	0.81	932	1217	61
NSEC_EMB1_4	47.8	1.78	17.3	9.92	3.49	0.20	8.40	5.46	2.71	0.78	931	1371	53
NSEC_EMB1_5	47.1	1.86	17.3	10.0	3.59	0.23	8.63	5.45	2.68	0.77	671	1549	45
NSEC_EMB1_6	48.0	1.85	17.8	10.2	3.65	0.21	8.68	5.39	2.69	0.76	565	1675	37
NSEC_EMB1_7	47.3	1.81	17.6	10.5	3.67	0.24	8.74	5.41	2.70	0.79	869	1025	29
NSEC_EMB1_8	47.1	1.83	17.5	10.4	3.75	0.24	8.86	5.14	2.63	0.79	564	1233	21
NSEC_EMB1_9	46.8	1.80	17.8	10.6	3.93	0.17	8.95	5.24	2.66	0.77	792	1244	13
NSEC_EMB1_10	45.2	1.90	18.2	10.3	3.94	0.19	8.74	5.57	2.77	0.78	898	1338	5
NSEC_EMB2_1	46.7	1.85	17.4	10.2	3.49	0.20	8.60	5.09	2.62	0.77	946	1336	106
NSEC_EMB2_2	47.7	1.94	17.1	10.1	3.67	0.24	8.49	4.98	2.65	0.76	1146	1307	90
NSEC_EMB2_3	47.4	1.82	17.1	10.0	3.66	0.20	8.58	5.04	2.62	0.74	856	1546	66
NSEC_EMB2_4	47.1	1.86	17.0	10.1	3.70	0.21	8.65	5.00	2.55	0.74	977	1199	58
NSEC_EMB2_5	47.2	1.79	17.2	10.1	3.62	0.20	8.68	5.06	2.62	0.66	855	1211	50
NSEC_EMB2_6	47.3	1.79	17.2	10.5	3.60	0.15	8.75	5.10	2.59	0.83	840	1301	42
NSEC_EMB2_7	47.2	1.79	17.6	10.2	3.71	0.13	8.77	4.89	2.60	0.79	1130	1152	34
NSEC_EMB2_8	47.3	1.80	17.3	10.2	3.72	0.22	8.71	5.27	2.56	0.82	641	1300	26
NSEC_EMB2_9	47.1	1.83	17.5	10.3	3.68	0.14	8.73	5.05	2.62	0.77	794	1288	18
NSEC_EMB2_10	47.6	1.78	17.7	9.94	3.75	0.21	8.47	4.95	2.62	0.78	474	1087	10

	SiO_2 wt%	TiO_2 wt%	Al_2O_3 wt%	FeO wt%	MgO wt%	MnO wt%	CaO wt%	Na_2O wt%	K_2O wt%	P_2O_5 wt%	S ppm	Cl ppm	µm
NSEC_EMB3_1	48.4	1.97	16.5	10.0	3.57	0.20	8.40	4.01	2.73	1.04	260	1374	82
NSEC_EMB3_2	47.7	1.87	16.4	10.0	3.43	0.21	8.42	5.16	2.86	0.99	153	1211	75
NSEC_EMB3_3	48.4	1.90	16.5	10.3	3.59	0.21	8.51	5.05	2.80	0.97	214	1259	67
NSEC_EMB3_4	48.1	1.78	16.5	10.2	3.56	0.22	8.53	5.13	2.82	0.98	336	1139	52
NSEC_EMB3_5	48.0	1.97	16.8	10.4	3.67	0.21	8.60	5.17	2.75	0.99	336	1210	45
NSEC_EMB3_6	47.9	1.92	16.8	10.4	3.54	0.21	8.55	5.21	2.81	0.91	412	1443	37
NSEC_EMB3_7	47.1	1.86	17.1	10.5	3.47	0.20	8.57	4.98	2.81	0.87	229	1383	30
NSEC_EMB3_8	47.5	2.02	17.8	10.1	3.45	0.21	8.25	5.42	2.96	0.86	137	1264	15
NSEC_EMB3_9	47.1	1.99	17.4	10.3	3.49	0.21	8.39	5.22	2.93	0.82	15	1330	7
NSEC_EMB4_1	47.5	1.86	17.8	10.1	3.29	0.21	8.78	4.96	2.62	0.78	747	1483	45
NSEC_EMB4_2	47.0	1.84	17.5	10.3	3.53	0.16	8.76	4.87	2.58	0.77	732	1251	38
NSEC_EMB4_3	47.5	1.81	17.4	10.3	3.55	0.23	8.83	5.12	2.56	0.78	777	1500	32
NSEC_EMB4_4	47.8	1.92	17.4	10.4	3.55	0.20	8.83	5.03	2.53	0.79	641	1084	25
NSEC_EMB4_5	47.9	1.85	17.6	10.4	3.57	0.23	8.71	5.06	2.60	0.74	808	1352	18
NSEC_EMB4_6	47.3	1.90	17.6	10.0	3.56	0.20	8.64	5.09	2.68	0.82	411	1233	12
NSEC_EMB5_1	47.7	1.77	17.0	10.4	3.33	0.19	8.70	5.07	2.67	0.76	945	1537	53
NSEC_EMB5_2	46.9	1.89	17.0	10.1	3.43	0.19	8.82	4.92	2.66	0.80	838	1345	47
NSEC_EMB5_3	47.0	1.81	16.9	10.3	3.39	0.25	8.92	4.86	2.62	0.78	959	1291	40
NSEC_EMB5_4	47.0	1.79	17.1	10.3	3.51	0.22	8.85	5.15	2.65	0.72	807	1041	34
NSEC_EMB5_5	47.9	1.92	16.9	10.4	3.46	0.25	8.84	4.90	2.59	0.73	610	1131	27
NSEC_EMB5_6	47.2	1.96	16.9	10.6	3.52	0.19	8.92	4.98	2.64	0.79	426	1332	20

	SiO_2 wt%	TiO_2 wt%	Al_2O_3 wt%	FeO wt%	MgO wt%	MnO wt%	CaO wt%	Na_2O wt%	K_2O wt%	P_2O_5 wt%	S ppm	Cl ppm	µm
VOR_EMB1_1	47.1	1.80	17.4	10.2	3.63	0.21	9.36	4.82	2.32	0.79	1086	1099	80
VOR_EMB1_2	47.0	1.84	17.3	10.3	3.78	0.15	9.34	4.96	2.35	0.73	1435	1307	70
VOR_EMB1_3	47.3	1.80	17.5	10.3	3.76	0.24	9.40	4.89	2.35	0.69	1192	1170	60
VOR_EMB1_4	47.2	1.79	17.5	10.3	3.57	0.17	9.42	4.84	2.36	0.71	1283	1515	50
VOR_EMB1_5	47.1	1.87	17.5	10.4	3.56	0.19	9.50	4.93	2.31	0.77	1099	1496	40
VOR_EMB1_6	47.2	1.80	17.5	10.7	3.49	0.29	9.45	4.98	2.32	0.75	1237	1217	30
VOR_EMB1_7	48.0	1.91	17.5	10.3	3.51	0.21	9.35	4.66	2.40	0.79	1070	1277	20
VOR_EMB1_8	47.9	1.83	17.4	10.6	3.45	0.23	9.20	4.95	2.49	0.79	703	1229	10
VOR_EMB2_1	47.4	1.90	17.3	10.4	3.67	0.21	9.32	5.10	2.50	0.76	1115	1342	108
VOR_EMB2_2	46.9	1.98	17.2	10.6	3.60	0.28	9.49	5.10	2.48	0.75	839	1299	98
VOR_EMB2_3	47.1	1.98	17.4	10.5	3.57	0.19	9.27	5.21	2.48	0.70	946	1342	88
VOR_EMB2_4	47.7	1.97	17.6	10.4	3.68	0.25	9.13	5.27	2.56	0.75	794	1384	78
VOR_EMB2_5	47.3	1.98	17.8	10.8	3.84	0.22	8.97	5.09	2.76	0.70	580	1467	53
VOR_EMB2_6	47.6	1.99	17.4	10.9	3.86	0.23	9.06	4.94	2.74	0.77	488	1151	46
VOR_EMB2_7	47.4	1.84	17.7	11.2	3.67	0.23	9.14	4.98	2.61	0.70	900	1062	31
VOR_EMB2_8	46.8	2.14	17.1	11.5	4.41	0.23	9.01	5.22	2.65	0.79	366	1263	15
VOR_EMB3_1	47.2	1.76	17.2	10.1	3.61	0.20	9.18	4.95	2.34	0.72	1100	1170	105
VOR_EMB3_2	47.5	1.78	17.4	10.0	3.73	0.17	9.20	4.82	2.36	0.78	734	1488	93
VOR_EMB3_3	47.6	1.78	17.2	10.0	3.85	0.19	9.09	4.96	2.32	0.71	1164	1555	81
VOR_EMB3_4	47.7	1.81	17.0	10.1	3.81	0.21	9.10	4.96	2.33	0.72	842	1315	69
VOR_EMB3_5	47.6	1.85	17.5	10.2	3.71	0.21	9.26	4.74	2.38	0.67	765	1721	57
VOR_EMB3_6	47.9	1.83	17.3	10.8	3.80	0.23	9.28	4.89	2.35	0.74	856	1279	47
VOR_EMB3_7	47.6	1.80	17.2	10.4	3.82	0.20	9.31	4.98	2.38	0.76	918	1267	37
VOR_EMB3_8	47.6	1.85	17.4	10.7	3.63	0.18	9.38	4.89	2.40	0.74	932	1093	27
VOR_EMB3_9	47.7	1.79	17.2	11.0	3.77	0.20	9.52	4.63	2.33	0.72	1330	1493	17

	SiO_2 wt%	TiO_2 wt%	Al_2O_3 wt%	FeO wt%	MgO wt%	MnO wt%	CaO wt%	Na_2O wt%	K_2O wt%	P_2O_5 wt%	S ppm	Cl ppm	µm
VOR_EMB4_1	47.1	1.84	17.6	10.3	3.73	0.26	9.12	5.03	2.32	0.70	1010	1279	63
VOR_EMB4_2	47.1	1.72	17.4	10.5	3.79	0.18	9.31	4.81	2.33	0.72	902	1159	55
VOR_EMB4_3	47.1	1.77	17.4	10.3	3.78	0.17	9.21	4.80	2.35	0.73	1056	1344	47
VOR_EMB4_4	47.0	1.86	17.2	10.4	3.86	0.26	9.36	4.69	2.29	0.64	947	1350	39
VOR_EMB4_5	46.7	1.85	17.6	10.3	3.98	0.20	9.36	4.75	2.26	0.72	1086	1278	31
VOR_EMB4_6	46.0	1.83	17.9	10.2	3.83	0.24	9.38	4.91	2.35	0.74	764	1092	23
VOR_EMB4_7	46.8	1.68	18.1	9.9	3.70	0.19	9.21	4.75	2.43	0.65	979	1273	15
VOR_EMB4_8	46.7	1.84	18.2	10.3	3.96	0.21	9.27	4.89	2.38	0.75	290	1104	5
VOR_EMB5_1	47.8	1.94	17.4	9.61	3.20	0.21	9.11	4.88	2.39	0.70	1054	1247	130
VOR_EMB5_2	46.8	1.95	17.5	10.2	3.85	0.17	9.00	4.78	2.24	0.75	1071	1326	120
VOR_EMB5_3	47.0	1.71	17.2	9.87	3.86	0.16	8.97	4.65	2.36	0.68	1086	1249	110
VOR_EMB5_4	47.4	1.90	17.2	10.0	3.90	0.13	8.85	4.45	2.32	0.65	1056	1369	100
VOR_EMB5_5	47.4	1.80	17.3	10.1	3.98	0.20	9.01	4.69	2.32	0.71	1102	1100	90
VOR_EMB5_6	47.3	1.84	17.2	10.2	4.00	0.15	8.97	4.57	2.30	0.73	1071	1381	80
VOR_EMB5_7	47.1	1.77	17.5	10.2	3.91	0.19	9.01	4.76	2.32	0.78	1392	1285	70
VOR_EMB5_8	47.1	1.83	17.1	10.1	3.81	0.18	9.04	4.66	2.32	0.71	903	992	60
VOR_EMB5_9	47.1	1.76	17.3	10.2	3.84	0.16	8.91	4.66	2.25	0.71	1040	1338	50
VOR_EMB5_10	47.2	1.71	17.1	10.5	3.93	0.27	9.12	4.69	2.24	0.73	948	1410	40
VOR_EMB5_11	47.1	1.88	17.4	10.7	4.01	0.25	9.28	4.66	2.31	0.71	1176	1319	30
VOR_EMB5_12	47.1	1.80	17.3	10.5	4.08	0.20	9.40	4.65	2.22	0.74	565	1188	20
VOR_EMB6_1	46.6	1.79	18.0	10.3	3.45	0.21	9.23	5.03	2.42	0.69	1237	1038	35
VOR_EMB6_2	46.5	1.87	18.3	10.3	3.45	0.17	9.28	5.05	2.39	0.70	718	1330	29
VOR_EMB6_3	46.3	1.97	18.3	10.6	3.56	0.21	9.33	4.95	2.44	0.70	915	1156	23
VOR_EMB6_4	46.1	1.90	18.2	10.3	3.71	0.14	9.24	4.95	2.41	0.71	1008	1097	17
VOR_EMB6_5	46.0	1.84	18.4	10.5	3.73	0.19	9.30	5.25	2.40	0.73	870	1139	11
VOR_EMB6_6	46.1	1.94	18.3	10.3	3.89	0.16	9.29	5.25	2.45	0.71	442	1329	5

	SiO_2 wt%	TiO_2 wt%	Al_2O_3 wt%	FeO wt%	MgO wt%	MnO wt%	CaO wt%	Na_2O wt%	K_2O wt%	P_2O_5 wt%	S ppm	Cl ppm	µm
DEC_EMB1_1	48.2	1.66	18.4	9.75	3.00	0.23	7.55	5.68	3.25	0.85	855	1658	54
DEC_EMB1_2	48.0	1.74	18.1	9.74	2.96	0.23	7.42	5.78	3.33	0.86	809	1848	47
DEC_EMB1_3	48.6	1.76	18.2	9.65	2.99	0.21	7.40	5.80	3.34	0.83	718	1812	40
DEC_EMB1_4	48.6	1.71	18.0	9.72	2.89	0.20	7.21	5.61	3.37	0.90	965	2137	33
DEC_EMB1_5	49.1	1.92	18.1	9.68	2.86	0.19	7.19	5.48	3.46	0.81	797	2108	26
DEC_EMB1_6	49.1	1.87	17.1	10.0	2.89	0.27	7.17	5.64	3.41	0.98	153	1937	12
DEC_EMB2_1	49.6	1.96	17.2	11.0	2.82	0.20	7.19	5.34	3.39	0.97	686	2030	33
DEC_EMB2_2	48.6	1.94	16.9	10.6	3.49	0.24	6.88	5.37	3.42	0.98	320	1912	27
DEC_EMB2_3	50.2	1.93	17.0	10.0	2.74	0.22	6.97	5.38	3.45	1.00	153	1894	21
DEC_EMB2_4	50.4	1.92	16.0	10.2	3.30	0.22	6.78	5.00	3.42	1.02	275	1634	14
DEC_EMB2_5	51.2	2.02	16.3	10.0	2.68	0.28	7.08	4.96	3.28	0.99	107	1420	7
DEC_EMB3_1	46.9	2.01	17.4	10.9	3.42	0.18	8.79	4.59	3.11	0.77	671	2143	70
DEC_EMB3_2	46.7	1.80	17.8	10.9	3.27	0.22	8.29	4.71	3.01	0.81	658	2123	53
DEC_EMB3_3	46.7	1.89	17.7	10.6	3.44	0.25	8.59	4.59	3.12	0.70	543	2127	35
DEC_EMB3_4	47.2	2.09	17.5	10.7	3.19	0.23	8.23	4.93	3.50	1.04	427	2126	18
DEC_EMB4_1	48.9	1.69	17.0	9.28	2.94	0.19	7.26	4.92	3.29	0.96	822	2147	40
DEC_EMB4_2	48.9	1.83	16.9	9.62	3.12	0.20	7.52	4.98	3.34	0.96	725	1999	60

Table A6: H_2O concentrations measured in melt embayments found in products from post-2011 activity at Mt. Etna by Raman Spectroscopy

Sample	I A_{OH}*	Norm. I**	H_2O wt% cubic baseline	µm***
NSEC_EMB1				
pt1 Z-2****	223510	310	1.07	60
pt2 Z-2	222699	309	1.06	55
pt3 Z-2	227353	316	1.09	50
pt4 Z-2	205083	285	0.97	45
pt5 Z-2	205845	286	0.97	40
pt6 Z-2	199148	277	0.94	35
pt7 Z-2	176331	245	0.82	30
pt8 Z-2	172912	240	0.80	25
pt9 Z-2	162091	225	0.74	20
pt10 Z-2	120223	167	0.52	15
pt11 Z-2	113320	157	0.48	10
NSEC_EMB2				
pt1 Z-2	273876	380	1.33	100
pt2 Z-2	270498	376	1.31	95
pt3 Z-2	255660	355	1.24	90
pt4 Z-2	253030	351	1.22	85
pt5 Z-2	249473	346	1.20	80
pt6 Z-2	242299	337	1.17	75
pt7 Z-2	246017	342	1.19	70
pt8 Z-2	249002	346	1.20	65
pt9 Z-2	245777	341	1.18	60
pt10 Z-2	234532	326	1.13	55
pt11 Z-2	227016	315	1.09	50
pt12 Z-2	223711	311	1.07	45
pt13 Z-2	207078	288	0.99	40
pt14 Z-2	204588	284	0.97	35
pt15 Z-2	184702	257	0.87	30
pt16 Z-2	178553	248	0.84	25
pt17 Z-2	162496	226	0.76	20
pt18 Z-2	154390	214	0.72	15
pt19 Z-2	145427	202	0.67	10
pt20 Z-2	120497	167	0.54	5
NSEC_EMB3				
pt1 Z-2	306587	426	0.96	82
pt2 Z-2	323313	449	1.01	75
pt3 Z-2	294850	410	0.92	68
pt4 Z-2	298942	415	0.94	61
pt5 Z-2	290715	404	0.91	54
pt6 Z-2	242593	337	0.77	47
pt7 Z-2	239520	333	0.76	40
pt8 Z-2	230450	320	0.73	33
pt9 Z-2	186784	259	0.60	26
pt10 Z-2	162562	226	0.53	19
pt11 Z-2	127607	177	0.43	12
pt12 Z-2	102757	143	0.35	5
NSEC_EMB4				
pt0 Z-2	337759	469	0.93	45
pt1 Z-2	329321	457	0.90	40
pt2 Z-2	335725	466	0.92	35
pt3 Z-2	328181	456	0.90	30
pt4 Z-2	289204	402	0.79	25
pt5 Z-2	265896	369	0.73	20
pt6 Z-2	259357	360	0.71	15
pt7 Z-2	233212	324	0.63	10
pt8 Z-2	184146	256	0.49	5

Sample	I A_{OH}	Norm. I	H_2O wt% cubic baseline	µm
NSEC_EMB5				
pt1 Z0	283297	393	0.76	55
pt2 Z-2	316971	440	0.85	50
pt3 Z-2	300926	418	0.80	45
pt4 Z-2	301971	419	0.81	40
pt5 Z-2	271184	377	0.73	35
pt6 Z-2	271259	377	0.73	30
pt7 Z-2	248415	345	0.67	25
pt8 Z-2	222766	309	0.60	20
pt9 Z-2	192730	268	0.52	15
pt10 Z-2	170174	236	0.46	10
pt11 Z-2	104844	146	0.29	5
VOR_EMB1				
pt1 Z-2	228116	317	1.29	85
pt2 Z-2	200774	279	1.14	77
pt3 Z-2	213462	296	1.21	69
pt4 Z-2	203541	283	1.15	61
pt5 Z-2	197283	274	1.12	53
pt6 Z-2	215167	299	1.22	45
pt7 Z-2	194430	270	1.10	37
pt8 Z-2	169103	235	0.96	29
pt9 Z-2	133158	185	0.75	21
pt10 Z-2	114300	159	0.65	13
pt11 Z-2	65491	91	0.37	5
VOR_EMB2				
pt1 Z-2	187916	261	0.94	105
pt2 Z-2	183490	255	0.92	97
pt3 Z-2	184764	257	0.93	89
pt4 Z-2	168208	234	0.84	81
pt5 Z-2	181721	252	0.91	73
pt6 Z-2	164671	229	0.82	65
pt7 Z-2	167270	232	0.84	57
pt8 Z-2	144931	201	0.72	45
pt9 Z-2	149824	208	0.75	37
pt10 Z-2	123654	172	0.61	29
pt11 Z-2	105874	147	0.52	21
pt12 Z-2	78264	109	0.38	13
pt13 Z-2	56066	78	0.26	5
VOR_EMB3				
pt1 Z-2	327522	455	1.48	101
pt2 Z-2	321699	447	1.45	93
pt3 Z-2	328673	456	1.49	85
pt4 Z-2	308371	428	1.39	77
pt5 Z-2	312073	433	1.41	69
pt6 Z-2	299711	416	1.35	61
pt7 Z-2	295566	411	1.33	53
pt8 Z-2	272838	379	1.22	45
pt9 Z-2	256035	356	1.13	37
pt10 Z-2	238916	332	1.05	29
pt11 Z-2	179402	249	0.76	21
pt12 Z-2	140706	195	0.58	13
pt13 Z-2	106474	148	0.41	5

Sample	I A_{OH}	Norm. I	H_2O wt% cubic baseline	µm
VOR_EMB4				
pt1 Z-2	288230	400	1.27	59
pt2 Z-2	287300	399	1.27	51
pt3 Z-2	289657	402	1.28	43
pt4 Z-2	261783	364	1.15	35
pt5 Z-2	248816	346	1.09	27
pt6 Z-2	229138	318	0.99	19
pt7 Z-2	171957	239	0.72	11
pt8 Z-2	125635	174	0.50	5
VOR_EMB5				
pt1 Z-2	371520	516	1.68	136
pt2 Z-2	363627	505	1.64	128
pt3 Z-2	368850	512	1.67	120
pt4 Z-2	362432	503	1.64	112
pt5 Z-2	379580	527	1.72	104
pt6 Z-2	369887	514	1.67	96
pt7 Z-2	362288	503	1.64	88
pt8 Z-2	360353	500	1.63	80
pt9 Z-2	353559	491	1.60	72
pt10 Z-2	329301	457	1.49	64
pt11 Z-2	328861	457	1.48	56
pt12 Z-2	312717	434	1.41	48
pt13 Z-2	310353	431	1.40	40
pt14 Z-2	295977	411	1.33	32
pt15 Z-2	264898	368	1.19	24
pt16 Z-2	229167	318	1.03	16
pt17 Z-2	186078	258	0.83	10
pt18 Z-2	148579	206	0.66	5
VOR_EMB6				
pt1 Z-2	234314	325	1.01	45
pt2 Z-2	224198	311	0.97	40
pt3 Z-2	223095	310	0.96	35
pt4 Z-2	216643	301	0.94	30
pt5 Z-2	219078	304	0.95	25
pt6 Z-2	176800	246	0.77	20
pt7 Z-2	146254	203	0.64	15
pt8 Z-2	113925	158	0.50	10
pt9 Z-2	94337	131	0.42	5
DEC_EMB1				
pt1 Z-2	155139	215	0.54	55
pt2 Z-2	163238	227	0.56	50
pt3 Z-2	160091	222	0.55	45
pt4 Z-2	161883	225	0.56	40
pt5 Z-2	149119	207	0.52	35
pt6 Z-2	141983	197	0.49	30
pt7 Z-2	130281	181	0.46	25
pt8 Z-2	121533	169	0.43	20
pt9 Z-2	115822	161	0.41	15
pt10 Z0	89247	124	0.33	10
pt11 Z0	67155	93	0.26	5

Sample	I A_{OH}	Norm. I	H_2O wt% cubic baseline	µm
DEC_EMB2				
pt1 Z-2	121974	169	0.33	40
pt2 Z-2	114257	159	0.31	35
pt3 Z-2	121469	169	0.33	30
pt4 Z-2	113756	158	0.31	23
pt5 Z-2	97156	135	0.26	18
pt6 Z-2	107557	149	0.29	13
pt7 Z-2	83158	115	0.22	8
pt8 Z-2	57540	80	0.14	3
DEC_EMB3				
pt1 Z-2	261828	364	0.62	60
pt2 Z-2	240061	333	0.57	52
pt3 Z-2	232370	323	0.55	44
pt4 Z-2	228389	317	0.54	36
pt5 Z-2	202303	281	0.48	28
pt6 Z-2	198329	275	0.47	23
pt7 Z-2	158159	220	0.37	18
pt8 Z-2	138804	193	0.33	13
pt9 Z-2	75151	104	0.18	8
DEC_EMB4				
pt1 Z-2	299406	416	0.78	63
pt2 Z-2	248636	345	0.66	55
pt3 Z-2	264833	368	0.69	47
pt4 Z-2	229410	319	0.61	42
pt5 Z-2	220219	306	0.59	37
pt6 Z-2	251516	349	0.66	32
pt7 Z-2	225265	313	0.60	27
pt8 Z0	183215	254	0.50	22

* I. A_{OH}: Area intensity of the water band between 3000 and 3700 cm^{-1};

** Norm. I: normalized intensity to acquisition time [A_{OH}/(power × time)];

*** Each spot distance is measured from the bubble at outlet embayment;

**** Z-2: focus depth fixed at 2 µm under the surface; Z0: focus depth fixed on the surface.

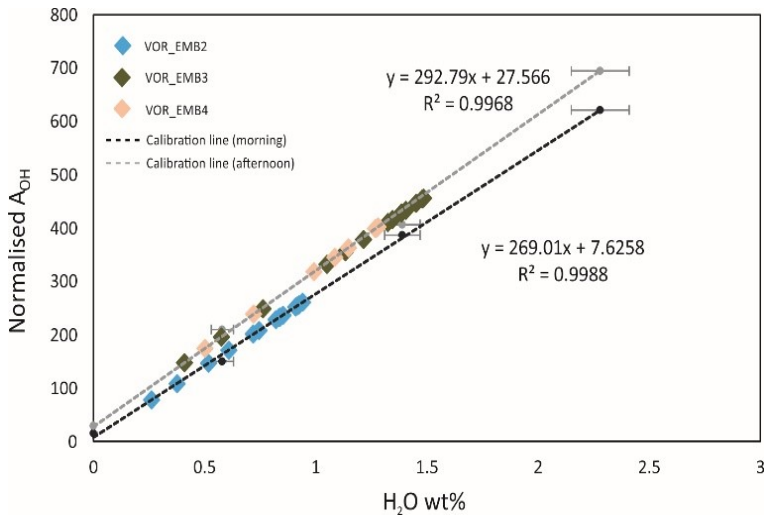

Figure S1: *Example of external calibration lines used for H_2O quantification by Raman analyses.*

Table A7: Whole rock compositions used for H_2O-SiO_2 loss correction on melt inclusion analyzed for the selected eruption from the post 2011 activity at Mt. Etna. Samples b32 and c7a2 from Viccaro et al. (2014); samples VOR5 and SEC12 from Viccaro et al. (2019).

	NSEC 2013		VOR 2015 – DEC 2018	
Date	5-Jan-12	5-Mar-13	4-Dec-2015	19-apr-17
Sample	b32	c7a2	VOR5	SEC12
Type MI	1	2	1	2
SiO_2 wt%	46.4	48.5	47.5	48.7
TiO_2 wt%	2.00	1.80	1.85	1.71
Al_2O_3 wt%	16.1	17.7	15.8	17.2
FeOt wt%	11.9	10.4	11.4	10.0
MnO wt%	0.22	0.20	0.20	0.18
MgO wt%	5.54	3.95	5.76	4.67
CaO wt%	10.9	9.40	10.5	10.2
Na_2O wt%	3.29	4.17	3.36	3.81
K_2O wt%	1.97	2.18	1.88	1.88
Total	98.2	98.3	98.3	98.4

Table A8: Results from volatile diffusion modeling on melt-embayments of February 19, 2013, December 3, 2015 and December 24-27, 2018 eruptions at Mt. Etna.

	H_2O_i (wt%)	S_i (ppm)*	P_i (MPa)	P_f (MPa)	*dP/dt* (MPa/s)	t (min)	v (m/s)	range *dP/dt*	χ^2
NSEC_emb1	2.19	825	106	1	0.20 (0.17-0.23)	8.7	7.7 (6.5-8.6)	0.1-1.0	24.6
NSEC_emb2	2.23	942	110	2	0.26 (0.22-0.31)	6.9	10.0 (8.5-11.9)	0.1-1.0	5.6
NSEC_emb3	1.99	412	84	1	0.11 (0.09-0.13)	12.6	4.2 (3.5-5.0)	0.01-0.5	12.0
NSEC_emb4	2.15	724	101	2	0.41 (0.35-0.47)	4.0	15.8(13.4-18.1)	0.1-1.0	2.5
NSEC_emb5	2.21	888	108	1	0.13 (0.11-0.15)	13.7	5.0 (4.2-5.8)	0.01-0.5	9.6
Average					0.22 (±0.12)	9.2 (±4.0)	9.6 (±4.6)		
VOR_emb1	2.31	1245	120	1	0.34 (0.29-0.40)	5.5	13.1 (11.6-15.4)	0.1-1.0	18.5
VOR_emb2	2.24	992	112	1	0.044 (0.038-0.052)	42.1	1.7 (1.5-2.0)	0.01-0.1	57.2
VOR_emb3	2.24	999	112	2	0.34 (0.27- 0.38)	5.4	13.1 (10.4-14.6)	0.1-1.0	50.4
VOR_emb4	2.24	989	112	2	0.57 (0.50-0.68)	3.2	21.9 (19.2-26.2)	0.1-1.0	8.1
VOR_emb5	2.26	1073	114	2	0.57 (0.49-0.71)	3.3	21.9 (18.9-27.3)	0.1-1.0	4.6
VOR_emb6	2.23	956	110	1	0.48 (0.39-0.56)	3.8	18.5 (18.1-24.6)	0.1-1.0	17.5
Average**					0.46 (±0.12)	4.2 (±1.1)	17.7 (±5.0)		
DEC_emb1	2.23	965	110	1	0.055 (0.047-0.065)	33.0	2.1 (1.8-2.5)	0.01-0.1	1.4
DEC_emb2	2.13	686	99	1	0.017 (0.014-0.019)	96.1	0.7 (0.5-0.7)	0.01-0.05	12.3
DEC_emb3	2.12	671	97	1	0.024 (0.021-0.029)	66.7	0.9 (0.8-1.1)	0.01-0.1	57.9
DEC_emb4	2.17	773	103	1	0.075 (0.063-0.088)	22.7	2.9 (2.4-3.4)	0.01-0.1	5.7
Average					0.043 (±0.027)	54.6 (±33.4)	1.6 (±1.0)		

* S initial concentrations are average values considering the first 1-4 spots measured in the embayments interior

** sample VOR2015_emb2 is not considered in the calculation of average values

REFERENCES

Ágústsdóttir, T., Woods, J., Greenfield, T., Green, R.G., White, R.S., Winder, T., Brandsdóttir, B., Steinthórsson, S., Soosalu H., (2016). Strike-slip faulting during the 2014 Bárdarbunga–Holuhraun dike intrusion, central Iceland. Geophysical Reseasrch Letteres, 43 (4), 1495-1503.

Aiuppa, A., Moretti, R., Federico, C., Giudice, G., Liuzzo, M., Papale, P., Shinohara, H., Valenza, M. (2007). Forecasting Etna eruptions by real-time observation of volcanic gas composition. Geology, 35, 1115-1118.

Allan, A.S.R., Morgan, D.J., Wilson, C.J.N. Millet, M. (2013). From mush to eruption in centuries: assembly of the super-sized Oruanui magma body. Contributions to Mineralogy and Petrology, 166, 143–164.

Allard, P., Alparone, S., Andronico, D., Burton, M., Lodato, L., Mure`, F., Sgroi, T. (2003). Source process of cyclic fire fountaining at Mt. Etna in 2000: A multidisciplinary study of the June 14 (63rd) event. Geophysical Research Abstracts, 5, 13079–13080.

Allard, P., Burton, M., Mure, F. (2005), Spectroscopic evidence for a lava fountain driven by previously accumulated magmatic gas. Nature, 433, 407–410.

Alparone, S., Andronico, D., Lodato, L., Sgroi, T., 2003. Relationship between tremor and volcanic activity during the Southeast Crater eruption on Mount Etna in early 2000. Journal of Geophysical Research: Solid Earth, 108 (B5), 2241.

Alparone, S., Barberi, G., Giampiccolo, E., Maiolino, V., Mostaccio, A., Musumeci, C., Scaltrito, A., Scarfì L., Tuvè, T., Ursino, A. (2020). Seismological constraints on the 2018 Mt. Etna (Italy) flank eruption and implications for the flank dynamics of the volcano. Terra Nova, 1–11.

Armienti, P., Innocenti, F., Petrini, R., Pompilio, M., Villari, L. (1988). Sub-aphyric alkali basalts from Mount Etna: inferences on the depth and composition of the magma source. Rendiconti Società Italiana di Mineralogia e Petrologia, 43, 877–891.

Armienti, P., Perinelli, C., Putirka, K. D. (2013) A New Model to Estimate Deep-level Magma Ascent Rates, with Applications to Mt. Etna (Sicily, Italy). Journal of Petrology, 54, 795-813.

Arzilli, F., La Spina, G., Burton, M.R. et al. (2019). Magma fragmentation in highly explosive basaltic eruptions induced by rapid crystallization. Nature Geoscience, 12, 1023–1028.

Barth, A., Newcombe, M.E., Plank, T., Gonnermann, H., Hajimirza, S., Soto, G.J., Saballos, A., Hauri, E. (2019). Magma decompression rate correlates with explosivity at basaltic volcanoes - constraints from water diffusion in olivine. . Journal of Volcanology and Geothermal Research, 387, 106664.

Behncke, B., Branca, S., Corsaro, R.A., De Beni, E., Miraglia, L., Proietti C. (2014). The 2011–2012 summit activity of Mount Etna: Birth, growth and products of the new SE crater. Journal of Volcanology and Geothermal Research, 270, 10–21.

Behrens, H., Zhang, Y., Xu, Z. (2004). H_2O diffusion in dacitic and andesitic melts. Geochimica et Cosmochimica Acta, 68, 5139–5150.

Behrens, H., Roux, J., Neuville, D.R., Siemann, M. (2006). Quantification of dissolved H_2O in silicate glasses using confocal microRaman spectroscopy. Chemical Geology, 229 (1), 96–112.

Berry, A.J., Hermann, J., O'Neill, H.S.C., Foran, G.J. (2005). Fingerprinting the water site in mantle olivine. Geology, 33, 11, 869–872.

Bonaccorso, A., Currenti, G., Linde, A., Sacks, S. (2013). New data from borehole strainmeters to infer lava fountain sources (Etna 2011–2012). Geophysical Research Letters, 40 (14), 3579–3584.

Bonaccorso, A., Calvari, S. (2017). A new approach to investigate an eruptive paroxysmal sequence using camera and strainmeter networks: Lessons from the 3–5 December 2015 activity at Etna volcano. Earth and Planetary Science Letters 475, 231–241.

Borzi, A.M., Giuffrida, M., Zuccarello, F., Palano, M., Viccaro, M. (2020). The Christmas 2018 eruption at Mount Etna: Enlightening how the volcano factory works through a multiparametric inspection. Geochemistry, Geophysics, Geosystems, 21.

Branca, S., Del Carlo, P. (2005). Types of eruptions of Etna Volcano AD 1670-2003: Implications for short-term eruptive behavior. Bulletin of Volcanology, 67, 732-742.

Branca, S., Coltelli, M., De Beni, E., Wijbrans, J. (2008). Geological evolution of Mount Etna volcano (Italy) from earliest products until the first central volcanism (between 500 and 100 ka ago) inferred from geochronological and stratigraphic data. International Journal of Earth Sciences, 97, 135-152.

Branca, S., Coltelli, M., Groppelli, G. (2011). Geological evolution of a complex basaltic stratovolcano: Mount Etna, Italy. Italian Journal of Geosciences, 130 (3), 306-317.

Browne B.L., Gardner JE (2006). The influence of magma ascent path on the texture, mineralogy, and formation of Hornblende reaction rims. Earth and Planetary Science Letters, 246, 161-176.

Browne B.L., Szramek, L. (2015). Rates of Magma Ascent and Storage, in H. Sigurdsson et al., eds, Encyclopedia of Volcanology (2nd ed). London: Academic Press, 203-214.

Calvari, S., Coltelli, M., Neri, M., Pompilio, M., Scribano, V. (1994). The 1991-1993 Etna eruption: chronology and lava. Acta Vulcanologica, 4, 1–14.

Cannata, A., Spedalieri, G., Behncke, B., Cannavò, F., Di Grazia, G., Gambino, S., Gresta, S., Gurrieri, S., Liuzzo, M., Palano, M. (2015). Pressurization and depressurization phases inside the plumbing system of Mount Etna volcano: Evidence from a multiparametric approach. Journal of Geophysical Research: Solid Earth, 120, 5965–5982.

Cannata, A., Di Grazia, G., Giuffrida, M., Gresta, S., Palano, M., Sciotto, M., Viccaro, M. Zuccarello, F. (2018). Space-time evolution of magma storage and transfer at Mt. Etna volcano (Italy): The 2015–2016 reawakening of Voragine crater. Geochemistry, Geophysics, Geosystems, 19, 471–495.

Charlier, B.L.A., Morgan, D.J., Wilson, C.J.N., Wooden, J.L., Allan, A.S.R., Baker, J.A. (2012). Lithium concentration gradients in feldspar and quartz record the final minutes of magma ascent in an explosive supereruption. Earth Planetary Science Letters 319, 218–227.

Clocchiatti, R., Joron, J.L., Treuil, M., (1988). The role of selective alkali contamination in the evolution of recent historic lavas of Mt. Etna. Journal of Volcanology and Geothermal Research, 34, 241–249.

Clocchiatti, R., Condomines, M., Guenot, N., Tanguy, J.C., (2004). Magma changes at Mount Etna: The 2001 and 2002–2003 eruptions. Earth and Planetary Science Letters, 226, 397–414.

Collins, S.J., Pyle, D.M., Maclennan, J. (2009). Melt inclusions track pre-eruption storage and dehydration of magmas at Etna. Geology, 37, 571–574.

Coltelli, M., Del Carlo, P., Vezzoli, L., (1998). Discovery of a Plinian basaltic eruption of Roman age at Etna volcano, Italy. Geology, 26, 1095 – 1098.

Coltelli, M., Del Carlo, P., Pompilio,M., Vezzoli, L. (2005). Explosive eruption of a picrite: the 3930 BP subplinian eruption of Etna volcano (Italy). Geophysical Research Letters, 32, L23307.

Correale, A., Paonita, A., Martelli, M., Rizzo, A., Rotolo, S.G., Corsaro, R.A., Di Renzo,V. (2014). A two-component mantle source feeding Mt. Etna magmatism: insights from the geochemistry of primitive magmas. Lithos, 184-187, 243–258.

Corsaro, R.A., Pompilio, M. (2004). Buoyancy-controlled eruptions of magmas at Mt. Etna. Terra Nova 16, 6–22.

Costa F., Chakraborty, S. (2004). Decadal time gaps between mafic intrusion and silicic eruption obtained from chemical zoning patterns in olivine. Earth and Planetary Science Letters 227, 517-530.

Costa, F., Dohmen, R., Chakraborty, S. (2008). Time scales of magmatic processes from modeling the zoning patterns of crystals. In: Putirka, K.D., and Tepley F.J.III. (eds), Minerals, Inclusions and Volcanic Processes. Reviews in Mineralogy and Geochemistry, 69, 545-594.

Crank, J. (1975). The Mathematics of Diffusion. 2nd edition. Oxford Science Publication, Oxford.

deGraffenried R., Shea T. (2020). How Robust Are Our Assumptions in Using Crystal-Hosted Melt Embayments to Estimate Magma Ascent Rate?. AGUFM, V13C-0168.

D'Aleo, R., Bitetto, M., Delle Donne, D., Coltelli, M., Coppola, D., McCormick Kilbride, B., Pecora, E., Ripepe, M., Salem, L.C., Tamburello, G. Aiuppa, A. (2019). Understanding the SO_2 Degassing Budget of Mt Etna's Paroxysms: First Clues From the December 2015 Sequence. Frontiers in Earth Science, 6, 239.

Danyushevsky, L., Della-Pasqua, F. & Sokolov, S. (2000). Re-equilibration of melt inclusions trapped by magnesian olivine phenocrysts from subduction-related

magmas: petrological implications. Contribution to Mineralogy and Petrology, 138, 68–83.

Danyushevsky, L.V., Plechov, P. (2011). Petrolog3: integrated software for modeling crystallization processes. Geochemistry, Geophysics, Geosystems, 12, Q07021.

Demouchy, S., Mackwell, S.J. (2003). Water diffusion in synthetic iron-free forsterite. Physics and Chemistry of Minerals, 30, 486–494.

Demouchy, S., Mackwell, S.J. (2006). Mechanisms of hydrogen incorporation and diffusion in iron-bearing olivine. Physics and Chemistry of Minerals, 33, 347–355.

Di Genova, D., Sicola, S., Romano, C., Vona, A., Fanara, S., Spina, L. (2017). Effect of iron and nanolites on Raman spectra of volcanic glasses: a reassessment of existing strategies to estimate the water content. Chemical Geology, 475, 76–86.

Dixon, J.E. (1997). Degassing of alkalic basalts. American Mineralogist 82, 368–378.

Doglioni, C., Innocenti, F., Mariotti, G. (2001). Why Mt Etna?. Terra Nova, 13 (1), 25-31.

Falloon, T.J., Green, D.H. (1987). Anhydrous partial melting of MORB pyrolite and other peridotite compositions at 10 kbar: implication for the origin of primitive MORB glasses. Mineralogy and Petrology, 37, 181–219.

Ferguson, D.J., Gonnermann, H.M., Ruprecht, P., Plank, T., Hauri, E.H., Houghton, B.F., Swanson, D.A. (2016). Magma decompression rates during explosive eruptions of Kilauea volcano, Hawaii, recorded by melt embayments. Bulletin of Volcanology, 78 (10).

Ferlito, C., Viccaro, M., Cristofolini, R. (2008). Volatile-induced differentiation in the plumbing system of Mt. Etna volcano (Italy): evidence from glass in tephra of the 2001 eruption. Bulletin of Volcanology, 70, 455–473.

Ferlito, C., Lanzafame, G. (2010). The role of supercritical fluids in the potassium enrichment of magmas at Mount Etna volcano (Italy). Lithos, 119, 642–650.

Ferlito, C., Viccaro, M., Nicotra, E., Cristofolini, R. (2012). Regimes of magma recharge and their control on the eruptive behaviour during the 2001-2005 period at Mt. Etna (Italy). Bullettin of Volcanology, 74533-54.

Ferriss, E., Plank, T., Walker, D., Nettles, M. (2015). The whole-block approach to measuring hydrogen diffusivity in nominally anhydrous minerals. American Mineralogist, 100 (4), 837–851.

Frazzetta, G., Romano, R. (1984). The 1983 Etna eruption: Event chronology and morphological evolution of the lava flow. Bullettin of Volcanology, 47, 1079–1096.

Freda, C., Baker, D.R., Scarlato, P. (2005). Sulfur diffusion in basaltic melts. Geochimica et Cosmochimica Acta, 69, 5061–5069.

Freret-Lorgeril, V., Donnadieu, F., Scollo, S., Provost, A., Fréville, P., Guéhenneux, Y., Hervier, C., Prestifilippo, M. Coltelli, M. (2018). Mass Eruption Rates of Tephra Plumes During the 2011–2015 Lava Fountain Paroxysms at Mt. Etna From Doppler Radar Retrievals. Frontiers in Earth Science, 6-73.

Gaetani, G.A., O'Leary, J.A., Shimizu, N., Bucholz, C.E., Newville, M. (2012). Rapid reequilibration of H_2O and oxygen fugacity in olivine-hosted melt inclusions. Geology, 40, 915–918.

Genareau, K., Clarke, A. B. (2010). In situ measurements of plagioclase growth using SIMS depth profiles of $^{7}Li/^{30}Si$: a means to acquire crystallization rates during short duration decompression events. American Mineralogist, 95, 592–601.

Gennaro, E., Iacono-Marziano, G., Paonita, A., Rotolo, S.G., Martel, C., Rizzo, A.L., Pichavant, M., Liotta, M. (2019). Melt inclusions track melt evolution and degassing of Etnean magmas in the last 15 ka. Lithos, 324–325, 716–732.

Geschwind, C. H., Rutherford, M. J. (1995). Crystallization of microlites during magma ascent M the fluid-mechanics of 1980-1986 eruptions at Mount St. Helens. Bulletin of Volcanology, 57(5), 356-370.

Ghiorso, M.S., Gualda, G.A.R. (2015). An H_2O–CO_2 mixed fluid solubility model compatible with rhyolite-MELTS. Contributions to Mineralogy and Petrology, 169, 53.

Giacomoni, P.P., Ferlito, C., Coltorti, M., Bonadiman, C., Lanzafame, G. (2014). Plagioclase as archive of magma ascent dynamics on "open conduit" volcanoes: the 2001–2006 eruptive period at Mt. Etna. Earth Science Reviews, 138, 371–393.

Giudicepietro, F., López, C., Macedonio, G. et al. (2020). Geophysical precursors of the July-August 2019 paroxysmal eruptive phase and their implications for Stromboli volcano (Italy) monitoring. Scientific Reportsm 10, 10296.

Giuffrida, M., Viccaro, M. (2017). Three years (2011–2013) of eruptive activity at Mt. Etna: Working modes and timescales of the modern volcano plumbing system from micro-analytical studies of crystals. Earth Science Reviews, 171, 289–322.

Giuffrida, M., Holtz, F., Vetere, F, Viccaro, M., (2017). Effects of CO_2 flushing on crystal textures and compositions: experimental evidence from recent K-trachybasalts erupted at Mt. Etna. Contributions to Mineralogy and Petrology, 172, 90.

Giuffrida, M., Viccaro, M. Ottolini, L. (2018). Ultrafast syn-eruptive degassing and ascent trigger high-energy basic eruptions. Scientific Reports, 8, 147.

Gonnermann, H.M., Manga, M. (2007). The fluid mechanics inside a volcano. Annual Review of Fluid Mechanics, 39, 321–356.

Gonnermann, H.M. (2015). Magma fragmentation. Annual Review of Earth and Planetary Sciences, 43, 431–458.

Gualda, G.A.R., Ghiorso, M.S., Lemons, R.V., Carley, T.L. (2012). Rhyolite-MELTS: a modified calibration of MELTS optimized for silica-rich, fluid-bearing magmatic systems. Journal of Petrology, 53, 875–890.

Hanyua, T., Yamamoto, J., Kimoto, K., Shimizu, K., Ushikubo, T. (2020). Determination of total CO2 in melt inclusions with shrinkage bubbles. Chemical Geology, 557.

Hartley, M.E., Maclennan, J., Edmonds, M. and Thordarson, T. (2014). Reconstructing the deep CO_2 degassing behaviour of large basaltic fissure eruptions. Earth and Planetary Science Letters, 393, 120–131.

Houghton, B.F., Gonnermann, H.M. (2008). Basaltic explosive volcanism: constraints from deposits and models. Chemie der Erde, 68, 117–140.

Humphreys, M.C.S., Menand, T., Blundy, J.D., Klimm, K. (2008). Magma ascent rates inexplosive eruptions: Constraints from H_2O diffusion in melt inclusions. Earth and Planetary Science Letters, 270 (1-2), 25-40.

Johnson, E.R., Wallace, P.J., Cashman, K.V., Delgado Granados, H. (2010). Degassing of volatiles (H_2O, CO_2, S, Cl) during ascent, crystallization, and eruption of basaltic magmas in the central Trans-Mexican Volcanic Belt. Journal of Volcanology and Geothermal Research, 197, 225–238.

Kahl, M., Chakraborty, S., Pompilio, M., Costa, F. (2015). Constraints on the Nature and Evolution of the magma plumbing system of Mt. Etna Volcano (1991–2008) from a combined thermodynamic and kinetic modelling of the compositional record of minerals. Journal of Petrology 56, 2025-2068.

Kamenetsky, V., Clocchiatti, R. (1996). Primitive magmatism of Mt. Etna: insights from mineralogy and melt inclusions. Earth and Planetary Science Letters, 142 (3-4), 553-572.

Kamenetsky, V.S., Pompilio, M., Metrich, N., Sobolev, A.V., Kuzmin, D.V., Thomas, R. (2007). Arrival of extremely volatile-rich high-Mg magmas changes explosivity of Mount Etna. Geology, 35, 255-258.

Kawakami, Y., Yamamoto, J., Kagi, H. (2003) Micro-Raman densimeter for CO_2 inclusions in mantle-derived minerals. Applied Spectroscopy, 57, 1334–1339

Kerrick, D.M. Jacobs, G.K. (1981). A modified Redlich-Kwong equation for H_2O, CO_2 and H_2O-CO_2 mixtures at elevated pressures and temperatures. American Journal of Science, 281, 735-767.

Kohlstedt, D.L., Mackwell, S.J., 1998, Diffusion of hydrogen and intrinsic point defects in olivine. Zeitschrift für Physikalische Chemie, 207, 147–162.

Le Losq, C., Neuville, D., Moretti, R., Roux, J., 2012. Determination of water content in silicate glasses using Raman spectrometry: implications for the study of explosive volcanism. American Mineralogist, 97, 779–790

Le Voyer, M., Asimow, P.D., Mosenfelder, J.L., Guan, Y., Wallace, P., Schiano, P., Stolper, E.M., Eiler, J.M. (2014). Zonation of H_2O and F concentrations around melt inclusions in olivines. Journal of Petrology, 55 (4), 685–707.

Lemaire, C., Kohn, S., Brooker, R.A., 2004. The effect of silica activity on the incorporation mechanisms of water in synthetic forsterite: a polarised infrared spectroscopic study. Contribution to Mineralogy and Petrology, 147, 48–57.

Lentini, F. (1982). The Geology of Mt. Etna Basement. vol. 23. Memorie della Società Geologica Italiana, 7–25.

Liu, Y., Anderson, A.T., Wilson, C.J.N. (2007). Melt pockets in phenocrysts and decompression rates of silicic magmas before fragmentation. Journal of Geophysical Research-Solid Earth, 112(B6), 12.

Lloyd, A., Plank, T., Ruprecht, P., Hauri, E., Rose, W. (2013). Volatile loss from melt inclusions in pyroclasts of differing sizes. Contributions to Mineralogy and Petrology, 165, 129–153.

Lloyd, A., Ruprecht, P., Hauri, E., Rose, W., Gonnermann, H.H., Plank, T. (2014). NanoSIMS results from olivine-hosted melt embayments: Magma ascent rate during explosive basaltic eruptions. Journal of Volcanology and Geothermal Research, 283, 1–18.

Lloyd, A.S., Ferriss, E., Ruprecht, P., Hauri, E., Brian, R.J., Plank, T. (2016). An assessment of clinopyroxene as a recorder of magmatic water and magma ascent rate. Journal of Petrology, 57(10), 1865-1886.

Mackwell, S.J., Kohlstedt, D.L. (1990). Diffusion of hydrogen in olivine: Implications for water in the mantle. Journal of Geophysical Research, 95, B4, 5079–5088.

Maclennan J. (2017). Bubble formation and decrepitation control the CO2 content of olivine-hosted melt inclusions. Geochemistry, Geophysics, Geosystems, 18, GC006633.

Mangan, M.T., Cashman, K.V. (1996). The structure of basaltic scoria and reticulite and inferences for vesiculation, foam formation, and fragmentation in lava fountains. Journal of Volcanological and Geothermarl Research, 73, 1–18.

Mercier, M., Di Muro, A., Giordano, D., Métrich, N., Lesne, P., Pichavant, M., Scaillet, B., Clocchiatti, R., Montagnac, G., 2009. Influence of glass polymerisation and oxidation on micro-Raman water analysis in alumino-silicate glasses. Geochimica et Cosmochimica Acta, 73, 197–217.

Métrich N., Clocchiatti, R. (1996). Sulfur abundance and its speciation in oxidized alkaline melts. Geochimica et Cosmochimica Acta, 60, 4151– 4160.

Métrich, N., Allard, P., Spilliaert, N., Andronico, D., Burton, M. (2004). 2001 flank eruption of the alkali- and volatile-rich primitive basalt responsible for Mount Etna's evolution in the last three decades. Earth and Planetary Science Letters, 228, 1–17.

Mollo, S., Giacomoni, P. P., Coltorti, M., Ferlito, C., Iezzi, G., Scarlato, P. (2015). Reconstruction of magmatic variables governing recent Etnean eruptions: constraints from mineral chemistry and P-T-fO_2-H_2O modelling. Lithos, 212–215, 311–320.

Monaco, C., Tapponier, P., Tortorici, L., Gillot, P. Y. (1997). Late Quaternary slip rates on the Acireale-Piedimonte normal faults and tectonic origin of Mt. Etna (Sicily). Earth and Planetary Science Letters 147, 125-139.

Moore, R.L., Mirinov, N., Portnyagin, M., Gazel, E. and Bodnar, R.J. (2018). Volatile contents of primitive bubble-bearing melt inclusions from Klyuchevskoy volcano, Kamchatka: Comparison of volatile contents determined by mass-balance versus experimental homogenization. Journal of Volcanology and Geothermal Research, 358, 124-131.

Moore, L. R., Gazel, E., Tuohy, R., Lloyd, A.S., Esposito, R., Steele-MacInnis, M., Hauri, E. H., Wallace, P.J., Plank, T., Bodnar R.J. (2015). Bubbles matter: An assessment of the contribution of vapor bubbles to melt inclusion volatile budgets. American Mineralogist. 100, 806–823.

Moretti, R., Métrich, N., Arienzo, I., Di Renzo, V., Aiuppa, A., Allard, P. (2018). Degassing vs. eruptive styles at Mt. Etna volcano (Sicily, Italy). Part I: Volatile stocking, gas fluxing, and the shift from low-energy to highly explosive basaltic eruptions. Chemical Geology, 482, 1-17.

Morgan, D.J., Blake, S., Rogers, N.W.B., DeVivo, B., Rolandi, G., Macdonald, R., Hawkesworth, C. J. (2004). Time scales of crystal residence and magma chamber

volume from modelling of diffusion profiles in phenocrysts: Vesuvius 1944. Earth Planetary Science Letters 222, 933-946.

Moussallama, Y., Edmonds, M., Scaillet, B., Peters, N., Gennaro, E., Sides, I., Oppenheimer, C., (2016). The impact of degassing on the oxidation state of basaltic magmas: a case study of Kilauea volcano. Earth and Planetary Science Letters, 450, 317-325.

Mysen, B.O., Richet, P., 2005. Silicate Glasses and Melts: Properties and Structure. Elsevier Science.

Nichols, A.R.L., Wysoczanski, R.J. (2007). Using micro-FTIR spectroscopy to measure volatile contents in small and unexposed inclusions hosted in olivine crystals. Chemical Geology, 242 (3-4), 371-384.

Newman, S., Lowenstern, J.B. (2002). VolatileCalc: a silicate melt–H_2O–CO_2 solution model written in Visual Basic for excel. Computers & Geosciences, 28, 597–604.

Padrón-Navarta, J.A., Hermann, J., O'Neill, H.S.C., 2014. Site-specific hydrogen diffusion rates in forsterite. Earth and Planetary Science Letters, 392, 100–112.

Papale, P., Moretti, R., Barbato, R. (2006). The compositional dependence of the saturation surface of H_2O + CO_2 fluids in silicate melts. Chemical Geology, 229, 78-95.

Pardini, F., Queißer, M., Naismith, A., Watson, I.M., Clarisse, L., Burton, M.R. (2018). Initial constraints on triggering mechanisms of the eruption of Fuego volcano (Guatemala) from 3 June 2018 using IASI satellite data. Journal of Volcanology and Geothermal Research, 376, 54-61.

Parfitt, E.A. (2004). A discussion of the mechanisms of explosive basaltic eruptions. Journal of Volcanology and Geothermal Research, 134, 77–107.

Patanè, D., Aiuppa, A., Aloisi, M., Behncke, B., Cannata, A., Coltelli, M., Di Grazia, G., Gambino, S., Gurrieri, S., Mattia, M., Salerno, G. (2013). Insights into magma and

fluid transfer at Mount Etna by a multiparametric approach: A model of the events leading to the 2011 eruptive cycle. Journal of Geophysical Research, 118, 3519-3539.

Pérez, W., Freundt, A., Kutterolf, S., Schmincke, H.U. (2009). The Masaya Triple Layer: A 2100 year old basaltic multi-episodic Plinian eruption from the Masaya Caldera Complex (Nicaragua). Journal of Volcanology and Geothermal Research, 179 (3-4), 191-205.

Pioli, L., Azzopardi, B.J., Cashman, K.V. (2009). Controls on the explosivity of scoria cone eruptions: magma segregation at conduit junctions. Journal of Volcanology and Geothermal Research, 186 (3-4), 407–415.

Plank, T., Kelley, K.A., Zimmer, M.M., Hauri, E.H., Wallace, P.J. (2013). Why do mafic arc magmas contain ~4 wt% water on average? Earth and Planetary Science Letters, 364, 168–179.

Polacci, M., Corsaro, R.A., Andronico, D. (2006). Coupled textural and compositional characterization of basaltic scoria: Insights into the transition from Strombolian to fire fountain activity at Mount Etna, Italy. Geology, 34 (3), 201–204.

Pompilio, M., Bertagnini, A., Del Carlo, P., Di Roberto, A. (2017). Magma dynamics within a basaltic conduit revealed by textural and compositional features of erupted ash: the December 2015 Mt. Etna paroxysms. Scientific Reports, 7, 4805.

Portnyagin, M., Almeev, R., Matveev, S., Holtz, F. (2008). Experimental evidence for rapid water exchange between melt inclusions in olivine and host magma. Earth and Planetary Science Letters, 272, 541–552.

Portnyagin, M., Mirinov, N., Botcharnikov, R., Gurenko, A., Almeev, R.R., Luft, C., Holtz, F. (2019). Dehydration of melt inclusions in olivine and implications for the origin of silica-undersaturated island-arc melts. Earth and Planetary Science Letters, 517, 95–105.

Privitera, E., Sgroi, T., Gresta, S. (2003). Statistical analysis of intermittent volcanic tremor associated with the September 1989 summit explosive eruptions at Mount Etna, Sicily. Journal of Volcanology and Geothermal Research, 120, 235-247.

Pyle, D. M. (2000). Sizes of volcanic eruptions, in H. Sigurdsson et al., eds, Encyclopedia of Volcanology, Academic Press, 263 - 269.

Qin, Z., Lu, F., Anderson, A.T. (1992). Diffusive reequilibration of melt and fluid inclusions. American Mineralogist, 77 (5-6), 565–576.

Ripepe, M., Marchetti, E., Delle Donne, D., Genco, R., Innocenti, L., Lacanna, G., Valade, S. (2018). Infrasonic early warning system for explosive eruptions. Journal of Geophysical Research: Solid Earth, 123, 9570–9585.

Richter, D., Eaton, J., Murata, K., Ault, W., Krivoy, H. (1970). Chronological narrative of the 1959–60 eruption of Kilauea Volcano, Hawaii. U.S. Geological Survey Professional Paper, 537-E. pp. E1–E73.

Romero, J.E., Vera., F., Polacci, M., Morgavi, D., Arzilli, F., Alam, M.A., Bustillos, J.E., Guevara, A., Johnson, J.B., Palma, J.L., Burton, M., Cuenca, E., Keller, W. (2018). Tephra From the 3 March 2015 Sustained Column Related to Explosive Lava Fountain Activity at Volcán Villarrica (Chile). Frontienrs in Earth Science, 6-98.

Rutherford, M.J., Hill, P.M. (1993). Magma ascent rates from amphibole breakdown: Experiments and the 1980–1986 Mount St. Helens eruptions. Journal of Geophyscal Research, 98, 19,667–19,685.

Rutherford, M. J. (2008). Magma Ascent Rates. In: Putirka, K.D., Tepley III, F., J., (eds) Minerals, Inclusions and Volcanic Processes. Reviews in Mineralogy and Geochemistry 69, Mineralogical Society of America, Chantilly, VA, USA, 241-271.

Sable, J.E., Houghton, B.F., Wilson, C. J. N. Carey, R. J. (2006). Complex proximal sedimentation from Plinian plumes: the example of Tarawera 1886. Bulletin of Volcanology, 69, 89.

Schiano, P., Clocchiatti, R., Ottolini, L., Busà, T. (2001). Transition of Mount Etna lavas from a mantle-plume to an island-arc magmatic source. Nature, 412, 900–904.

Schiavi, F., Bolfan-Casanova, N., Withers, A.C., Médard, E., Laumonier, M., Laporte, D.,Flaherty, T., Gómez-Ulla, A., 2018. Water quantification in silicate glasses by Ramanspectroscopy: correcting for the effects of confocality, density and ferric iron. Chemical Geology, 483, 312–33.

Shishkina, T.A., Botcharnikov, R.E., Holtz, F., Almeev, R.R., Jazwa, A.M., Jakubiak, A.A. (2014). Compositional and pressure effects on the solubility of H2O and CO2 in mafic melts. Chemical Geology, 388, 112–129.

Sigmundsson, F., Hooper, A., Hreinsdóttir, S. et al., (2015). Segmented lateral dyke growth in a rifting event at Bárðarbunga volcanic system, Iceland. Nature, 517, 191–195.

Sisson, T.W., Layne, G.D. (1993). H_2O in basalt and basaltic andesite glass inclusions from 4 subduction related volcanoes. Earth Planetary Science Letters, 117, 619–635.

Spilliaert, N., Allard, P., Metrich, N., Sobolev, A.V. (2006a). Melt inclusions record of the conditions of ascent, degassing, and extrusion of volatile-rich alkali basalt during the powerful 2002 flank eruption of Mount Etna (Italy). Journal of Geophysical Research, Solid Earth, 111, B04203.

Spilliaert, N., Allard, P., Métrich, N., Sobolev. A.V. (2006b). Melt inclusion record of the conditions of ascent, degassing and extrusion of volatile-rich alkali basalt during the powerful 2002 flank eruption of Mount Etna (Italy). Journal of Geophysical Research, 111, B04203.

Tanguy, J. C., Condomines, M., Kieffer, G. (1997). Evolution of Mount Etna Magma: constraint on the present feeding system and eruptive mechanism. Journal of Volcanology and Geothermal Research, 75, 221-250.

Tonarini, S., Armienti, P., D'Orazio, M., Innocenti, F. (2001). Subduction-like fluids in the genesis of Mt. Etna magmas: evidence from boron isotopes and fluid mobile elements. Earth and Planetary Science Letters, 192, 471–483.

Tucker, J.M., Hauri, E.H., Pietruszka, A.J., Garcia, M.O., Marske, J.P., Trusdell, F.A. (2019). A high carbon content of the Hawaiian mantle from olivine-hosted melt inclusions. Geochimica et Cosmochimica Acta, 254, 156–172.

Venugopal, S., Schiavi, F., Moune, S., Bolfan-Casanova, N., Druitt, T., Williams-Jones, G. (2020). Melt inclusion vapour bubbles: the hidden reservoir for major and volatile elements. Scientific Reports, 10, 9034.

Vergniolle, S., Jaupart, C. (1986). Separated twophase flow and basaltic eruptions. Journal of Geophysical Research, 91, 12842–12860.

Viccaro, M., Ferlito, C., Cortesogno, L., Cristofolini, R., Gaggero, L. (2006). Magma mixing during the 2001 event at Mt. Etna (Italy): effects on the eruptive dynamics. Journal of Volcanology and Geothermal Research 149, 139-159.

Viccaro, M., Cristofolini, R. (2008). Nature of mantle heterogeneity and its role in the short-term geochemical and volcanological evolution of Mt. Etna (Italy). Lithos 105, 272-288.

Viccaro, M., Nicotra, E., Millar, I.L., Cristofolini, R. (2011). The magma source at Mount Etna volcano: perspectives from the Hf isotope composition of historic and recent lavas. Chemical Geology, 281, 343-351.

Viccaro, M., Garozzo, I., Cannata, A., Di Grazia, G., Gresta, S. (2013). Gas burst vs. gas-rich magma recharge: a multidisciplinary study to reveal factors controlling

triggering of the recent paroxysmal eruptions at Mt. Etna. Journal of Volcanology and Geothermal Research, 278-279, 1-13.

Viccaro, M., Calcagno, R., Garozzo, I., Giuffrida, M., Nicotra, E. (2014). Continuous magma recharge at Mt. Etna during the 2011-2013 period controls the style of volcanic activity and compositions of erupted lavas. Mineralogy and Petrology 109, 67-83.

Viccaro, M., Zuccarello, F., Cannata, A., Palano, M., Gresta, S. (2016). How a complex basaltic volcanic system works. Constraints from integrating seismic, geodetic, and petrological data at Mount Etna volcano during the July–August 2014 eruption. Journal of Geophysical Research: Solid Earth, 121, 5659–5678.

Viccaro, M., Zuccarello, F. (2017). Mantle ingredients for making the fingerprint of Etna alkaline magmas: implications for shallow partial melting within the complex geodynamic framework of Eastern Sicily. Journal of Geodynamics, 109, 10–23.

Viccaro, M., Giuffrida, M., Zuccarello, F., Scandura, M., Palano, M., Gresta, S. (2019). Violent paroxysmal activity drives self-feeding magma replenishment at Mt. Etna. Scientific Reports, 9, 6717.

Von Aulock, F.W., Kennedy, B.M., Schipper, C.I., Castro, J.M., Martin, D.E., Watkins, J.M., Wallace, P.J., Puskar, L., Bégué, F., Nochols, A.R.L., Tuffon, H. (2014). Advances in Fourier transform infrared spectroscopy of natural glasses: From sample prepration to data analysis. Lithos, 206–207, 52–64.

Wallace, P.J., Kamenetsky, V.S., Cervantes, P. (2015). Melt inclusion CO_2 contents, pressures of olivine crystallization, and the problem of shrinkage bubbles. American Mineralogist, 100, 787–794.

Witham, F., Blundy, J., Kohn, S. C., Lesne, P., Dixon, J., Churakov, S. V., Botcharnikov, R. (2012). SolEx: a model for mixed COHSCl-volatile solubilities and exsolved gas compositions in basalt. Computers and Geosciences, 45, 87-97.

Zellmer, G. F., Blake, S., Vance, D., Hawkesworth, C., Turner, S. (1999). Plagioclase residence times at two island arc volcanoes (Kameni island, Santorini, and Soufriere, St. Vincent) determined by Sr diffusion systematics. Contribution to Mineralogy and Petrology, 136, 345-357.

Zhang, Y., Xu, Z., Zhu, M.,Wang, H. (2007). Silicate melt properties and volcanic eruptions. Reviews of Geophysics, 45, RG4004.

Zhang, Y., Ni, H. (2010). Diffusion of H, C, and O components in silicate melts. Reviews in Mineralogy and Geochemistry, 72, 171–225.